FLUORESCENCE DETECTION OF BIOLOGICAL THIOLS AND AXIALLY CHIRAL BODIPY DERIVATIVES & ALTERNATIVE METHODOLOGIES FOR SINGLET OXYGEN GENERATION FOR PHOTODYNAMIC ACTION

A DISSERTATION SUBMITTED TO
MATERIALS SCIENCE AND NANOTECHNOLOGY PROGRAM
OF THE GRADUATE SCHOOL OF ENGINEERING AND SCIENCE
OF BILKENT UNIVERSITY
IN PARTIAL FULFILLMENT OF THE REQUIREMENTS
FOR THE DEGREE OF
DOCTOR OF PHILOSOPHY

By
SAFACAN KÖLEMEN
September, 2014

I certify that I have read this thesis and that in my opinion it is fully adequate, in scope and in quality, as a thesis of the degree of Doctor of Philosophy.

…….

Prof. Dr. Engin U. Akkaya (Advisor)

I certify that I have read this thesis and that in my opinion it is fully adequate, in scope and in quality, as a thesis of the degree of Doctor of Philosophy.

…….

Prof. Dr. Metin Zora

I certify that I have read this thesis and that in my opinion it is fully adequate, in scope and in quality, as a thesis of the degree of Doctor of Philosophy.

…….

Assoc. Prof. Dr. Tamer Uyar

I certify that I have read this thesis and that in my opinion it is fully adequate, in scope and in quality, as a thesis of the degree of Doctor of Philosophy.

…….

Assoc. Prof. Dr. Özgür Altan Bozdemir

I certify that I have read this thesis and that in my opinion it is fully adequate, in scope and in quality, as a thesis of the degree of Doctor of Philosophy.

…….

Assist. Prof. Dr. Bilge Baytekin

Approved for the Graduate School of Engineering and Science:

…….

Prof. Dr. Levent Onural

Director of the Graduate School of Engineering and Science

ABSTRACT

FLUORESCENCE DETECTION OF BIOLOGICAL THIOLS AND AXIALLY CHIRAL BODIPY DERIVATIVES &
ALTERNATIVE METHODOLOGIES FOR SINGLET OXYGEN GENERATION FOR PHOTODYNAMIC ACTION

SAFACAN KÖLEMEN

PHD IN MATERIALS SCIENCE AND NANOTECHNOLOGY

SUPERVISOR: PROF. DR. ENGİN UMUT AKKAYA

SEPTEMBER, 2014

Calorimetric and luminescent detection of biological thiols namely cysteine (Cys), homocysteine (Hcy) and glutathione (GSH) have attracted great interest due to the their biological significance. There are many reported fluorescent probes for Cys and Hcy, however selective probe designs for GSH remained elusive. We represented in thesis (Chapter 3) a BODIPY based selective fluorescent probe for the *in vitro* detection of GSH in cancer cell lines. Photodynamic therapy (PDT) is one of the promising and developing treatment modality for certain indications. Therapeutic action is achieved by the generation of cytotoxic singlet oxygen (SO). Most critical compartment of SO production pathway is the sensitizer molecule. In order to get effective inter-system crossing, which is highly needed for singlet oxygen generation, common strategy is to incorporate heavy atoms on sensitizers. However, presence of heavy atoms increases the dark toxicity that is not desired in clinical applications. In Chapter 4, we are introducing a new concept for activatable heavy atom free sensitization of PDT by designing novel orthogonal BODIPY derivatives and detailed computational analysis of this new concept. While dealing with orthogonal BODIPYs, we synthesized for the first time two axially chiral BODIPY derivatives and characterized the enantiopure products, which holds great promise for enantioselective sensing applications (Chapter 5). PDT has two major problems, which are light penetration depth of the incident light and the hypoxia. These two restrictions are addressed in chapter 6, by combining gold nanorods and aromatic endoperoxides.

Keywords: GSH probe, axial chirality, photodynamic therapy, singlet oxygen, gold nanorods/endoperoxides

ÖZET

BİYOLOJİK TİYOLLERİN FLORESAN TAYİNİ VE AKSİYAL KİRAL BODIPY TÜREVLERİ & FOTODİNAMİK ETKİ İÇİN ALTERNATİF YOLLAR İLE SİNGLET OKSİJEN ÜRETİMİ

SAFACAN KÖLEMEN

MALZEME BİLİMİ VE NANOTEKNOLOJİ, DOKTORA

TEZ YÖNETİCİSİ: PROF. DR. ENGİN UMUT AKKAYA

EYLÜL, 2014

Biyolojik tiyoller sistein (Cys), homosistein (Hcy) ve glütatyonun (GSH) floresan moleküler ajanlar ile tayin edilmesi, bu tiyollerin taşıdıkları biyolojik rollerden ötürü çok büyük önem arz etmektedir. Literatürde yer alan pek çok çalışmada Cys ve Hcy tayini için dizayn edilmiş ajanlar bulunabilmektedir. Ancak GSH için seçici floresan moleküler görüntüleme ajanları çok az sayıdadır. Bu tez kapsamında GSH'ın kanser hücre kültürleri içerisindeki tayini seçici olarak BODIPY tabanlı floresan boya yardımı ile yapılmıştır (Bölüm 3). Fotodinamik terapi (PDT) fazlaca umut vaat eden ve gelişmekte olan bir kanser tedavi yöntemidir. PDT kapsamındaki terapatik etki zararlı singlet oksijen (SO) üretimi ile gerçekleşmektedir. SO üretimi sırasında yer alan parçalardan en önemlisi duyarlaştırıcı moleküldür. SO elde edilmesi için gerekli olan sistemler arası geçişin sağlanabilmesi için sıklıkla uygulanan dizayn prensibi duyarlaştırıcı molekülü ağır atomlar ile modifiye etmektir. Ancak ağır atomların varlığı duyarlaştırıcının uyarıcı ışık olmaksızın toksik etki göstermesine neden olmaktadır. Bu doğrultuda bölüm 4'te yer alan çalışmalarda ağır atom içermeyen ve sadece kanserli hücrede aktifleşebilen yeni duyarlaştırıcı dizaynları ve ortaya çıkarılan yeni konseptin detaylı teorik çalışması sunulmuştur. BODIPY kimyası üzerinde yürüttüğümüz çalışmalar sonunda ilk kez aksiyal kiral özelliğe sahip BODIPY türevleri tasarlamış, sentezlenmiş ve karakterize edilmiştir. PDT mekanizmasının iki önemli problemi mevcuttur. Bunlar uyarma ışığının dokulardan kısıtlı bir miktarda geçiş yapması ve hipoksiyadır. Bölüm 6'da altın nanoçubuklar ve aromatik endoperoksitler yardımı ile bu sorunlara çözüm sunulmaktadır.

Anahtar Kelimeler: GSH ajanı, aksiyal kiral, fotodinamik terapi, singlet oksijen, altın nanorod/endoperoksit

Dedicated to my mother and father

ACKNOWLEDGEMENTS

I would like to start acknowledgement part with my PhD supervisor Prof. Engin U. Akkaya, whom I will definitely miss after finishing my studies at Bilkent University. He is the smartest, foreseeing, enthusiastic, kind and the funniest person that I have ever met. I feel proud and lucky for being a member of his research group. With immense respect, I would like to express my gratitude to him for his guidance, support, patience and for teaching us how to become a good scientist and more importantly a good person. I would also like to thank him for always giving us the opportunity to try new things and pursue our own ideas. I appreciate all his contributions, discussions and valuable thoughts to make my PhD experience productive and sensational. I will never forget him and his support throughout my life.

I am sincerely grateful to my PhD thesis progress committee members, Prof. Metin Zora and Assoc. Prof. Dr. Tamer Uyar for their valuable advices and fruitful discussions.

I owe a special thank to Assoc. Prof. Dr. Özgür Altan Bozdemir for him endless help and support, guidance to improve my skills in the field of supramolecular and organic chemistry as well as his unlimited knowledge and experience that I have benefited from greatly. I would also like to express my graduate for him for his valuable friendship.

I would like to express my special thanks to Dr. Yusuf Çakmak, Dr. Ruslan Guliyev, Dr. Murat Işık, Yiğit Altay, Tuğçe Karataş, Ziya Köstereli and Cpt. Bilal Kılıç for their partnership in my PhD studies. Their support patience and contributions are so valuable and unforgettable.

I am sincerely grateful to my close friend Tuğba Özdemir Kütük. She made my PhD period joyful, tolerable and easy with her precious friendship, endless support, everlasting help and understanding. I am sure everything would have been much difficult without her. I will thoroughly miss working with her.

I want to thank our present and past group members Dr. Fazlı Sözmen, Dr. Sündüs Erbaş Çakmak, Dr. Esra Tanrıverdi, Dr. Onur Büyükçakır, Dr. Serdar Atılgan, Dr. Ali Çoşkun, Taha Bilal Uyar, Ahmet Atılgan, Tuba Yaşar, Tuğçe Durgut, Nisa Yeşilgül, Sencer&Hande Selçuk, Hale Atılgan, Jose Bila, Ceren Çamur, Darika Okeava, Cansu Kaya, Melek Baydar, Veli Polat, Ahmet Bekdemir, Elif Ertem, Şeyma Öztürk Guliyeva, Dr. Dilek Taşgın, Işın Sakallıoğlu, Dr. Özlem Seven, Seylan Ayan, Özge Yılmaz, İlke Şimşek Turan, Dr. Seda Demirel, Deniz Yıldız and rest of the SCL (Supramolecular Chemistry Laboratory) members for great friendships, wonderful collaborations, and perfect ambiance in the laboratory. They are very precious for me. It was wonderful to work with them.

I also would like to thank Dr. Yavuz Dede, Muhammed Buyuktemiz and Selin Duman for breakthrough computational studies, helpful discussions and collaborations.

I am grateful to Dr. Lale Doğan, Dr. Dicle Güç, Dr. Turgay Tekinay, Dr. Juyoung Yoon and Berna Şentürk for their impressive efforts during the cell culture studies.

My thanks also go out to Bora Bilgiç for fantastic and creative graphical designs. I also wish to express my warm and sincere thanks to my friends İlker Kütük, Oya Ertunç Bilgiç, Dr. Görkem Günbaş, Dr. Asuman Günbaş, and Nurhan&Reşat Çiftçi for being with me all the time.

Special thanks are extending to my beloved mother Filiz Kölemen and father Fikret Kölemen for their infinite support, huge love and understanding. It is really reassuring to known that there are always some people waiting there for you.

During the last four years, a lot of things have changed in my life but the most beautiful change happened when I met with Birsu Teoman (soon to be Kölemen). Finally and most importantly, with great love, I would like to thank my intended wife for her understanding, love, patience, tolerance and support. It would not have been possible to write this thesis without her apprehension and help.

Finally I would like to thank TUBITAK for financial support (project no: 113T029).

LIST OF ABBREVIATIONS

BODIPY	**:**	4,4-difluoro-4-bora-3a,4a-diaza-s-indacene
CASSCF	**:**	Complete active-space self consistent field methodology
$CHCl_3$	**:**	Chloroform
DCM	**:**	Dichloromethane
DS-TR	**:**	Doubly substituted-tetra radicalic
DFT	**:**	Density functional theory
ISC	**:**	Intersystem crossing
FRET	**:**	Förster resonance energy transfer
HOMO	**:**	Highest occupied molecular orbital
LUMO	**:**	Lowest unoccupied molecular orbital
MALDI	**:**	Matrix-assisted laser desorption/ionization
MS	**:**	Mass spectrometry
NMR	**:**	Nuclear magnetic resonance
NOON	**:**	Natural orbitals and occupation numbers
PDT	**:**	Photodynamic therapy
PS	**:**	Photosensitizer
SS	**:**	Singly substituted
SOMO	**:**	Singly occupied molecular orbital
TLC	**:**	Thin layer chromatography

TABLE OF CONTENTS

1. INTRODUCTION 1

2. BACKGROUND 6

2.1. Fluorescent Molecular Sensors 6

2.1.1. General Information 6

2.1.2. Overview of Fluorescence 8

2.1.3. Fluorescent Probes 9

2.2. BODIPY Dyes 12

2.3. Photophysics of Sensing Mechanism 16

2.3.1. Photo-induced Electron Transfer (PeT) 16

2.3.2. Photo-induced Charge Transfer (PCT) 18

2.3.3. Fluorescence Resonance Energy Transfer (FRET) 20

2.3.4. Excimer Formation 21

2.3.5. Aggregation Induced Emission (AIE) 21

2.4. Detection of Biological Thiols 22

2.4.1. Michael Addition 23

2.4.2. Cyclization with Aldehydes 27

2.4.3. Conjugate Addition & Cyclization 28

2.4.4. Cleavage of Sulfonamide and Sulfonate Esters 28

2.4.5. Thiol-Halogen Nucleophilic Substitution 29

2.4.6. Disulfide Exchange Reaction 30

2.4.7. Metal Complexation 30

2.5. Photodynamic Therapy 31

2.5.1. General Information 31

2.5.2. Milestones of PDT 32

2.5.3. Mechanism of PDT Action 33

2.5.4. Basic Components of PDT 36

2.5.5. PDT Effects on Tumors 37

2.6. Triplet Photosensitization for PDT: Design Principles 39

2.6.1. Heavy Atom Effect 40

2.6.2. Heavy Atom Free Photosensitization 41

2.6.3. Chromophores with Low-Lying n-π* Transitions 42

2.6.4. Exciton Coupling 43

2.6.5. Spin Convertors 44

2.6.6. Glutathione Mediated Activation of PDT Sensitizers and Low pH of Cancer Cells 45

2.7. Axial Chirality 48

2.7.1. Atropisomerism 50

2.7.2. Chiral BODIPY Dyes 52

2.8. Polycyclic Aromatic Endoperoxides 54

2.8.1. Preparation of Endoperoxides 55

2.8.2. Thermolysis of Endoperoxides 56

2.9. Gold Nanorods 58

2.9.1. Preparation of Gold Nanorods 60

2.9.2. Functionalization of Gold Nanorods 62

2.9.3. Plasmonic Properties and Photothermal Conversion 63

3. Selective Fluorescence Sensing of Glutathione Using a Bifunctional Probe 67

3.1. Objective 68

3.2. Introduction 68

3.3. Results and Discussion 70

3.4. Experimental Details 77

3.5. Conclusion 83

4. Activatable Heavy Atom Free Sensitizers for Photodynamic Therapy Application 85

4.1. Singlet Oxygen Generation by Using Heavy Atom Free Orthogonal BODIPY Derivatives 86

4.1.1. Objective 86

4.1.2. Introduction 86

4.1.3. Results and Discussion 88

4.1.4. Experimental Details 105

4.1.5. Conclusion 116

4.2. Activatable Heavy Atom Free Sensitizers: Selective Enhancement of Photocytotoxicity 117

4.2.1. Objective 117

4.2.2. Introduction 117

4.2.3. Results and Discussion 118

4.2.4. Experimental Details 131

4.2.5. Conclusion 141

5. Axially Chiral BODIPY Derivatives 142

5.1. Objective 143

5.2. Introduction 143

5.3. Results and Discussion 144

5.4. Experimental Details 148

5.5. Conclusion 152

6. Controlled Singlet Oxygen Generation on Gold Nanorods: Advancing Photodynamic Therapy 153

6.1. Objective 154

6.2. Introduction 154

6.3. Results and Discussion 157
6.4. Experimental Details 164
6.5. Conclusion 168
7. CONCLUSION 169
BIBLIOGRAPHY 173
APPENDIX 187

LIST OF FIGURES

Figure 1. Tsien's Ca^{2+} probe.[4] 7

Figure 2. The Jablonski diagram. 8

Figure 3. Stokes shift. 9

Figure 4. Molecular structures of common fluorescent probes. 11

Figure 5. Molecular structures of BODIPY and its precursors. 12

Figure 6. Synthetic pathways for *meso*-functionalized symmetric BODIPYs. 13

Figure 7. Synthetic pathways for *meso*-unsubstituted symmetric BODIPYs. 14

Figure 8. Functionalization of 3,5 and 1,7 positions by Knoevenagel condensation reaction. Copyright © 2009, American Chemical Society. Reprinted with permission from ref (41).[41] 16

Figure 9. Schematic representation of PeT. Copyright © 2009, Royal Society of Chemistry. Reprinted with permission from ref (62).[62] 17

Figure 10. Schematic representation of reverse-PeT. 18

Figure 11. Some PeT based fluorescent probes. 18

Figure 12. Schematic representation of PCT. Copyright © 2007, American Chemical Society. Reprinted with permission from ref (2). 19

Figure 13. Some PCT based probes. 20

Figure 14. 1-methyl-1,2,3,4,5-pentaphenylsilole **(13)** as an AIE probe. 21

Figure 15. Molecular structures of bio-thiols. 22

Figure 16. Maleimide substituted probes for bio-thiol detection. 23

Figure 17. Coumarin and fluorescein based Michael addition mechanism for selective detection of bio-thiols. 24

Figure 18. Intracellular detection of Cys via Michael addition. 25

Figure 19. BODIPY based probes for selective Cys detection. 26

Figure 20. A FRET based chemodosimeter. 26

Figure 21. Coumarin based detection of bio-thiols via cyclization mechanism. 27

Figure 22. Conjugate addition and cyclization approach for Cys detection. 28

Figure 23. Cleavage of sulfonate ester bonds with bio-thiols. 29

Figure 24. BODIPY based thiol-halogen substitution. 29

Figure 25. Disulfide exchange reaction mechanism on a naphthalimide derivative.. 30

Figure 26. Metal complexation approach for the detection of bio-thiols. 31

Figure 27. Molecular structures of Photofrin and Foscan. 33

Figure 28. Modified Jablonski diagram. 36

Figure 29. Heavy atom mediated ISC. 40

Figure 30. Near-IR absorbing, water-soluble BODIPY sensitizer. 41

Figure 31. Charge transfer mediated ISC. 43

Figure 32. BODIPY based exciton-coupling behavior. 43

Figure 33. BODIPY-C_{60} conjugate. Copyright © 2012, American Chemical Society. Reprinted with permission from ref (127).[127] 44

Figure 34. GSH activated phthalocyanine sensitizer. 46

Figure 35. GSH activated graphene oxide-chlorine 6 conjugate for PDT. Copyright © 2012, Royal Society of Chemistry. Reprinted with permission from ref (136). 47

Figure 36. Some common molecules with axial chirality. 48

Figure 37. Schematic representation of axially chiral plane. 48

Figure 38. Schematic representation of atropisomerism. 50

Figure 39. Nomenclature of atropisomeric compounds. 51

Figure 40. Enantioselective detection of α-Hydroxycarboxylic acids. 52

Figure 41. Boron asymmetry on a BODIPY dye. Copyright © 2010, American

Chemical Society. Reprinted with permission from ref (148).[148] 53

Figure 42. Molecular structure of binaphthalene-BODIPY conjugate. 53

Figure 43. Axially chiral BODIPY derivatives. 54

Figure 44. Synthesis of aromatic endoperoxides. 55

Figure 45. Thermolysis pathways for aromatic endoperoxides. 56

Figure 46. Activation parameters for the thermolysis of various aromatic endoperoxides and singlet oxygen generation yields. 57

Figure 47. Formation and decomposition of naphthalene based endoperoxides. 58

Figure 48. Temperature dependence of anthracene **(51)** thermolysis. Copyright © 2008, Elsevier. Reprinted with permission from ref (160). [160] 58

Figure 49. Comparative LSPR peaks of nano-sphere, shell and rod. Copyright © 2010, John Wiley and Sons. Reprinted with permission from ref (166).[166] 60

Figure 50. Preparation of gold NRs according to El-Sayed's seed mediated synthesis. Copyright © 2009, John Wiley and Sons. Reprinted with permission from ref (164)[164] 61

Figure 51. Control of plasmonic properties by adjusting the aspect ratio of NRs. Copyright © 2013, Royal Society of Chemistry. Reprinted with permission from ref (165) [165] 64

Figure 52. Selective photothermal therapy of cancer cells with anti-EGFR/Au. At 80 mW cancer cells (HSC and HOC) are injured while there is no effect on healthy cells (HaCat) Copyright © 2006, American Chemical Society. Reprinted with permission from ref (183). 65

Figure 53. Schematic illustration of gold nanorods-PDT complex for NIR imaging and PDT. Copyright © 2011, American Chemical Society. Reprinted with permission from ref (184). 66

Figure 54. The structure and the signal modulation sites of the target probe. The distance between the terminal amine and the thiol suggests a much better match for GSH and the probe, than the other two biological thiols. Copyright © 2014, American Chemical Society. Reprinted with permission from ref (185). 69

Figure 55. Synthetic route for the synthesis of GSH probe **(Dye 1)**. Copyright ©

2014, American Chemical Society. Reprinted with permission from ref (185). 70

Figure 56. Absorbance spectra of **(Dye 1)** (8.0×10^{-6} M) and **(Dye 1)** + Thiols (200 equivalents) at pH 6.0 in 60% MES Buffer (30 mM) / 40% MeCN and at pH 7.4 in 60% MOPS Buffer (30 mM) / 40% MeCN. Copyright © 2014, American Chemical Society. Reprinted with permission from ref (185). 71

Figure 57. Partial ^{1}H-NMR (in CD_3OD, 298 K) spectra depicting the changes on GSH conjugate addition to the **(Dye 1)**: The adduct was isolated by preparative HPLC following a room temperature reaction of the probe and GSH in aqueous acetonitrile. *Trans*-coupled protons disappear in the product, and the azacrown peaks show a more spread out cluster of peaks, suggesting an emergence of non-covalent, non-symmetric interaction. Copyright © 2014, American Chemical Society. Reprinted with permission from ref (185). 72

Figure 58. Emission response to biological thiols at two different pH values, 7.4 (left, 60:40, 30 mM MES buffer/acetonitrile) and 6.0 (right, 60:40, 30 mM MOPS buffer/acetonitrile). Small change in pH causes more than 5-fold increases in emission intensity for the GSH – **(Dye 1)** adduct. For Cys and Hcy, the change is approximately 2.5 fold. The concentrations of the thiols and other amino acids (Gly, His, Ile, Leu, Met, Phe, Pro, Ser, Thr, Tyr, Val) were 1.6 mM and the **(Dye 1)** concentration was 8.0 μM. Excitation was at 500 nm, with 5 nm slit-widths. Copyright © 2014, American Chemical Society. Reprinted with permission from ref (185). 73

Figure 59. Selective emission response of the **(Dye 1)**. Blue bars correspond to the emission enhancement ratios (Io being the emission intensity of the probe) when biological thiols are introduced at their respective intracellular concentrations[79,196,197] in aqueous medium (60:40, pH 6.0, 30 mM MOPS buffer/acetonitrile) with 8.0 μM **(Dye 1)** concentration. Red bars show the emission enhancement when all analytes are introduced at 1.6 mM, in the same solvent system and probe concentration. Excitation was at 500 nm, emission data at 522 nm (I and I_0) were used in calculations. Copyright © 2014, American Chemical Society. Reprinted with permission from ref (185). 74

Figure 60. Electronic absorption and emission spectra of **(Dye 1)** (8.0 μM) in 30 mM MES:CH_3CN (60:40, v/v, pH=6.0, 25 °C) in increasing GSH concentrations (0 to 500 eq.). Excitation wavelength is 500 nm. Copyright © 2014, American Chemical Society. Reprinted with permission from ref (185). 75

Figure 61. Following synthetic route was pursued to get **(Dye 3)**. Copyright © 2014, American Chemical Society. Reprinted with permission from ref (185). 75

Figure 62. The structures of control BODIPY (**Dye 2)** and **(Dye 3)**. **(Dye 2)** has a binding site for ammonium moiety, but no reactive group for thiols. (left) **(Dye 3)** is thiol reactive, but it does not have a site for ammonium recognition. (right) Dye concentrations were 8.0 μM, and the biological thiols were introduced at 1.6 mM. Aqueous buffer solutions were used as solvents, for pH 7.4 (60:40, 30 mM MES buffer/acetonitrile) and for pH 6.0 (60:40, 30 mM MOPS buffer/acetonitrile). Excitation was at 500 nm, with 5 nm slit-widths. Copyright © 2014, American Chemical Society. Reprinted with permission from ref (185). 76

Figure 63. Time-lapse confocal microscopy pictures of Human breast adenocarcinoma cells (MCF-7) cells incubated with **(Dye 1)** at 0.5 μM (a: 0 min, b: 1 min, c: 120 min). d, e, 120 min, fluorescence, optical images and f: merged image. Human umbilical vein endothelial cells (HUVEC) cells pre-treated with 5 mM BSO (g), DIC image (h), merge (i). The selective inhibition of GSH synthesis reduces fluorescence emission from the cells to a very low level, attesting the selectivity of the designed probe. Copyright © 2014, American Chemical Society. Reprinted with permission from ref (185). 77

Figure 64. Frontier molecular orbitals. HOMO (left) LUMO (right), of the parent BODIPY core at B3LYP/6-31G(d,p) level of theory. Surfaces are plotted at 0.2 a.u. Copyright © 2011, John Wiley and Sons. Reprinted with permission from ref (121)..... 88

Figure 65. Orthogonal BODIPY designs. Copyright © 2011, John Wiley and Sons. Reprinted with permission from ref (121). 89

Figure 66. Structures of the dimeric Bodipys. a) X-ray diffraction structure of the orthogonal 8,2' dimer **(3)**. b) Optimized geometry of orthogonal 8,8' dimer **(6)** at CAS(6e in 6o)/cc-pVDZ level. Dihedral angle between the two Bodipy units is very close (± 0.5^{o}) to 90^{o} in both dimers. Copyright © 2011, John Wiley and Sons. Reprinted with permission from ref (121)..... 89

Figure 67. Building up bis-BODIPY S_1 wave function. MO energies are 90

Figure 68. Left: (Top) BODIPY HOMO and LUMO. (Bottom) Frontier orbitals and natural orbital occupation numbers of S_1 states of dimers **(3)** and **(6)**. Right: Leading configurations of S_0, S_1, and T_1 CASSCF wave functions for **(3)** and **(6)**. Copyright © 2012, American Chemical Society. Reprinted with permission from ref (227)..... 91

Figure 69. Synthesis of the target photosensitizers. a) $POCl_3$, DMF, $ClCH_2CH_2Cl$,

$50^{o}C$; b) 2,4-dimethylpyrrole, trifluoroacetic acid (TFA), CH_2Cl_2, p-chloranil, Et_3N, $BF_3 \cdot OEt_2$; c) TFA, CH_2Cl_2, *p*-chloranil, Et_3N, $BF_3 \cdot OEt_2$. Copyright © 2011, John Wiley and Sons. Reprinted with permission from ref (121)..... 92

Figure 70. Singlet oxygen phosphorescence with sensitization from BODIPY derivatives: **(3)** (blue), **(6)** (black) and **(7)** (red), **(1)** (green) in $CHCl_3$ at equal absorbances (0.2) at the peak wavelength of their respective absorbances. Copyright © 2011, John Wiley and Sons. Reprinted with permission from ref (121). 93

Figure 71. Comparative singlet oxygen generation experiment. Absorbance decrease of DPBF at 414 nm with time in dichloromethane in the presence of BODIPY photosensitizers: **(3)** (black), **(6)** (blue), **(7)** (red) and reference photosensitizer methylene blue (green). Copyright © 2011, John Wiley and Sons. Reprinted with permission from ref (121). 94

Figure 72. Singlet oxygen generation experiment in aqueous solution. Decrease in Absorbance spectrum of trap molecule (anthracene derivative) in the presence of 1.69 μM compound **(3)** in phosphate buffer saline (PBS). Details are given in singlet oxygen measurements part. Copyright © 2011, John Wiley and Sons. Reprinted with permission from ref (121). 95

Figure 73. Photocytotoxicity of the sensitizer **(3)** as demonstrated by MTT assay. Cell suspensions (K562, human erythroleukemia cells) were seeded in 96-well flat-bottom plates and varying concentrations of the sensitizers were added into each well. Cells were kept either in dark, or under illumination with a green (520 nm) LED array at 2.5 mW/cm^2 fluence rate for a period of 4 h at 37^0C in a humidified incubator containing 5% CO_2. Copyright © 2011, John Wiley and Sons. Reprinted with permission from ref (121)..... 96

Figure 74. Photocytotoxic activity of the dimeric BODIPY **(3)** visualized via confocal microscopy. Cell suspensions (K562, human erythroleukemia cells) were seeded in 24-well plates. a, Cells in Control 1 (upper plates) wells were incubated in dark for 24 hours; b, Cells in Control 2 wells (second row plates) were incubated with 500 μl/well Cremophor-EL solubilized **(3)** (at a final concentration of 164 nM) and kept in dark for 24 hours in the same incubator, c, Cells in Control 3 well were illuminated for 4 h without the sensitizer and incubated for a further 20 h in dark at the incubator. d, Cells in Control 4 (bottom row of plates) well were illuminated for 4 h after addition of 164 nM **(3)** and incubated for a further 20 h in dark at the incubator. Cells in wells were collected after 24 h and imaged at 40x magnification. Live cells are preferentially stained with acridine orange (AO, green) (a), whereas dead cells

are preferentially stained with the dye propidium iodide (PI, red) due to increased cellular permeability (b). Copyright © 2011, John Wiley and Sons. Reprinted with permission from ref (121). 97

Figure 75. Effect of inter-plane angle (θ) variation on $S_0 \rightarrow S_1$ excitation characteristics (DS-TR/SS). Copyright © 2012, American Chemical Society. Reprinted with permission from ref (227). 98

Figure 76. Synthesis of **(bis-10a')**. Copyright © 2012, American Chemical Society. Reprinted with permission from ref (227). 99

Figure 77. Electronic absorption spectrum of **(bis-10a')**. Copyright © 2012, American Chemical Society. Reprinted with permission from ref (227). 99

Figure 78. The set of monomers and dimers studied. Copyright © 2012, American Chemical Society. Reprinted with permission from ref (227). 100

Figure 79. Selected natural orbitals and occupation numbers for **(bis-9)**, **(bis-10)** and **(bis-10a)**. Calculations were done at CAS(6,6)/CEP-31G//(U)B3LYP/CEP-31G level. Copyright © 2012, American Chemical Society. Reprinted with permission from ref (227). 103

Figure 80. Relation of DS-TR character of S_1 to the extent of π conjugation in butadienyl- and styryl-substituted BODIPY dimers **(bis-9′)** and **(bis-10′)**. Copyright © 2012, American Chemical Society. Reprinted with permission from ref (227). 104

Figure 81. Size distribution of compound micellar compound **(3)**. Cremophor EL was used for embedding the dye. Copyright © 2011, John Wiley and Sons. Reprinted with permission from ref (121). 109

Figure 82. Reaction of singlet oxygen with 1,3-Diphenylisobenzofuran. 110

Figure 83. Reaction of singlet oxygen with 2,2'-(Anthracene-9,10-diylbis(methylene))dimalonic acid..... 110

Figure 84. Decrease in absorbance of DPBF in dichloromethane in the presence of compound **(3)** in medium. Details are given in singlet oxygen measurements part. Copyright © 2011, John Wiley and Sons. Reprinted with permission from ref (121)..... 111

Figure 85. Decrease in absorbance of DPBF in dichloromethane in the presence of compound **(6)** in medium. Details are given in singlet oxygen measurements

part. Copyright © 2011, John Wiley and Sons. Reprinted with permission from ref (121). 111

Figure 86. Decrease in absorbance of DPBF in dichloromethane in the presence of compound **(7)** in medium. Details are given in singlet oxygen measurements part. Copyright © 2011, John Wiley and Sons. Reprinted with permission from ref (121). 112

Figure 87. Decrease in absorbance of DPBF in dichloromethane in the presence of MB in medium. Details are given in singlet oxygen measurements part. Copyright © 2011, John Wiley and Sons. Reprinted with permission from ref (121). 112

Figure 88. Packing diagrams of compound **(3)**. Dashed lines indicate inter H-bond between C2 and F4 atoms. Copyright © 2011, John Wiley and Sons. Reprinted with permission from ref (121). 113

Figure 89. Design principles (top) and Orbital energies (eV) and plots of (**PS)** and **(actPS)** relevant to the CT excitation from BODIPY to methylpyridinium (bottom). 119

Figure 90. Synthesis of activatable sensitizer **(PS)**. 121

Figure 91. Reduction of compound **(PS)** in the presence of mercaptoethanol. ^{1}H NMR spectra of **(PS)** and **(actPS)**. HR-MS spectrum of **(actPS)** (Δ (ppm) = 4.9 ppm). 122

Figure 92. Normalized electronic absorption spectra of **(dimBDY)**, **(pydimBDY)**, **(PS)** and **(actPS)** in DCM. 123

Figure 93. Relative $^{1}O_2$ generation efficiency of top: **(dimBDY)**, **(PS)** and **(actPS)** in DCM and bottom: **(PS)** and **(actPS)** in 90:10 (Hepes buffer, pH 7.2, 20mM : MeCN) detected by the absorbance decrease of DPBF at 414 nm and 2'-(Anthracene-9,10 diylbis(methylene))dimalonic acid (ADMDA) at 378 nm respectively with time. During first 60 seconds (right) and 15 minutes (left), the samples were kept in the dark. 124

Figure 94. Left: The T_1-T_n transient absorption spectra of **(actPS)** in argon saturated THF and MeCN with laser excitation at 355 nm (the absorbance at 355 nm is 0.402). Right: The decay of triplet state T_1 of **(actPS)** at 425 nm in argon saturated THF and MeCN with laser excitation at 355 nm (the absorbance at 355 nm is 0.402). The triplet lifetimes are 8.7 μs (MeCN) and 27.6 μs (THF). 125

Figure 95. Comparison of electronic absorption spectrum of left: **(PS)** (30μM) and **(PS)** (30μM)+ GSH (5mM), right: **(PS)** (25μM) and **(PS)** (25μM) + Cys (25μM) & Hcy (25μM) in 90:10 (Hepes buffer, pH 7.2, 20mM : MeCN). Reaction time is 12 hours in all cases. 127

Figure 96. Photocytotoxicity of the sensitizer **(PS)** (blue) and **(actPS)** (red) as demonstrated by MTT assay. Cells were kept either in the dark (bottom), or under illumination with a green (520 nm) LED array (top). 128

Figure 97. Cytotoxic effects of sample **(PS)** (blue), **(actPS)** (red). Cells were incubated with **(PS)**, **(actPS)** for 4 hr and irradiated with green LED. Cytotoxic effects were examined by MTT assay. Normal cell lines : NIH 3T3, WI38 VA13, cancer cell lines : HeLa, SK Hep 1. 128

Figure 98. The HeLa cells were incubated with **(PS)**, **(actPS)** for 4 hrs. Cells were irradiated with green LED for 30 min and incubated another 3 hrs or kept under dark and stained with Annexin V-AF594 (apoptosis marker). Fluorescence images were acquired by confocal microscopy. For nucleus stain, 1 μg/ml DAPI costained for 30 min. (a) DAPI (ex. 405 nm, em. 430-455 nm), (b) **(PS)**, **(actPS)** (ex. 473 nm, em. 490-590 nm), (c) Annexin V-AF594 (ex. 559 nm, em. 575-675 nm), (d) DIC, (e) Merge. Scale bar: 10 μm 129

Figure 99. Michael addition of mercaptoethanol to compound **(PS)** in the absence of base in aqueous solution (90:10 (HEPES buffer, pH 7.2, 20mM : MeCN)). HR-MS spectrum of **(Michael adduct)** (Δ (ppm) = 31.8 ppm). 130

Figure 100. The normalized fluorescence emission spectra of **(dimBDY)**, **(pydimBDY)**, and **(PS)** in DCM. 132

Figure 101. The normalized fluorescence emission spectra of **(actPS)** in different solvents with excitation at 418 nm (absorbance 0.090). 132

Figure 102. Fluorescence decay of **(actPS)** in EtOH with excitation at 509 nm diode laser (150 *ps*), the emission was monitored at 520 nm, the concentration of dyes is ca. 3.0 μM. 133

Figure 103. Decrease in absorbance of DPBF in DCM in the presence of **(dimBDY)** ($1X10^{-6}$ M). Excitation @508 nm. 135

Figure 104. Decrease in absorbance of DPBF in DCM in the presence of **(PS)** ($1X10^{-6}$ M). Excitation @508 nm. 135

Figure 105. Decrease in absorbance of DPBF in DCM in the presence of **(PS)** ($1X10^{-}$

^{6} M). Excitation @607 nm. 135

Figure 106. Decrease in absorbance of ADMDA in 90:10 (20 mM Hepes buffer:MeCN) in the presence of **(PS)** (1X10^{-6} M). Excitation @513 nm. 136

Figure 107. Decrease in absorbance of ADMDA in 90:10 (20 mM Hepes buffer:MeCN) in the presence of **(PS)** (1X10^{-6} M). Excitation @590 nm. 136

Figure 108. Decrease in absorbance of DPBF in DCM in the presence of **(actPS)** (1X10^{-6} M). Excitation @511 nm. 136

Figure 109. Decrease in absorbance of ADMDA in **90:10 (20 mM Hepes buffer:MeCN)** in the presence of **(5r) (1X10^{-6} M).** Excitation @508 nm..... 137

Figure 110. Synthesis of the atropisomeric BODIPY derivative **(4)** and **(5)**. As expected, **(4)** and **(5)** are produced as racemates. For both **(4)** and **(5)** (*R*) enantiomers are depicted. Copyright © 2014, American Chemical Society. Reprinted with permission from ref (150). 144

Figure 111. HPLC separation of compound **(4)** to **(4a)** (20.3 min) and **(4b)** (33.4 min), (95% / 5 %, heptane / IPA, detection @270 nm) (top), and compound **(5)** to **(5a)** (18.5 min) and **(5b)** (20.6 min), (98% / 2%, heptane / ethanol, detection @510 nm) (bottom). Copyright © 2014, American Chemical Society. Reprinted with permission from ref (150). 145

Figure 112. Electronic absorption (red) and emission (blue) spectra of **(4)** (left) and **(5)** (right). Ext @ 500 nm for **(4)** and 510 nm for **(5)**. Copyright © 2014, American Chemical Society. Reprinted with permission from ref (150). 146

Figure 113. Electronic absorption (red) and emission (blue) spectra of **(4a)**(left) and **(4b)** (right). Ext @ 500 nm. Copyright © 2014, American Chemical Society. Reprinted with permission from ref (150). 146

Figure 114. Electronic absorption (red) and emission (blue) spectra of **(5a)** (left) and **(5b)** (right). Ext @ 510 nm. Copyright © 2014, American Chemical Society. Reprinted with permission from ref (150). 146

Figure 115. Circular dichroism spectra of racemic mixture **(4)** and the two enantiomers following resolution using Chiralcel-OD columns via preparative HPLC. The structures shown on the figure are the energy-minimized structures (employing the MM method as implemented in Spartan 08) and the assignment is arbitrary. Copyright © 2014, American Chemical Society. Reprinted with permission from ref (150). 147

Figure 116. Circular dichroism spectra of racemic mixture **(5)** and the two enantiomers following resolution using Chiralcel-OD columns via preparative HPLC. The structures shown on the figure are the energy-minimized (employing the MM method as implemented in Spartan 08) structures and the assignment is arbitrary. Copyright © 2014, American Chemical Society. Reprinted with permission from ref (150). 147

Figure 117. Electronic absorption (solid line) and emission (dashed line) spectra of compounds **(4)** and **(5)**. Copyright © 2014, American Chemical Society. Reprinted with permission from ref (150). 148

Figure 118. Therapeutic design. 156

Figure 119. TEM images of gold nanorods (~40 nm) and electronic absorption spectrum of GNRs in HEPES buffer (pH 7.2, 20 mM). 158

Figure 120. Reaction scheme for the target compound. 158

Figure 121. Top: Absorption spectra that is taken during the endoperoxide formation reaction. Bottom: Thermolysis of endoperoxide **(8)** to parent compound **(7)**. 159

Figure 122. Left: Thermolysis of $5x10^{-5}$ M **(9)** in DMSO at different temperature. Right: Absorbance vs. temperature graph of the thermolysis. The time of heating was 30 min for all selected temperatures. 160

Figure 123. Thermolysis of $5x10^{-5}$ M **(9)** in DMSO at 95^{o}C for 6 hours. Inset: Absorbance of $5x10^{-5}$ M **(9)** in DMSO at 37^{o}C. Sample was heated for 6 hours. 161

Figure 124. Thermolysis of $1x10^{-5}$ M **(9)** at 100^{o}C for 1 hr in HEPES buffer (pH 7.2, 20 mM). 161

Figure 125. Decrease in absorbance of DPBF in DMSO in the presence of $1x10^{-5}$ M upon heating at 70^{o}C **(9)** and the reappearance of parent anthracene absorbance bands. 162

Figure 126. Left: TEM image of GNR-**(9)** conjugate. Right: Normalized electronic absorption spectra of CTAB-GNR, **(9)-GNR(**in HEPES (pH 7.2, 20 mM) and **(9)-GNR** in DMSO. 162

Figure 127. Decrease in absorbance of DPBF at 414 nm in DMSO in the presence of **(9)-GNR** upon heating in oil bath. 163

Figure 128. Decrease in absorbance of DPBF at 414 nm in DMSO in the presence of

(9)-GNR. Excitation @830 nm. 163

Figure 129. Absorbance of DPBF in DMSO in the presence of **GNRs only** (0.125 nM). Excitation @830 nm. 164

Figure 130. Relative $^1O_2$ generation efficiency of **(9)-GNR** and **GNR only** in DMSO detected by the absorbance decrease of DPBF @414 nm with time. During first 4 min the samples were kept in the dark. 164

LIST OF TABLES

Table 1. FDA approved PDT drugs.[93,107] 34

Table 2. Selected photophysical parameters for the **(Dye 1)** and its conjugate adduct. 71

Table 3**.** Comparative spectroscopic properties of BODIPY compounds..... 93

Table 4. Photophysical Properties of the Synthesized BODIPY Compounds. 100

Table 5. Selected Parameters for Modified BODIPY Cores and Associated Orthogonal Bis-BODIPYs. 102

Table 6. Relative Energies (eV) of S_2 and S_3 States for Selected Species at CAS(6,6)/CEP-31G level of theory. 105

Table 7. Photophysical characterization of sensitizers. 123

Table 8. The quantum yields for T_1 state formation of **(actPS)** in different solvents 126

Table 9. Fluorescence quantum yield (Φ_f) and lifetime (τ_f) of **(actPS)** in different solvents..... 133

Table 10. Photophysical characterization of compound **(4)** and **(5)**. 148

CHAPTER 1

INTRODUCTION

Cancer appears to be one of the most challenging health problems faced by large amount of people all around the world. Number of patients is expected to reach more extended life spans in the coming years. State-of-the-art diagnostic tools and treatments must emerge in order to have more effective results, decreased invasiveness, fewer side effects and more patient compliance with respect to the conventional methods (chemotherapy and radiotherapy).

Conventional imaging methods for diagnosis applications mostly rely on contrast agents. These agents emit signal continuously regardless of target cell ("always on"). As a natural consequence of this, sensitivity cannot be achieved sufficiently due to the low target to background signal ratios. At that point, molecular optical imaging by means of fluorescent probes arises as a good alternative. These probes can be designed in such a way that they become active only under certain conditions ("turned on"). Thus, signal from well-designed probe can only be detected after selective interaction between target cells and probe that increases the specificity and selectivity. This improves target to background ratio and provides opportunity for detection of even very small tumours. Furthermore, molecular fluorescence imaging offers simple and cheap instrumentation as well as real time analysis.

Design, synthesis and characterization of molecular fluorescent probes, which are selective to various diseases marker is the key of targeted fluorescent imaging. At that point, BODIPY (4,4-difluoro-4-bora-3a,4a-diaza-s-indacene) dyes with their high fluorescence quantum yields/absorption coefficients, tunable absorption/fluorescence peaks, ease of synthetic methods and various sides for functionalization were most widely employed in fluorescence imaging studies during

the last decade. Therefore, in chapter 3, we introduced a BODIPY based glutathione selective turn-on fluorescent probe. Levels of biological thiols such as cystein (Cys), homocystein (Hcy) and glutathione (GSH) in living systems are known to be important parameters in health and sickness. Since their presences are vital for the maintenance of cellular redox status and alterations in their levels is linked to a number of debilitating diseases, probes that respond to these thiols by color change, emission wavelength change, or both are highly valued. Additionally, level of GSH in cancer cells is 2-50 fold higher than health cells, which makes GSH a promising target for cancer diagnosis. A vast amount of examples in which Cys and/or HCY are selectively detected and monitored appeared in the literature, however there are only few examples for GSH probes. This is the result of limited design principles for bio-thiols detection, which are mainly based on Michael addition, cyclization and cleavage of the disulfide bond. Structural differences between GSH and other two bio-thiols make GSH monitoring a challenging task. In chapter 3, for the purpose of selective GSH sensing, we thought that two binding sites on a probe are essential. We modified the BODIPY core with a crown ether moiety at *meso* position. Crown moiety is the modulation site for photo-induced electron transfer (PET) and it is a very well known binding site for the ammonium end of the GSH. In addition to that we incorporated a nitro styryl group on the BODIPY core in order to create a thiol-binding site. In this work, we have shown that selectivity for reaction-based probes can be improved by applying additional photophysical manipulation sites.

Photodynamic therapy (PDT) is a promising candidate for treatment of certain malignant (skin, head and neck, gastrointestinal, gynecological cancers), premalignant (actinic keratosis), and nonmalignant (psoriasis, AMD-age related macular degeneration) indications since it offers non-invasive and activatable therapy alternatives. PDT utilizes light, sensitizer and molecular oxygen to cause cancer cell death via apoptosis or necrosis. The therapeutic action is taking place upon the generation of cytotoxic singlet oxygen through excitation of a particular chromophore (sensitizer) followed by an energy transfer to the dissolved oxygen in tumor tissues.

One of the most substantial parts of the PDT designs is the choice of sensitizer. An effective sensitizer should hold some unique characteristics such as low toxicity in the absence of light, high extinction coefficients, photostability, amphiphilicity and biocompatibility. More importantly, a sensitizer should have high triplet quantum yield such that transition of an excited electron from singlet excited state to triplet excited (inter-system crossing (ISC)) takes place smoothly. Common strategy for achieving efficient ISC is to decorate sensitizers with heavy atoms such as iodine and bromine. However, presence of heavy atoms increases the dark toxicity of sensitizers. We have been interested in finding out some possible different ways of achieving increased intersystem crossing (ISC) without incorporating heavy atoms in order to minimize dark toxicity for photodynamic therapy applications, turning our attention to the excited state properties of the sensitizers. In chapter 4, we are introducing a new excited state concept, which we named it as doubly substituted tetra radical state (DS-TR) by realizing orthogonal arrangement of BODIPY monomers. DS-TR character of S_1 was shown to have a strong correlation with $S_1 \rightarrow T_1$ ISC yielding $^1O_2$.

Detailed study of DS-TR excited state was also provided by π-extended BODIPY derivatives in Chapter 4. Near-IR absorption, desired for potential photodynamic therapy applications, was not pursuable for bis-chromophores by the standard strategy of π -extension, as DS singlet states are destabilized. Decreased exchange coupling in π -extended cases appears to be responsible for this destabilization. On the other hand, by using the accumulated knowledge of excited state configurations and triplet photosensitization, we further improved our new concept through activatable heavy-atom free PDT sensitization. There is no doubt that targeted sensitizers increase the therapy efficacy and decrease the side effects. To do so, we extended the π-conjugation on the orthogonal dimer core, which removes the DS-TR picture and makes our sensitizer inactive. In the presence of GSH only, a cancer marker, double bond is reduced and the conjugation is broken that yields effective charge transfer mediated ISC. The detailed results of this project have been given in chapter 4.

While we were dealing with orthogonal BODIPY dimers for PDT applications, we recognized the potential of our dimers for atropisomerism. Synthesis, separation and detection of chiral molecules are at the heart of drug discovery studies. If a chiral molecule do have fluorescence property than its application areas can be expanded. For instance, fluorescence enantioselective sensing is one of the most up-to-date and improvable topics among the optical sensing studies due to its potential as a simple detection tool in chiral assays. This detection is quite important for drug discovery, biological labeling, catalysts, and understanding the mechanism of molecular recognition in biological systems. There are number of fluorescent sensors for recognition of chiral amines, carboxylic acids, alcohols and amino acids. Especially biologically important hydroxy acids and amino acids have been attracting much interest.

Rich BODIPY chemistry allows us to design, synthesize and characterize axially chiral BODIPY derivatives. In chapter 5, we presented the first example of atropisomeric BODIPY derivatives with persistent chirality due to multiple methyl group clashes. Circular dichroism studies clearly demonstrate successful separation of the two enantiomers. The orthogonally linked BODIPY compounds have been demonstrated to have interesting photophysical properties but also we show that they can be isolated as atropisomeric chiral compounds.

In chapter 6, I switched my attention back to PDT concept. On the way of fight against cancer, nanotechnology that combines life science, medicine, electronics and biomaterials is a good choice of weapon. As a result of increasing nanotechnology based biomedical applications and out coming new properties, there is a growing interest to use inorganic nanoparticles in cancer treatments. Nanomaterials can be used in various therapies (Photothermal, photodynamic therapies), ultrasensitive detection of cancer markers, imaging techniques as contrast agents, carriers for drug delivery, control release, and regenerative medicine. Among possible nanomaterials, gold nanoparticles have many advantages and unique properties that make them suitable for therapy, diagnosis and theranostic (therapy + diagnosis) applications. Biocompatibility, bioinertness, presence of tunable surface plasmon resonance peak,

which covers almost all of the electromagnetic spectrum, well establish surface chemistry for easy functionalization (targeting), compact size and insignificant toxicity are some of the well known properties of gold nanoparticles. It is important to note that; localized surface plasmon resonance (LSPR) wavelength of a gold nanoparticle can be tuned by simply adjusting the size and the shape of the nanoparticle during the chemical synthesis. For instance gold nanorods have red shifted LSPR peaks that span through near-IR region, which make them highly suitable for biomedical studies. Gold nanorods like other types of gold nanoparticles can be heated by external factors such as light (near IR). In fact, since these nanoparticles can be targeted to the tumor tissue, this heating alone is being considered as a viable treatment modality (photothermal therapy).

Applicability of PDT is severely limited by two major factors, penetration depth of the excitation light and hypoxia (low oxygen concentration) in tumor tissues. In chapter 6, we tried to address these restrictions by combining aromatic endoperoxides and gold nanorods. Our primary goal is to deliver the principal cytotoxic agent of photodynamic therapy, singlet oxygen, directly by thermal decomposition of otherwise stable endoperoxides, which are located on gold nanorods and observe cell death due to the thermal and singlet oxygen effects. Near-IR excitation mediated temperature rise on the surface of gold nanorods triggers the thermal decomposition and release of trapped singlet oxygen from endoperoxides. Thus, this design is not using heat as an end product as in the case of classical photothermal therapy. This project, which is a radical rewriting of the photodynamic therapy concept, is poised to revamp photodynamic therapy, offering potential solutions for major problems hitherto blocking broader clinical applications.

CHAPTER 2

BACKGROUND

2.1. Fluorescent Molecular Sensors

2.1.1. General Information

A *sensor* is a device, which yields a measurable output (signal) upon interacting with matter or energy.[1] Sensors are considered only as macroscopic devices (such as pH electrode or thermometer) until the beginning of the nineties.[1] Followed by the increased recognition of nanotechnology in sensing applications, properly designed molecules are also appeared to be suitable candidates. Today we have an accepted and well-known term *molecular sensor,* which is a molecule that signals the presence of an analyte by some physical output. Signaling mechanism of molecular sensors basically involves selective interaction of a molecule with an analyte of interest, which forms measurable form of energy that can be detectable with various simple spectroscopic techniques such as optical tools (e.g., UV, visible, fluorescence), or electrochemical methods (e.g., cyclic voltammetry). Optical sensors utilize light-based detection of analytes and are considered to be useful in practical applications because of their high sensitivity, low cost, and simplicity of instrumentation.[1] One type of the optical sensing is the *calorimetric sensor*, which involves the color change (shift in absorbance spectrum) upon interaction with an analyte. Second and more promising method is to sense analyte concentrations with fluorescent signal transduction and these types of molecular sensors can be referred as *fluorescent sensors*. In these type of sensors, photophysical mechanisms that control the response of a molecular probe mainly include photo-induced electron transfer (PeT), photo-induced charge transfer (PCT), excimer/exciplex formation, Förster resonance energy transfer (FRET), and aggregation-induced emission (AIE).[2] These

mechanisms will be discussed briefly in the section 2.3.

Fluorescent molecular sensor design strategies mostly involve three main approaches:[3] (i) binding site-signaling subunit, (ii) displacement approach, and (iii) chemodosimeter designs. In the case of first principle, a molecular sensor contains covalently bonded binding site(s) that is selective to a certain analyte and an optical signaling sub-unit in such a way that the interaction of an analyte with the binding site triggers electronic modulations in the optical signaling unit in the form of fluorescence (emission) change. Second modality (the displacement approach) suggests non-covalent interaction of the binding and signaling sites. Molecular ensemble between these two units is destroyed upon coordination of an analyte to the binding site causes displacement of the binding moiety that yields detectable optical changes. Chemodosimeter designs are realized by the chemical reactions on a molecular probe with specific analytes (a cation, an anion or a molecule) resulting in fluorescence alterations. It involves irreversible bond breaking or formation. Recent studies in the field reveal novel approaches that involve the use of nanoparticles in combination with molecular probes.

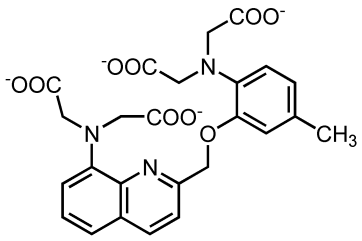

(1)

Figure 1. Tsien's Ca^{2+} probe.[4]

Fluorescent molecular sensor development has evolved into an attractive field of study after Tsien's pioneering study[4] on fluorescent Ca^{2+} detection in 1980 (figure 1), followed by large number of promising examples emerging at a steady pace with worldwide participation in this endeavor.[5] Major application areas of fluorescent molecular sensors are real time imaging of biological systems/processes and medical diagnosis.[6] It is known that living organisms and their environment are composed of elements, ions and molecules, which are constantly forming network of chemical

reactions including acid-base chemistry, electron transfer, metal-ligand interactions and catalytic transformations.[6] A molecular level understanding of these processes and detection of rich array of analytes (e.g., ions, molecules) that living organisms provide are real challenges, but also provides great opportunity for researchers to investigate biological systems in their own medium and create new tools especially for medical diagnosis. Towards addressing these challenges, molecular imaging (sensors) offers powerful modality for real time monitoring of living samples with high resolution, quick response and selectivity.

2.1.2. Overview of Fluorescence

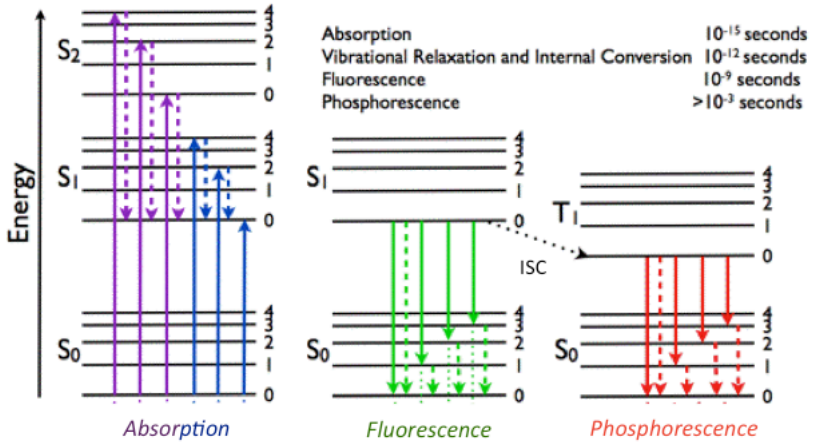

Figure 2. The Jablonski diagram.

It is important to review fluorescence concept before getting in to detail with fluorescent molecular probes. The absorption of light by a molecule results in excitation of one electron from ground electronic state (S_0) to one of the higher vibrational levels of a singlet-excited state. In a very short time, excited electron relaxes back to lowest vibrational level of the excited state (S_1). There are several pathways for an electron to release its stored energy after reaching to S_1 state. It can turn back to its ground state by releasing heat only (non-radiative path) or by emitting light, which is known as *fluorescence*. In addition to these, if the molecule contains suitable modifications and has sufficiently long-lived excited state lifetime, an electron in the singlet excited state can pass to lower energy triplet excited state (inter-system crossing). Relaxation from excited triplet electronic level to ground

state by emitting photons is named as *phosphorescence*. Time for fluorescence to occur is around nano or microseconds (10^{-9} - 10^{-6} s), on the other hand phosphorescence is more time consuming process (10^{-3} - 10^{2} s) since it involves several transitions.[7] Possible deactivation pathways for an excited electron are summarized in the Jablonski diagram (figure 2). One should note that emission wavelength of a molecule is always located at longer wavelengths than absorption wavelength due to the rapid decay of an excited electron to lowest vibrational level S_1 (figure 3). This phenomenon is called as *Stokes' shift*[7] and it is counted as one of the positive characteristics of fluorescent molecular sensors.

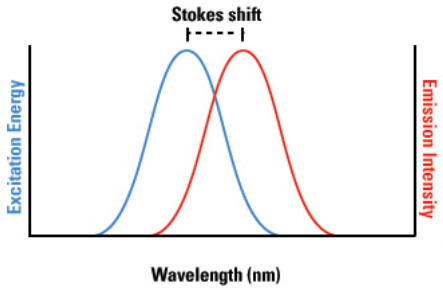

Figure 3. Stokes shift.

2.1.3. Fluorescent Probes

Fluorescence is well-accepted optimum signaling mechanism for optical molecular sensors due to some superior properties as mentioned before. Most important characteristic of fluorescent probes (fluorophore) is their extreme sensitivity due to Stokes' shift that provides different wavelengths for excitation and emission. Thus, analyte detection can be realized by low or almost zero background signals. Fluorescence signal can detect analytes even at picomolar concentrations, whereas with chromogenic probes can detect concentrations as low as micromolar levels (one million times higher).[8] It is also important to note that, presence of Stokes' shift by itself is not sufficient to diminish background signal at some cases. For instance, biological samples have their own autofluorescence signals up to 600 nm. Probes absorbing/emitting at longer wavelengths of electromagnetic spectrum mostly overcome these interferences. So appropriate fluorescent sensors for biological studies should have optimized wavelength range between 600-900 nm so called

therapeutic window.[9] Upper limit of this scale is arranged according to water absorption. Thus it is possible to monitor and analyze morphological details in tissues with subcellular resolution both *in vitro* and *in vivo* by using non-invasive fluorescence sensing tools. Biochemistry and molecular biology applications such as medical diagnosis, DNA sequencing and bioassays regularly take advantage of fluorescent molecular sensors in daily life practices. Another useful property of this optical method is the widespread availability of instrumentation that requires minimal maintenance. An additional advantage of fluorescence sensing is that detection of analytes can be performed via time resolved measurements.

Basic requirements for a fluorescent molecular probe can be summarized as follows;[1] (i) the binding site must have high selectivity for the analyte of interest (ii) there must be signal transduction mechanism between probe and analyte (iii) sensor-analyte conjugate should be bio-compatible and stable in physiological medium (iv) out-coming signal should not be affected by environmental factors (e.g., pH and fluorescent quenchers) (v) irradiation and detection instrumentation have to be user friendly and cheap. It must be emphasized that it is really hard task to combine all of these properties in one probe and requirements may differ according to end-use of a molecular senor.

There are many fluorophores, which are employed in fluorescent detection of certain analytes. Endogenous molecules are an important class. For instance, aromatic amino acids including phenylalanine and tyrosine are weakly emissive compounds.[10] Tryptophan (Trp) shows the highest fluorescence among amino acids at 353 nm under UV excitation with fluorescence quantum yield of 0.13.[11] Trp can be used to monitor protein folding and ligand binding processes as well as it can be included in FRET[12] and PeT[13] applications. Other and maybe the most popular naturally occurring fluorescent dye is porphyrin, which has tunable absorption and emission peaks through visible and red region.

Synthetic small molecules such as cyanine, fluorescein, perylene, coumarin, BODIPY and rhodamine are well known and extensively studied fluorescent probes (figure 4), which are applied in many applications including anion, cation and

biologically relevant molecules detection, food analysis, environmental monitoring, medical diagnosis and many other disciplines.[14]

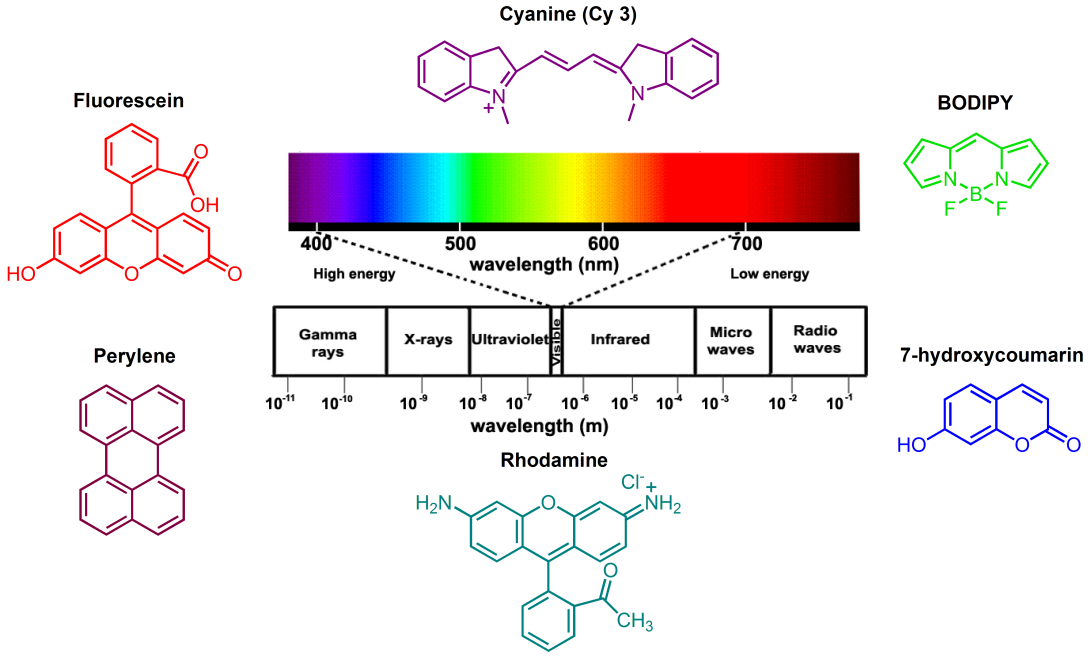

Figure 4. Molecular structures of common fluorescent probes.

For all of these probes, it is possible to tune absorption and emission wavelengths, however coumarin dyes mostly known as UV probe whereas fluorescein and rhodamine derivatives are well recognized by their strong emission at near-IR region. Suitable chemical modifications that can be done on these dyes favor the incorporation of analyte binding side according to particular purposes. Different classes of dyes show unique properties. For instance coumarin dyes have very large Stokes' shift, which makes them suitable for biological applications. Most popular coumarin dyes are heteroatom substituted ones. Fluorescein dyes after their first synthesis in 1871[15] have widely been used in chemosensor designs. It has very high fluorescence quantum yield, water solubility and it also possesses versatile modification sides for many different applications. However, this class of dyes have very high rate of photo-bleaching and pH sensitivity. On the other hand, rhodamine dyes, another well-studied fluorescent probes offer very low pH sensitivity and tunable absorption/emission peaks.[16] Cyanine dyes are constructed with two polymethine chains between nitrogens. They are intensively used as DNA stains and

membrane sensors.[17] Intramolecular chain twisting makes cyanine dyes flexible and alters their fluorescence properties. Fluorescent probes based on perylene dyes have strong absorption in visible range and high fluorescent quantum yield but difficult derivatization restricts their wide application.[18] BODIPY dyes will be discussed in the following section separately since they will show up extensively throughout this dissertation.

2.2. BODIPY Dyes

BODIPY (4,4-difluoro-4-bora-3a,4a-diaza-s-indacene) dye was synthesized for the first time accidently in 1968 while Treibs and Kreuzer were trying to react 2,4-dimethylpyrrole with acetic anhydride in the presence of $BF_3.OEt_2$.[19] After 17 years, in 1985 Hauglang and Kang reported the fluorescent characteristics of BODIPY dyes.[20] Since then BODIPY dyes have been well recognized as fluorescent molecular sensors and employed intensively for bio-labeling applications.[21-23]

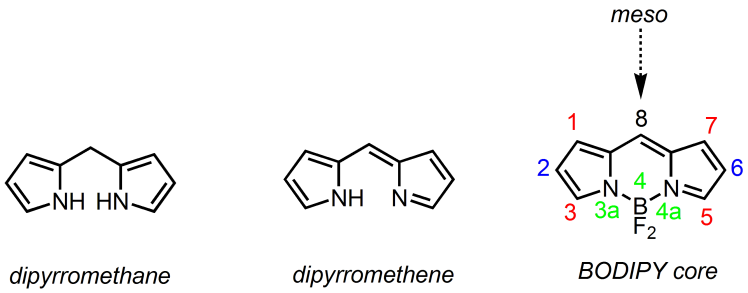

Figure 5. Molecular structures of BODIPY and its precursors.

BODIPY core can be obtained after two consecutive steps.[24] In general, dipyrromethene group is obtained by combining two pyrrole moieties with a methine bridge. After that, dipyrromethene unit is coordinated with a disubstituted (mostly a BF_2 group) boron atom, which completes the formation of rigid and constrained core structure. Simple BODIPY core structure, its IUPAC numbering and structures for BODIPY precursors are given in figure 5.

There are three different synthetic pathways for the synthesis of *unsubstituted* BODIPY dyes. According to Bruce *et al*. procedure,[25] after the formation of dipyrromethane core, it is oxidized by DDQ in order to obtain dipyrromethene

structure followed by the addition of tertiary amine base and $BF_3{\cdot}OEt_2$. Second pathway involves the acid-catalyzed condensation of unsubstituted pyrrole and pyrrole-2-carbaldehyde just before the addition of base and $BF_3{\cdot}OEt_2$ complexation.[26] In the final procedure, Pene-Cabrera and co-workers introduced the palladium-catalyzed reaction of 8-thiomethyl BODIPY and triethylsilane in the presence of copper(I) thienyl-2-carboxylate (CuTc) with very high yield.[27]

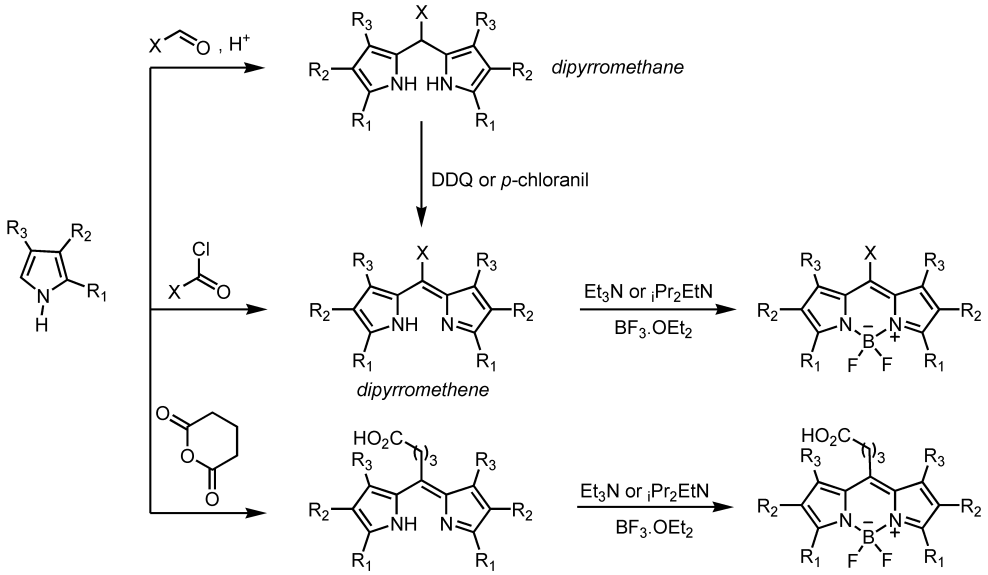

Figure 6. Synthetic pathways for *meso*-functionalized symmetric BODIPYs.

Symmetric BODIPY dyes with *meso* (8-position) functionalization are synthesized by acid-catalyzed condensation of excess pyrroles with aldehydes, acid chlorides or anhydrides in the presence of amine base and $BF_3{\cdot}OEt_2$ (figure 6).[28,29] When aldehydes are employed in condensation, initially dipyrromethane intermediate is formed which is then oxidized to dipyrromethene by using quinone derivatives. Substituted BODIPY dyes at *meso* position are widely used due to their advantageous characteristics with respect to unsubstituted analogues. They provide high stability, enhanced solubility in organic solvents and free functional groups for further modifications depending on the end-use.

It is also possible to synthesize *meso*-unsubstituted symmetric BODIPY derivatives by the condensation of excess pyrrole derivatives (~2.2 eq) with orthoester.[30] Initially dipyrromethene intermediate is formed and afterwards base and

borontrifloride are added to get BODIPY skeleton. Burgess and co-workers propose another possible mechanism in which pyrrole-2-carbaldehyde is used together with $POCl_3$ without any need for excess pyrrole.[31] Synthetic pathways for both strategies are given in figure 7. On the other hand, in the case of *asymmetric* BODIPY synthesis, condensation of pyrrole-2-carbaldehyde with other pyrrole derivatives has to be carried out.[32]

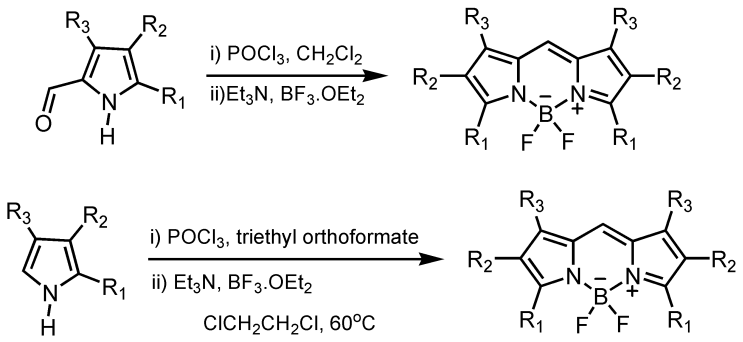

Figure 7. Synthetic pathways for *meso*-unsubstituted symmetric BODIPYs.

The parent BODIPY unit has a major absorption peak (S_0-S_1 transition) near 500-520 nm with moderate to high absorption coefficients (40.000 – 100.000 M^{-1} cm^{-1}). One should also note that in the absorption spectrum of a BODIPY dye, it is very common to observe a weak peak at high-energy region around 370 ± 10 nm that corresponds to S_0-S_2 transition.[33] A sharp and strong emission peak due to the relaxation of an excited electron from S_1 state is mostly observed between 530-550 nm suggesting approximately 30 nm Stokes' shift. BODIPY dyes have very high fluorescence quantum yield (ϕ_f > 0.50) and long fluorescence lifetimes (in the order of nanoseconds). Phosphorescence is very rare since this class of dye normally have very low triplet quantum yields.[34] They have high thermal and photostability as well as physiological medium compatibility.[24]

Simple BODIPY core has some drawbacks such as solubility in aqueous solution, absence of functional groups for further modifications and low absorbance/emission wavelengths for biomedical applications. These challenges can be addressed by suitable derivatization of the core at *meso*, 3-5, 1-7, 2-6 and boron center.[24] *Meso* (8) functionalization is straightforward since it can be realized by just choosing the

appropriately substituted aldehyde or acid chloride while performing the condensation reaction.[35] Phenyl bearing substitutions at *meso* position in the presence of methyl groups at 1 and 7 positions of the core force phenyl moiety to be almost perpendicular to BODIPY core, which evokes some design strategies for the modulation of fluorescence signal. A different approach for functionalization of the 8-position is to replace *meso*-carbon atom with nitrogen that yields aza-BODIPYs.[36] Incorporation of aza-substitution pushes absorption/emission peaks into the red end of the visible spectrum (650-850 nm).

2-6 positions are susceptible to electrophilic attack due to their relatively electron rich character. At these positions sulfonation[37] (important for water solubility), formylation,[35] nitration[38] and halogenation[39] reactions can be performed. While heavy atom introduction such as iodine and bromine quenches the fluorescence due to effective inter-system crossing,[40] they provide sides for well-known coupling reactions (e.g., Suzuki, Sonagashira and Stille). 1-7 and 3-5 positions have acidic character and they are suitable for Knoevenagel condensation reaction.[41] This type of condensation is quite important because it is the simplest way to get red shifted absorption and emission peaks by extending the π-conjugation via incorporation of styryl groups (figure 8). Mono-, di-, tri-, and tetrastyryl modifications seem to offer a greater degree of versatility as judged by the recent interest,[42-45] after Akkaya group report.[41] This clearly stems from the following facts: (i) Knoevenagel reaction of the 3- and 5-methyls is in most cases high yielding; (ii) the reaction conditions tolerate the use of a variety of aldehydes with different stereo-electronic characteristics; (iii) strong charge donor substituents are likely to yield switchable fluorescent molecules with internal charge transfer characteristics useful as chemosensors and molecular logic gates.[46,47] In addition to Knoevenagel type condensation reaction, 3 and 5 positions when decorated with good leaving groups, they are open to nucleophilic aromatic substitution. According to Dehaen and Boens studies 3,5-dichloroBODIPY dyes can be easily modified by nucleophiles.[48] Ziessel *et al*. reported the replacement of two fluorine atoms at boron center by alkoxides and aryl groups to get highly photo-stable and redox active BODIPY derivatives, which have been used as sensitizers for dye-sensitized solar cells and organic photovoltaics.[49]

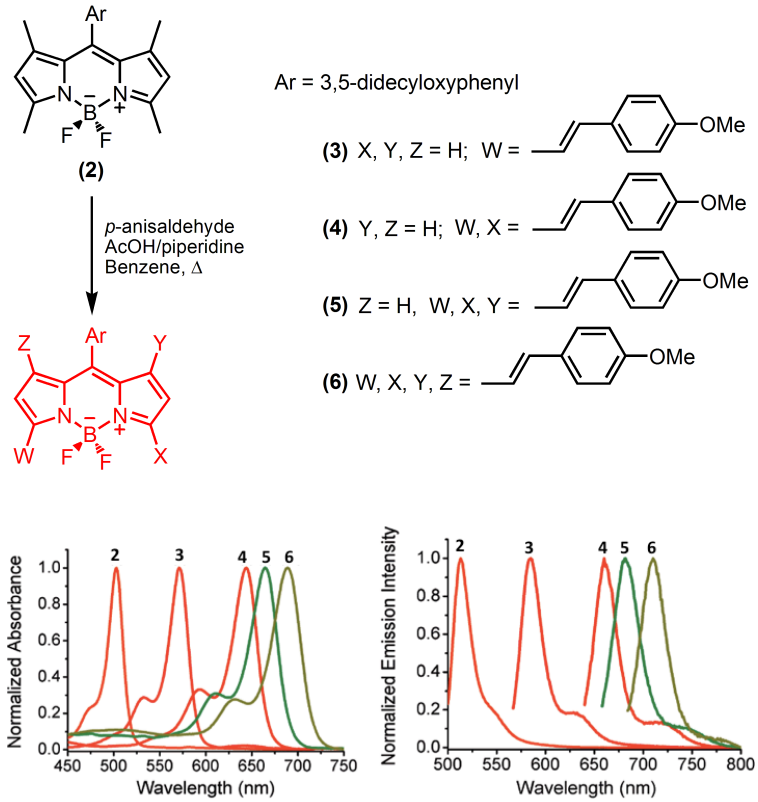

Figure 8. Functionalization of 3,5 and 1,7 positions by Knoevenagel condensation reaction. Copyright © 2009, American Chemical Society. Reprinted with permission from ref (41).[41]

BODIPY dyes were known only as bright fluorescent dyes for use in cellular imaging as supplied by a few commercial sources. However, especially within the last ten years, there has been a veritable Bodipy renaissance. This is in large part sparked by the new tactics[24,29] in the functionalization of the BODIPY core, which led to the synthesis of longer wavelength absorbing/emitting fluorescent dyes,[50,51] energy transfer cassettes,[52] light harvesters,[53] sensitizers for solar cells,[54,55] photodynamic therapy,[56,57] nonlinear optical materials,[58] mesogenic materials,[59] supramolecular polymers,[60] and molecular logic systems.[61]

2.3. Photophysics of Sensing Mechanism

2.3.1. Photo-induced Electron Transfer (PeT)

An electron is excited from HOMO level of a luminophore (light absorbing molecule) to its LUMO upon irradiation followed by vibrational loses within the excited state. If there is a receptor group, which is capable of donating or accepting

electrons, is linked to a luminophore without any conjugation then particular orbital of this receptor that contains lone electron pairs can be represented as separate orbital (figure 9). When the energy of this orbital lies between the luminophore's HOMO and LUMO, an electron transfer occurs from lone electron pair to the hole in the HOMO that is created after excitation takes place. This phenomenon is known as *photo-induced electron transfer* (PeT). In the case of PeT, excited electron relaxes back to its ground state by non-radiative path and this leads to decrease in emission intensity or quenching of the fluorescence. Fluorescence can be regained if lone electron pair is involved in binding interactions (e.g., protonation or metal binding). Binding lowers the energy of receptor molecular orbital due to stabilization and blocks the electron transfer (figure 9).

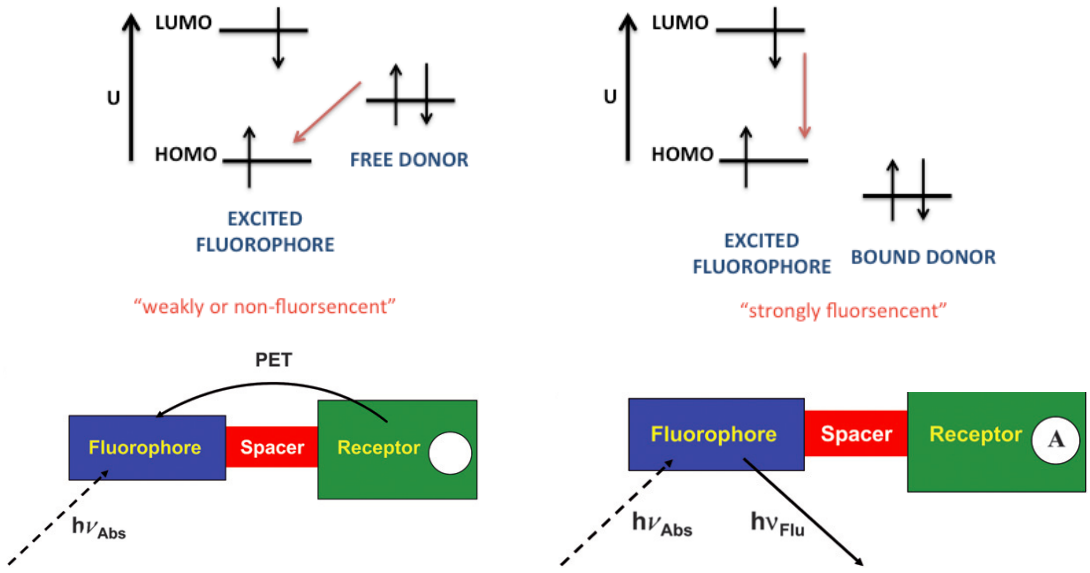

Figure 9. Schematic representation of PeT. Copyright © 2009, Royal Society of Chemistry. Reprinted with permission from ref (62).[62]

There is another alternative PeT mechanism, which is known as "*oxidative PeT*", which involves the electron transfer from excited molecule to electron acceptor receptor. Mechanism for oxidative PeT is given in figure 10. Contrary to conventional PeT, now initially luminophores are mostly fluorescent at the initial state (exceptions do exist, e.g., Nagano *et al.*)[63] and upon binding, it becomes almost non-fluorescent due to the electron transfer from LUMO of luminophore to LUMO of receptor.

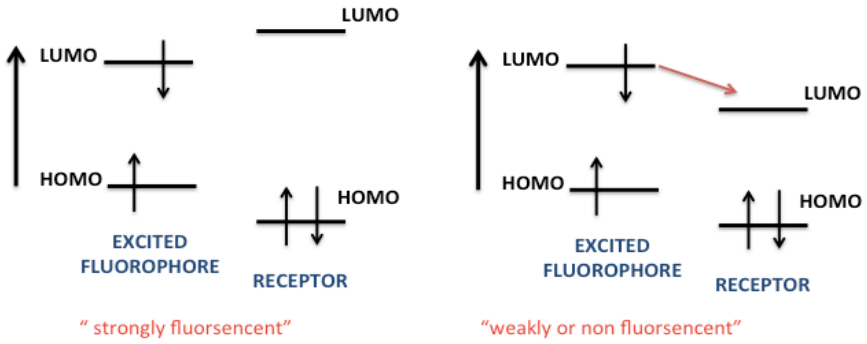

Figure 10. Schematic representation of reverse-PeT.

PeT is one of the most traditional mechanisms for turn on-off fluorescence signal transduction and it can be utilized for detection of various analytes by employing wide range of probes and receptors.[64,65] Some PeT based fluorescent probe examples are given in figure 11. An anthracene derivative fluorophore with crown-ether binding side is one of the simplest and well-known examples of PeT sensors. Upon addition of K^+ on **(7)**, fluorescence quantum yield increases from 0.003 to 0.14.[66] In the case of **(8)**, polyazamacrocycle rings were used to detect Zn^{2+} cation by turn-on PeT signaling mechanism.[67] Compound **(9)** is a BODIPY based Cu(II) probe in which hydrolysis of ester to alcohol takes place after recognition of the analyte that blocks the PeT and increases the emission intensity.[68]

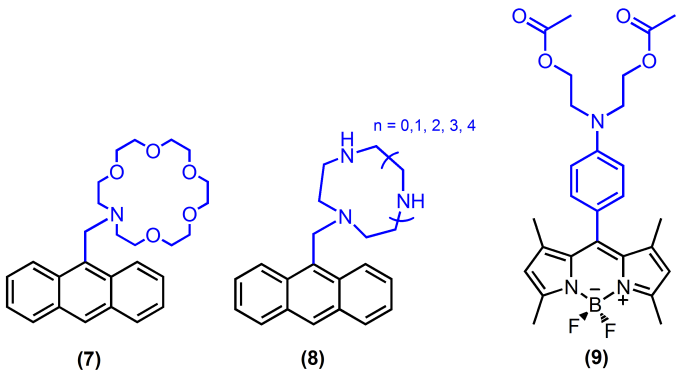

Figure 11. Some PeT based fluorescent probes.

2.3.2. Photo-induced Charge Transfer (PCT)

Photo-induced charge transfer (PCT) is another popular signaling mechanism for molecular sensors. PCT probes contain electron donor and acceptor moieties, which

are conjugated to fluorophore. Upon excitation charge transfer occurs from donor groups to acceptors that causes charge redistribution throughout the molecule. Re-localization of electron density makes this charge transfer process highly sensitive to microenvironment. It is generally accepted that interaction of analytes with receptor, which is an electron acceptor or donating group, results in significant amount of shifts in both absorption and emission spectra (figure 12).[2] If the fluorophore-analyte interaction takes place at donor side, then electron donation capacity of donor group will be lowered which results in conjugation loss and blue-shift in the absorption spectrum. On the other hand, if the receptor is electron-withdrawing group then binding of analyte will improve the electron withdrawing character of probe and red-shifted absorption will be observed. Fluorescence peaks mostly behave similarly with absorption spectra (exceptions do exists). PCT strategy is mostly employed in calorimetric sensor designs in which naked eye detection of an analyte can be possible due to the immediate color change.

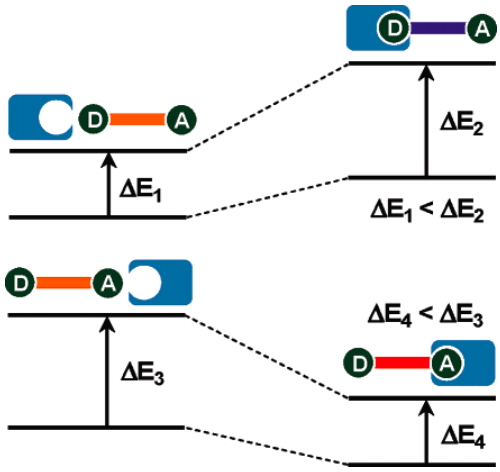

Figure 12. Schematic representation of PCT. Copyright © 2007, American Chemical Society. Reprinted with permission from ref (2).

Compound **(10)**[69] contains crown-ether (electron donating) moiety as a calcium ion receptor (it is also suitable for K^+). Thus binding of Ca^{2+} results in blue shift in the absorption spectrum. Parent fluorophore has absorption wavelength of 463 nm, which is blue-shifted to 360 nm after calcium complexation. This is expected result for absorption but fluorescence spectrum of **(10)** + Ca^{2+} shows some interesting results. While shift in absorption spectrum is almost 100 nm, emission maximum is

only shifted 28 nm. This can be explained by redistribution of electron density. PCT decreases the coordination capacity of nitrogen atom on crown-ether group by reducing the electron density on it, which makes the crown ether moiety almost non-coordinating. Thus fluorescence spectrum is only slightly affected since emission is coming out from a fluorophore with very weak or no analyte interaction. Other two PCT examples in figure 13 are pH sensitive BODIPY based dyes. In the case of **(11)**, electron donating dimethylamino phenyl moieties were used as a receptor. Proton binding to the receptor causes blue shift as expected.[70] Compound **(12)** is very similar to the former probe, but it contains electron accepting pyridine groups. Upon protonation, red shift was observed in the absorption spectrum.[69]

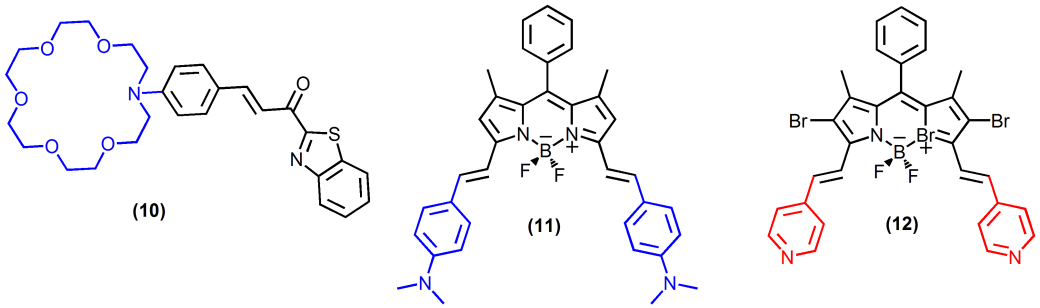

Figure 13. Some PCT based probes.

2.3.3. Fluorescence Resonance Energy Transfer (FRET)

FRET based molecular sensors are composed of two (or more) dissimilar fluorophores in which one behave as a donor and the other one is an acceptor. Donor fluorophore is the one that absorbs/emits at shorter wavelength. Upon irradiation at absorption wavelength of donor, the acceptor absorbs emitted light from donor and at the end while donor returns back to its ground state, emission of the acceptor compound is detected. FRET itself is a non-radiative process. In order to have efficient FRET,[2] (i) there has to be a spectral overlap between donor emission and acceptor absorbance spectra, and (ii) orientation of dipole moments of donor and acceptor is critical. Fluorophores are mostly linked together by non-conjugated linkers, thus there is no orbital overlap between two units. It is noted in literature that, if the distance between two fluorophores are in the range of 10-100 Å, then FRET can be active.[2] This type of signal transduction is mostly useful when a

fluorophore of interest has small Stokes' shift.

2.3.4. Excimer Formation

Fluorophores that contain aromatic rings such as anthracene and pyrene can form excited state dimers upon irradiation, which is known as excimer formation. In the case of excited state excimer, two emission peaks are observed one corresponds to monomer and the second one is the result of excimer formation and located at longer wavelengths.[69] Addition of analytes may favor or hinder the excimer structure and the detection can be achieved by observing the relative emission intensity ratios of monomer and excimer.

2.3.5. Aggregation Induced Emission (AIE)

Rapid development of supramolecular chemistry emerge new fluorescent sensing mechanisms. Aggregation induced emission (AEI) is one of the promising and new emerging signal transduction mechanisms. It is well known that aggregated form of fluorophores in solution quenches the fluorescence (aggregation induced quenching). For that matter, many bulky and long chains are incorporated on to the fluorophore to avoid this type of aggregate formation in solution. However, some compounds that are almost non-fluorescent in solution were shown to have enhanced fluorescence upon aggregation.[5]

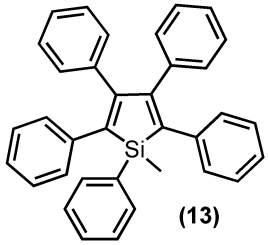

(13)

Figure 14. 1-methyl-1,2,3,4,5-pentaphenylsilole **(13)** as an AIE probe.

This behavior was first observed by Tang *et al*., by using 1-methyl-1,2,3,4,5-pentaphenylsilole **(13)** (figure 14).[71] Compound **(13)** is initially non-emissive in ethanol, but when the water content of the solution is raised up to 90%, fluorescence quantum yield is found to be 0.21. With the help of other examples, it is concluded

that AEI is the result of restricted rotation of the aggregate form. When there is no aggregation, intramolecular rotation activates the non-radiative path for relaxation, but in aggregate form this rotation is blocked and high fluorescence can be observed. Most common AEI probes are derived from silole and tetraphenylethylene (TPE) derivatives.[72]

2.4. Detection of Biological Thiols

During the last decade, calorimetric and luminescent detection of biological thiols namely cysteine (Cys), homocysteine (Hcy) and glutathione (GSH) have attracted great interest due to the biological significance of these thiol bearing molecules. Cys, Hcy and GSH (figure 15) are known to be important biomarkers for various diseases and chronic heath conditions.

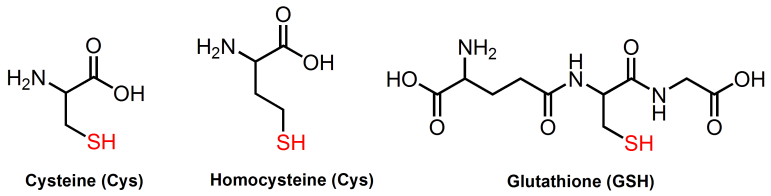

Figure 15. Molecular structures of bio-thiols.

Specifically, high cysteine concentration is clearly associated with myocardial and cerebral infarctions, whereas deficiency of Cys can be related with liver damage, loss of muscle, skin lesions, lethargy and slow growth in children.[73] In addition to these Cys is the main thiol source for iron-sulfur clusters that are best known for their role in oxidation/reduction reactions of mitochondria related electron transport.[74] On the other hand, elevated Hcy level is an indicator of arterial and venous thrombosis (e.g., cardiovascular disease) as well as Alzheimer's, folate and B12 vitamin deficiency.[75] Change in plasma total Hcy (tHcy) concentration is associated with the birth abnormalities and cognitive impairment in the elderly.[76] It is also important to note that intracellular concentrations of Cys and Hcy are in the level of micromolar, whereas plasma concentrations of these two bio-thiols are found to be 0.25mM-0.38mM.[76] GSH is one of the most abundant (1-10 mM) intracellular nonprotein thiols, which is composed of cysteine, glycine and glutamic acid.[77] It has important

roles in controlling intracellular redox activities and signal transduction. More specifically, it appears in the oxidative stress control mechanisms to maintain the redox homeostasis for cell growth and function.[78] In addition to its intracellular activities; it is directly related with cardiovascular disease and cancer such that its intracellular concentration is 2 to 50 fold higher in cancer cells.[79]

Calorimetric and fluorescent detection strategies of bio-thiols are mostly utilized the strong nucleophilic character of thiols and their high affinity towards metal ions.[76,80] Accordingly, almost all of the optical sensors for bio-thiol detection comprise chemodosimeter approach, which is realized by the reactions between molecular sensors and thiols.[76,81] Mechanisms of these specific reactions can be summarized as Michael addition, cyclization with aldehydes, cleavage of sulfonamide/sulfonate esters, thiol-halogen substitution and metal complex coordination.

2.4.1. Michael Addition

Michael addition/reaction is the nucleophilic addition of nucleophiles to α,β-unsaturated carbonyl groups. Thiols are known to be good candidates as a nucleophile in this type of reaction, which makes Michael addition one of the most employed strategies for the detection of bio-thiols via molecular probes. In 1998, de Silva and co-workers introduced serious of fluorophores with maleimide receptor for the detection of thiols.[81]

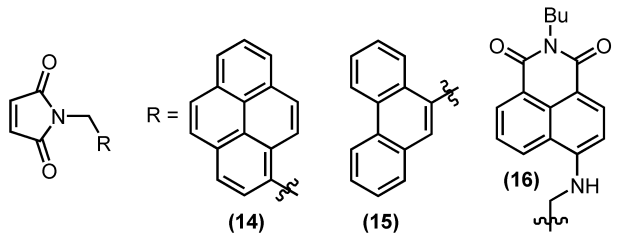

Figure 16. Maleimide substituted probes for bio-thiol detection.

Michael acceptor maleimide moieties are connected to fluorophores with spacer groups, so compounds **14-16** are chemodosimeters (figure 16), which use PeT as a signal transduction mechanism. Initially probes are almost non-fluorescent due to the PeT, after the Michael addition of Cys and simple mercaptoethanol to the electron

deficient alkene group in aqueous methanol solution, PeT is blocked and fluorescence is restored.

Recently, a coumarin based bio-thiols probe **(17)** is reported by Sun *et al*. in which nitroalkene moiety is used as a Michael acceptor group (figure 17).[82] Turn-on fluorescence response is observed in the presence of all bio-thiols and the reaction is highly selective towards Cys, Hcy and GSH than other amino acids. Cys is the one that reacts fastest followed by Hcy and GSH due to the steric factors. Fluorescent enhancement is mostly due to the inhibition of PeT upon addition of thiols to the nitroolefin group.

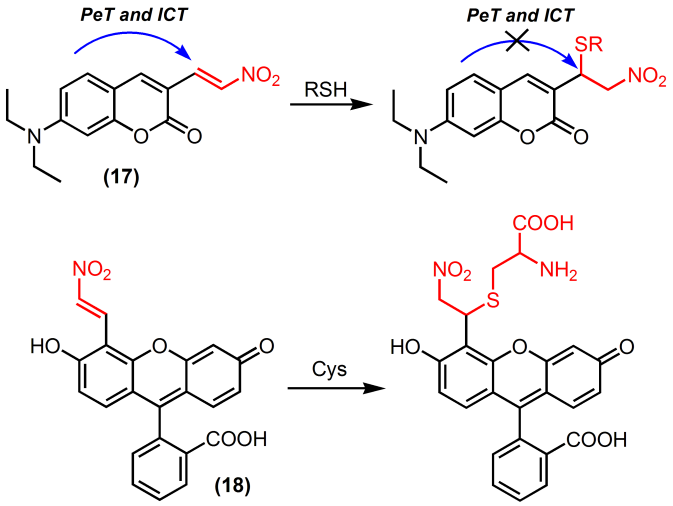

Figure 17. Coumarin and fluorescein based Michael addition mechanism for selective detection of bio-thiols.

A similar approach is also introduced by using fluorescein based probe **(18)** (figure 17).[83] After the addition of bio-thiols to nitroalkene, blue shifted absorption spectrum and emission intensity increase (at 520 nm) in fluorescence spectrum are detected. These optical changes are the result of spiro ring opening after the addition of bio-thiols. Cys showed very fast response (k_{obs} = 2.3 min^{-1}) with a detection limit of 0.2 μM. High fluorescence quantum yields of probe-thiol conjugates make them suitable for monitoring thiols concentration in cell and zebrafish. In Michael addition reactions of bio-thiols, larger and bulkier GSH mostly faces more steric hindrance while it is trying to reach the α,β-unsaturated carbonyl center. Accordingly, it has lower reaction rate and highest interaction energy compared to Cys and Hcy in most

of the time.

Jung *et.al.* introduced that the pK_a differences of three bio-thiols can be considered as an additional point while dealing with the reaction rates of these thiols.[84] pK_a values of Cys, Hcy and GSH are 8.30, 8.87 and 9.20 respectively. So, Cys is the strongest nucleophile in physiological medium (pH 7.4) with its lowest pK_a value. Jung and co-workers utilized this set of information in Michael-type addition of Cys to **(19)** (figure 18). Turn-on fluorescent signal is observed as a result of the reaction and probe is also used for imaging of Cys in HepG2 cells.

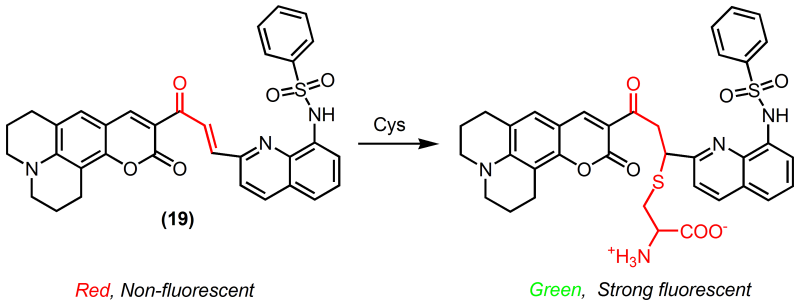

Figure 18. Intracellular detection of Cys via Michael addition.

Akkaya *et al*., designed two BODIPY dyes (**20** and **21**) carrying nitroethenyl substituents in conjugation with the BODIPY core which yields probes that responds to biological thiols via change in both absorbance and emission wavelength (figure 19).[85]

While **(20)** has absorption maximum at 520 nm, **(21)** has longer wavelength absorption due to the π-extension as a result of Knoevenagel-type condensation reaction. Both probes showed very fast and sensitive responses with color changes and "turn-on" fluorescence. This fluorescence enhancement is at least partly due to a reduction in the efficiency of the PeT process upon the attack of the Cys thiol on probes resulting an increase in the energy level of the BODIPY centered LUMO. Under identical conditions, other biological thiols, such as Hcy and GSH afforded similar turn on fluorescence responses as well. However, the response to Cys is much faster than that to Hcy and GSH. Thus, by controlling the reaction time, exquisite selectivity for Cys can be obtained. The result is bright signaling of

biologically relevant thiols in the longer wavelength region of the visible spectrum and in aqueous solutions (in the case of **21**).

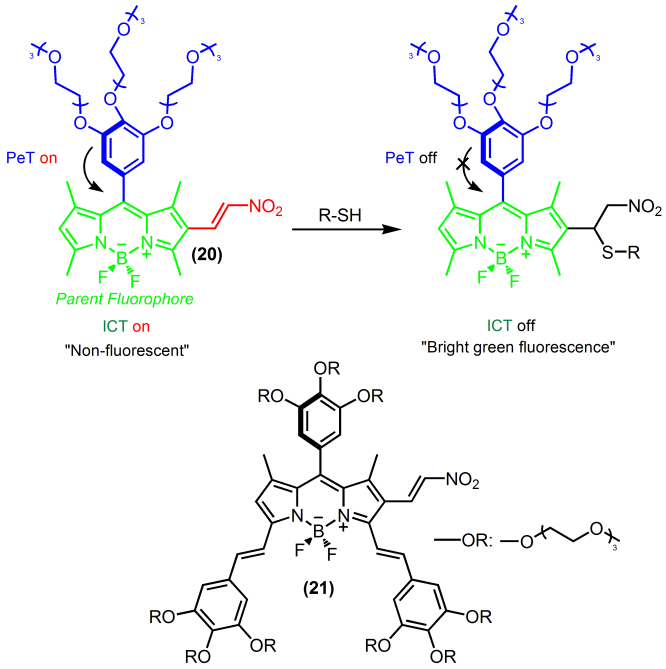

Figure 19. BODIPY based probes for selective Cys detection.

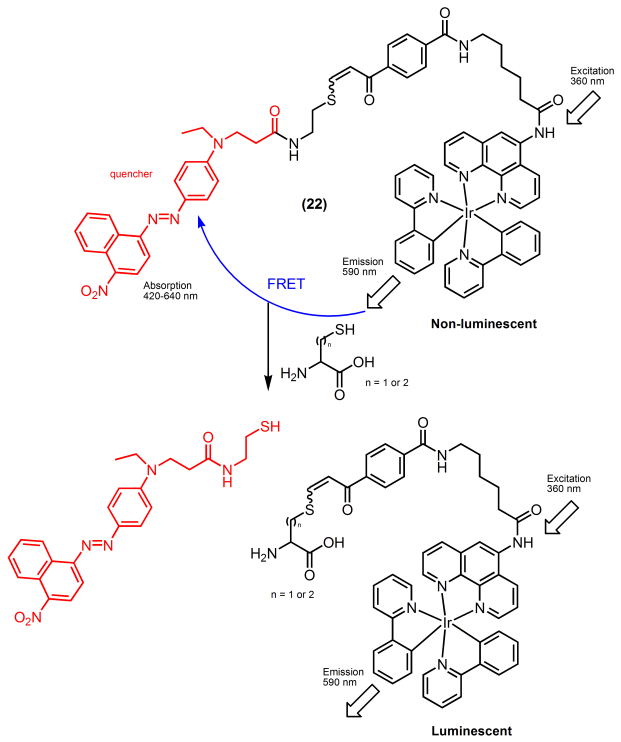

Figure 20. A FRET based chemodosimeter.

Shui *et al.*, developed a FRET based chemodosimeter with iridium (III) metal complex **(22)**, which is linked to diarylazo quencher via vinyl sulfide linker (figure 20).[86] When metal complex is irradiated at 360 nm, nearby non-luminescent quencher absorbs emitted light at 590 nm, thus probe is initially non-fluorescent. In the presence of Cys and Hcy, fluorescence of metal complex is restored. This is the result of thiol-assisted cleavage of vinyl sulfide linkage that releases the quencher from probe, which blocks the FRET. The probe is also capable of detecting the concentration of Cys and Hcy in human blood plasma. Plasma concentration is found to be 0.31 mM, which is in good agreement with the theoretical range (0.25 – 0.38 nM).

2.4.2. Cyclization with Aldehydes

Cyclization with aldehydes is another widely used strategy for fluorescent sensing of Cys and Hcy. Molecular probes containing aldehyde functional group can be involved in 6- or 5-membered ring formation with suitable 1,3- or 1,2-aminothiols like Hcy and Cys. On the other hand, larger GSH is not suitable for similar ring formation. Hu *et al.* demonstrated this approach recently. Probe **(23)** is a 7-dimethylamino-1,4-benzoxazin-2-one derivative, which contains electron donating amino and electron withdrawing carbonyl groups (figure 21).[87] Push-pull system on the probe offers weak fluorescence and makes **(23)** a good PCT type probe. In the presence of Cys and Hcy, absorption maximum is shifted 70 nm from orange to yellow and 5-fold enhancement of emission intensity is observed at 560 nm in CH_3CN-HEPES buffer (3:7, v/v) due to the cyclization process of probe with thiol bearing molecules Cys and Hcy at carbonyl side. Probe is also used to monitor bio-thiols in living cells.

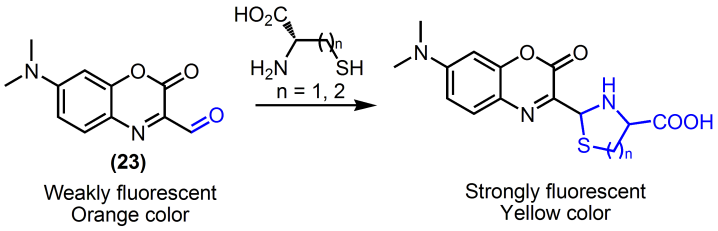

Figure 21. Coumarin based detection of bio-thiols via cyclization mechanism.

2.4.3. Conjugate Addition & Cyclization

Wang *et al.* designed a fluorescein based fluorescent probe that utilizes conjugate addition and cyclization processes together (figure 22).[88] When small bio-thiols (Cys and Hcy) are introduced to chemodosimeter **(24)**, they are added on acryloyl moiety followed by the cleavage of the ester bond due to the cyclization that forms fluorescein core, which is highly emissive. When incubation time of thiols with the probe is limited to 10 min, **(24)** is highly selective towards to Cys. In the absorption spectrum, upon addition of Cys in EtOH-phosphate buffer (pH 7.4, 2:8, v/v), a shifted peak at 490 nm is detected.

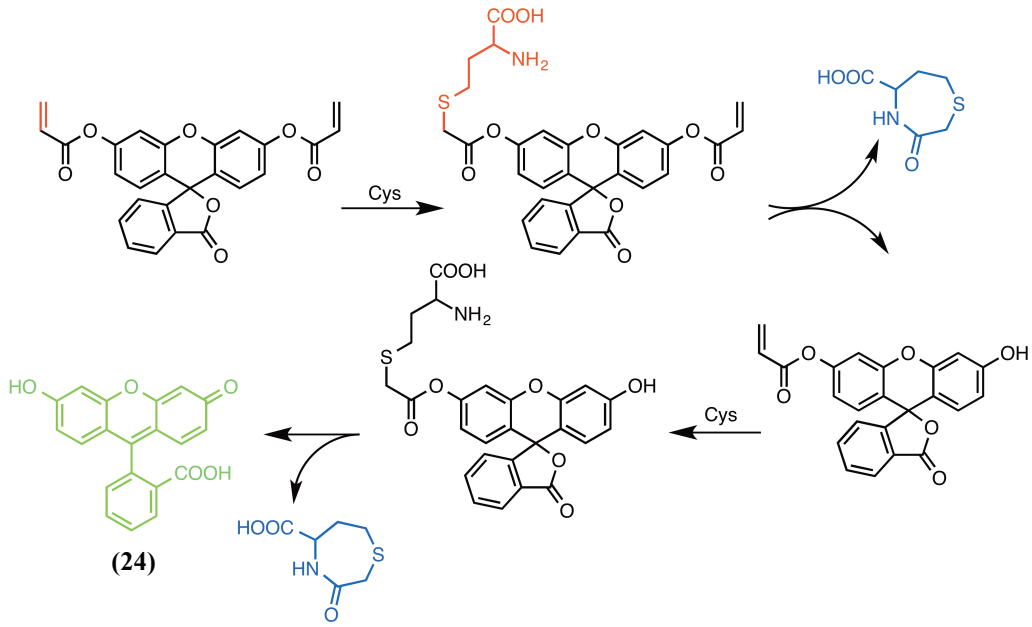

Figure 22. Conjugate addition and cyclization approach for Cys detection.

2.4.4. Cleavage of Sulfonamide and Sulfonate Esters

Nucleophilic substitutions of phenols and amines in the presence of thiols have been used in many bio-thiol detection studies. One example is the Jiang and co-workers work (figure 23) in which they introduced BODIPY based near-IR probe **(25)**.[89] Probe is decorated with 2,4-dinitrobenzenesulfonyl moiety, which is known to be a good electron acceptor and reaction site for thiols. Thiol specific cleavage of sulfonate ester blocks the oxidative PeT mechanism. Thus, turn-on response is observed at 755 nm with bio-thiols in a co-solvent (CH_3CN-H_2O-DMSO) with a

detection limit of 0.5 μM.

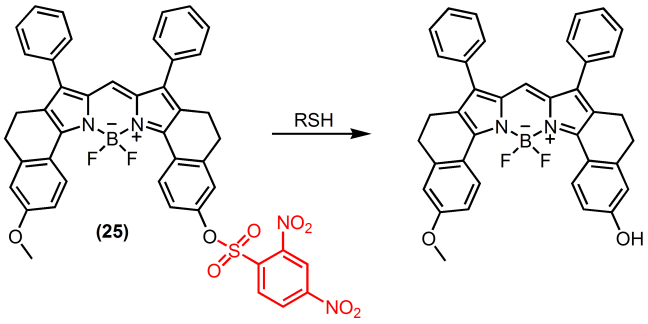

Figure 23. Cleavage of sulfonate ester bonds with bio-thiols.

2.4.5. Thiol-Halogen Nucleophilic Substitution

Thiol-halogen nucleophilic substitution is an important approach for the selective detection of GSH, which is otherwise difficult by Michael addition or cyclization of aldehydes strategies as mentioned before. Yang *et al.* reported a fascinating example of thiol-halogen nucleophilic substitution method for the selective fluorescent sensing of GSH (figure 24).[90]

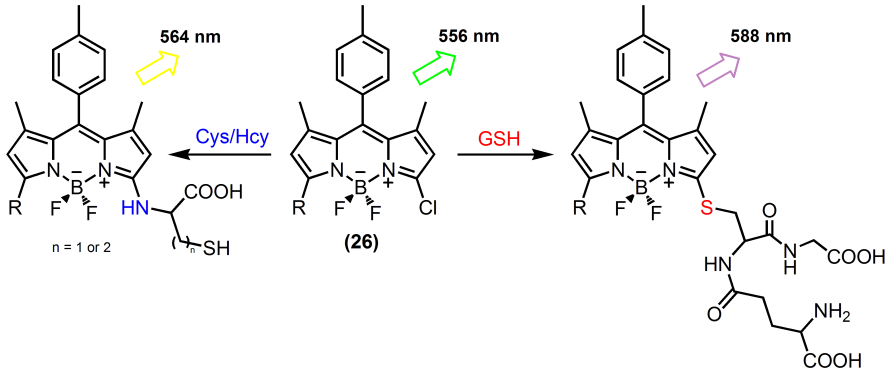

Figure 24. BODIPY based thiol-halogen substitution.

Chlorine on the chlorinated-BODIPY derivative **(26)** undergoes nucleophilic aromatic displacement with the thiolates of the bio-thiols. While thioether adduct, which is formed by GSH is stable, Cys/Hcy encounter further intramolecular replacement of thiolates with primary amine groups on Cys/Hcy that involves the formation of 5- or 6-memebered rings in the transition states. At the end, two products are obtained; one is the sulfur-substituted BODIPY (in the case of GSH)

and the second one is amino-substituted BODIPY derivative (in the case of Cys/Hcy). As expected these two products have different optical characteristics such as, in the case of Cys/Hcy, absorption and emission maxima are blue shifted (λ_{ems} = 556), whereas thioether adduct has red shifted absorption and emission spectra (λ_{ems} = 588 nm). So, by monitoring the emission signal at 588 nm, highly selective GSH probe is introduced, which is also applicable in cell culture studies.

2.4.6. Disulfide Exchange Reaction

Disulfide exchange reaction mechanism mainly involves the cleavage of disulfide bond by thiols. Zhu *et al.* combined two 4-aminonaphthalimide probes (typical PCT-type dye) with a disulfide linkage in their recent study (figure 25).[91] Addition of GSH on to the probe **(27)** cleaves the disulfide based carbamate linker followed by cyclization and release of 1,3-oxathiolan-2-one, which yields two 4-aminonaphthalimide cores. Consequently, red shifted absorption and emission peaks are observed. Concentration dependent titration experiment with GSH suggests ratiometric detection of GSH both in solution and in cancer cells.

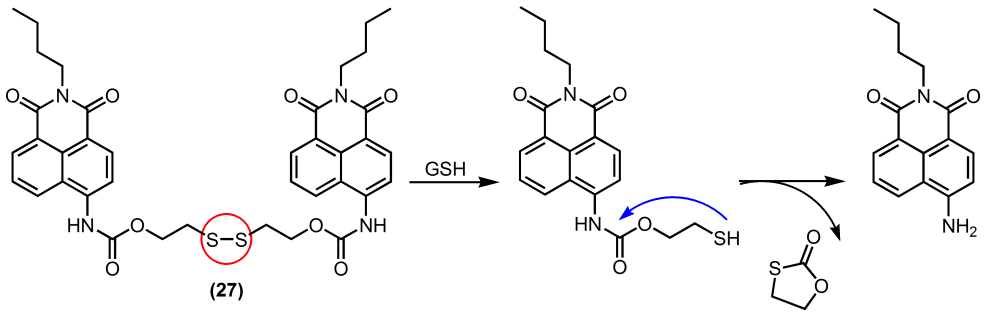

Figure 25. Disulfide exchange reaction mechanism on a naphthalimide derivative.

2.4.7. Metal Complexation

Chemodosimeter design strategies for the detection of bio-thiols also include nucleophilic displacement approach in the presence of metal ions. In order to realize this, thiols should have high affinity towards the particular metal ion. Tae group reported one interesting example about metal complexation based detection of bio-thiols (figure 26).[92] They synthesized rhodamine hydroxylamine containing 2-

deoxyribose group. Sugar functionalization has two important roles. It increases the water solubility and metal binding strength (e.g., towards Au^{+}) of the probe. Initially rhodamine derivative **(28)** is non-fluorescent and has no color since **(28)** is in the spirolactam form. Tae and coworkers reported that addition of Au^{+} ion increases the emission intensity due to the ring opening reaction. In addition to that, complexation of Cys and Hcy with Au^{+}-**(28)** conjugate further increases the fluorescence and shifted the color from colorless to red. Various amino acids are also employed but only Cys and Hcy selectively bonded to the gold ion with the help of well-known Au-S interaction. Detection limit of the probe for Cys is noted as 100 nM.

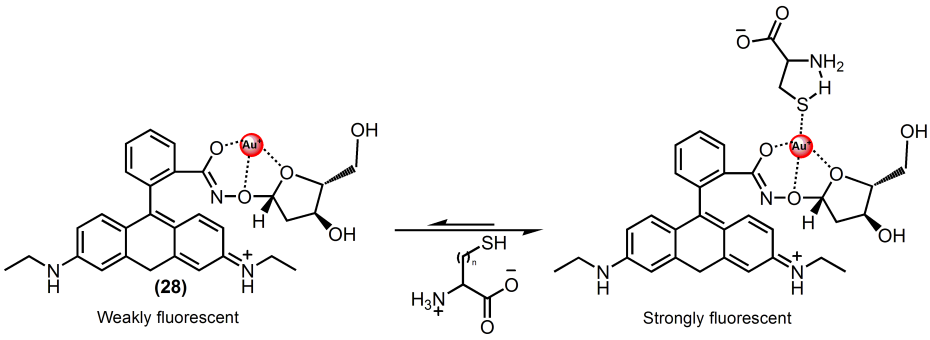

Figure 26. Metal complexation approach for the detection of bio-thiols.

2.5. Photodynamic Therapy

2.5.1. General Information

Photodynamic therapy (PDT) is a promising non-invasive treatment modality for certain malignant (skin, head and neck, gastrointestinal, gynecological cancers), premalignant (actinic keratosis), and nonmalignant (psoriasis, AMD-age related macular degeneration) indications.[93] The therapeutic action is contingent upon the generation of singlet oxygen through excitation of a particular chromophore (sensitizer) followed by an energy transfer to the dissolved oxygen in tumor tissues. Thus, PDT involves three individually non-toxic components; light, sensitizer and molecular oxygen, which are come together to generate cytotoxic singlet oxygen. Singlet oxygen and other secondary products (reactive oxygen species, ROS) are responsible for the apoptotic and necrotic deaths of the tumor cells. Main cellular targets are membrane structures of the cells and organelles.[94] Since all three effectors

must be at the same spatiotemporal coordinates for singlet oxygen generation and administration of the sensitizer is done by intravenously or topically around the diseased regions PDT has the potential to be a very localized and selective modality of cancer treatment. Moreover, irradiation of the tumor area in the body can be realized by means of flexible fiber optics. Unlike chemotherapy and radiation therapy, PDT does not cause serious side effects. Mechanism of PDT action and its effects on tumors will be discussed in the following sections.

2.5.2. Milestones of PDT

Light-induced therapy is traced back to more than three thousand years ago.[94,95] In the ancient Egypt and India, light was being extensively used to treat various diseases such as psoriasis, rickets and vitiligo.[96] At the beginning of nineteenth century, Oscar Raab demonstrated that when certain chemicals interact with the light, they are able to generate cytotoxic effects.[97] In 1903, the use of light to treat several diseases was named as "*phototherapy*" by a Nobel laureate Niels Finsen.[98] In the same year, Herman Von Tappeiner and Jesionek showed that skin tumors could be effectively treated with eosin dye in the presence of white light, which is then classified as "*photodynamic action*".[99]

Porphyrin is one of the most widely studied sensitizers in the mid-nineteenth century. W. Hausmann introduced the iron coordinated porphyrin derivative (haematoporphyrin) to treat paramecium and red blood cells.[100] Later, a German physician Meyer-Betz injected a porphyrin sensitizer into his body. After walking on a sunny day, he reported pain and swelling. Also, he remained light sensitive for months. This trial is the first reported study with a PDT sensitizer on humans.[101] Richard Lipson and coworkers further improved the initial haematoporphyrin **(29)** designs (figure 27).[102] They showed that administration dose of their haematoporphyrin derivative (HPD) is much smaller than crude haematoporphyrin due to the high level of accumulation of HPD in tumor sites. First *in vivo* study was reported in 1972 with porphyrins in tumor-implanted rats in which tumor growth was delayed for 20 days.[103] Dougherty established a pioneering study in 1975 by stopping the tumor growth in mice completely with the help of HPD and red light.[104] Clinical

applications were started to appear in 1976.[93] Recurrent bladder carcinoma growth in one patient was slowed down and necrosis of the tumor cells with the help of HPD sensitizer was observed. Then, Dougherty and colleagues used similar approach to treat 25 skin cancer patients.[105] Hayata *et al.* tried to enlarge PDT action to deeper cancer cells (lung tumors) but only 7% of patients were cured successfully.[106] After 1984, PDT was applied extensively to many cancer types including oesphageal, lung, gastric, breast, head/neck and pancreatic carcinomas.[93] These studies showed that PDT was mostly effective in early-stage patients.[94]

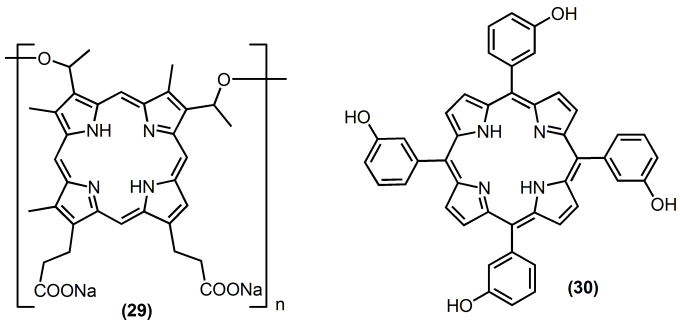

Figure 27. Molecular structures of Photofrin and Foscan.

In 1993, partially purified form of HPD (Photofrin) (figure 27) got approval for the first time in Canada for prophylactic treatment of bladder cancer.[94] Later, FDA and other worldwide agencies also approved it with extended scope (esophageal cancer, Barrett esophagus which is a pre-cancerous condition that may lead to esophageal cancer; gastric and papillary bladder cancer, cervical dysplasia and cancer, endobronchial cancer). There are also some other FDA approved PDT agents (table 1) such as ALA, 5-aminolevulinic acid (skin, bladder and brain cancers) and Verteporfin (ophthalmic, pancreatic and skin cancers). In addition to these additional approved drugs in certain countries (Levulan, Metvix, Foscan **(30)** (figure 27), ALA esters - EU, NPe6 - Japan) do exist with many others in trial phases.[94,107] It is highly possible to further increase the efficacy of PDT action in clinic by improved specificity, better localization and deeper light penetration. This might be achieved by new generation of drugs, which combine novel protocols and equipments.

2.5.3. Mechanism of PDT Action

The absorption of light by a sensitizer results in excitation of one electron from ground electronic state (S_0) to one of the higher vibrational levels of a singlet-excited state.

Table 1. FDA approved PDT drugs.[93,107]

PS	Structure	Wavelength (nm)	Approved	Trials	Cancer Type
HPD-Photofrin	Porphyrin	630	Worldwide		Lung, esophagus, bladder, brain
ALA-Levulan	Porphyrin	635	Worldwide		Skin, bladder, brain, esophagus
ALA esters-Metvix	Porphyrin	635	Europe		Skin, bladder
Temoporfin-Foscan	Chlorin	652	Europe	United States	Head and neck, lung, brain, skin
Verteporfin	Chlorin	690	Worldwide		Ophthalmic, pancreatic, skin
Talaporfin-Npe6	Chlorin	660	Japan	United States	Liver, colon, barin
Silicon phthalocyanine-Pc4	Phthalocyanine	675		United States	Cutaneous T-cell lymphoma
Padoporfin-Tookad	Bacteriochlorin	762		United States	Prostate
Motexafin lutetium-Lutex	Texaphyrin	732		United States	Breast

In a very short time, excited electron relaxes back to lowest vibrational level of the excited state (S_1). At that point, if the sensitizer contains heavy atoms (e.g., iodine, bromine) or some transition metal complexes (e.g., Ru, Ir) or intramolecular spin convertors (e.g., C_{60}), it is highly possible to observe inter-system crossing (ISC) from singlet excited state to long-lived triplet excited state.[108] Furthermore, ISC can also be achieved with sensitizers that have low-lying n-π* transition and exciton coupling behaviors.[109] After reaching to triplet excited states there are two possible reactions that can undergo at this excited state.[93] First one is the reaction with a substrate, such as cell membrane or a molecule in which electron transfer takes place from excited (activated) sensitizer to form radicals. These radicals then react with the molecular oxygen ($^3O_2$) to yield oxygenated products like highly reactive singlet oxygen, $^1O_2$. In the second type of reaction, triplet excited state energy is directly transferred to nearby molecular oxygen to produce cytotoxic $^1O_2$ (figure 28). Both reactions are clearly oxygen dependent thus, it is reported that induction of tissue *hypoxia* (absence of molecular oxygen) limits the singlet oxygen production.[93] Generally, ratio between these two types of reactions is related with the type of sensitizer, its affinity towards substrate, and concentration of oxygen.

Singlet oxygen is a highly reactive species with a short lifetime in aqueous media (<0.04 μs, with an approximate diffusion distance of <0.02 μm.[109] So, cells that are close to the area of the singlet oxygen generation are the ones that are mostly affected. Actually, this excited state species is 94.3 kJ/mol above the ground state, however the transition between the triplet ground state ($X^3\Sigma_g^-$) and the first singlet-excited state is strictly forbidden by spin, symmetry and parity selection rules.[110] Therefore, singlet oxygen cannot be produced by the direct excitation of the ground state molecular oxygen, so it is always generated by sensitization through energy transfer from sensitizers. Photosensitization and generation of singlet oxygen in this way, with the intermediacy of these dyes also require an efficient intersystem crossing between the singlet and triplet manifolds as mentioned before. Overall efficiency of PDT action and its cytotoxic effect are multifactorial and highly dependent on the type of sensitizer, administration and light exposure doses, oxygen availability, localization of sensitizer and the time interval between administration of

the sensitizer and irradiation.[93]

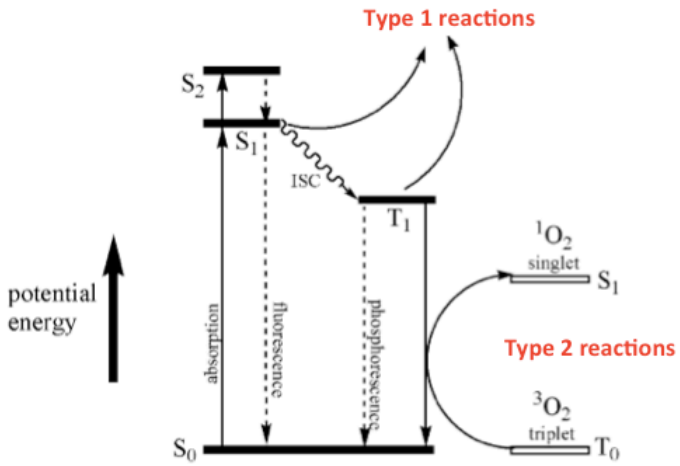

Figure 28. Modified Jablonski diagram.

2.5.4. Basic Components of PDT

There are three major components of a PDT action; a photosensitizer, light source and molecular oxygen. Choice of a suitable photosensitizer (PS) is one of the most critical steps while generating cytotoxic singlet oxygen in PDT action. An ideal PS should have easy manufacturing processes with good stability and long shelf life. Furthermore, high absorption coefficient at longer wavelengths (600-900 nm) is another important requirement. At theses wavelengths (therapeutic window) it is known that incoming light has highest tissue penetration depth.[111] It has to be non-toxic in the absence of light, in other words it should have no dark toxicity. In addition to these, clearance rate of a PS from healthy cells should be rapid in order to avoid phototoxic side effects. For effective and safe cell penetration it has to have amphiphilic character. Other desirable properties of a PS are high triplet quantum yield for effective ISC and long triplet lifetime for efficient reactions. These are probably most challenging requirements, which will be discussed in detail in the forthcoming sections. Finally presence of targeting moieties on a sensitizer increases the efficacy of therapy while decreasing the dark toxicity and possible side effects.

In clinical applications, Photofrin is the most commonly employed PDT sensitizer as mentioned before, however its complicated structure, low absorption coefficient and

low selectivity forced scientist to reveal new sensitizers. After significant efforts, most of the problems associated with the Photofrin such as need for high concentration of drug/light exposure and long-term photosensitivity was solved with a chlorine sensitizer, Foscan.[107] Nevertheless some other complications were reported due to its high potency. ALA and ALA ester derivatives are also important class of photosensitizers with their high potential for clinical applications.[107] There are also many other sensitizers apart from porphyrin derivatives, which have been used in *in vitro* and *in vivo* studies such as rose bengal, methylene blue, eosin B, phthalocyanine and BODIPY derivatives.[108]

Light source is another critical component of PDT action. It is not just significant for irradiation of a PS but also deterministic for the efficiency of the therapy. It is known that penetration depth of blue light is very limited, whereas red and near-IR radiations penetrate deeper through tissues. Most effective range for irradiation is introduced as between 600 to 900 nm.[111] Longer wavelengths are not useful since the energy of the light is not sufficient to initiate PDT reactions and at that wavelengths water and some physiological molecules start to absorb most of the incoming light. Mostly employed light sources are lasers and light emitting diodes (LEDs). Moreover, optical fibers with diffusing tips are appeared to be important class of light sources especially for the influential delivery of light to the tumor sites in the body. One should note that total light dose, light exposure time and light delivery are important points for clinical efficacy. Final component for the PDT action is the molecular oxygen as it is mentioned before. It is the major reagent of light-triggered singlet oxygen generation reactions.

2.5.5. PDT Effects on Tumors

Generation of cytotoxic singlet oxygen can trigger the tumor destruction in three different ways: (i) direct killing of tumor cells, (ii) tumor infarction by damaging tumor vasculature and (iii) activation of an immune response against cancer cells.[93] All of these three pathways are contributing to cancer cell killing process and long-term tumor control. Almost all of the processes are related with the oxidative damage of $^1O_2$. Singlet oxygen reacts with bio-molecules very rapidly. Lipid peroxidation,

oxidations of thiols and amines, DNA strand break and cross-linking are some examples for $^1O_2$ bio-reactions. As a result of these reactions cell death is observed according to apoptosis or necrosis mechanisms depending on the localization of PS. Mitochondria localizing agents induce apoptosis, while plasma membrane localizing sensitizers are more likely to cause necrosis on irradiation.[112]

PDT triggered photodamage can directly kill cancer cells,[113] however complete removal of tumors cannot be achieved due to the several reasons. Korbelik and co-workers reported that tumor cells, which are away from the vascular supply, mostly survive due to the inefficient PDT action.[113] Another issue is lack of molecular oxygen around the tumor sites due to the consumption of it during the PDT action and damaged vasculature as a result of PDT.[114] This situation is directly restricted the long-term tumor response. In order to avoid hypoxia, light fluence rate has to be lowered or light exposure dose should be arranged carefully.

There is no doubt that cancer cells are growing very fast and they need high amount of nutrients and oxygen, which is supplied by blood vessels. Thus, it should not be surprising to shutdown this feeding mechanism while treating cancer. In 1989, Barbara Hendersen showed that Photofrin caused vascular shut down around tumor sites, limiting nutrient and oxygen supply to the cancer cells.[115] Decrease in tumor growth was also mentioned in the same study. Furthermore, it was shown that PDT induced vascular damage is the result of thrombus formation.[116] Further studies on well-known sensitizers HPD, Photofrin and benzoporphyrin derivative (BPD) demonstrated that vascular endothelial growth factor was upregulated during the PDT action proving the vascular constriction.[117] Time interval between sensitizer injection and light irradiation can determine the killing mechanism of tumor cells. For instance, if the time between the administration and light exposure is short (15 min) then sensitizers mostly localize in the vasculatures, which causes indirect killing of cells due to the vasculature damage.[93]

In detailed studies with cells that are exposed to PDT action, signs of some immune system elements such as lymphocytes, leukocytes and macrophages were detected suggesting the activation of immune response in the PDT-treated tissues.[118] Delay in

tumor growth was observed in deVree's work because of the neutrophil accumulation in the PDT-activated tumor cells, which triggered the immune response against tumor.[119] Activation of immune response is counted as one of the most advantageous issue of PDT since conventional cancer therapies namely chemotherapy and radiotherapy are known as immunosuppressive treatments.

2.6. Triplet Photosensitization for PDT: Design Principles

The triplet state of a photosensitizer can be populated by non-radiative $S_1 \rightarrow Tn$ ($n \geq 1$) transition after successful excitation, which is known as inter-system crossing (ISC) process. So, in order to obtain powerful triplet sensitizers, strong absorption of the incoming light followed by efficient ISC are highly desired. Ideal triplet state sensitizers should also have long-lived triplet excited state since it behaves as a triplet energy donor to trigger many photochemical and photophysical processes, which play active roles in many application areas such as PDT, photocatalytic organic reactions and triplet-triplet anhilation (TTA) upconversion.[108] It is also possible to apply triplet PSs to phosphorescent imaging, electroluminescence and molecular sensing studies. In the following sections PDT application will be discussed extensively.[108]

In a singlet excited state, electrons have opposite spins according to Pauli exclusion principle however, triplet excited state electrons have parallel spins. Thus, ISC ($S_1 \rightarrow T_n$ or $S_1 \rightarrow T_1$) is normally quantum mechanically forbidden process since it involves spin reversion. This is why triplet excited state is less probably observed with most of the chromophores upon excitation. ISC mainly involves two different spin states and can be realized only in some circumstances. It is generally accepted that for an effective ISC process, there has to be a coupling between electron spin and orbital angular momentum, which is named as *spin-orbit coupling (SOC)*.[120] This coupling favors the ISC and during SOC, energy and total angular momentum are conserved. Spin-orbit coupling is one of the most important interactions that make ISC possible.

2.6.1. Heavy Atom Effect

Sensitizers that are decorated with atoms (figure 29), which have large atomic numbers, can induce effective ISC.[108] If an electron is moving around a nucleus with highly positive charge, motion of that electron accelerates, which increases the spin (μ_S) and angular (μ_L) momentum. As a result, coupling between two states become more feasible. Heavy atom containing sensitizers are great example of SOC modulation. Probability of getting SOC by using nuclear-charge effect scales with Z^4, where Z is the nuclear charge.[108] Thus, as the atomic number of an atom incorporated on the sensitizer increases, chance to have an efficient ISC also increases. Most organic dyes have low triplet quantum yields, and in many recent candidates for photodynamic sensitizers, heavy atoms are incorporated into the structure as a strategy to improve spin–orbit coupling leading to facilitated intersystem crossing.[56] While this approach seems fail-safe, incorporation of heavy atoms such as Br, I, Rh, Ir, Pt, Ru and Os *etc*. very often leads to increased "dark toxicity".[121]

Incorporation of transition metal complexes is a well-known strategy for heavy atom triggered SOC and ISC.[122] However, small absorption coefficients of transition metal complexes in the visible region restrict their widespread usage. Thus, iodo- and bromo-substituted sensitizers have been more excessively employed to obtain effective sensitizers for PDT. Rose bengal **(31)** and eosin blue **(32)** are important classes of triplet PSs for generation of singlet oxygen (figure 29).

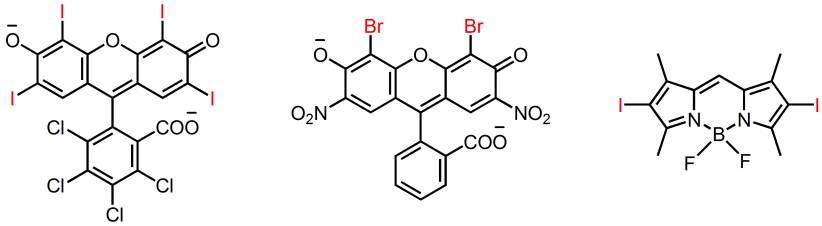

Figure 29. Heavy atom mediated ISC.

Another remarkable triplet sensitizer class is BODIPY chromophore. BODIPY dyes due to their unique characteristics such as high absorption coefficients, resistance to

photobleaching, low dark toxicity and environment insensitivity are accepted as ideal sensitizers and have been used extensively in PDT studies.[123] Nagano and coworkers reported first report of BODIPY sensitizer for PDT application in 2005. They introduced a 2,6-Diiodo-BODIPY **(33)** derivative to investigate heavy atom mediated singlet oxygen generation on this class of dyes (figure 29).[34] Fluorescence quantum yield is observed to be 2% indicating efficient ISC for the excited electron. **(33)** is also applied to *in vitro* cancer cell successfully.

After the first report of Nagano, red/near-IR absorbing and water-soluble BODIPY derivatives started to appear. Akkaya group reported a di-styryl bromo-substituted BODIPY derivative **(34)** with red-shifted absorption maximum and improved water solubility due to the addition oligoethylene glycol moieties (figure 30).[57] Cytotoxic effect of **(34)** on cancer cell line is detected by the cell-membrane damage via fluorescence microscopy.

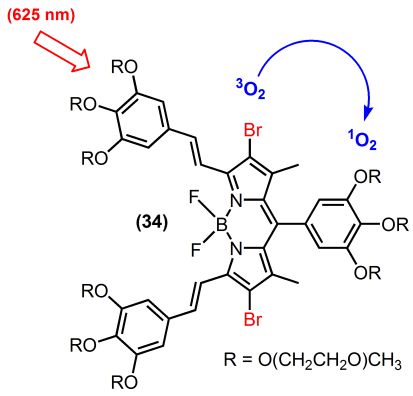

Figure 30. Near-IR absorbing, water-soluble BODIPY sensitizer.

2.6.2. Heavy Atom Free Photosensitization

There are also some other strategies that offer design principles for the comprising of heavy atom free sensitizers. As mentioned above incorporation of heavy atoms unfortunately increase the dark toxicity of the sensitizer. Unlike traditional chemotherapy agents, in principle, photodynamic therapy sensitizers themselves should be nontoxic, either at cellular or organ levels, even at relatively high concentrations. This projection at least partially can be realized by the use of heavy atom free sensitizers. Some design principles towards realization of heavy atom free

sensitizers are given below.

2.6.3. Chromophores with Low-Lying n-π* Transitions

One of the important requirements for effective SOC is that the energy difference between singlet and excited states should be close enough for strong transition. If the electronic configurations of S_1 and T_1 states are same, then the energy difference between these two states appears to be twice of the electron exchange integral (*J*). On the other hand, in the case of n-π* transitions (charge transfer) it is reported that energy gap between S_1/T_1 is much smaller. Therefore, most of the organic compounds with high π-extension undergo π-π* transition which dramatically decreases triplet quantum yield. El-Sayed generalized this phenomenon. According to El-Sayed's selection rule S_1 (n-π*) → T_1 (π-π*) is an allowed transition since angular momentum is conserved and the energy gap is small. However, S_1 (π-π*) → T_1 (π-π*) transition is forbidden. Rate constant equation for ISC is given below, where H_{SO} is the probability of getting SOC and *E* is the energy gap between S_1 and T_1 state. This equation clearly shows once more that small energy gap is highly needed for effective ISC. This is a typical case for excited states, which have charge transfer character and a simple example of low-lying n-π* transition mediated ISC is benzophenone (aromatic ketone) in which ISC rate constant is very fast due the S_1 (n-π*) → T_1 (π-π*) transition.[108]

$$k_{ISC} \propto <T_1|H_{SO}|S_1>^2 / (\Delta E_{S1\text{-}T1})^2$$

Dede *et al.*, reported an informative study on charge transfer mediated ISC very recently (figure 31).[124] In this theoretical study, excited state of pH dependent quinolizinium fluorophore **(35)** is investigated. S_1 → T_1 transition (ISC) is reported in the deprotonated form of **(35)**, whereas triplet state hop could not be observed when **(35)** is protonated. Detailed calculations showed that in the case of **(35)** (deprotonated) excited state charge transfer from aminophenyl moiety to the benzoquinolizinium ring occurs. This excitation can be referred as n-π* type of charge transfer transition. On the other hand in the case of protonated **(35)**,

aminophenyl group is no longer a charge donor and typical π-π* type excitation is detected. Consequently, almost degenerate S_1 and T_1 states are calculated in the case of deprotonated **(35)**, which favors the ISC according to El-Sayed's rule.

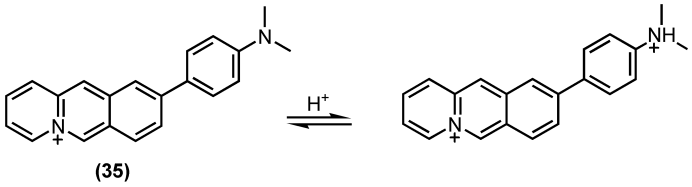

Figure 31. Charge transfer mediated ISC.

2.6.4. Exciton Coupling

Excitation of a molecule that contains identical chromophores, which are closely linked together without π-conjugation, results in two delocalized excited states for each of the single chromophore. In other words, each chromophore is excited separately. If one of the singlet exciton states (mostly the one at lower energy) is closely oriented to the triplet-excited state, then ISC can be realized.[125] There are also some recent examples in which similar two chromophoric systems are introduced, however exciton coupling could not be detected (see chapter 4).

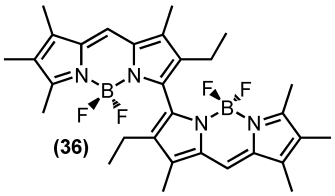

Figure 32. BODIPY based exciton-coupling behavior.

Flamigni group demonstrated an example of exciton absorption for the construction of heavy atom free sensitizers.[126] They performed the synthesis of a dimeric BODIPY derivative **(36)** (figure 32). When the absorption spectra of dimer and its corresponding monomer are compared, different absorption characteristics are observed in the case of **(36)**. Absorption spectrum of monomer shows a typical $S_0 \rightarrow S_1$ excitation behavior of BODIPY core around 530 nm, whereas two sharp and strong absorption peaks are detected in the case of dimer **(36)** at 381 and 534 nm. Presence of two singlet-excited states with different energy levels makes singlet

oxygen generation feasible according to exciton coupling mediated ISC.

2.6.5. Spin Convertors

It is a challenging task to design heavy atom free sensitizers that are able to populate triplet-excited state. One should optimize the chemical modifications on a sensitizer according to tight selection rules. Insertion of an intramolecular energy acceptor with intrinsic ISC character (spin convertor) to an organic molecule, which has low triplet quantum yield, is a promising method for designing heavy atom free sensitizers for PDT. A typical spin convertor is C_{60} moiety that can be easily coupled with chromophores covalently. Out coming dyads/triads can be used for $^1O_2$ generation due to the effective ISC.[108]

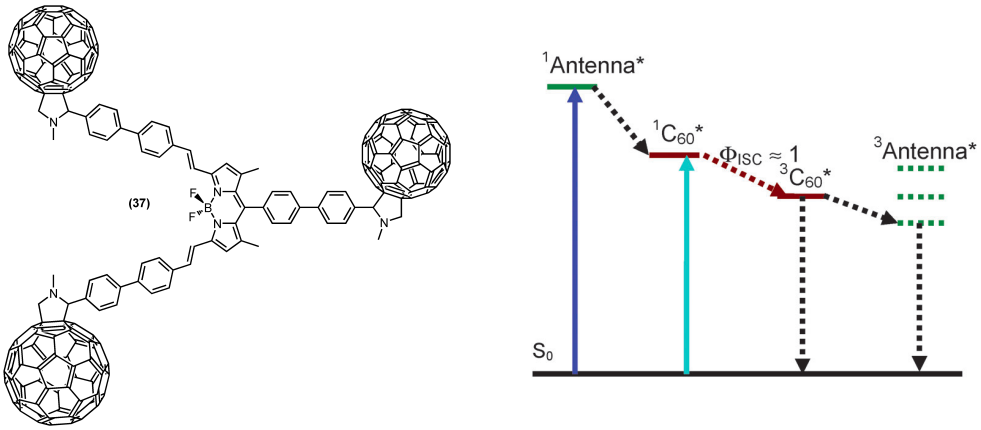

Figure 33. BODIPY-C_{60} conjugate. Copyright © 2012, American Chemical Society. Reprinted with permission from ref (127).[127]

Zhao and coworkers reported the use of fullerene (C_{60}) as a spin convertor in combination with styryl BODIPY derivatives **(37)** in order to introduce heavy-atom free PDT sensitization.[127] C_{60} moiety has an intrinsic ISC property but by itself it is not an ideal sensitizer since its predominant absorption peak is located at UV region. C_{60} has a very weak additional absorption peak around 700 nm, which makes it suitable for intramolecular energy transfer processes when it is coupled with conjugated chromophores (antenna). In the case of Zhao group study, BODIPY core that absorbs at the visible region works as an antenna group. Upon irradiation of the BODIPY, excited electron in the S_1 state (1.93 eV) of an antenna passes to low lying C_{60} singlet excited state (1.72 eV). After that, due to the intrinsic ISC of C_{60}, electron

is transferred to triplet state of C_{60} and finally the electron reaches to nearby triplet state of antenna molecule (figure 33).

2.6.6. Glutathione Mediated Activation of PDT Sensitizers and Low pH of Cancer Cells

Targeting is an important issue while designing a PS, such that it increases the accumulation of the drug at the tumor site and decreases the possible side effects. Passive targeting is the simplest method, which is widely employed for this purpose.[93] It can be realized due to the minimum lymphatic drainage of tumor cells. Because of the leaky vasculature of the tumor tissues, sensitizers can easily accumulate in the tumor. This process is known as enhanced permeation and retention (EPR). However, passive targeting is not sufficient for effective forwarding of PDT sensitizers through cancer cells. There has to be additional targeting elements in combination with EPR approach for selective therapy. PSs that are covalently attach to various molecules, which have great affinity towards cancer cells or to receptors that are expressed on tumors (e.g., monoclonocal antibodies, peptides, epidermal growth factors, various carbohydrates, glucose receptors and low-density lipoprotein) are also widely used in targeting strategies.[128] It is also possible to control the activation/deactivation of PSs by modulating the photophysics of sensitizers. Initially quenched PSs can be selectively activated after photophysical alterations in the cancer cells with tumor related inputs such as folic acid, GSH and many others. For instance, singlet-singlet energy transfer or self-quenching mechanism can deactivate PSs before transition to triplet excited state.[129] Moreover, PeT[130] and FRET[131] processes can be modulated for successful quenching of PSs. In addition to these, singlet oxygen scavengers can be used to trap $^1O_2$ before its cytotoxic effect following ISC.[132]

Among possible targeting strategies, GSH activated sensitizers have attracted considerable attention and appeared to be promising in recent years. As it is mentioned before GSH plays important roles in cellular redox activity. Synthesis of GSH is realized by combining its amino acid precursors (glycine, cysteine and glutamine) in the presence of γ-glutamylcysteine synthetase and glutathione

synthetase. Reduced form of GSH acts as a strong antioxidant and mostly reduced the reactive oxygen species, which are produced as a result of oxygen metabolism intracellularly. After reduction, oxidized form of GSH, which is also known as di-sulfide form (GSSG) can be readily obtained. Glutathione reductase enzyme is responsible for reducing GSSG back to GSH. GSSG is transferred to extracellular matrix and decomposition of it takes place there, whereas GSH is an intracellular bio-molecule. Thus, there is a great balance between GSH and GGSG within the cell, which is crucial for redox reactions and maintenance of cell life cycle.[133] Therefore extracellular amount of GSH is low, which is around micromolar levels. On the other hand, intracellular level is around millimolar concentrations. Reducing capacity of GSH regulates signal transduction mechanisms. In the case of tumor, fast growing cancer cells try to decrease the amount of reactive oxygen species, which are known to be primary reason for oxidative stress that limits the survival and proliferation of cells. The high level of reducing bio-molecules NADH and GSH are responsible for this reduction. It is also observed that cancer-promoting transcription factor such as MYC is highly regulated that increases the glutamine uptake, which is needed for GSH synthesis. As a result of this cycle, reduced GSH level is elevated in cancer cells (2 to 50 fold).[134] Thus, incorporation of GSH selective groups on a PS or GSH mediated activation of a PS are powerful and extensively applied modalities to get targeted PDT agents.

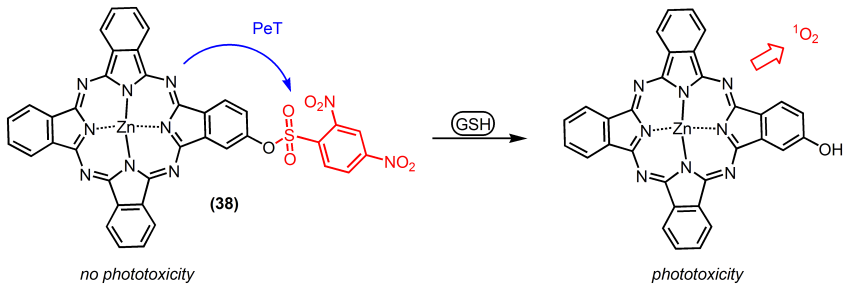

Figure 34. GSH activated phthalocyanine sensitizer.

Dennis Ng and coworkers reported a 2,4-dinitrobenzenesulfonate substituted zinc (II) phthalocyanine based activatable sensitizer very recently.[135] Initially compound **(38)** is weakly fluorescent because of the 2,4-dinitrobenzenesulfonate group mediated reverse PeT mechanism. Since PeT mechanism is a very fast transition, presence of a

PeT pathway blocks the ISC and PSs become de-activated. When GSH is added, cleavage of sulfonate ester bond terminates the PeT route and singlet oxygen generation takes place with bare phthalocyanine sensitizer as in the case of porphyrin dyes (figure 34). **(38)** is also applied to MCF-7 cancer cell line.

Choi *et al*. introduced a nano-sized graphene oxide (GO)-sensitizer (chlorine 6) complex, where redox-responsive cleavable disulfide linker satisfies successful complexation between GO and chlorine 6. Initially conjugate is non-fluorescent and non-toxic even under irradiation due to the effective FRET from excited chlorine 6 to the GO.[136] Complex is getting activated only in cancer cells (where GSH level is very high) after exocytosis due to the GSH mediated disulfide bond breakage. Released sensitizer then becomes fluorescent and phototoxic (figure 35). This activatable conjugate is a highly promising example for the next generation theranostic (therapy + diagnosis) sensitizers.

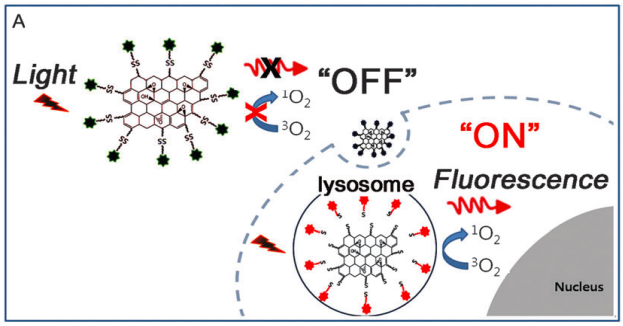

Figure 35. GSH activated graphene oxide-chlorine 6 conjugate for PDT. Copyright © 2012, Royal Society of Chemistry. Reprinted with permission from ref (136).

Low pH value of cancer cells: Hypoxia and mitochondria damage force cancer cells to supply their energy need by increasing the rate of glycolysis (formation of ATP and pyruvate from glucose in the presence of pyruvate kinase) and lactic acid formation.[137] Consequently change in energy metabolism and ion transport processes cause lactic acid and pyruvate accumulation in the cancer cells, which decreases the extracellular pH of cancer cells to pH 6.0-6.5.

2.7. Axial Chirality

It is well known that sufficient condition for an organic molecule to be chiral is that it has to have a non-superposable mirror image. This condition is widely satisfied with a single and stable stereocenter (central chirality) in most of the organic compounds. Presence of central chirality is adequate but not a necessary one. There are also some other types of chiral molecules in which there are no chiral centers (chirality in molecules devoid of chiral centers). In 1956, Chan, Ingold and Prelog introduced the term "axial chirality" in their pioneering study.[138] They stated that three-dimensional space could also be occupied by asymmetrically around a line or a plane in addition to a point (or a center).

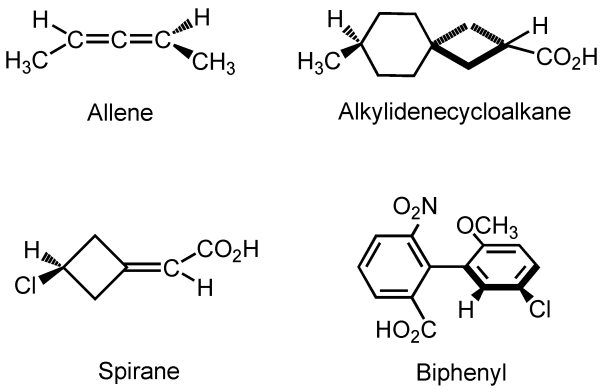

Figure 36. Some common molecules with axial chirality.

Chiral axis is typically maintained by; (i) chain stiffness of a double bond, (ii) the molecular framework itself, (iii) a combination of these two or (iv) hindered rotation around a single bond.[139] Consequently, axial chirality is mostly observed in allenes, spiranes, alkylidenecycloalkanes, and biphenyls (figure 36).

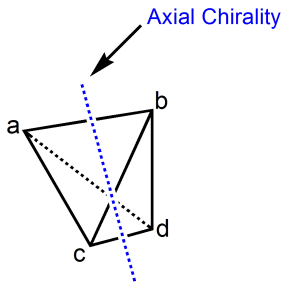

Figure 37. Schematic representation of axially chiral plane.

In these types of molecules, if the tetrahedron framework is stretched along its S_4 axis, desymmetrized D_{2d} framework is obtained.[139] Thus, the long axis of this framework can be chosen as a chiral axis (figure 37). Since the stretched tetrahedron has lower symmetry compared to a parent tetrahedron, it is not required to have four different groups around a chiral axis such that, sufficient condition for chirality can be written as a≠b and c≠d. This is typical case for allene derivatives (abC=C=Cab).[139]

Circular dichroism (CD) is the primary analytical tool for the analysis and detection of chiral molecules.[140] It depends on the differential absorption of left/right circularly polarized light by a chiral sample. One type of circularly polarized light is absorbed more than the other at particular wavelengths and CD calculates the absorbance difference (ΔA).

$$\Delta A = A_L - A_R$$

where A_L is the absorbance of left circularly polarized light and A_R is the right circularly polarized light. According to Beer's law, this equation can also written as follow;

$$\Delta\varepsilon = (\varepsilon_L - \varepsilon_R) = \Delta A / cl$$

ε_L and ε_R are molar extinction coefficients of left and right circularly polarized light respectively, c is the concentration and l is the path length. The term molar ellipticity $[\theta]_M$ can also be used to represent CD results.

$$[\theta]_M = 100\theta / cl$$

As it is mentioned before left or right circularly polarized light is absorbed more by a chiral sample, thus the amplitude of one type of light is always smaller.[140] When amplitudes of these two incoming light are combined, they form ellipsoid shape. θ is the angle between the long and short axes of ellipsoid. Relation between extinction coefficient difference and molar ellipticity is given below.

$$\Delta\varepsilon = [\theta]_M / 3298.2$$

2.7.1. Atropisomerism

Axial chirality in atropisomeric (named from the Greek *a* meaning not, and *tropos* meaning turn) compounds is the result of a non-planar arrangement of different groups on both sides of the chiral plane, and enantiopure products can be isolated because of the restricted rotation of a single bond on that chiral axis.[141] Most extensively studied and known atropisomeric compounds are *ortho*-substituted biphenyl derivatives in which steric factors form rotation barrier between the substituents.[142] In figure 38, schematic representation of a biphenyl is given. When X≠Y and A≠B and furthermore, if the steric interactions that arise from X-A, Y-B and/or X-B, Y-A clashes make planer arrangement of two rings highly energetic, axial chirality can be obtained. Two nonplanar enantiomers can be resolved under suitable conditions if the perpendicular to planer interconversion about a sp^2-sp^2 bond is slow enough. Christie and Kenner introduce the first example of this type of axial chirality in 1922.[143] Later, Kuhn named it as atropisomerism in 1933.[143]

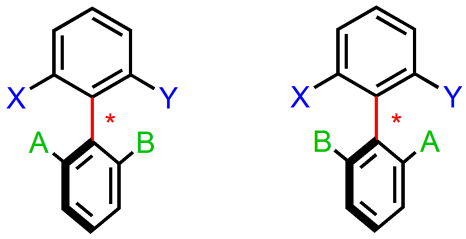

Figure 38. Schematic representation of atropisomerism.

Oki and coworkers generalized the suitable conditions for getting resolved atropisomeric enantiomers.[144] It is generally accepted that, successful separation of two isomers is almost impossible if the energy barrier between them is low (~85 kJ/mol) and so interconversion is taking place very rapidly at room temperature. It is difficult to introduce exact free energy values for efficient separation since it highly depends on temperature. Some estimated values are, 93.3 kJ/mol at 300 K, 109.6 kJ/mol at 350 K and 61.5 kJ/mol at 200 K. In addition to energy barrier requirement, it is noted that half-life of an enantiopure product has to be at least 1000s (16.7 min)

for effective and stable isolation.

Biphenyl and binaphthyl derivatives are very common examples of sp^2-sp^2 single bond type atropisomerism. There also some other types of atropisomerism such as axial chirality about sp^2-sp^3 (9-Arylfluorenes) and sp^3-sp^3 (dibenzobicyclo[2.2.2]octatriene) bonds.[139] Asymmetric synthesis of atropisomers mostly involves well established Kharasch, Negishi, Stille and Suzuki coupling reactions.[139]

Nomenclature of atropisomers involves some additional priority rules[139] such as "near groups precede far groups" and priority of the substituents on each of the units along the axis of hindered rotation is determined separately according to Cahn-Ingold-Prelog priority rules (figure 39). Stereochemistry of atropisomers then can be assigned by moving from the substituent of highest priority on the closest ring to the highest priority group on the other ring by tracking the shortest path. If the direction is clockwise then isomer is named as *P* (plus) or *S*. On the other hand anti-clockwise direction can be designated as *M* (minus) or *R*. Sometimes *aS* or *aR* may be used, where "*a*" stands for axial chirality, but usage of *"a"* is optional. Schematic representation of sequence rule for atropisomers is given in figure 39. In this figure, it is assumed that priority of A>B and X>Y.

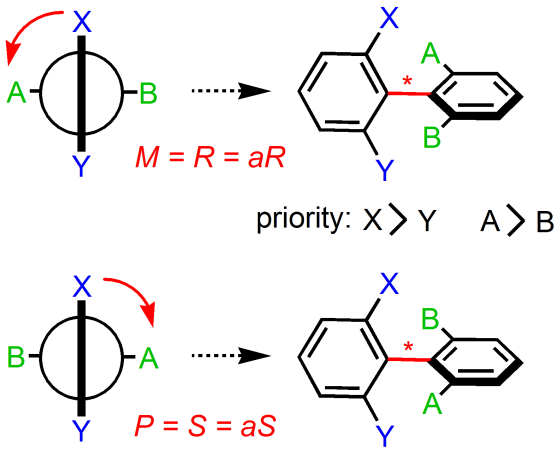

Figure 39. Nomenclature of atropisomeric compounds.

Chiral discrimination between enantiomers is highly significant for pharmaceutical and food chemistry.[145,146] Atropisomeric compounds, especially binaphthyl

derivatives have been widely employed for enantioselective sensing of chiral molecules such as amino acids, amines, acids and alcohols.[146] Lin Pu and co-workers introduced one example of fluorescent enantioselective detection of α-Hydroxycarboxylic acids.[147] They synthesized a 1,1'-bi-2-naphthol(BINOL)-amino alcohol derivative **(39)** (figure 40) and isolated the *S*-isomer. *S*-**(39)** has two characteristics fluorescence peaks one at 372 nm and the other one at 448 nm. Longer wavelength emission is assigned to the excimer formation, whereas the other peak is the monomer emission. When *S*-**(39)** is treated with *S*- and *R*-phenyllactic acid separately, it is observed that, *S*-phenyllactic acid quenches the monomer emission and increases the excimer fluorescence, conversely *R*-phenyllactic acid enhances the monomer emission. Similar results are also obtained by using mandelic acid. For both cases, ratio of fluorescence intensities for monomer emission after the addition of *R*/*S* acids can be used to achieve enantioselective sensing of α-Hydroxycarboxylic acids. In the case of phenyllactic acid I_R/I_S ratio is calculated as 11.2, which is the highest reported value for fluorescent enantioselective detection.

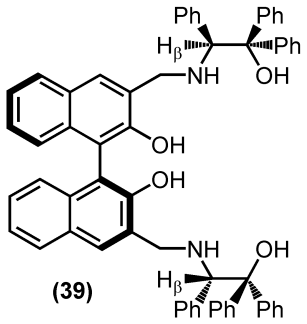

Figure 40. Enantioselective detection of α-Hydroxycarboxylic acids.

2.7.2. Chiral BODIPY Dyes

Chiral fluorophores and chromophores are highly desired as it is mentioned in the previous section. Thus, the synthesis of chiral BODIPY (one of the most commonly used fluorescent dye) derivatives has great importance since this class of dye can be used in various applications. Rich BODIPY chemistry offers great opportunities for the functionalization of the core. Ziessel *et al.*, reported a chiral BODIPY derivative **(40)** in which boron atom is used as a chiral center (boron asymmetry) (figure 41).[148]

Dissymmetrization at boron is achieved by the selective oxidation of methyl group at 3-position and replacing one of the fluoride atom by naphthalene derivative. Enantiomers are isolated by chiral high performance liquid chromatography (HPLC) and presence of enantiopure products are detected by circular dichroism (CD) data.

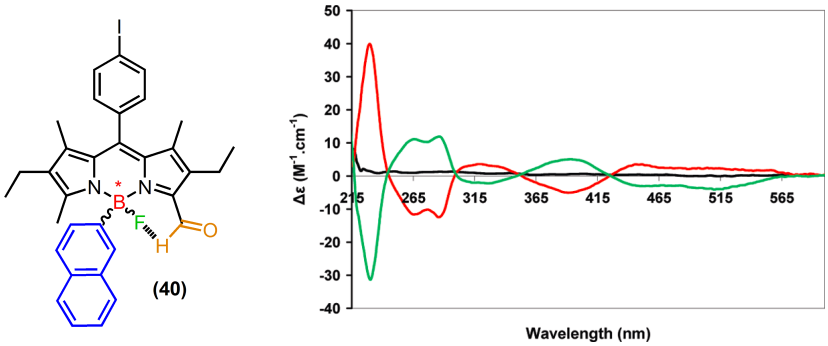

Figure 41. Boron asymmetry on a BODIPY dye. Copyright © 2010, American Chemical Society. Reprinted with permission from ref (148).[148]

Daub and Rurack introduced a binaphthalene-BODIPY conjugate **(41)** for fluorescent chiral discrimination of optically active phenylethylamine (PEA).[149] In the presence of base, deprotonation of hydroxy groups causes effective PeT, which decreases the emission intensity of BODIPY at 542 nm. When **(41)** is treated with R-/S-PEA, decrease in fluorescence intensity is more pronounced in the case of S-PEA due to the better association of it with **(41)** suggesting enantioselective detection of an optically active base.

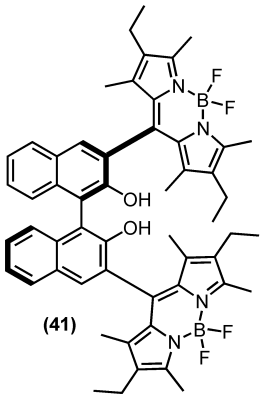

Figure 42. Molecular structure of binaphthalene-BODIPY conjugate.

After our first report[150] on atropisomeric BODIPY derivatives (see chapter 5), during the preparation of this dissertation, Hall *et al.*, revealed new axially chiral BODIPY

dyes **(42, 43, 44)** (figure 43).[151] They modified the *meso*-position of the BODIPY core with an aryl substitution and 1- / 7-positions of the core with methyl groups in order to hinder the rotation of single bond at *meso*-position. In addition to that, *ortho*-position of the *meso*-aryl and 2- / 6-positions of the BODIPY core are decorated with chemically differentiable groups to dissymetritized the axis of hindered rotation. Enantiopure products are separated by chiral HPLC.

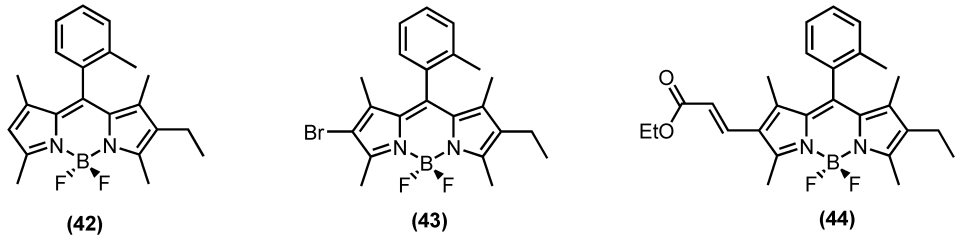

Figure 43. Axially chiral BODIPY derivatives.

2.8. Polycyclic Aromatic Endoperoxides

It is obvious that the chemical reactivity of singlet oxygen is different than the triplet ground state oxygen such that, it can undergo addition reactions to form endoperoxides. Many polycyclic aromatic compounds including naphthalene and anthracene can trap singlet oxygen, and some of these resulting endoperoxides (EPOs) exhibit an interesting feature, which is the release of singlet and/or triplet oxygen in the excited state upon warming or light irradiation.[152] The first example discovered was the case of rubrene in 1926, which is followed by the studies on 9,10-diphenylanthracene.[152] Further investigations showed that in some instances (e.g., 1,4-dimethoxy-9,10-diphenylanthracene), the dissociation to produce singlet oxygen can take place at room temperature.[152] In accordance with this feature, water-soluble naphthalene endoperoxide derivatives have been prepared and employed as singlet oxygen carriers and source in biological environment by several research groups.[153] It is now clear that by different substitution patterns, it is possible to control the rate and temperature of thermal decomposition process of polycyclic aromatic endoperoxides that suggests promising utilization on many application areas.

2.8.1. Preparation of Endoperoxides

Most of the aromatic endoperoxides themselves are prepared by photosensitized oxygenation, which involves [4+2] cycloaddition of $^1O_2$.[154] Due to the electrophilic nature of $^1O_2$, the reactivity of aromatic hydrocarbons with $^1O_2$ increases with electron density of the hydrocarbons involved. Incorporation of electron donating substituents on the reaction site of $^1O_2$ dramatically increases the rate constant of the addition reaction in the order H < C_6H_5 < CH_3 < OCH_3.[152] For example, unsubstituted naphthalene does not react with $^1O_2$, whereas it is possible to observe endoperoxide formation with 1-methyl naphthalene.[152] Another structural effect on reactivity is the number of fused ring. Investigations on anthracene, tetracene and pentacene showed that as the fused ring number increases, reactivity increases by about 2 fold.[155]

In addition to electronic effects, steric factors also play an important role in determining the reaction rate. For instance, in the case of [2,2] paracyclophane diene, phenyl rings are distorted in such a way that reaction with singlet oxygen can take place easily.[156] 1,8-dimethyl anthracene is another interesting example, in which steric strain between two methyl moieties is relaxed in the excited state suggesting high reactivity.[152] Unlike Diels-Alder cycloadditions however, there is a significant solvent dependence in reaction rates. The cycloaddition reaction of singlet oxygen rate increases 100-fold from cyclohexane to DMF, and becomes even faster in water with water-soluble analogs.[152]

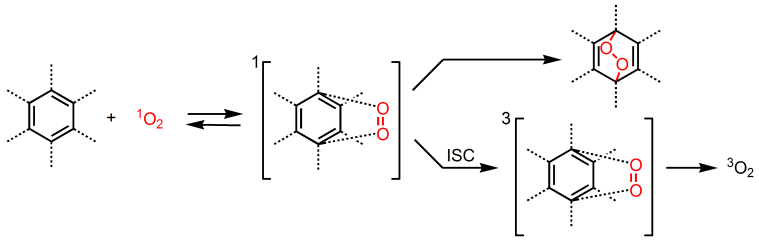

Figure 44. Synthesis of aromatic endoperoxides.

The suggested mechanism for the [4+2] cycloaddition of singlet oxygen to the aromatic compounds is very similar to the classical Diels-Alder type reactions but

with little alterations. Recent studies revealed that singlet oxygen addition to the aromatic ring is a concerted, single step reaction, which exhibits strong charge transfer from the aromatic organic donor to singlet oxygen (figure 44).[157] During the reaction a reversible intermediate conjugate between aromatic ring and oxygen is formed in the singlet state. This conjugate has a significant charge transfer character due to the electrophilicity of singlet oxygen. After the formation of intermediate state, one can obtain the aromatic endoperoxide through concerted mechanism or charge-transfer mediated ISC may takes place that switches the intermediate conjugate to the triplet state and at the end molecular oxygen $^3O_2$ is dissociated.

2.8.2. Thermolysis of Endoperoxides

In the dissociation of endoperoxides upon heating, in principle there are two primary pathways, cycloreversion, leading to the substrate and O_2 (in either triplet or singlet state) and cleavage of the peroxide bond, which is often accompanied by rearrangements or decomposition to hydroxyketones or quinones (figure 45).[158]

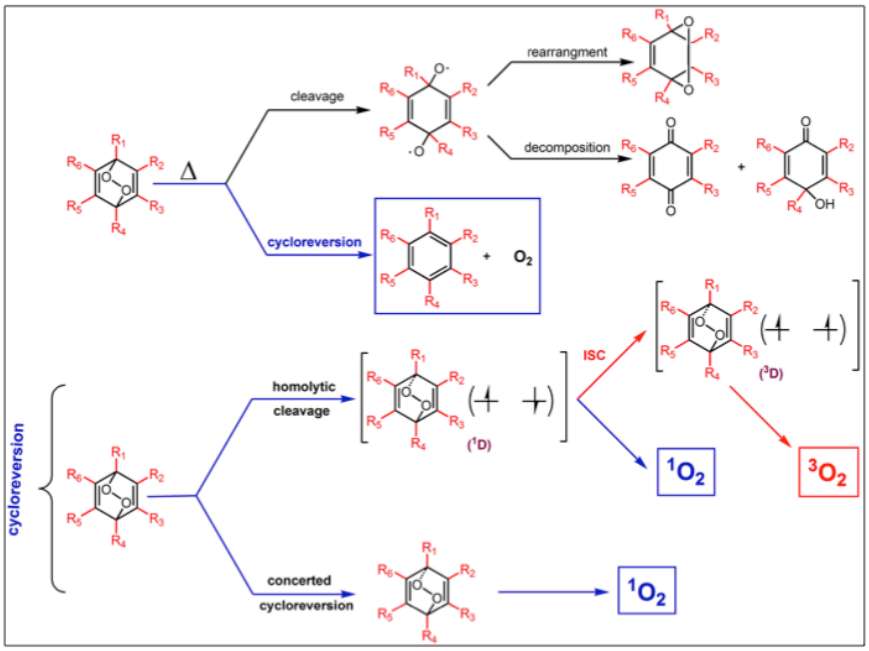

Figure 45. Thermolysis pathways for aromatic endoperoxides.

Activation enthalpy values for cycloreversion are directly affecting the ratio between cleavage and cycloreversion. Figure 46 represents some activation parameters for the

thermolysis of several aromatic endoperoxides.[152] Activation enthalpy for cycloreversion increases from simple benzene to substituted naphthalene and 1,4-substituted anthracene derivatives and then 9,10-substituted anthracenic endoperoxide. Thus, it is clear that cleavage strongly compete with the cycloreversion process in the case of compounds similar to those.

Recent studies showed that incorporation of aromatic moieties to the bridgehead position of aromatic EPOs favors the cycloreversion process.[152] For thermal cycloreversion decomposition pathway, there are also two possible mechanisms. In a concerted cycloreversion, singlet oxygen is produced quantitatively. On the other hand, homolytic cleavage involves ISC and leads both molecular and singlet oxygen. Turro and coworkers introduced that 1,4-substituted aromatic endoperoxides (**45**, **46**, **47**) decomposes singlet oxygen in a high yield, whereas 9,10-substituted ones (**48**) produce $^1O_2$ and $^3O_2$ (figure 46).[158] As mentioned before, there are many examples in the literature in which naphthalene and anthracene derivatives have been employed as reversible singlet oxygen carriers in both organic and aqueous solutions.[152]

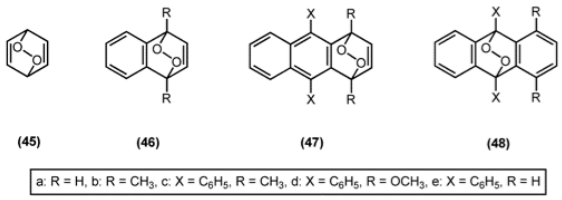

Endoperoxide	$\Delta H^{\neq}$ (kJ/mol)	$\Delta S^{\neq}$ (J/K mol)	$^1O_2$ (%)
45	74.4±2	-1.7±8	**90±3**
46 (a)	97.0±4	0.8±5	**≈100**
46 (b)	101.1±1	8.4±4	**76±1**
47 (c)	124.6±1	-7.5±3	**92±1**
47 (d)	101.1±1	-1.3±3	**95±5**
48 (e)	135.8±1	40.1±2	**32±1**
48 (c)	132.9±1	30.9±3	**52±4**

Figure 46. Activation parameters for the thermolysis of various aromatic endoperoxides and singlet oxygen generation yields.

Some examples are given in figure 47 and 48. In addition to small molecules, polymeric endoperoxides have also been prepared as well, for example, naphthalene derivatives are successfully grafted on a chloromethylated styrene divinylbenzene beads, or polymerization of methyl substituted vinylnaphthalene.[159]

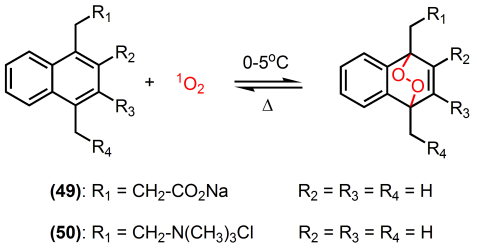

Figure 47. Formation and decomposition of naphthalene based endoperoxides.

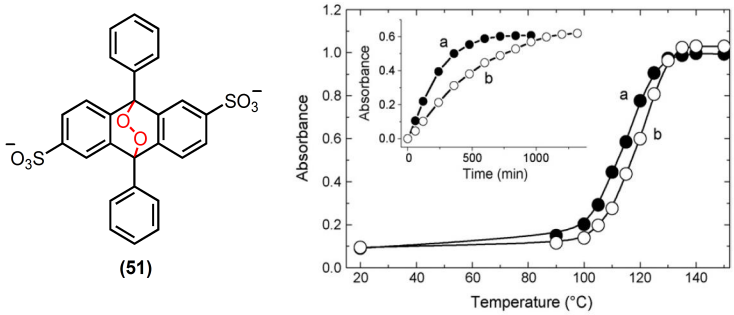

Figure 48. Temperature dependence of anthracene **(51)** thermolysis. Copyright © 2008, Elsevier. Reprinted with permission from ref (160). [160]

2.9. Gold Nanorods

Richard Feynman in his famous talk, which is entitled as "*There is a plenty of room at the bottom*" at American Physical Society Meeting at Caltech on 1959, introduced a new, fascinating and promising field with its potential application areas and impressive recommendations to the scientific community.[161] This talk was approved to be the pioneering attempt for initiating the small-scale science, which is so called "nanotechnology" today. He started to present his new point of view by asking a remarkable question: "*Why cannot we write the entire 24 volumes of the Encyclopedia Britannica on the head of a pin*?" This was actually a good starting point, which strictly explains how small he meant when he was talking about small-scale science. From that day to today, nanotechnology have been receiving extensive attention. Nanoparticles are one of the significant contributors to the field due to their attractive application areas such as biomedical technologies, catalytic activities, optoelectronic devices and plasmon-enhanced spectroscopies.

It is very well known that the type and the pathway of free electron motion are

directly affecting the physical and chemical properties of a matter in most cases, highlighting the importance of the type and shape of the materials (figure 49). Detailed studies revealed that when the electrons are confined in a very small nanometer scale (1-100 nm), in other words as the size of a matter change from bulk to nano-scale; its properties (electronic, optical and catalytic) are dramatically changing due to the restricted electron motion, suggesting new and promising application areas.[162] This is mostly the result of large surface area-to-volume ratio and quantum confinement effect (for 2-10 nm nanoparticles, where the size is comparable or smaller than the Bohr radius) in sufficiently small materials. This phenomenon is also valid for transition metal nanoparticles including gold nanostructures. The electron confinement in nanostructures of gold results in characteristic properties such as enhanced optical transition probabilities, confinement-induced shifts of energy levels and nonlocal dielectric responses.[163] As a result of these properties, gold nanoparticles in the form of sphere, core-shell, cage and rod have been intensively studied and attracted great interest.[164]

One of the most intriguing properties of gold nanoparticles is the ability to induce localized surface plasmon oscillations of conduction band electrons by confining the incoming photons in a small area. As a result of this confinement, the amplitude of the light wave increases by orders of magnitude (increase in electric field), which results in several potential applications including optical imaging, photothermal conversion, Rayleigh and enhanced Raman scattering.[165] It is important to note that; localized surface plasmon resonance (LSPR) wavelength of a gold nanoparticle can be tuned by simply adjusting the size and the shape of the nanoparticle during the chemical synthesis. At that point, *gold nanorods (NRs)* are quite favored since these rod-like nanoparticles have two distinct LSPR peaks, which are longitudinal and transverse and former can be tuned by chemical synthetic methodologies across a broad range, covering visible and near-IR region of electromagnetic spectrum (figure 49). This tuning is mostly realized by the control of the aspect ratio and varying the head shape of the nanorods.[165] In addition to strong and controllable LSPR peak, gold NR has some other promising characteristics such as biocompatibility/bioinertness, ease of functionalization and compact size, which

makes it suitable for imaging, therapy and theranostic studies.[164] These applications of Au NRs have been pursued extensively during the last decade.

2.9.1. Preparation of Gold Nanorods

Michael Faraday obtained gold nanocrystals in 1857 by reducing gold chloride in the presence of phosphorous for the first time.[164] After this initial report, many techniques including chemical/electrochemical reduction, photochemical reduction and some other different physical methods have been introduced for the synthesis of gold nanoparticles (nanospheres, nanorods, nanoplates, nanocubes, nanoshells, and nanocages).[164] For the growth of gold NRs, there are basically two methods, which are bottom-up and top-down approaches, and some other different physical methods have been introduced for the synthesis of gold nanoparticles (nanospheres, nanorods, nanoplates, nanocubes, nanoshells, and nanocages).[164]

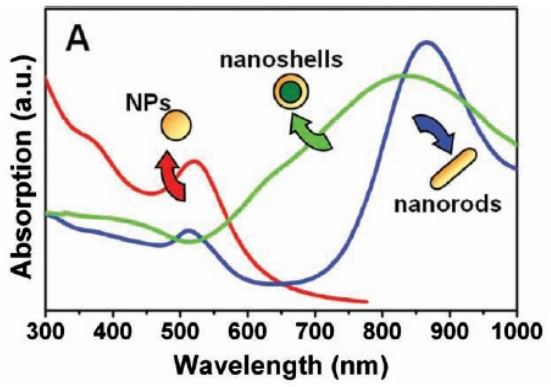

Figure 49. Comparative LSPR peaks of nano-sphere, shell and rod. Copyright © 2010, John Wiley and Sons. Reprinted with permission from ref (166).[166]

Popular bottom-up techniques for the synthesis of gold NRs are wet-chemical,[167] electrochemical,[168] solvothermal,[169] microwave-assisted,[170] and photochemical reduction[171] methods in the presence of several reducing agents including ascorbic acid, sodium borohydride and 1-2 nm gold clusters. In addition to these, some directive templates are included in the synthesis in order to achieve growth along one direction. Most common templates for this purpose are cationic ammonium surfactants, among which cetyltrimethylammonium bromide (CTAB) is commonly employed.[172] CTAB-like surfactants have two major roles; (i) they prevent the

aggregation of nanorods and (ii) direct the longitudinal growth of rods by forming micelle.

In general, chemists prefer to use bottom-up, wet chemical seed-mediated growth in which gold salts are reduced in the presence of CTAB. This method is quite useful since it yields almost mono-disperse, uniform and high yield (yield in nanorod synthesis represents the ratio between the number of rod-like structures to the total number of gold nanocrystals in solution) nanorods.[164]

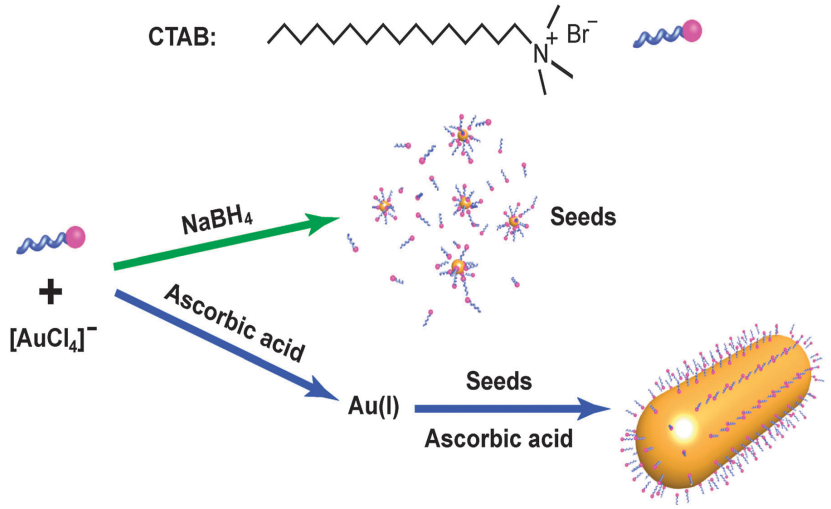

Figure 50. Preparation of gold NRs according to El-Sayed's seed mediated synthesis. Copyright © 2009, John Wiley and Sons. Reprinted with permission from ref (164)[164]

Seed-mediated growth was introduced by El-Sayed and Murphy independently.[167,173] In a typical procedure (figure 50), initially, seed solution that contains 1-2 nm small gold nanoparticles are prepared by reducing chloroauric acid ($HAuCl_4$) in the presence of cold sodium borohydride ($NaBH_4$) in a aqueous CTAB solution. Then, small amount of seed solution is introduced to the growth solution, which is prepared separately by reducing $HAuCl_4$, Au (III) to Au (I) with ascorbic acid in the presence of $AgNO_3$ again in aqueous CTAB solution. Au (I) ions further reduced to Au (0) by added seed to form gold nanorods. One of the most important contributors of growth solution is $AgNO_3$ since Ag (I) ions are thought to bond selectively to the {110} face of the gold nanocrystals during the growth, which favors the deposition of gold atoms on {100} face that causes the longitudinal growth and rod-like shape. 99% nanorod yield can be achieved by using seed-mediated growth. Moreover, this

growth method offers high control on size and shape of the nanorod product by careful adjustments of amount of surfactant and reagents, the pH of the solution, temperature, and the structure of seeds. Aspect ratio can be varied between 2.4 to 8.5, which directly affects the plasmonic properties. For instance, by just changing the concentration of $AgNO_3$, it is possible to change the length and aspect ratio of the nanorod. Furthermore, low amount of ascorbic acid yields dogbone-like rod structures. As in the case of almost all synthetic methodologies, there are also some drawbacks of this method.[164] First of all, it is impossible to control the location of added gold nanocrystals to the rod during the growth, since gold salts are randomly reduced. Secondly, the size and the shape of the rods vary in each experiment even if the same procedure is applied.

Top-down approaches for the synthesis of gold NRs involve removal of gold from pre-deposited gold film by using focused ion beam or some etching techniques, Second method is to use lithographic methods. Electron-beam lithography is the most applied one in which 10-100 nm rods can be obtained.[164]

2.9.2. Functionalization of Gold Nanorods

CTAB coated gold nanorods have to be functionalized with suitable organic/inorganic moieties for better stability under different conditions and to get functional reaction sites for further modifications according to desired end-use.[174] While performing the synthesis of gold NRs, dissolved bromide ions adsorbed on the surface of nanorod, which causes electrostatic interaction between positively charged ammonium end of the CTAB and bromide on the rod surface. This interaction forms the inner layer. Hydrophobic alkyl groups do not like to interact with water, thus an additional CTAB layer is formed in which ammonium end is pointing outside and hydrophobic tail is located inside. Consequently, presence of bilayer structure makes the surface of nanorod positively charge and it becomes stable in aqueous solution.[175] This bilayer can be broken if the concentration of the CTAB on the surface is lower than the critical micelle concentration and/or some other reagents with very high affinity toward gold is added.

Affinity of thiols towards gold is mostly utilized in functionalization of gold nanorods. Small molecules containing thiol as a functional group are not desired since they are not able to overcome the large attractive force between NRs. Thiol-substituted high molecular weight polymers such as poly(ethylene glycol)s (PEGs) are more suitable for thiol-gold bonding chemistry.[164] In general, functionalization with thiol molecules is realized at the two ends of the rod, suggesting that CTAB concentration is higher at the center.[176] Modification of NRs with thiol terminated PEGs makes NRs more biocompatible and enhances their retention time in biological medium. Moreover, PEGlyation prevents the aggregation of rod in aqueous solvent and polar environments such as alcohols, acetone, dimethylformamide (DMF), dimethyl sulfoxide (DMSO) and phosphate buffer saline (PBS).[164] Disulfides and dithiocarbamates can be also used to functionalize the surface of NRs. Polymers containing bifunctional groups also useful for further modification of gold NRs.[177] There are some other approaches different than Au-thiol bond chemistry including electrostatic, antibody-antigen interactions and DNA sequence recognition.[164] For instance negatively charge polyelectrolytes (e.g, polystyrenesulfonate and polyacrylic acid) and proteins can be employed through electrostatic adsorption.[178]

2.9.3. Plasmonic Properties and Photothermal Conversion

It is mentioned before that collective oscillation of the conduction band electrons upon excitation of gold nanorods is responsible for the well-defined LSPR peaks of these nanostructures. Localization of incoming electromagnetic waves in a region that is very close (100 nm) to the surface, is one the unique characteristics of the metal nanoparticles. This property yields large electric field enhancements, extremely high absorption and photothermal conversion abilities. Desymmetritization of gold nanospheres as in the case of gold NRs dramatically changes the plasmonic behavior of the nanoparticles. Gold NRs with their cylindrical geometries offer different directions and path lengths for conduction electron to move around. As a result, NRs have two characteristic LSPR peaks, a longitudinal and a transverse peaks.[164,165] In the former one, electron oscillations take place along the length direction and since the pathway is much longer, longitudinal LSPR peak is

located at longer wavelengths of the electromagnetic spectrum. Transverse mode is the result of transverse electron oscillations as the name implies and can be observed at the blue side of the longitudinal peak around 500 nm. Adjustment of the aspect ratio during the wet-chemical synthesis of NRs determines the absorption wavelength of longitudinal peak (600-1100 nm) (figure 51).

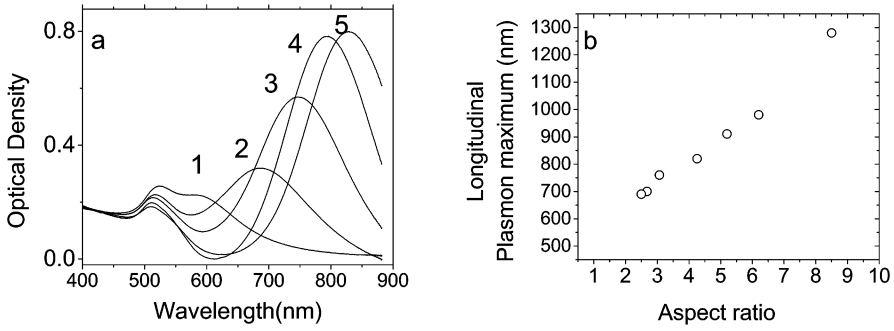

Figure 51. Control of plasmonic properties by adjusting the aspect ratio of NRs. Copyright © 2013, Royal Society of Chemistry. Reprinted with permission from ref (165) [165]

In gold nanoparticles absorbed energy is relaxed back through thermalization with the lattice, which generates heat as a result of plasmon resonance decay. This temperature increase on the surface of gold nanoparticles and surrounding medium have been recognized as a promising methodology for various applications such as photothermal therapy, gene/drug release and drug delivery.[165] Gold NRs are also suitable for photothermal conversion with additional features. NRs have strong absorption behaviors with controllable and tunable LSPR peaks that can be shifted to the red region, where tissue penetration depth is high and absorption of organic tissues is low. Thus, NRs are one of the most striking candidates as a photothermal conversion agent for biomedical applications. Photothermal conversion process constantly compete with the radiative and other non-radiative decays, thus for effective conversion, plasmonic properties and geometry of the rods have to be adjusted carefully. It is shown that photothermal conversion efficiency increases as the match between incoming laser wavelength and the longitudinal plasmon wavelengths of nanoparticle increases.[179] This is related with the better excitation of the rod under these conditions. In addition to the wavelength match, geometry of the rod is also significant for photothermal conversion. Theoretical and experimental studies revealed that radiative decay is reduced in rods with small particle volume

that causes effective photothermal conversion. On the other NRs with large particle volume showed reduced photothermal conversion. Furthermore, Choi and coworkers introduced correlation between concentration of NRs and photothermal conversion. They showed that as the concentration of rods increases, large temperature gradient occurs, indicating better conversion at high concentrations.[180]

It is really a great challenge to know the heat generation and temperature distribution on gold nanoparticles precisely, which is important for applications in which localized heating is needed (tissue repair, catalysis). Quidant *et al*. recently reported a thermal microscopy technique to overcome this obstacle.[181] This method utilizes the molecular fluorescence polarization anisotropy in order to image the heat distribution on a single gold NR. Results showed that heat distribution around NRs is almost uniform. However, resolution of this technique is not sufficient enough, thus improvements are highly needed.

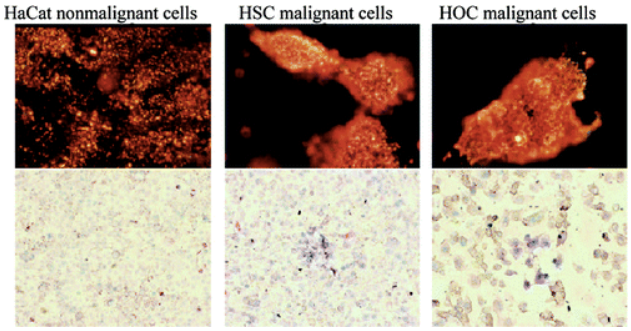

Figure 52. Selective photothermal therapy of cancer cells with anti-EGFR/Au. At 80 mW cancer cells (HSC and HOC) are injured while there is no effect on healthy cells (HaCat) Copyright © 2006, American Chemical Society. Reprinted with permission from ref (183).

Photothermal therapy (*hyperthermia*) is one of the most studied outcomes of photothermal conversion that is satisfied by metallic nanoparticles. It is a viable approach, which microwaves, ultrasound, radiofrequency and lasers are used in accordance with gold nanoparticles to initiate heating at a region of cancer.[182] Upon heating that raises the local temperature above 40^{o}C causes tumor cell deaths (without any conjugated drugs) by necrosis/apoptosis, denaturation of enzymes, promoting functional changes in DNA and RNA.

In vivo photothermal studies require deeper penetration of incoming light through

skin and tissues. This causes the modification of gold nanoparticles in such a way that the SPR peak is shifted through the near-IR (NIR) region of the spectrum. Thus, gold NRs are promising structures and widely used in hyperthermia due to their physicochemical characteristics. El-Sayed *et al*. demonstrated that the NIR excitation of gold nanorods, which are modified with anti-EGFR antibodies, resulted in theranostic affect (both imaging and selective photothermal therapy).[183] Results showed a clear distinction between healthy and cancer cells (figure 52). After the imaging of tumor region by the scattering light from NRs, irradiation was performed with Ti: sapphire laser (800 nm) and malignant cell death occurred at half the energy required to damage healthy cells.

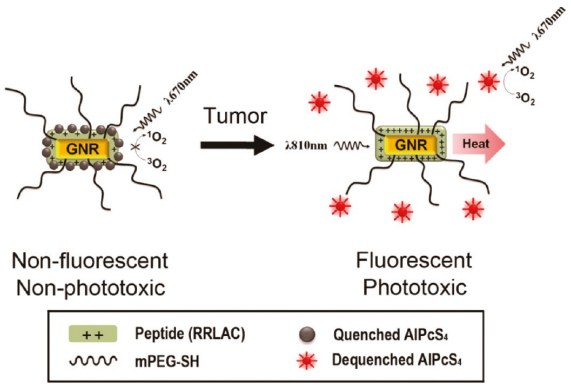

Figure 53. Schematic illustration of gold nanorods-PDT complex for NIR imaging and PDT. Copyright © 2011, American Chemical Society. Reprinted with permission from ref (184).

Gold NRs mediated photothermal therapy has been also used in combination with PDT. Choi *et al*. designed a gold nanorod – PDT complex for NIR imaging and cancer therapy (figure 53).[184] In the case of complex formation between PDT drug and gold, fluorescence emission and singlet oxygen generation are quenched due to the high absorption capacity of NRs. In other words, initially PDT agent is very close to the gold nanorod, which favors the energy transfer from PDT sensitizer to nanorod upon irradiation. Thus, initially there is no fluorescence and phototoxicity effect. After intracellular uptake of the PDT-gold conjugate at tumor sites, PDT agent is released from the gold nanorods, which causes emission enhancement and singlet oxygen generation. To sum up, in this recent article tumor sites are identified and PDT action took place that yielded 79% reduction of the tumor growth.

CHAPTER 3

Selective Fluorescence Sensing of Glutathione Using a Bifunctional Probe

This work is partially described in the following publication:

Işık, M.; Guliyev, R.; **Kolemen, S.**; Altay, Y.; Senturk, B.; Tekinay, T.; Akkaya, E. U. *Org. Lett.*, **2014**, *16*, 3260.

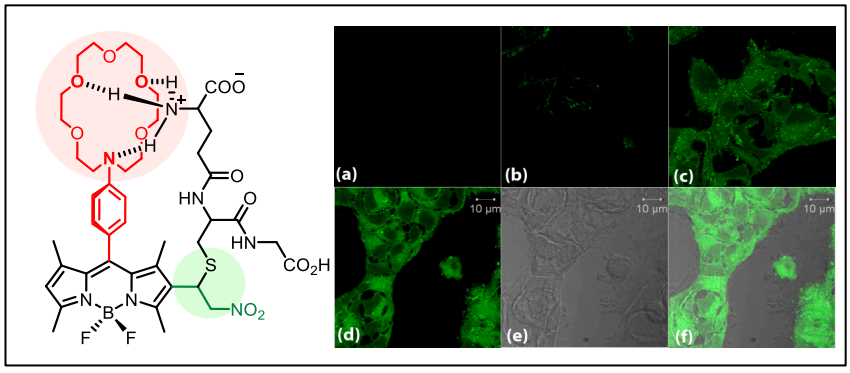

3.1. Objective

In this work,[185] a selective probe for glutathione was designed and synthesized. The design incorporates spatial and photophysical constraints for the maximal emission signal. Thus, pHs, as well as the intracellular thiol concentrations, determine the emission signal intensity, through a tight control of charge transfer and PeT processes. The probe works satisfactorily inside the Human breast adenocarcinoma cells, highlighting GSH distribution in the cytosol.

3.2. Introduction

Chemosensor development has evolved into an attractive field of study, with a large number of promising examples emerging at a steady pace with worldwide participation in this endeavor.[186-188] Most successful probes or chemosensors emerge through modulation of photophysical processes operational for the selected chromophore. The modulation can be the result of a reversible association (e.g., ligand-metal ion), or a chemical conversion of the probe in the presence of a targeted analyte. Rational design of selectivity on the other hand, would benefit tremendously by the judicious incorporation of multiple structural and electronic handles on the signal transduction process.

Biological thiols namely cysteine (Cys), homocysteine (Hcy) and glutathione (GSH) are known to be important parameters in health and disease states as mentioned in the chapter 2.[74] Consequently, a great deal of recent effort has been placed on developing sensors and probes for each and every one of these three species. The substantial progress made in the field has been reviewed recently by Yoon and co-workers.[80] It is an interesting side note that a probe selective for GSH remained elusive until recently.[90,189] Commercially available probes have acknowledged deficiencies such as the need for UV excitation (*o*-phthaldialdehyde, naphthalene-2,3-dicarboxaldehyde, ThiolTracker Violet), high background signal, nuclear accumulation of the adduct (Monochlorobimane) and non-selective reactions in all cases.

In our works focusing on advancing new strategies and/or tactics in sensing and signalling,[190] we found BODIPY dyes to be particularly useful and amenable to modification in accordance with any design requirements.[24,32] Their impressive spectroscopic properties (quantum yield, extinction coefficient, tunability) coupled with the ease of modulation of these properties through, among other photophysical processes, photoinduced electron transfer[191] (PeT) and internal charge transfer[192] (ICT) made them a favorite among similar fluorophores. In designing a selective GSH sensor, we also noted that sensing of thiols is mostly based on their strong nucleophilic character, apparent even in aqueous solutions.[193] Conjugate addition reactions, altering the spectroscopic properties of the probe is a very common theme encountered in a large number of molecular sensor designs.[194] Our goal was to target GSH specifically, and we thought that could be achieved by incorporating an additional recognition site for the N-terminal ammonium group found in GSH. The structure of our target molecule is shown in figure 54.

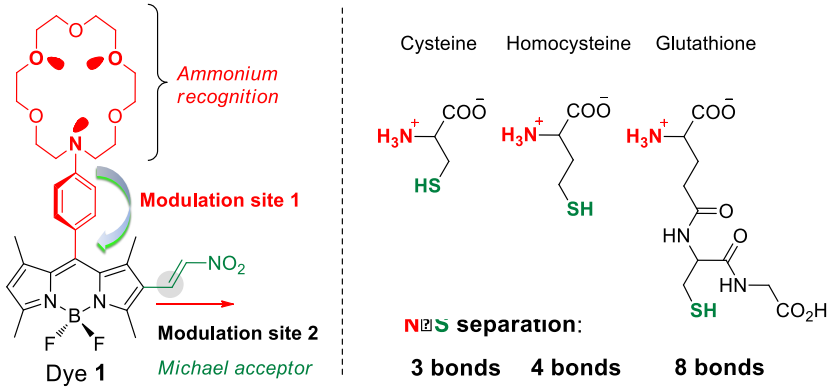

Figure 54. The structure and the signal modulation sites of the target probe. The distance between the terminal amine and the thiol suggests a much better match for GSH and the probe, than the other two biological thiols. Copyright © 2014, American Chemical Society. Reprinted with permission from ref (185).

We also thought the emission signal of the probe could be further modulated by the protonation state of the azacrown amine moiety which would alter the rate of PeT. The quenching in meso-dialkylaminophenyl substituted BODIPYs is most likely a combination of ICT and PeT processes, the former being more apparent in less polar organic solvents. For use in polar or aqueous solvents, rationally designed probes

based on PeT modulation in BODIPY dyes are abound, and Nagano group has reported many, with significant potential.[63,195]

3.3. Results and Discussion

The target molecule was synthesized in a couple of straightforward steps (figure 55) starting from corresponding aza-crown substituted benzaldehyde. Formylation[121] of the 2-position of the BODIPY core, followed by nitromethane condensation, yielded the desired product. It is very well known that electron donating and withdrawing substituents alter both the ground state and excited state properties and result in larger changes in dipole moment on excitation. Thus, **(Dye 1)** shows a red-shifted absorbance with maximum at 518 nm (figure 56) and it is essentially non-fluorescent ($\phi_{fl} < 0.01$). A control reaction with mercaptoethanol causes an enhancement of the emission intensity with a concomitant blue shift (-20 nm) in the absorption spectrum (figure 56). Biological thiols (Cys, Hcy and GSH) also react similarly. Selected photophysical data are presented in table 2.

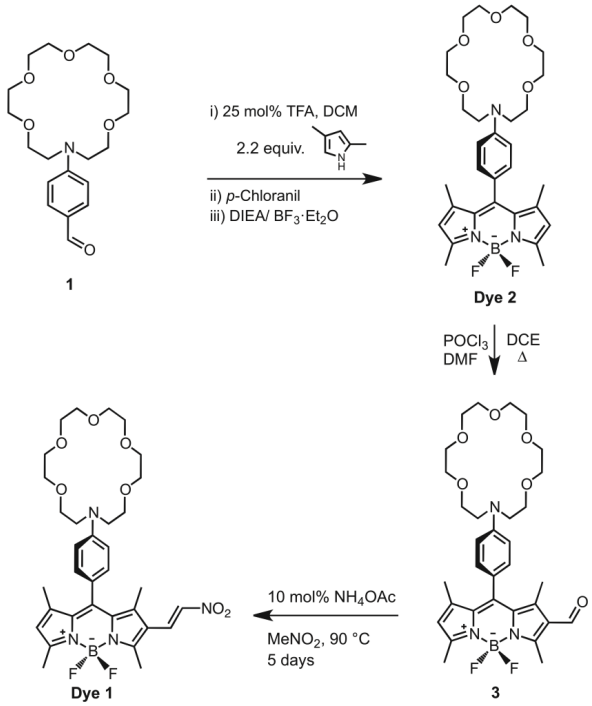

Figure 55. Synthetic route for the synthesis of GSH probe **(Dye 1)**. Copyright © 2014, American Chemical Society. Reprinted with permission from ref (185).

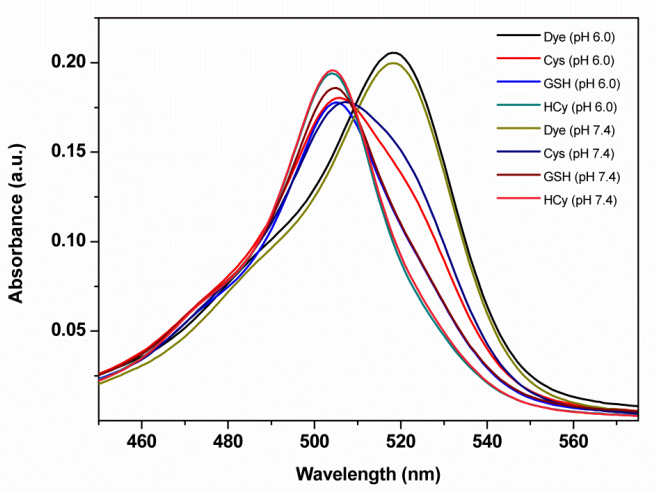

Figure 56. Absorbance spectra of **(Dye 1)** (8.0×10^{-6} M) and **(Dye 1)** + Thiols (200 equivalents) at pH 6.0 in 60% MES Buffer (30 mM) / 40% MeCN and at pH 7.4 in 60% MOPS Buffer (30 mM) / 40% MeCN. Copyright © 2014, American Chemical Society. Reprinted with permission from ref (185).

Table 2. Selected photophysical parameters for the **(Dye 1)** and its conjugate adduct.

probes	λ_{abs} [a] (nm)	ε_{max} [a] ($M^{-1}cm^{-1}$)	λ_{ems} [a] (nm)	fwhm (cm^{-1})	φ_f [b] (%)
Dye 1	518	76,000	522	1590	<1
Dye 1 + GSH (pH 6.0)	505	68,000	522	1523	24
Dye 1 + GSH (pH 7.4)	505	68,000	522	1505	2

[a] In buffered aqueous-acetonitrile (60:40) solutions. [b] Quantum yields were determined in reference to Rhodamine 6G (0.95 in ethanol).

Thus, we felt confident that the first criterion for the putative GSH sensor namely, reactivity towards thiols and thus transforming the probe so that the typical green emission of an unaltered BODIPY core could be enhanced, was satisfied. This is a result of diminished conjugation and charge withdrawal, as initially the nitroethenyl substituent is in conjugation with the BODIPY core, and on reaction with a thiol, the nitro group becomes isolated from the BODIPY π- system, due to the formation of the thioether adduct. ^{1}H NMR data (figure 57) strongly corroborates with the emission intensity changes, providing clear evidence for the conjugate addition.

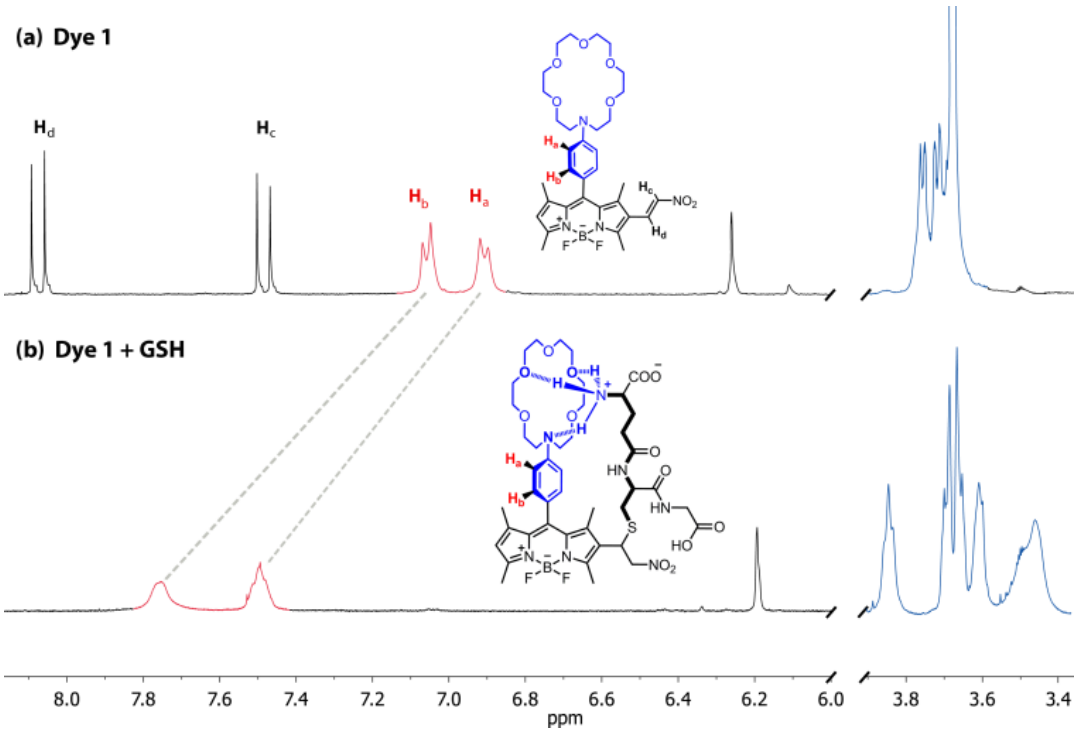

Figure 57. Partial ^{1}H-NMR (in CD_3OD, 298 K) spectra depicting the changes on GSH conjugate addition to the **(Dye 1)**: The adduct was isolated by preparative HPLC following a room temperature reaction of the probe and GSH in aqueous acetonitrile. *Trans*-coupled protons disappear in the product, and the azacrown peaks show a more spread out cluster of peaks, suggesting an emergence of non-covalent, non-symmetric interaction. Copyright © 2014, American Chemical Society. Reprinted with permission from ref (185).

It is also evident that, if there is any difference between the biological thiols in terms of the intensity of the emission signal, it should be most likely due to the relative rate of the reactions, perhaps in competition with any side reactions. Thus, unless there are other built-in structural selection criteria, cysteine and homocysteine should react faster than the larger/bulkier nucleophile GSH, and for shorter reaction (incubation) periods, they should generate larger emission responses.

Next, we tested the response of the probe to three biological thiols in aqueous solutions. We carried out the first set of experiments in pH 7.4 buffered aqueous solutions. When the reactions are complete, we observed a turn on of fluorescence emission (figure 58, right), together with a blue shift, just as it was in the case of simpler thiol, mercaptoethanol. However, when the reactions were repeated in slightly acidic solutions mimicking the typical pH values for tumor tissues (pH 6.0),

in accordance with our design, the results showed a very clear-cut preference for GSH for the strongest emission signal (figure 58, left).

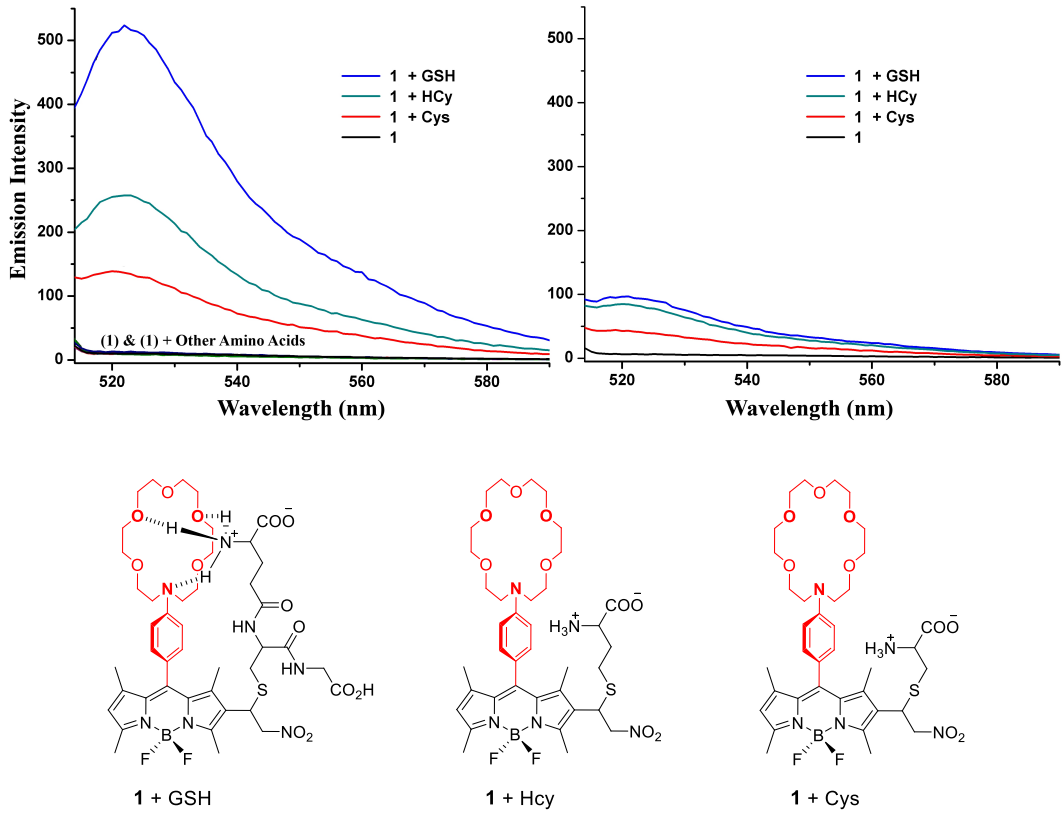

Figure 58. Emission response to biological thiols at two different pH values, 7.4 (left, 60:40, 30 mM MES buffer/acetonitrile) and 6.0 (right, 60:40, 30 mM MOPS buffer/acetonitrile). Small change in pH causes more than 5-fold increases in emission intensity for the GSH – **(Dye 1)** adduct. For Cys and Hcy, the change is approximately 2.5 fold. The concentrations of the thiols and other amino acids (Gly, His, Ile, Leu, Met, Phe, Pro, Ser, Thr, Tyr, Val) were 1.6 mM and the **(Dye 1)** concentration was 8.0 μM. Excitation was at 500 nm, with 5 nm slit-widths. Copyright © 2014, American Chemical Society. Reprinted with permission from ref (185).

Selectivity at pH 6.0 was further established in a series of measurements including number of amino acids and the three biological thiols (figure 59). Non-thiol amino acids showed no response, and selectivity at actual intracellular concentrations of three biological thiols was spectacular. Two conclusions can be drawn from these results, the steric fit of the protonated ammonium group at the N-terminal is optimal in GSH, and since the other two thiols, Cys and Hcy, are shorter and they cannot provide an ammonium group reaching the N-phenylazacrown receptor as the second recognition site (figure 54), once the thiol adduct is formed. The second more

important result is the PeT modulation: the *N*-phenylazacrown is a strong PeT donor. Its protonation would stop or slow down PeT leading to strong enhancement of the emission (off-on type). However, our expectation based on the pK_a data of the aromatic amines, was such that the aromatic amine moiety should not be protonated to a significant extent at even pH 6.0, so no clear enhancement should be seen in the case of Cys or Hcy. We also performed titration experiments with increasing GSH concentration. As expected blue shift in absorption and turn-on response in fluorescence were observed (figure 60).

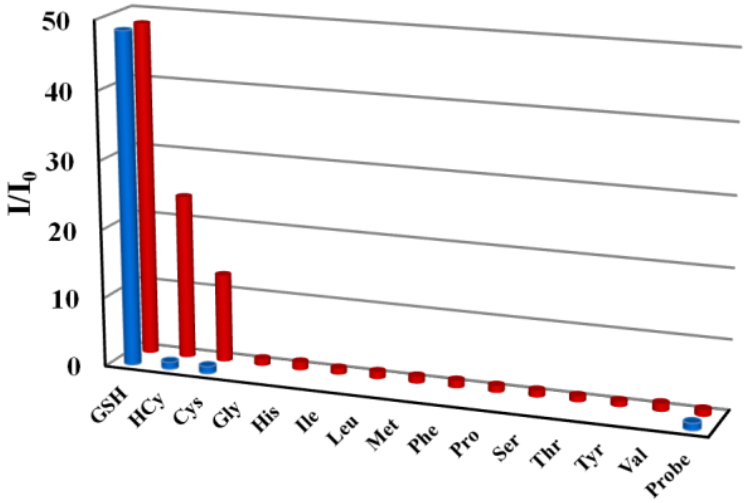

Figure 59. Selective emission response of the **(Dye 1)**. Blue bars correspond to the emission enhancement ratios (Io being the emission intensity of the probe) when biological thiols are introduced at their respective intracellular concentrations[79,196,197] in aqueous medium (60:40, pH 6.0, 30 mM MOPS buffer/acetonitrile) with 8.0 μM **(Dye 1)** concentration. Red bars show the emission enhancement when all analytes are introduced at 1.6 mM, in the same solvent system and probe concentration. Excitation was at 500 nm, emission data at 522 nm (I and I_0) were used in calculations. Copyright © 2014, American Chemical Society. Reprinted with permission from ref (185).

In addition, the protonation state would not be in any way linked to the thiol reaction. In GSH however, N-terminal ammonium is in the right place for an effective ion-dipole and H-bonding interactions, which would change in the pKa of the azacrown amine, and thus it will be protonated to larger extent at pH 6.0. We did not want to leave this issue as simple conjecture, and synthesized two control compounds to check this experimentally. **(Dye 2)** is a simple phenylazacrown substituted BODIPY

and **(Dye 3)** has nitroethenyl Michael acceptor and an amine function (figure 61). These two compounds are to serve as negative controls of our design.

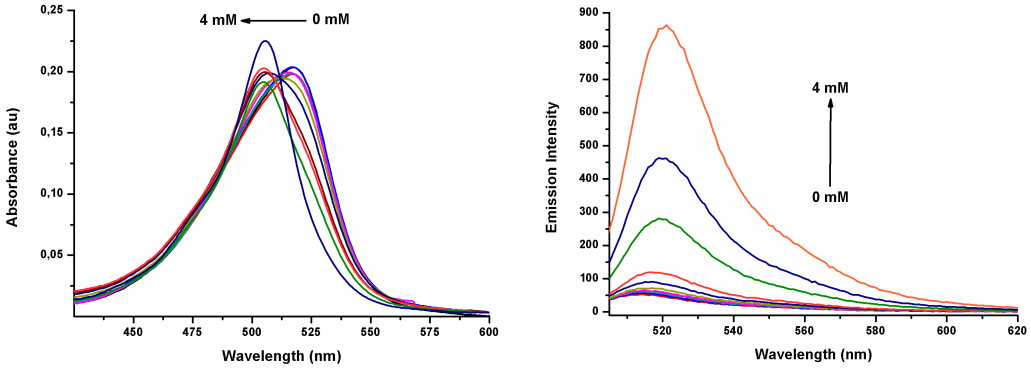

Figure 60. Electronic absorption and emission spectra of **(Dye 1)** (8.0 μM) in 30 mM MES:CH_3CN (60:40, v/v, pH=6.0, 25 °C) in increasing GSH concentrations (0 to 500 eq.). Excitation wavelength is 500 nm. Copyright © 2014, American Chemical Society. Reprinted with permission from ref (185).

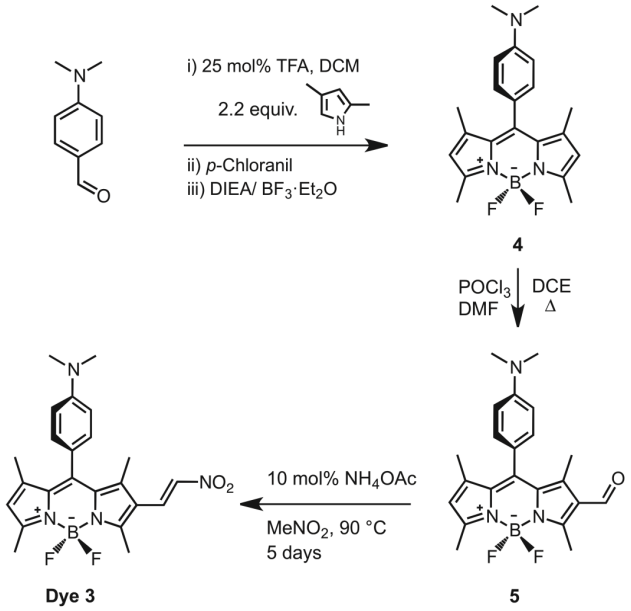

Figure 61. Following synthetic route was pursued to get **(Dye 3)**. Copyright © 2014, American Chemical Society. Reprinted with permission from ref (185).

To our delight, control **(Dye 2)** showed essentially no response to either moderate change in pH (7.4 to 6.0) or to the thiols (figure 62, left). Control **(Dye 3)** also as expected, showed only a small enhancement in emission on reaction with thiols, with small discrimination in terms of signal intensity, but PeT from the

dimethylaminophenyl substitituent showed no signs of change within the pH range mentioned (figure 62, right).

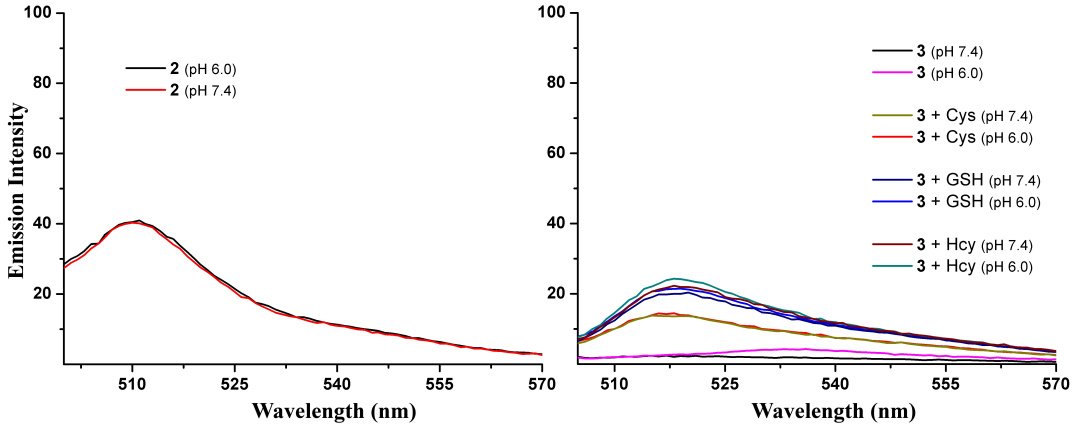

Figure 62. The structures of control BODIPY (**Dye 2)** and **(Dye 3)**. **(Dye 2)** has a binding site for ammonium moiety, but no reactive group for thiols. (left) **(Dye 3)** is thiol reactive, but it does not have a site for ammonium recognition. (right) Dye concentrations were 8.0 μM, and the biological thiols were introduced at 1.6 mM. Aqueous buffer solutions were used as solvents, for pH 7.4 (60:40, 30 mM MES buffer/acetonitrile) and for pH 6.0 (60:40, 30 mM MOPS buffer/acetonitrile). Excitation was at 500 nm, with 5 nm slit-widths.

The control experiments prove that the designed **(Dye 1)**, has a strong steric differentiation between the GSH and the other two biologically relevant thiols, more so at pH 6.0. pH 6.0 versus pH 7.4 responses are important as pH difference in this range is one of the characteristics separating tumors from healthy tissues. GSH is known to be present at highly elevated concentrations in tumor cells compared to healthy tissues.[79]

Finally, we wanted to demonstrate the feasibility of the designed probe for GSH imaging in intracellular medium using cell cultures. Figure 63 shows time-lapse images of **(Dye 1)** incubated cells. Within 2 hours, strong green emission of the GSH adduct is clearly visible in the cytosol of the cells. Considering intracellular concentrations of all biological thiols, the green emission is clearly resulting from the reaction with intracellular GSH. As a control to eliminate the possibility of the contribution of non-specific reactions (with other biological thiols, including proteins) to the generated emission signal, we performed an inhibition experiment (Figure 63). Buthionine sulphoximine (BSO) is a known selective inhibitor[198] of γ-

glutamylcysteine synthetase (γ-GCS). HUVEC cells pre-treated with the inhibitor showed very low residual emission compared to untreated cells on staining with **(Dye 1)**.

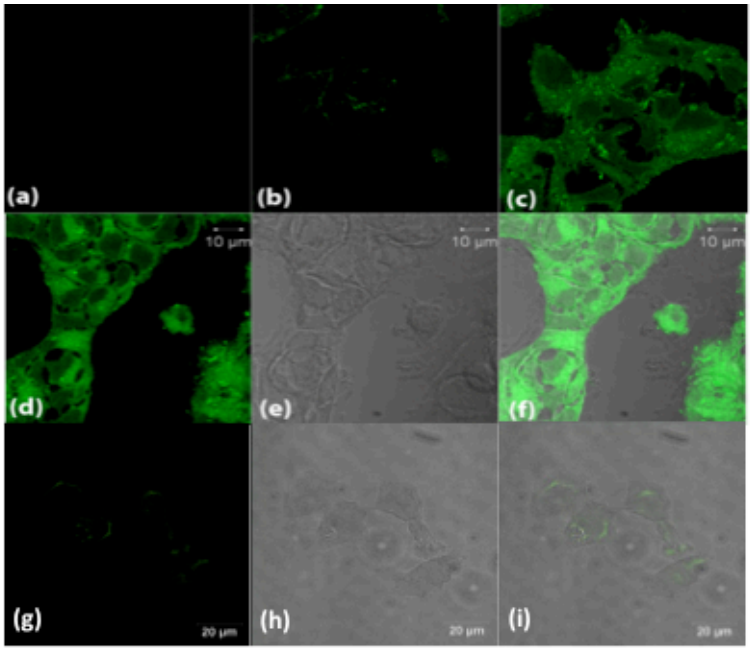

Figure 63. Time-lapse confocal microscopy pictures of Human breast adenocarcinoma cells (MCF-7) cells incubated with **(Dye 1)** at 0.5 μM (a: 0 min, b: 1 min, c: 120 min). d, e, 120 min, fluorescence, optical images and f: merged image. Human umbilical vein endothelial cells (HUVEC) cells pre-treated with 5 mM BSO (g), DIC image (h), merge (i). The selective inhibition of GSH synthesis reduces fluorescence emission from the cells to a very low level, attesting the selectivity of the designed probe. Copyright © 2014, American Chemical Society. Reprinted with permission from ref (185).

3.4. Experimental Details

General: ^{1}H NMR and ^{13}C NMR spectra were recorded on Bruker DPX 400 spectrometer using $CDCl_3$ as the solvent. Chemical shifts values are reported in ppm from tetramethylsilane as internal standard. Spin multiplicities are reported as the following: s (singlet), d (doublet), m (multiplet). HRMS data were acquired on an Agilent Technologies 6530 Accurate-Mass Q-TOF LC/MS. UV-Vis Absorption spectra were taken on a Varian Cary-100 spectrophotometer. Fluorescence measurements were conducted on a Varian Eclipse spectrofluorometer. Flash column chromatography (FCC) was performed by using glass columns with a flash grade silica gel (Merck Silica Gel 60 (40–63 μm)). Reactions were monitored by thin layer

chromatography (TLC) using pre-coated silica gel plates (Merck Silica Gel PF-254), visualized by UV-Vis light and DNP stains as appropriate. All organic extracts were dehydrated over anhydrous Na_2SO_4 and concentrated by using rotary evaporator before being subjected to FCC. N-(4-Formylphenyl)-aza-18-crown-6[190] and compound (**4**)[199] were synthesized following reported literature procedures. All other chemicals and solvents were supplied from commercial sources and used as received.

HPLC Separation of Dye 1-GSH adduct: Analytical and preparative HPLC separations of **(Dye 1)** + GSH adduct were performed on Agilent Technologies HPLC-1200 Series with multi-wavelength detector (MWD) and Agilent Technologies Preparative HPLC-1200 Series with diode array detector (DAD). In the case of analytical separation Agilent Technologies Zorbax Eclipse XDB-C18 analytical 4.6 x 150 mm 5-micron column was employed and for preparative separation Agilent Technologies PrepHT XDB-C18 preparative Cartridge 21.2 x 150 mm 5 micron column was used. For analytical resolution, adduct was dissolved in distilled water (%0.1 TFA), filtered and injected to the column. The flow rate was 1 mL/min and UV detection wavelengths were 250, 370 and 520 nm. This separation was performed on a 4.6 x 150 mm column. Only one injection was done (10μL). In the case of preparative resolution of adduct, again it was dissolved in distilled water (%0.1 TFA), filtered and injected to the column. The flow rate was adjusted as 20 mL/min and UV detection wavelength was 505 nm. This separation was performed on a 21.2 x 150 mm column. In preparative separation 5 injections were done (5 mg/injections, 2000μL/injections), in order to get reasonable amount of the pure adduct.

Electronic absorption and fluorescence spectroscopy experiments: Unless otherwise noted, all absorption and fluorescence spectra were recorded upon the addition of 200 equivalents (1.6 mM) of analytes on to 8 mM of the probe **(1)** or dyes **(2)**, and **(3)**. Each mixture (dyes + analytes) were incubated at room temperature for 15 hours prior to spectrophotometric measurements. All data were collected in aqueous solutions (buffer-acetonitrile, 60:40). The pH was adjusted to 7.4 and 6.0, using 30 mM of MES and MOPS buffers, respectively and then diluted with

acetonitrile as the co-solvent.

Detection Limit Calculation: Fluorescence titration experiments were conducted with increasing GSH concentrations. Slope of the emission intensity versus GSH concentration graph were calculated. In addition to that emission spectrum of **(Dye 1)** without GSH was taken seven times and the standard deviation of the emission intensity was detected. Finally detection limit was calculated according to given formula below; where *s* is the standard deviation of 7 blank measurements and *m* is the slope of the emission intensity versus GSH concentration graph.

$$\text{Detection limit} = 3s/m$$

According to formula, detection limit was found to be 3.58 μM.

Cell Culture Studies: Human breast adenocarcinoma cells (MCF-7) were grown to confluence at 37 ^{o}C under 5% CO_2 in Dulbecco's Modified Eagle Serum (DMEM) containing 1% penicillin/streptomycin, 10% fetal bovine serum (FBS) and 2 mM L-glutamine. The cells were seeded in 24-well plates at $5x10^3$ cells/well. After a 24 h incubation period, the cells were treated with 0.5 μM of **(Dye 1)** at 37 ^{o}C for 2h in a humidified incubator. Cells were washed three times with phosphate-buffered saline (PBS), fixed with 4% paraformaldehyde in PBS, covered with mounting medium and stored at -20 ^{o}C. In order to show that the probe specifically interacts with GSH, The cells (HUVEC) were we treated with buthionine sulphoximine (BSO), an inhibitor of GSH biosynthesis. After 24 h of treatment with 5 mM BSO, cells were stained with 0.5 μM of dye. The samples were analyzed with Zeiss LSM-510 confocal microscope with an oil-immersion 63x objective lens. An argon laser of 488 nm wavelength was used with NFT 515 filter. **Cell culture studies were done in Dr. Turgay Tekinay group at Bilkent University, UNAM, Ankara, Turkey.**

Synthetic Details:

Synthesis of (Dye 2):

Trifluoroacetic acid (TFA; 57μL, 0.75 mmol) was added dropwise to a vigorously

stirring solution of N-(4-Formylphenyl)-aza-18-crown-6[1,2] (1102 mg, 3.0 mmol) and 2,4-dimethylpyrrole (627 mg, 6.6 mmol) in 350 mL Ar-deaerrated dichloromethane (DCM). The resulting red solution was stirred at room temperature in the dark for 1 day. *p*-Chloranil (738 mg, 3.0 mmol) was then added in one portion and reaction was stirred for an additional hour. Diisopropylethyl amine (DIEA) (9.0 mL) was then added dropwise to this mixture over a period of 15 min, and the resulting dark brown solution was allowed to stir for an additional 15 min. BF_3•OEt_2 (9.0 mL) was then added dropwise over a period of 15 min., and the resulting dark red solution was allowed to stir further for 2h at rt. The slurry reaction mixture was washed with water (3 × 300 mL) and dried over anhydrous Na_2SO_4. The solvent was evaporated and the residue was purified by silica gel flash column chromatography (FCC) using $CHCl_3$:MeOH (95:5) as the eluant. Compound **(2)** was solidified as a dark orange solid (790 mg, 45% yield).^{1}H NMR (400 MHz, $CDCl_3$) δ 7.01 (d, J = 8.4 Hz, 2H), 6.75 (d, J = 8.4 Hz, 2H), 5.96 (s, 2H), 3.81 – 3.51 (m, 24H), 2.54 (s, 6H), 1.49 (s, 6H). ^{13}C NMR (100 MHz, $CDCl_3$) δ 154.6, 148.4, 143.2, 132.2, 128.9, 121.8, 120.8, 111.9, 70.9, 70.8, 70.7, 68.6, 51.3, 43.5, 14.7, 14.5.MS (TOF-ESI): m/z: Calcd: 585.3191 $[M-H]^+$, Found: 585.3365 $[M-H]^+$, Δ=29.72 ppm.

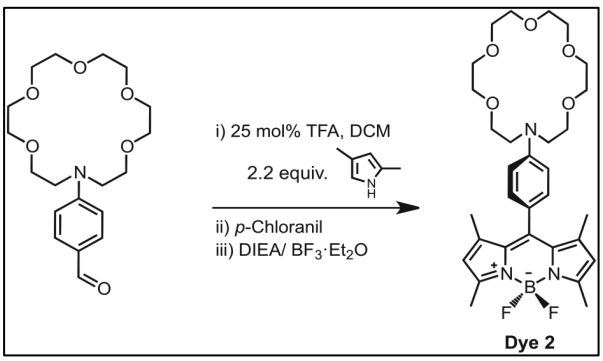

Synthesis of (3):

$POCl_3$ (1 mL) was added dropwise to a vigorously stirring anhydrous DMF (1 mL), which was kept in ice bath under N_2. Resulting pale yellow viscous liquid was allowed to stir at room temperature for additional 30 min. To this, 1,2-dichloroethane (DCE) (50 mL) solution of **(Dye 2)** (585 mg, 1.0 mmol) was then slowly introduced and the resultant brown solution was heated at 60 °C for 3 h. (Attention: 60 °C is

critical to get mono-formylated product **(3)** as the major, side product (di-formylated BODIPY) formation was observed otherwise at higher temperatures.) Reaction was cooled to room temperature, and poured into ice-cold sat'd $NaHCO_3$ solution. This mixture was extracted with DCM (100 mL portions) and dried over anhydrous Na_2SO_4. Solvent was evaporated in vacuo and compound was purified by silica gel FCC using DCM:MeOH (98:2) as the eluent. Product **3** was obtained as dark brown waxy solid with a green luster (521 mg, 85% yield). ^{1}H NMR (400 MHz, $CDCl_3$) δ 9.98 (s, 1H), 6.97 (d, J = 8.8 Hz, 2H), 6.76 (d, J = 8.8 Hz, 2H), 6.11 (s, 1H), 3.71 – 3.63 (m, 24H), 2.78 (s, 3H), 2.56 (s, 3H), 1.75 (s, 3H), 1.53 (s, 3H). ^{13}C NMR (100 MHz, $CDCl_3$) δ 185.9, 160.6, 155.8, 148.9, 147.4, 145.2, 142.8, 134.7, 130.6, 128.8, 126.1, 123.6, 120.6, 112.0, 70.84, 70.77, 70.66, 68.4, 51.2, 25.6, 15.3, 15.0, 12.9, 12.0. MS (TOF-ESI): m/z: Calcd: 613.3135 $[M-H]^+$, Found: 613.3324 $[M-H]^+$, Δ= 30.81 ppm.

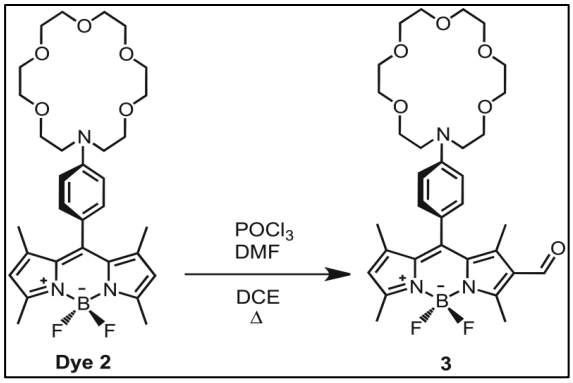

Synthesis of(Dye 1):

NH_4OAc (3.8 mg, 0.049 mmol) was added to a nitromethane (5 mL) solution of compound **(3)** (300 mg, 0.49 mmol) and the solution was left to stir at 90 ºC for 5 days. Product formation was monitored with TLC using DCM:MeOH (99:1) as the eluant. At the end of reaction, nitromethane was removed in vacuo and obtained crude mixture was subjected to silica gel FCC using DCM:MeOH (99:1) as the eluent. Product **(1)** was obtained as a wine-red waxy solid (288 mg, 89% yield). ^{1}H NMR (400 MHz, $CDCl_3$) δ 8.07 (d, J = 13.7 Hz, 1H), 7.37 (d, J = 13.7 Hz, 1H), 7.03 (d, J = 8.6 Hz, 2H), 6.81 (d, J = 8.6 Hz, 2H), 6.15 (s, 1H), 3.82 – 3.64 (m, 24H), 2.71 (s, 3H), 2.62 (s, 3H), 1.62 (s, 3H), 1.57 (s, 3H). ^{13}C NMR (100 MHz, $CDCl_3$) δ

213.7, 160.6, 153.8, 148.9, 147.4, 145.3, 144.3, 140.3, 134.3, 131.6, 131.2, 129.0, 123.6, 120.6, 112.0, 70.91, 70.84 , 70.71 , 68.5, 51.2, 15.4, 15.0, 13.8, 13.3, 1.0. MS (TOF-ESI): m/z: Calcd: 656.3193 $[M-H]^+$, Found: 656.3240 $[M-H]^+$, Δ= 7.16 ppm.

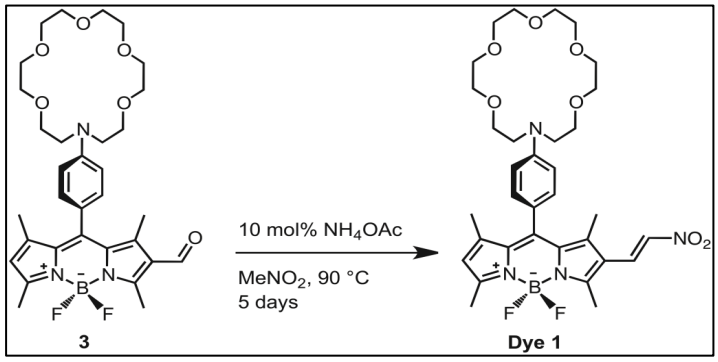

Synthesis of (5):

$POCl_3$ (1 mL) was added dropwise to a vigorously stirring anhydrous DMF (1 mL), which was kept in ice bath under N_2. Resulting pale yellow viscous liquid was allowed to stir at room temperature for additional 30 min. To this, 1,2-dichloroethane (DCE) (50 mL) solution of compound **(4)** (367 mg, 1.0 mmol) was then slowly introduced and the resultant brown solution was heated at 60 °C for 3 h. (Attention!: 60 °C is critical to get mono-formylated product **(5)** as the major, side product formation was observed otherwise at higher temperatures.) Reaction was cooled to room temperature, and poured into ice-cold sat'd $NaHCO_3$ solution. This mixture was extracted thrice with DCM (100 mL portions) and dried over anhydrous Na_2SO_4. Solvent was evaporated in vacuo and compound was purified by silica gel FCC using DCM:MeOH (98:2) as the eluent. Product **(5)** was obtained as dark brown waxy solid with a green luster (335 mg, 85% yield). ^{1}H NMR (400 MHz, $CDCl_3$) δ 10.04 (s, 1H), 7.07 (d, J = 8.7 Hz, 2H), 6.82 (d, J = 8.7 Hz, 2H), 6.15 (s, 1H), 3.06 (s, 6H), 2.84 (s, 3H), 2.62 (s, 3H), 1.79 (s, 3H), 1.56 (s, 3H). ^{13}C NMR (100 MHz, $CDCl_3$) δ 185.99, 160.68, 156.01, 150.97, 147.39, 145.20, 128.66, 123.56, 112.45, 77.32, 77.00, 76.69, 40.27, 15.22, 15.00, 12.97, 11.92. MS (TOF-ESI): m/z: Calcd: 394.1980$[M-H]^+$, Found: 394.1917 $[M-H]^+$, Δ= 15.98 ppm.

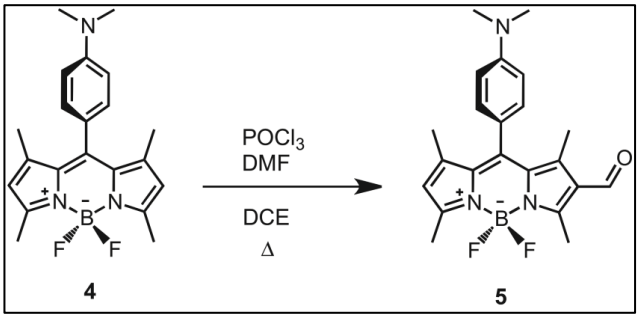

Synthesis of (Dye 3):

NH_4OAc (3.8 mg, 0.049 mmol) was added to a nitromethane (5 mL) solution of compound **(5)** (193 mg, 0.49 mmol) and the solution was left to stir at 90 ºC for 5 days. Product formation was monitored with TLC using DCM:MeOH (99:1) as the eluant. At the end of reaction, nitromethane was removed in vacuo and obtained crude mixture was subjected to silica gel FCC using DCM:MeOH (99:1) as the eluent. Product **(Dye 3)** was obtained as a wine-red solid (194 mg, 90% yield). ^{1}H NMR (400 MHz, $CDCl_3$) δ 8.07 (d, J = 13.7 Hz, 1H), 7.37 (d, J = 13.7 Hz, 1H), 7.11 – 7.01 (m, 2H), 6.82 (d, J = 8.8 Hz, 2H), 6.16 (s, 1H), 3.07 (s, 6H), 2.72 (s, 3H), 2.62 (s, 3H), 1.61 (s, 3H), 1.57 (s, 3H). ^{13}C NMR (100 MHz, $CDCl_3$) δ 160.63, 153.69, 151.05, 147.48, 144.37, 140.36, 134.27, 131.15, 128.79, 123.62, 120.91, 112.36, 77.34, 77.02, 76.71, 40.22, 15.29, 15.00, 13.78, 13.21. MS (TOF-ESI): m/z: Calcd: 437.2039 $[M-H]^+$, Found: 437.1973 $[M-H]^+$, Δ= 15.09 ppm.

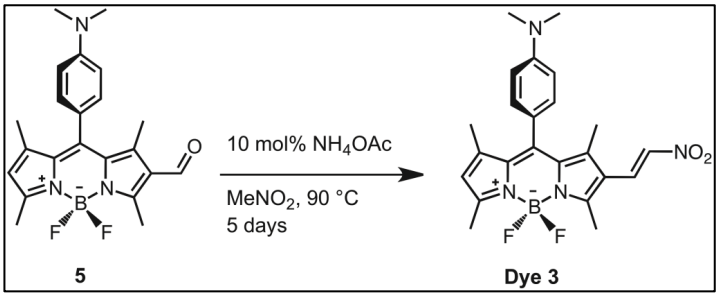

3.5. Conclusion

In conclusion, we have shown that selectivity for reaction-based probes can be improved by applying additional photophysical constraints. In this work, this was made possible by the simultaneous modulation at two different sites, as the adduct

was generated. While the probe discussed here required a co-solvent (acetonitrile) for better solubility, the idea described in this work is perfectly transferable to other fluorophores and even to other reactions to be used in sensory systems.

CHAPTER 4

Activatable Heavy Atom Free Sensitizers for Photodynamic Therapy Application

The discussions on this chapter are partially based on the following publications:

Cakmak, Y.; **Kolemen, S.**; Duman, S.; Dede, Y.; Dolen, Y.; Kilic, B.; Kostereli, Z.; Yildirim, L. T.; Dogan, L.; Guc, D.; Akkaya, E. U. *Angew. Chem. Int. Ed.*, **2011**, 50, 11937.

Duman, S.; Cakmak, Y.; **Kolemen, S.**; Akkaya, E. U.; Dede, Y. *J. Org. Chem.*, **2012**, 77, 4516.

Kolemen, S.; Işık, M.; Kim, K. M.; Kim, D.; Geng, H.; Buyuktemiz, M.; Zhang, X.; Dede, Y.; Yoon, J.; Akkaya, E. U

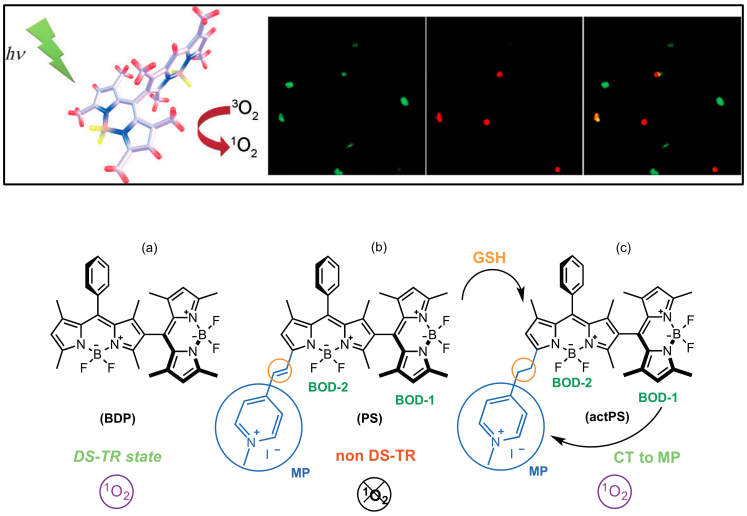

4.1. Singlet Oxygen Generation by Using Heavy Atom Free Orthogonal BODIPY Derivatives

4.1.1. Objective

S_0, S_1, and T_1 states of various orthogonal 8,8' and 8,2' bis-BODIPYs were utilized as heavy atom free photosensitizers for O_2 ($^1\Delta_g$) generation, and studied by multi-reference quantum chemical approaches. $S_0 \rightarrow S_1$ excitation characteristics of certain bis-BODIPYs are shown to be radically different than the parent BODIPY chromophore. Whereas a simple HOMO→LUMO type single substitution perfectly accounts for the BODIPY core S_1 state of certain orthogonal bis-BODIPYs are described as a linear combination of doubly substituted (DS) configurations that yield four electrons in four singly occupied orbitals (tetra-radical, TR). DS-TR character of S_1 was shown to have a strong correlation with $S_1 \rightarrow T_1$ ISC yielding $^1O_2$ and this was also proved experimentally through synthesis followed by characterization including phosphorescence measurements, use of trap molecules and cell culture studies; leading to a series of orthogonal dimers of BODIPY chromophore with remarkable singlet oxygen efficiencies without incorporation of heavy atoms. A new path for rational development of efficient photosensitizers is revealed.

Near-IR absorption, desired for photosensitizers, did not look viable for bis-chromophores by the standard strategy of π-augmentation, as DS-TR singlet states are destabilized presumably via decreased exchange coupling in π-extended cases. Although red-shifting the absorption wavelength to enter the therapeutic window does not seem attainable for orthogonal bis-BODIPYs, modifications in the chromophore cores are promising in fine-tuning the excitation characteristics and suggested as future synthetic directions.

4.1.2. Introduction

Broader acceptance of PDT by the medical community and applicability is hampered by the restricted photophysical characteristics of the porphyrin derivatives. This

situation sparked a worldwide search for novel sensitizers leading to new compounds, some holding more promise than others.[112,200] The primary cytotoxic agent involved in the photodynamic action is singlet oxygen, the efficient generation of which is linked invariably to the intersystem crossing (ISC) efficiency of the excited sensitizer. Most organic dyes have low triplet quantum yields, and in many recent candidates for photodynamic sensitizers, heavy atoms are incorporated into the structure as a strategy to improve spin–orbit coupling leading to facilitated intersystem crossing.[201] While this approach seems fail-safe, incorporation of heavy atoms such as bromine, iodine, selenium, and certain lanthanides very often leads to increased "dark toxicity".[202] We have been interested in trying to find alternative ways of achieving increased intersystem crossing without the use of heavy atoms to minimize dark toxicity, turning our attention to the excited state properties of the sensitizers.

Designing efficient photoinduced $^1O_2$ generators requires that any existing operative fluorescence cycle of the fluorophore, which is through the $S_0 \rightarrow S_1 \rightarrow S_0$ states, has to be perturbed so as to minimize or shutdown the $S_1 \rightarrow S_0$ deactivation, and switch to the triplet surface once S_1 is accessed. A general design principle for a favourable $S_1 \rightarrow T_1$ hop from an electronic structure viewpoint would in principle, require the structural and electronic compatibility of S_1 and T_1 states to surpass that of S_1 - S_0 pair. Once multiple electronic states come into play, quantum mechanical calculations providing a detailed understanding of the electronic structure are extremely helpful. Multi-configurational self-consistent field (MCSCF) techniques are the state of the art computational chemistry tools when near degeneracies and excited states are considered. These methods may not reach chemical accuracy (±2-3 kcal/mol) for computing total energies, but are crucial for a qualitatively correct description of the excited states and are capable of providing conceptually complete picture of the photophysics taking place. Therefore, we mainly employed a popular variant of MCSCF techniques; the complete active space SCF (CASSCF) method in combination with relatively large basis sets and different active spaces.

4.1.3. Results and Discussion

Our calculations on the parent BODIPY core showed that natural orbital occupancies of S_1 state do describe an open-shell singlet with essentially double (>1.9) or zero (<0.1) electrons for all orbitals except HOMO and LUMO that are singly occupied (figure 64).

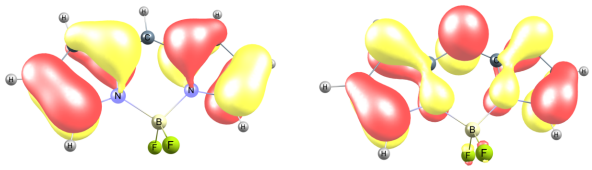

Figure 64. Frontier molecular orbitals. HOMO (left) LUMO (right), of the parent BODIPY core at B3LYP/6-31G(d,p) level of theory. Surfaces are plotted at 0.2 a.u. Copyright © 2011, John Wiley and Sons. Reprinted with permission from ref (121).

It is no surprise to observe a fluorophore with low triplet quantum yield to have an excited state possessing only two orbitals with single occupancy, hence to achieve our goal of efficient switching to the triplet manifold, we have to access to excited states different from the ones built by simple HOMO → LUMO transitions. Among multiply excited configurations, doubly substituted ones are particularly important in enhancing S_1 - T_1 coupling as shown by the seminal work of Salem and Rowland[203] and the following work by Michl.[204] Thus, the substitutions should invoke simultaneous two electrons excitation from the ground state, guiding us to search for molecules with a pair of degenerate or near-degenerate occupied frontier orbitals correlating with a similar virtual (unoccupied) pair and pointing out a design principle of orthogonal dimeric chromophores. This foundation has two important features: (i) orthogonal placement prevents mixing of the π-systems of the two subunits leaving us with two essentially undisturbed chromophore cores. (ii) Upon irradiation, both cores are almost equally likely to undergo a HOMO → LUMO electron transfer (referring to the original monomer MOs) yielding an excited state mainly comprised of double substitutions.

Our previous involvement with BODIPY dyes led us to seek ways to implement these design considerations using these dyes. BODIPY dyes are exceptional fluorophores with amazing versatility[29] and rich chemistry.[24] Heavy atom

functionalized BODIPY dyes showed some promise as potential sensitizers for photodynamic activity.[123] It is also interesting to note that a few years ago, dimeric (albeit non-orthogonal) BODIPY derivatives were reported[126] with peculiar properties linked to exciton coupling between the chromophores. We believe orthogonality to be an important distinction in our design (figure 65).

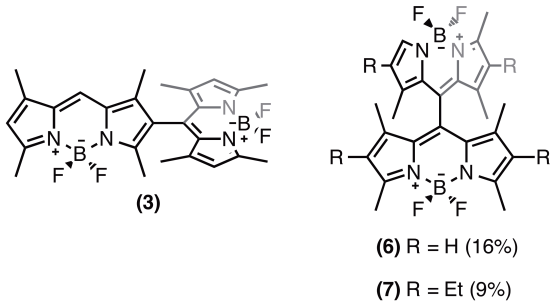

Figure 65. Orthogonal BODIPY designs. Copyright © 2011, John Wiley and Sons. Reprinted with permission from ref (121).

Orthogonality is secured by the strategic placement of the methyl substituents, resulting in a dihedral angle very close to 90° for the two BODIPY cores. Orthogonal arrangement of the BODIPY units was also experimentally verified by the X-ray diffraction structure (figure 66) of the compound **(3)**. The calculated energy differences (2.96, 2.97 eV) remaining very close to HOMO – LUMO gap of Bodipy core (3.10 eV) further support our claim of Bodipy cores remaining essentially unperturbed in the dimeric form. Thus the orthogonal dimer should possess the desired features sought in the excitation process.

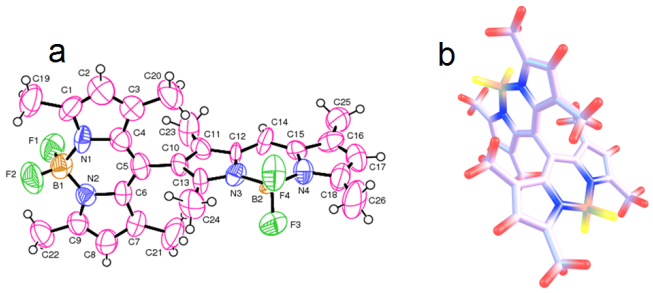

Figure 66. Structures of the dimeric Bodipys. a) X-ray diffraction structure of the orthogonal 8,2' dimer **(3)**. b) Optimized geometry of orthogonal 8,8' dimer **(6)** at CAS(6e in 6o)/cc-pVDZ level. Dihedral angle between the two Bodipy units is very close (± 0.5°) to 90° in both dimers. Copyright © 2011, John Wiley and Sons. Reprinted with permission from ref (121).

Spatial orthogonality is decisive on the excitation properties of **(3)**, **(6)** and **(7)** as it prevents the π -mixing among cores and maintains two essentially undisturbed chromophores almost retaining their monomeric orbital energies and electron density distributions. With the survival of BODIPY core levels in the dimer, its $S_0 \rightarrow S_1$ excitation should then be composed of the inherent HOMO→LUMO transitions of both monomers. Realization of this feature allows us to envisage the $S_0 \rightarrow S_1$ excitation to mainly include double substitutions from the reference wave function as depicted in figure 67 via construction of a conceptually useful valence bond (VB) wave function for S_1.

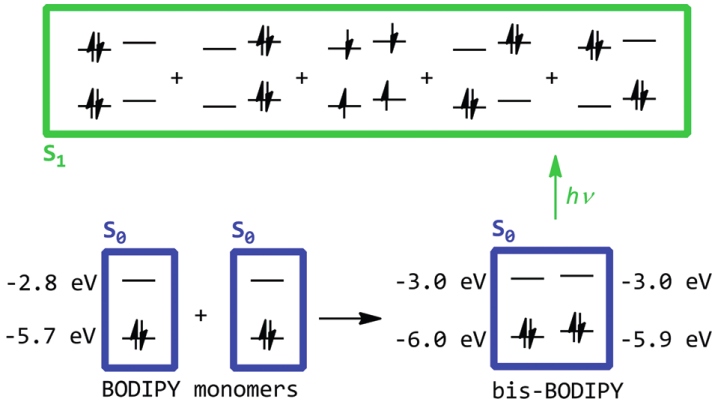

Figure 67. Building up bis-BODIPY S_1 wave function. MO energies are for the 8,8′ dimer **(6)**. In the S_1 state, only the leading configurations are shown, and minus signs to restrain antisymmetry are intentionally excluded for clarity. Copyright © 2012, American Chemical Society. Reprinted with permission from ref (227).

The general view demonstrated in Figure 67 is verified by the computed excited-state MO plots and NOONs as well as the details of the multi-configurational expansion given in Figure 68. The effect of constructing the S_1 wave function from essentially unperturbed monomeric states is clearly visible on NOONs since the sum over all five configurations in Figure 67 for S_1 (after normalization in the basis of the five configurations) yields a single electron in each of the four MOs, provided that the five configurations are essentially equally weighted. Four electrons in four molecular orbitals in an overall singlet coupled fashion, as confirmed by the NOONs of the CASSCF wave functions, is the basis for the TR designation. Moreover, distributions of the SOMOs for S_1 are found to be linear combinations of the HOMO and LUMO

of isolated BODIPY cores, a feature predicted to be an outcome of spatial orthogonality of monomers.

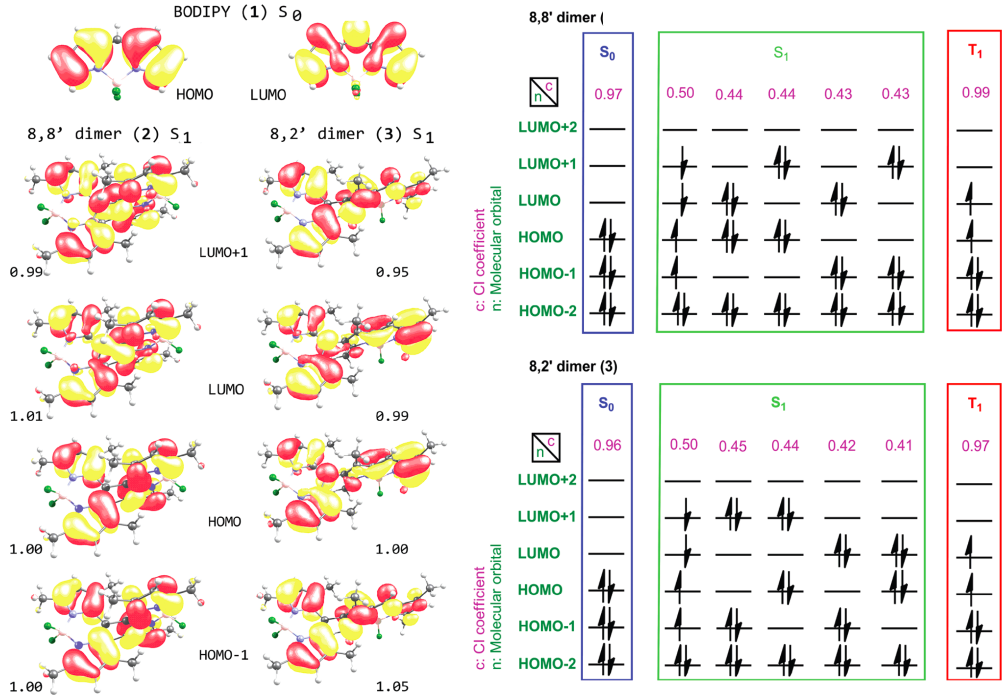

Figure 68. Left: (Top) BODIPY HOMO and LUMO. (Bottom) Frontier orbitals and natural orbital occupation numbers of S_1 states of dimers **(3)** and **(6)**. Right: Leading configurations of S_0, S_1, and T_1 CASSCF wave functions for **(3)** and **(6)**. Copyright © 2012, American Chemical Society. Reprinted with permission from ref (227).

The DS-TR natures of **(3)** and **(6)** are repeatedly observed at CASSCF levels employing varying numbers of active electrons and orbitals and with different basis sets, suggesting DS-TR to emerge as a qualitative and simple descriptor for S_1 states of the dimers. Facile $^1O_2$ production by **(3)** and **(6)** despite the absence of high nuclear charge atoms suggest that ISC is invoked via a specific electronic structure pattern as the general view of $^1O_2$ generation includes an effective hop of the photosensitizer to the triplet surface. We attribute ISC-promoted $^1O_2$ production by **(3)** and **(6)** to the DS-TR nature of S_1 states, as doubly substituted singlets are reported to better couple with triplets.[203,204] Similarly, charge separation, yielding facile access of excited dyads to the triplet manifold, implies the significance of zwitterionic (charge separated) excited states in ISC dynamics.

As a result, functionalization of the BODIPY core orthogonally, by a second

BODIPY is the key to switching to the triplet manifold. Based on these clearly encouraging computational results, we were highly motivated towards the synthesis of a series of orthogonally linked dimeric BODIPYs. The synthesis procedure for compound **(3)** is quite straightforward, especially in view of recent contribution to BODIPY chemistry by Jiao and co-workers.[35] The parent compound **(1)** was formylated through Vilsmeier reaction (figure 69). The BODIPY framework was then constructed around the formyl carbon using standard BODIPY chemistry. The absorption spectrum of the product showed a single band centered around 506 nm, not much different than the parent compound. Organic solutions of the orange colored compound were noticeably lacking detectable fluorescence emission under ambient or hand-held UV lamp irradiation, an indication of competing excited state process(es) in action. Recent progress in the derivatization of BODIPY dyes also allowed us to synthesize two different and more symmetrical, 8,8' orthogonal dimers as well. Thus, recently reported[205] 8-formyl-BODIPY derivative was transformed into orthogonal dimers **(6)** and **(7)**, using standard protocols (figure 69). A list of relevant photophysical parameters for the sensitizers is placed in table 3. It is interesting to note that for the dimers **(6)** and **(7)**, significant fluorescence emission quantum yield is preserved, opening the possibility for a dual use as therapeutic and imaging agents.

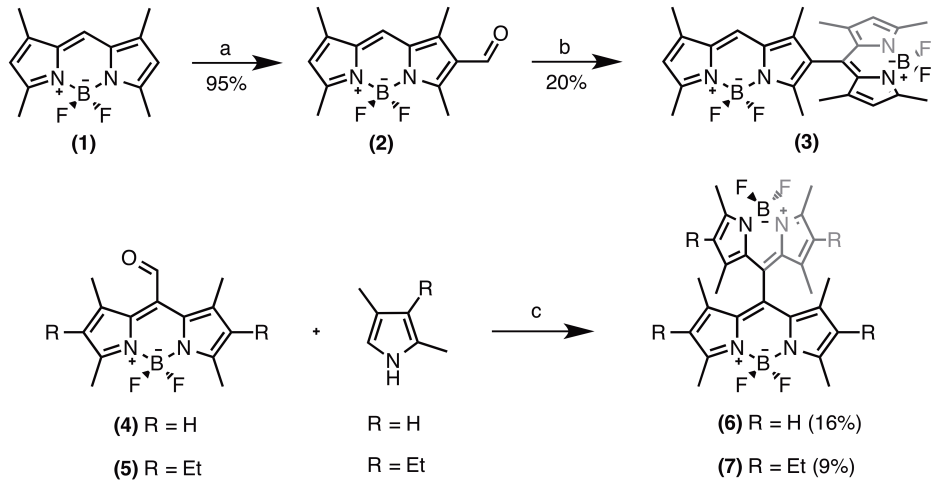

Figure 69. Synthesis of the target photosensitizers. a) $POCl_3$, DMF, $ClCH_2CH_2Cl$, 50°C; b) 2,4-dimethylpyrrole, trifluoroacetic acid (TFA), CH_2Cl_2, p-chloranil, Et_3N, $BF_3 \cdot OEt_2$; c) TFA, CH_2Cl_2, *p*-chloranil, Et_3N, $BF_3 \cdot OEt_2$. Copyright © 2011, John Wiley and Sons. Reprinted with permission from ref (121).

We surmised that a comparative study of compounds **(1)**, **(3)**, **(6)** and **(7)** would be instructive. First, we attempted to detect singlet oxygen phosphorescence at 1270 nm in chloroform for all four compounds excited with xenon-arc source at their respective absorption peaks, detection was done with a near IR sensitive detector. When excited at equal absorptivity concentrations for all compounds, dimer **(3)** yielded the strongest singlet oxygen phosphorescence emission (figure 70) at the signature wavelengths (peaking around 1270 nm), dimers **(6)** and **(7)** also showed phosphorescence peaks, but with somewhat reduced intensity.

Table 3**.** Comparative spectroscopic properties of BODIPY compounds.

Compound	λ_{abs}[a]/nm	λ_{ems}[a]/nm	ϕ_f	τ[a]/ns	ϕ_Δ[e]
1	509	514	0.80[d]	5.2	-
3	514	527	0.03[a,b]	2.5	0.51
6	515	588	0.31[a,c]	10.9	0.46
7	542	605	0.49[a,c]	5.0	0.21

[a] In $CHCl_3$. [b] In reference to Fluorescein in 0.1 M NaOH solution excited at 496 nm. [c] In reference to Rhodamine 6G in EtOH excited at 480 nm. [d] In EtOH. [e] Singlet oxygen quantum yield was determined with respect to Methylene Blue (0.57 in Dichloromethane)[206].

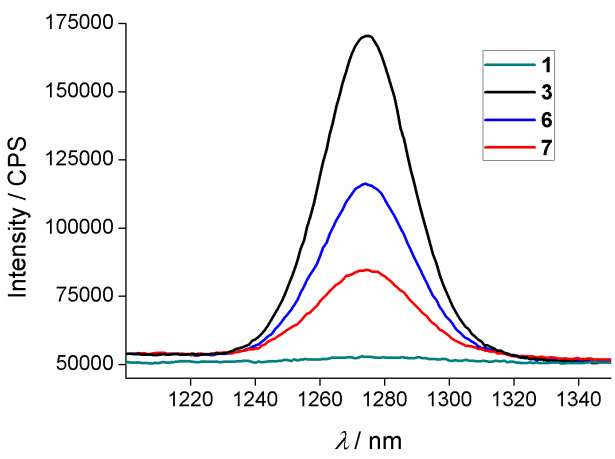

Figure 70. Singlet oxygen phosphorescence with sensitization from BODIPY derivatives: **(3)** (blue), **(6)** (black) and **(7)** (red), **(1)** (green) in $CHCl_3$ at equal absorbances (0.2) at the peak wavelength of their respective absorbances. Copyright © 2011, John Wiley and Sons. Reprinted with permission from ref (121).

On the other hand, no such emission was observed with compound **(1)** (figure 70). Non-halogenated BODIPY dyes having low intersystem crossing efficiency, is a well established fact,[202] indeed that is at least part of the reason for their bright fluorescence and photostability. While integral areas under the phosphorescence emission peak is a measure of singlet oxygen quantum yield, we opted for more quantitative assessment of singlet oxygen quantum yields using 1,3-diphenylisobenzofuran as a trap molecule and with Methylene Blue as the reference compound (Methylene Blue has a singlet oxygen quantum yield of 0.57 under the conditions of the study in dichloromethane[206]) (figure 71). Excitation of the dyes was carried out by irradiation at the respective absorbance peak wavelengths with monochromatized light source, at a fluence rate around 30 $\mu W/cm^{-2}$. The quantum yield for singlet oxygen generation for **(3)** is 0.51 in dichloromethane, much higher than all non-halogenated BODIPY dyes and many other organic chromophores and photosensitizers, under comparable conditions. The other BODIPY dimers **(6)** and **(7)** also showed respectable singlet oxygen quantum yields of 0.46 and 0.21, respectively.

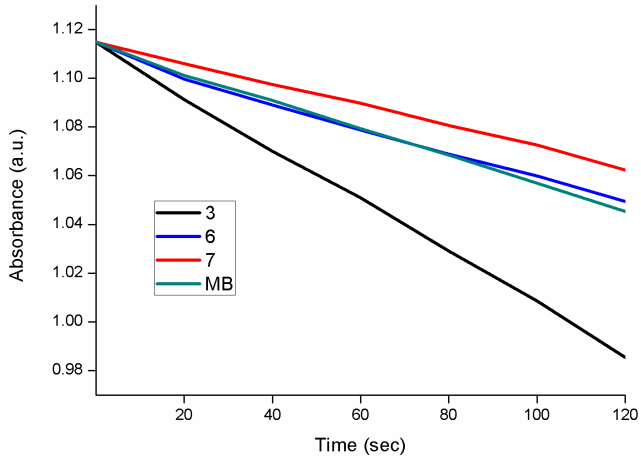

Figure 71. Comparative singlet oxygen generation experiment. Absorbance decrease of DPBF at 414 nm with time in dichloromethane in the presence of BODIPY photosensitizers: **(3)** (black), **(6)** (blue), **(7)** (red) and reference photosensitizer methylene blue (green).

For further demonstration of singlet generation capacity and photocytotoxicity of the most active dimeric dye **(3)**, we carried out a cell culture assay with cancer cell lines. To that end, we prepared a micellar formulation of the 8,2'-orthogonal dimeric dye

using Cremophor-EL. The size distribution of the micelles was determined using electrophoretic light scattering. The size distribution reveals a median size of 100 nm for the micellar constructs. Micelle embedded dye retained high levels of singlet oxygen generation capacity as revealed by another singlet oxygen trapping experiment, this time in aqueous media, using a water soluble anthracene derivative (2,2'-(Anthracene-9,10-diylbis(methylene))dimalonic acid) (figure 72).

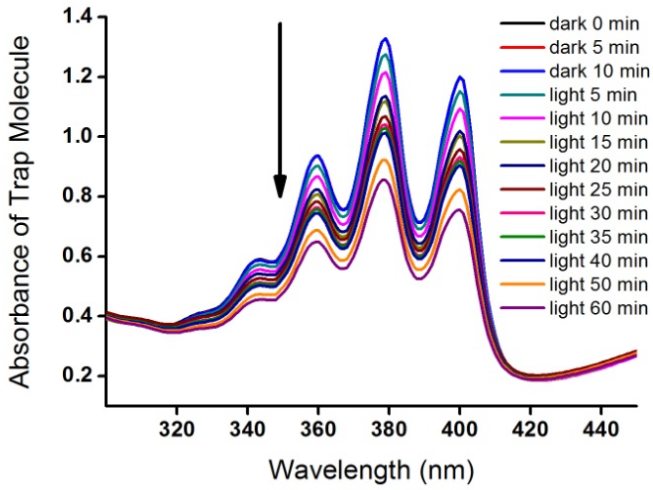

Figure 72. Singlet oxygen generation experiment in aqueous solution. Decrease in Absorbance spectrum of trap molecule (anthracene derivative) in the presence of 1.69 μM compound **(3)** in phosphate buffer saline (PBS). Details are given in singlet oxygen measurements part. Copyright © 2011, John Wiley and Sons. Reprinted with permission from ref (121).

Experimental verification of photocytotoxicity was carried out as follows: varying concentrations of the dimeric dye in Cremophor-EL micelles were incubated with K562 human erythroleukemia cells within a standard culture medium at 37 ^{o}C in a humidified incubator containing 5% CO_2. Cells were irradiated with the green LED source for 4 hours, followed 44 hours of incubation in dark. The control group was incubated in dark, under otherwise identical conditions. The cell viabilities were determined using standard MTT assay. The results are shown in figure 73. Even at very low concentrations of dyes (as embedded within micelles) significant decrease of cell viability was observed (green bars in figure 73) with a remarkable EC_{50} of 50 nM. No statistically significant change was observed when the cells were kept in

dark, in the presence of same concentration of the photosensitizer **(3)** (black bars in figure 73).

Photocytotoxicity was also revealed (figure 74) using confocal microscopy with two fluorescent probes of cell viability (acridine orange and propidium iodide). Cells incubated with the sensitizer **(3)** in dark show no changes as revealed by differential staining with the neutral and cell permeable acridine orange. These cells appear bright green under excitation at 488 nm. Cationic propidium iodide stains these cells only when membrane integrity is compromised; this happens only when both green LED irradiation and the sensitizer are acting on the cells. The use of excess propidium iodide results in red fluorescence in dead cells, or in cells dying via either apoptotic or necrotic pathways.

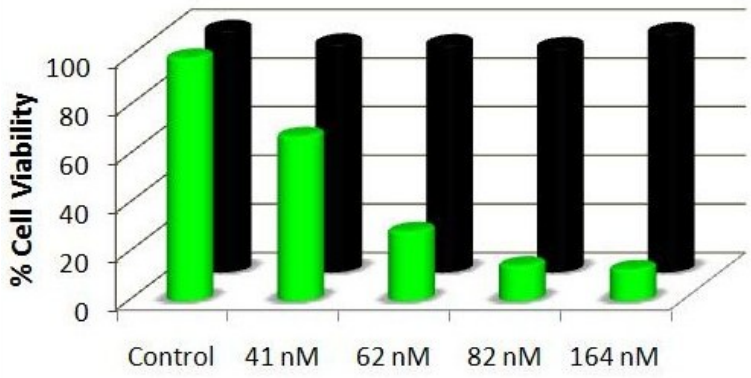

Figure 73. Photocytotoxicity of the sensitizer **(3)** as demonstrated by MTT assay. Cell suspensions (K562, human erythroleukemia cells) were seeded in 96-well flat-bottom plates and varying concentrations of the sensitizers were added into each well. Cells were kept either in dark, or under illumination with a green (520 nm) LED array at 2.5 mW/cm^2 fluence rate for a period of 4 h at 37^{0}C in a humidified incubator containing 5% CO_2.

Exploring the properties of these bis-BODIPYs further, in order to delineate the causes, extent, and control of this interesting electronic structure motif, is extremely important as the substantial $^1O_2$ generation yield in this new class of heavy atom free photosensitizers is linked to the extraordinary nature of S_1 state. Potential clinical applications are easily envisioned and were previously our major concern for **(3)** and **(6)**, however numerous questions regarding electronic structure of the S_1 state, such as the breadth of the orthogonality principle and control of excitation properties

under structural perturbations required further studies. Although general principles for regulating the frontier orbital levels are available,[207] strategies for fine-tuning orthogonal bis-BODIPYs to operate at longer wavelengths of the therapeutic window (620-850 nm) are desired. Currently it is unclear how to generalize the no-heavy atom ISC approach to bis-BODIPYs in general and/or to any orthogonal bis-chromophore. Comparison of the orthogonal bis-chromophore approach with heavy atom incorporation is also expected to provide new insights.

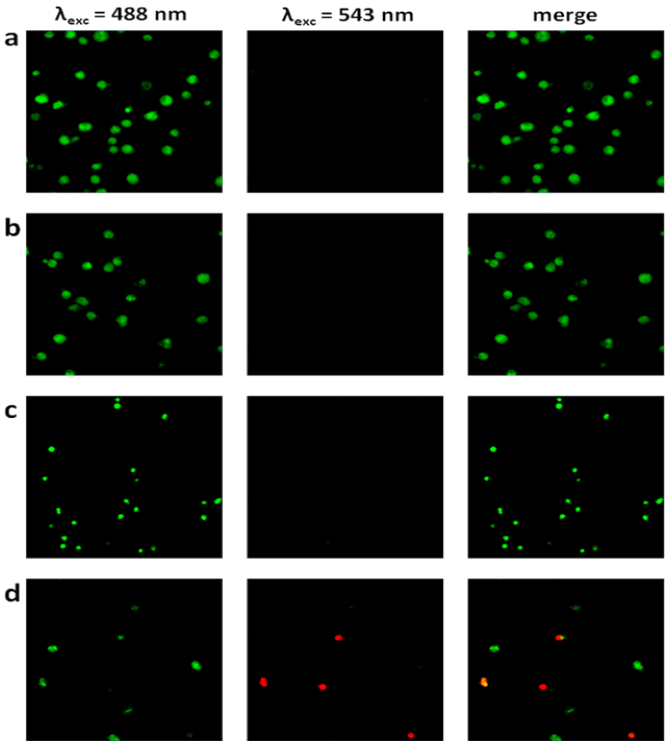

Figure 74. Photocytotoxic activity of the dimeric BODIPY **(3)** visualized via confocal microscopy. Cell suspensions (K562, human erythroleukemia cells) were seeded in 24-well plates. a, Cells in Control 1 (upper plates) wells were incubated in dark for 24 hours; b, Cells in Control 2 wells (second row plates) were incubated with 500 µl/well Cremophor-EL solubilized **(3)** (at a final concentration of 164 nM) and kept in dark for 24 hours in the same incubator, c, Cells in Control 3 well were illuminated for 4 h without the sensitizer and incubated for a further 20 h in dark at the incubator. d, Cells in Control 4 (bottom row of plates) well were illuminated for 4 h after addition of 164 nM **(3)** and incubated for a further 20 h in dark at the incubator. Cells in wells were collected after 24 h and imaged at 40x magnification. Live cells are preferentially stained with acridine orange (AO, green) (a), whereas dead cells are preferentially stained with the dye propidium iodide (PI, red) due to increased cellular permeability (b).

Effect of Orthogonality on S_1 State: Structural orthogonality is argued to be the key, in accessing DS-TR S_1 states, in the above view. This was further verified by the following computational experiment regarding the effect of relative positions of the two chromophore cores on excitation characteristics. Selecting the inter-plane angle as the transformation coordinate as shown in figure 75, and fixing all the remaining internal coordinates at their equilibrium values, CASSCF wave functions of the S_1 state were optimized for the corresponding conformations. Simple BODIPY core without any methyl groups was used instead of tetra-methyl BODIPY core as the methyl groups in the latter introduce huge steric effects even at small deviations from orthogonality. The one-electron density matrix for the S_1 states of corresponding conformations revealed that DS-TR nature of S_1 does not survive at small inter-plane angles and the classical HOMO→LUMO type SS excited state is generated at near planarity, where the π-systems start to mix significantly. Hence spatial orthogonality of the two monomers is central to generating a DS-TR S_1 state.

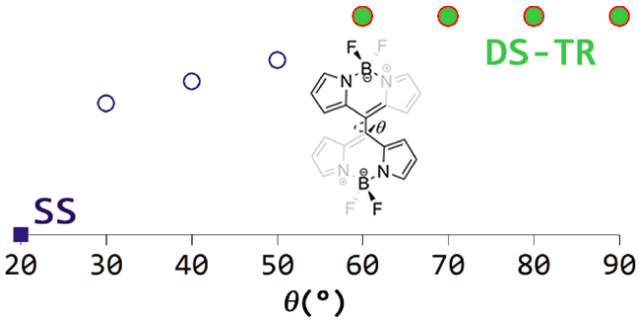

Figure 75. Effect of inter-plane angle (θ) variation on $S_0 \rightarrow S_1$ excitation characteristics (DS-TR/SS). Copyright © 2012, American Chemical Society. Reprinted with permission from ref (227).

Synthesis and Spectroscopic Properties of an Extended Conjugation Bis-BODIPY Derivative: The above results were motivating, particularly for utilizing many chromophores in heavy atom free ISC by only dimerizing them in an orthogonal fashion. Consequently, we aimed to surpass the accomplishments of **(3)** and **(6)** by synthesizing modified orthogonal bis-BODIPYs that will operate at the red end of the spectrum and, hence, potentially be better suited for photodynamic applications. The well-known modification to red shift λ_{abs}, i.e., decrease the energy gap between frontier orbitals is, extending[208] the π-system of the chromophore core.

For this purpose, synthesis of bis-8,2′-distyrylBODIPY derivative shown in figure 76 was performed.

Spectroscopic properties of **(bis-10a′)** (Figures 77, table 4) was investigated, and an emission at 680 nm together with a negligible triplet quantum yield were surprisingly observed, contrary to the expectation followed from the computed structural orthogonality (interplane angle = 90.1°). These results either suggest that excitation characteristics established for **(3)** and **(6)** by the CASSCF calculations are not complete descriptors for ISC or orthogonality alone does not afford the excited states bearing the features of interest. The former seems questionable in light of the reports on facile nonadiabatic reactions of related singlet states.[209] The latter hypothesis, on additional requirements to generate DS-TR S_1 states besides orthogonality, was tested via CASSCF calculations on the S_1 state of **(bis-10a′)**.

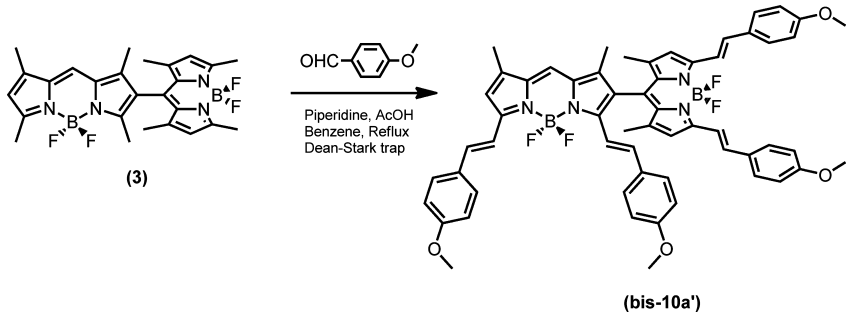

Figure 76. Synthesis of **(bis-10a')**. Copyright © 2012, American Chemical Society. Reprinted with permission from ref (227).

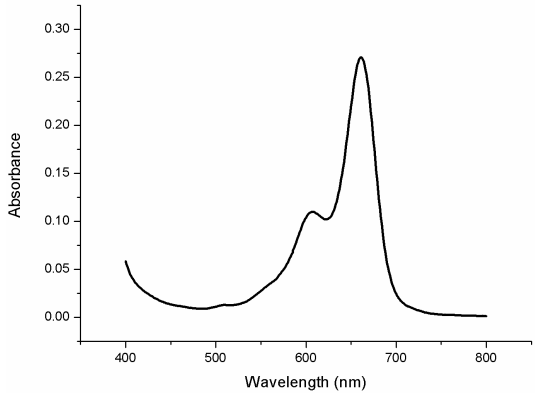

Figure 77. Electronic absorption spectrum of **(bis-10a')**. Copyright © 2012, American Chemical Society. Reprinted with permission from ref (227).

Effect of π-Extension on DS-TR Character of S_1: Since the disappearance of DS-TR character was apparently a result of extending the π framework, it is desirable to analyze the effect of increasing the size of the π -system with a smooth transition from **(3)** or **(6)** to **(bis-10a′)**.

Table 4. Photophysical Properties of the Synthesized BODIPY Compounds.

compound	λ_{abs}[a]/nm	ε_{max}/M^{-1} cm^{-1}	λ_{ems}[a]/nm	ϕ_f	τ[a]/nm	ϕ_Δ[d]
3	514	119400	527	0.025	2.5[a,c]	0.51
6	515	20300	588	0.31	10.9[a,b]	0.46
bis-10a'	**661**	**125300**	**680**	**0.06**	**2.2[a,c]**	**0.06**

[a] In $CHCl_3$. [b] With respect to Fluorescein in 0.1 M NaOH solution excited at 496 nm. [c] With respect to cresyl violet perchlorate in MeOH excited at 610 nm. [d] Singlet oxygen quantum yield was determined with respect to Methylene Blue (0.57 in Dichloromethane).[206]

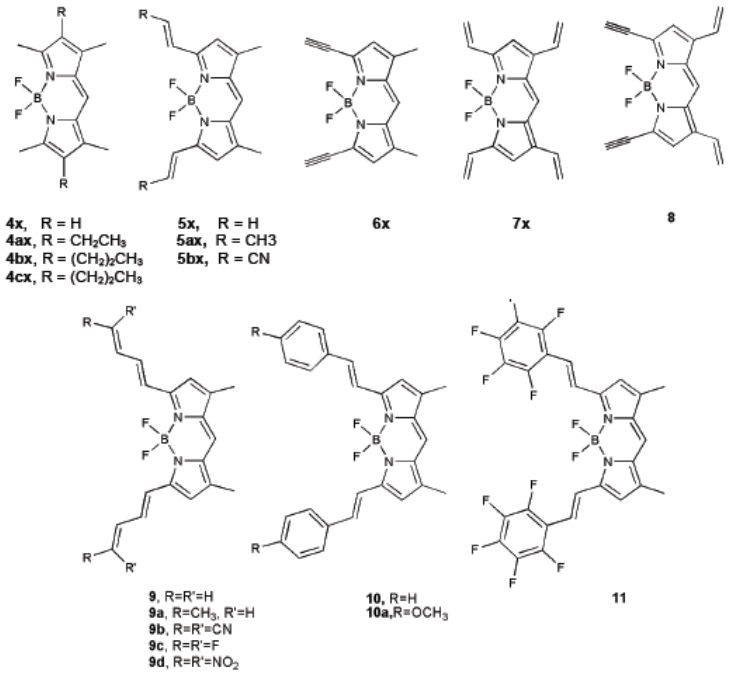

Figure 78. The set of monomers and dimers studied. Copyright © 2012, American Chemical Society. Reprinted with permission from ref (227).

This will enable us to monitor the cause of the drastic change in excitation

characteristics from DS-TR **(bis-4x)** and **(bis-4x′)** to SS (**bis-10a′**) where prime (′) indicates 8,2′ coupling motif of the monomers, and absence of the prime (′) shows 8,8′ binding. Therefore, we first generated computational models where BODIPYs bear only ethenyl/ethynyl substituents on various positions of the core. Further extension of the π –system was performed until SS-S_1 character persisted in the dimers. Also important was searching for any correlations between the characteristics of S_1 states of the bis-BODIPYs and the monomer electronic structure. Consequently, the set of monomers given in figure 78 and their 8,8′ and/or 8,2′ orthogonal dimers were studied.

Extending the conjugated π-systems of the monomers yielded four major sets of BODIPYs possessing the following substituents neighboring the core; none **(4x)**; ethenyl and/or ethynyl **(5x) to (8)**; butadienyl **(9)**; and styryl **(10), (11)**. All these models preserved an essentially planar geometry within the monomer, and their dimers were computed to be spatially orthogonal. Table 5 shows frontier orbital energies of ground states of all the monomers and dimers as well as the relative energies of S_1 and T_1 states of the orthogonal dimers. Excitation characteristics of the S_1 state (DS-TR or SS) of bis-BODIPYs are also shown.

It is clear from the frontier orbital energy differences that, orthogonality dictates formation of two pairs of near degenerate orbitals in the dimer that effectively preserve monomeric character. Extension of the π–system lowered the HOMO−LUMO gaps as anticipated, and interestingly, beyond the very first double bond added to the chromophore core; i.e., for set **(9)** to **(11)**, the DS-TR character of S_1 state disappears. In such cases, S_1 MOs were no longer delocalized on both chromophore cores (figure 79), which is also the case for **(bis-10a′)**. The lowering of the HOMO− LUMO gap and disappearance of DS-TR character of S_1 do correlate; however, it is illusory to conclude that DS-TR fades with decreased HOMO−LUMO gaps since the energy gap decrease itself is caused by a structural perturbation that extends the π-system. Thus, the fundamental reason of switching from DS-TR to SS type S_1 states needs further investigation (vide infra). Inspection of the relative energetic positioning of T_1 and S_1 states does not provide an answer since T_1 is

roughly equally separated from S_0 and S_1 states for all species and there is no significant pattern in favor of the DS-TR-S_1 or SS-S_1 possessing species. Incorporation of functional groups in order to donate or withdraw electron density as in the series of species **(5x)**, **(9)**, **(10)**, and **(11)** do result in deviations (from core BODIPY) in the anticipated directions for frontier MO levels but do not switch the excitation characteristics of S_1. Extension of the π-system shutting down the DS-TR S_1 state seems to be one net conclusion that could be drawn, despite the survival of near-degenerate monomer based orbitals for all the dimers considered. Nonetheless, from the four sets of models with increasing sizes of conjugated π-systems, the only groups with a DS-TR S_1 state were **(4x)** and **(5x)** to **(8)**, whose π-system extension is truncated at the very first C=C double bond. Apparently, one is only allowed to slightly modify S_0−S_1 energy difference without losing the DS-type excitation motif, and unfortunately, this does not result in the desired amount of HOMO−LUMO gap lowering.

Table 5. Selected Parameters for Modified BODIPY Cores and Associated Orthogonal Bis-BODIPYs.

	MONOMER				DIMER								
Species [a]	E_H (eV)	E_L (eV)	ΔE_{H-L} (eV)	ΔE_{H-L} (nm	E_{H-1} (eV)	E_H (eV)	E_L (eV)	E_{L+1} (eV)	$\Delta E_{L-(H-1)}$ (eV)	$\Delta E_{(L+1)-H}$ (eV	S_1 [b]	$E(T_1)$ [c] (eV)	$E(S_1)$ [c] (eV)
4x	-5.69	-2.78	2.91	426	-6.01	-5.92	-3.04	-3.04	2.97	2.88	*DS-TR*	1.79	3.69
4x'					-6.04	-5.69	-3.11	-2.76	2.93	2.93	*DS-TR*	2.35	4.16
4ax	-5.47	-2.60	2.87	432	-5.71	-5.62	-2.84	-2.81	2.87	2.81	*DS-TR*	2.28	3.90
4bx	-5.46	-2.60	2.86	433	-5.70	-5.60	-2.82	-2.80	2.88	2.80	*DS-TR*	1.69	3.45
4cx	-5.45	-2.59	2.86	433	-5.67	-5.58	-2.81	-2.77	2.86	2.81	*DS-TR*	1.69	3.44
5x	-5.51	-3.03	2.48	499	-5.82	-5.75	-3.39	-3.23	2.44	2.52	*DS-TR*	1.62	3.77
5x'					-5.84	-5.52	-3.33	-3.02	2.51	2.50	*DS-TR*	2.14	3.81
5ax	-5.22	-2.78	2.43	509	-5.46	-5.39	-3.07	-2.91	2.39	2.48	*DS-TR*	1.62	3.33
5ax'					-5.46	-5.21	-3.01	-2.75	2.45	2.46	*DS-TR*	1.69	3.33
5bx	-6.30	-3.97	2.33	532	-6.85	-6.79	-4.49	-4.34	2.36	2.45	*DS-TR*	1.57	3.68
5bx'					-6.81	-6.50	-4.44	-4.16	2.36	2.34	*DS-TR*	1.83	3.51
6x	-5.86	-3.31	2.55	487	-6.39	-6.33	-3.79	-3.62	2.60	2.72	*DS-TR*	1.66	3.43
6x'					-6.44	-5.84	-3.76	-3.29	2.68	2.55	*DS-TR*	1.71	3.41
7x	-5.65	-3.30	2.35	527	-6.02	-5.87	-3.53	-3.46	2.49	2.41	*DS-TR*	1.34	2.71
7x'					-5.90	-5.62	-3.56	-3.30	2.34	2.33	*DS-TR*	1.58	3.18
8	-5.95	-3.55	2.40	517	-6.42	-6.31	-3.89	-3.82	2.53	2.49	*DS-TR*	1.22	2.87
8'					-6.25	-5.88	-3.86	-3.51	2.38	2.37	*DS-TR*	1.63	3.30
9	-5.19	-3.03	2.16	574	-5.40	-5.35	-3.24	-3.24	2.16	2.10	*SS*	1.51	3.48
9'					-5.39	-5.20	-3.23	-3.02	2.16	2.17	*SS*	1.60	3.18
9a	-4.95	-2.83	2.12	584	-5.10	-5.05	-2.99	-2.98	2.12	2.07	*SS*	1.46	3.17
9a'					-5.09	-4.93	-2.98	-2.79	2.11	2.14	*SS*	1.60	3.17
9b	-6.44	-4.49	1.95	636	-6.92	-6.87	-4.83	-4.83	2.09	2.05	*SS*	1.47	3.18
9b'					-6.90	-6.54	-4.90	-4.57	1.99	1.96	*SS*	1.50	3.06
9c	-5.59	-3.42	2.17	570	-5.93	-5.86	-3.74	-3.72	2.19	2.14	*SS*	1.50	3.37
9c'					-5.91	-5.65	-3.72	-3.46	2.19	2.19	*SS*	1.59	3.20
9d	-6.91	-5.03	1.88	659	-7.60	-7.47	-5.67	-5.40	1.93	2.07	*SS*	1.38	3.19
9d'					-7.45	-7.05	-5.50	-5.14	1.95	1.91	*SS*	1.51	3.10
10	-5.09	-2.97	2.12	584	-5.28	-5.23	-3.16	-3.14	2.12	2.09	*SS*	1.54	3.26
10'					-5.25	-5.09	-3.13	-2.95	2.12	2.15	*SS*	1.61	3.17
10a	-4.84	-2.78	2.05	604	-4.91	-4.85	-2.92	-2.88	1.99	1.97	*SS*	1.55	2.76
10a'					-4.92	-4.82	-2.89	-2.75	2.04	2.08	*SS*	1.59	3.14
11	-5.98	-3.81	2.18	570	-6.30	-6.25	-4.12	-4.10	2.17	2.15	*SS*	1.53	2.56
11'					-6.35	-6.09	-4.16	-3.90	2.19	2.19	*SS*	1.54	2.52

[a] Prime (′) indicates 8,2′ coupling motif of the monomers, and absence of the prime (′) shows 8,8′ binding. [b] DS-TR: Doubly substituted tetraradical. SS: Singly substituted HOMO→LUMO-type open-shell singlet state. [c] Relative energies of T_1 and S_1 states with respect to the ground state S_0 of the dimer at the CAS(6,6) level.

The rationale of attributing the disappearance of DS-TR character to extension of the π-system was further tested by the following computational experiment performed on **(bis-9′)** and **(bis-10′)**. When the extension of π-conjugation is thought to be responsible for switching to SS from DS-TR, the DS-TR character of S_1 in the dimer should reappear if the π–electron density supplied by the substituents, does not communicate with the core.

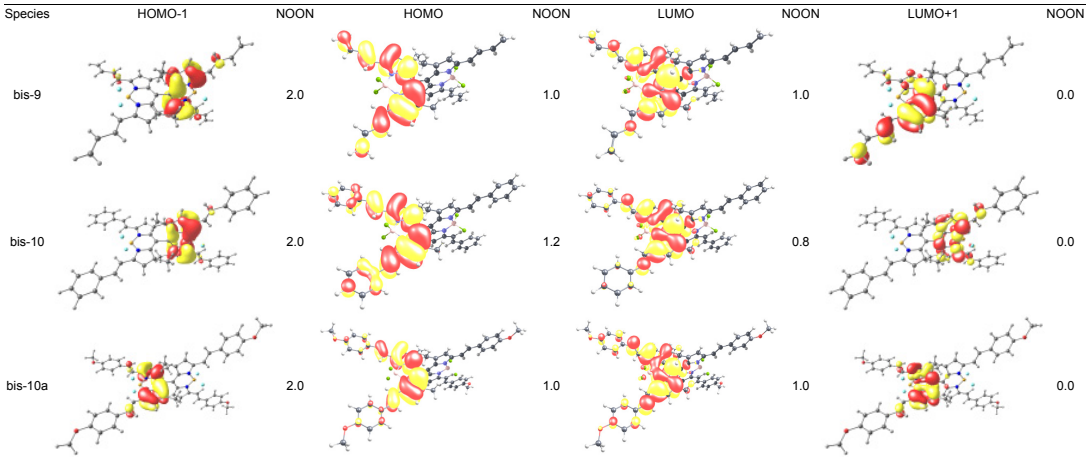

Figure 79. Selected natural orbitals and occupation numbers for **(bis-9)**, **(bis-10)** and **(bis-10a)**. Calculations were done at CAS(6,6)/CEP-31G//(U)B3LYP/CEP-31G level. Copyright © 2012, American Chemical Society. Reprinted with permission from ref (227).

Freezing the core coordinates in the optimized structure, we rotated the outermost π-system, i.e., last ethenyl unit for **(bis-9′)** and the phenyl for **(bis-10′)**, with respect to the core plane as shown in figure 80 and optimized the wave function of the S_1 state for the conformations generated accordingly. Since planarity is necessary for the conjugation of the π-system, any property caused by the extended conjugation should be affected by increasing angle θ. In line with the expectations, we observe that DS-TR is regenerated at large angles where the π-delocalization between the rotated units and the rest of the chromophore ceases. NOONs for the conformations tested above are close to 2, 1, or 0 at all times in line with SS or DS-TR nature of S_1 These findings suggest that π-extended bis-chromophores should not possess the target electronic structure motif with structural orthogonality alone. This failure encourages searching alternative strategies for tuning frontier MO energies; however, before moving further, we have to search for any insights provided from the analysis of electronic structure of excited singlet states in related heavy atom incorporated

systems, that are well-known for facilitated ISC.

In questioning the rationale of DS-TR to SS switching as a result of π-extension, we compared the electron density distribution of frontier MOs of bis-BODIPYs from both S_1 classes. In the SS cases, contrary to the delocalized SOMOs of DS-TR states, MOs were clearly concentrated on a single monomer (figure 79), which implied negligible coupling among monomer cores.

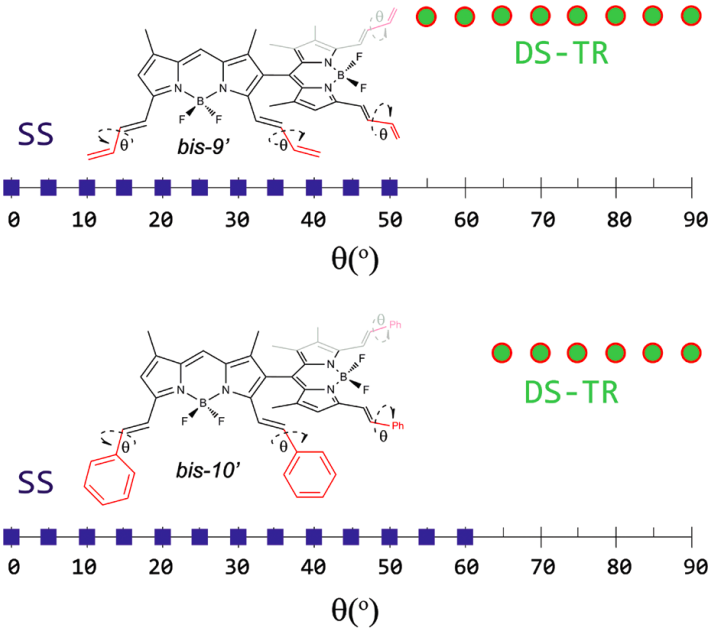

Figure 80. Relation of DS-TR character of S_1 to the extent of π conjugation in butadienyl- and styryl-substituted BODIPY dimers **(bis-9′)** and **(bis-10′)**. Copyright © 2012, American Chemical Society. Reprinted with permission from ref (227).

This suggests that, the so-called antiferromagnetic coupling of electrons among SOMOs weakens with increased size of the π-framework in a SOMO. Such a view well agrees with the foundations of electron correlation, which is more of a local effect.[210] Equivalently, the superexchange path is lost when electrons are more and more spread out in space. This difficulty encountered (for relatively largely separated electron densities) in obtaining a significant amount of quantum mechanical exchange energy is apparently manifested in a relative destabilization of the DS-TR with respect to the SS state.

These results were motivating in investigating DS-TR singlets lying higher than S_1

for π-extended bis-BODPYs, and we were successful in locating DS-TR singlet states for **(bis-9)**, **(bis-9′)**, **(bis-10)**, **(bis-10′)**, **(bis-10a)**, and **(bis-10a′)** as S_2 or S_3 (table 6). Severe convergence problems in the computation of the highlying-excited states were encountered, and the quantitative reliability of relative energies may be questionable; however, a useful trend of qualitative nature is noteworthy.

Table 6. Relative Energies (eV) of S_2 and S_3 States for Selected Species at CAS(6,6)/CEP-31G level of theory.

		S_2		S_3	
Species	**Binding Motif**	**ΔE_{rel} (eV)**	**NOON**	**ΔE_{rel} (eV)**	**NOON**
bis-4x	8,8'	4.97	2.0 1.6 1.4 0.9 0.2 0.0		
bis-4'x	8,2'	6.83	2.0 1.5 1.0 0.5 0.0 0.0		
bis-9	8,8'	3.92	2.0 1.0 1.0 1.0 1.0 0.0		
bis-9'	8,2'	3.41	2.0 2.0 1.0 1.0 0.0 0.0	4.84	2.0 1.0 1.0 1.0 1.0 0.0
bis-10	8,8'	2.16	2.0 1.5 1.0 0.5 0.0 0.0	3.47	2.0 1.0 1.0 1.0 1.0 0.0
bis-10'	8,2'	3.73	2.0 1.0 1.0 1.0 1.0 0.0		
bis-10a	8,8'	3.67	2.0 1.0 1.0 1.0 1.0 0.0		
bis-10a'	8,2'	3.24	2.0 1.6 1.0 1.0 0.4 0.0		*unconverged*

It is clear that whenever the S_1 state is not computed to be DS-TR as a result of the π-electron increasing structural perturbation that does not allow a superexchange path for vastly spread out SOMO electrons, an S_n ($n > 1$) state with DS-TR character exists. Thus, instead of envisioning DS-TR singlet states to disappear with extending the conjugation, we should better term this phenomenon as destabilizing the DS-TR singlet state as a result of decreasing quantum mechanical exchange stabilization for largely spread out spin-orbitals.

4.1.4. Experimental Details

General: General: ^{1}H NMR and ^{13}C NMR spectra were recorded on Bruker DPX-400 (operating at 400 MHz for ^{1}H NMR and 100 MHz for ^{13}C NMR) in $CDCl_3$ solvent with tetramethylsilane as internal standard. All spectra were recorded at 25^{o}C and coupling constants (*J* values) are given in Hz. Chemical shifts are given in parts per million (ppm). Absorption spectra were performed by using a Varian Cary-100 and Varian Cary 5000 UV-VIS-NIR absorption spectrophotometer. Fluorescence measurements were conducted on a Varian Eclipse spectrofluometer. The Fluorescence decay measurements were carried out with the Horiba Jobin-Yvon

Time-Resolved Fluorometer, Fluorolog FL-1057. The instrument response function was measured with an aqueous Ludox solution. Singlet oxygen phosphorescence around 1270 nm were determined by using Horiba Jobin-Yvon Fluoremeter with Hamamatsu NIR PMT module, model H-10330-75. The decays were analyzed with a multiexponential fitting function by iterative reconvolution and chi-square minimization. Mass spectra were recorded with Agilent Technologies 6224 TOF LC/MS and 6530 Accurate Mass Q-TOF LC/MS. Irradiation of photosensitizers **(3)**, **(6)** and **(7)** were accomplished at 520 nm by monochromatic light system composed of Spectral Products CM 110 1/8m monochromator, ASB-XE-175 Xenon light source, Newport Multi Function Optical Meter model 1835-C. Irradiation of **bis-10a'** was performed using 660 nm LED. Methylene blue was irradiated at 520 nm and 660 nm. Electrophoretic Light Scattering was performed with Malvern NanoZS zeta potential. Reactions were monitored by thin layer chromatography using Merck TLC Silica gel 60 F254. Silica gel column chromatography was performed over Merck Silica gel 60 (particle size: 0.040-0.063 mm, 230-400 mesh ASTM). 4,4-Difluoro-8-formyl-1,3,5,7-tetramethyl-4-bora-3a,4a-diaza-s-indacene **(4)**[205] and 4,4-Difluoro-8-formyl-2,6-diethyl-1,3,5,7-tetramethyl-4-bora-3a,4a-diaza-s-indacene **(5)**[205] were synthesized according to literature. All other reagents and solvents were purchased from suppliers and used without further purification. Micelle has been prepared with compound **3** according to the literature.[130] In singlet oxygen measurements 1,3-Diphenylisobenzofuran was used as a singlet oxygen trap in organic solvent measurements and was purchased from supplier. 2,2'-(Anthracene-9,10-diylbis(methylene))dimalonic acid was used a singlet oxygen trap in aqueous solvent and was synthesized according to the literature.[211]

Computational Details: Geometries were fully optimized with the *ab initio* Complete Active Space Self Consistent Field (CASSCF) methodology and B3LYP Density Functional[212] employing CEP-31G (SBKJC) and cc-pVDZ basis sets.[213] Harmonic vibrational frequencies were computed to assure that the species did not possess any imaginary frequencies and hence correspond to true minima. After a number of trial and error the active space in the CASSCF calculations were established as 6 electrons distributed over 6 valence orbitals (6,6) for the 8,2' dimer

(3) and 4 electrons distributed over 4 valence orbitals (4,4) for the 8,8' dimer **(6)** and. Enlarged active spaces up to 12,12 also reproduced the key features presented in the main text. For the sake of consistency a 6 electrons in 6 orbitals CAS is used for both dimers. Geometries of excited states T_1 and S_1 were also fully optimized. Natural orbitals of the CASSCF wavefunction and configuration state function coefficients were analyzed to understand the nature of the electronic state as being a single electron HOMO → LUMO type or multiply substituted type. Whereas BODIPY core S_1 is a clean HOMO → LUMO dominated $\pi\pi^*$ state, S_1 states of **(3)** and **(6)** are drastically different and showed a large degree of multi-reference character. Gaussian 03[214] suite was mainly used for the DFT calculations, CASSCF calculations were mainly performed with MOLCAS[215], and GAMESS-US[216] programs. For selected species, with no significant multi reference character, TD-DFT calculations in combination with a polarizable continuum model (PCM) were performed to investigate the excitation characteristics. Excited-state MCSCF calculations used the state averaged (SA) formalism with equal weights for all the states involved. No restrictions on symmetry were imposed. **Computational studies were done in Dr. Yavuz Dede group at Gazi University, Department of Chemistry, Ankara, Turkey.**

Cell Culture Studies and MTT Assay: K562 human erythroleukemia cells (ATCC) were cultured in 25 cm^3 culture flasks containing RPMI 1640 medium supplemented with heat inactivated 10 % fetal bovine serum, 2 mM L-glutamine,100 units.mL-1 penicillin G and 100 $\mu g.mL^{-1}$ streptomycin at 37^oC in a humidified incubator containing 5% CO_2. Micellar preparation of the sensitizer was dissolved in RPMI 1640 medium and test concentrations were prepared daily. The methlythiazolyltetrazolium (MTT) assay was used to evaluate cell viability. Briefly, 50 μL cell suspensions containing 4 x 10^4 K562 cells were seeded in 96-well flat-bottom plates (Costar, Cambridge, MA) and varying concentrations of Cremophor-EL solubilized dye **(3)** (Final concentrations= 41 nM - 164 nM) were added in 50 μL into each well. All dye concentrations were tested in triplicate for three times. Then, cells were kept either in dark or under illumination with a green (520 nm) LED array at 2.5 mW/cm^2 fluence rate for a period of 4 h at 37^oC in a humidified incubator

containing 5% CO_2. In order to evaluate the cytotoxicity of dye, 4 h irradiated plates were kept in dark for a further 44 h and then MTT solution was added for measuring cell viability. In addition, plates kept in dark for 4 h were also incubated for an additional 44 h for control. After 48 h, 25 μL of MTT solution (1.0 mg/mL final concentration) (Sigma Chemical Co., St. Louis, MO) were added to each well, and the plates were incubated for a further 4 h. The formazan precipitate was solubilized by adding 80 μL lysing buffer (pH=4.7) composed of 23% SDS (sodium dodecyl sulfate) dissolved in a solution of 45% N,N- dimethylformamide. After an overnight incubation at 370^{o}C, the absorbances were read at 570 nm using a microplate reader (Spectramax Plus, Molecular Devices, Sunnyvale, California, USA). Cells incubated in culture medium alone served as a control for cell viability (nontreated wells) either in irradiated plate or in plate that was kept in dark. Cell viability (%) was calculated as OD of treated wells/OD of nontreated cells x 100. **Cell culture and MTT assay studies were done in Dicle Guc group at Hacettepe University, Basic Oncology Department, Ankara, Turkey.**

Confocal Microscopy Imaging: Confocal microscopic analysis was also performed to evaluate cell viability. Briefly, 1500 μL cell suspensions containing 2 x 10^5 K562 cells/well were seeded in 24-well plates. Cells in Control 1 well were incubated in dark for 24 hours at 370^{o}C in a humidified incubator containing 5% CO_2. Cells in Control 2 well were incubated with 500 μL/well Cremophor-EL solubilized dye **3** (Final dye concentration = 164 nM) and kept in dark for 24 hours in the same incubator. Cells in Control 3 well were illuminated for 4 h without dye and incubated for a further 20 h in dark at the incubator. Cells in Control 4 well were illuminated for 4 h after addition of 164 nM dye **(3)** and incubated for a further 20 h in dark at the incubator. All conditions were studied in duplicate. Cells in wells were collected after 24 h and confocal microscopy images were acquired.

A stock solution of propidium iodide (PI) (Sigma P-4170) was prepared in distilled water, and used at a concentration of 0.5 mg/mL. Acridine orange (AO) was dissolved in phosphate buffered saline at a concentration of 100 μg/mL. One tablet of phosphate buffered saline (PBS) (Amresco) was dissolved in the distilled water to

yield a pH=7.4 buffered solution.

Chromophore-EL solubilisation: Photosensitizer **(3)** (5 x 10^{-5} moles) was dissolved in THF (1mL) treated with Cremophor EL (CrEL, 150 mg) and sonicated for 30 mins. THF was removed under reduced pressure, the remaining oil was dissolved in phosphate-buffered saline (PBS) (5mL), filtered through a 0.2 μm membrane filter and made up to 10 mL with PBS (1X , pH= 7.4). Average size was found to be ca. 90 nm (figure 81).

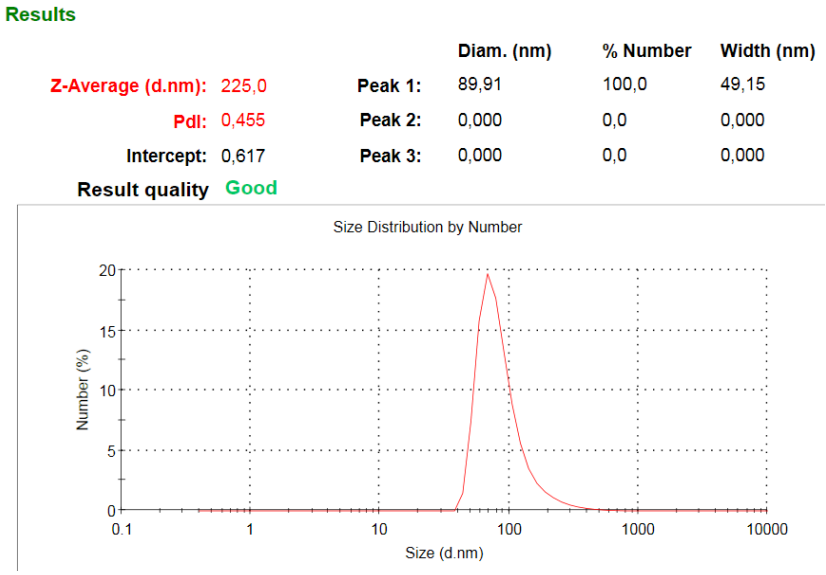

Figure 81. Size distribution of compound micellar compound **(3)**. Cremophor EL was used for embedding the dye. Copyright © 2011, John Wiley and Sons. Reprinted with permission from ref (121).

Singlet Oxygen Trap Experiments: In singlet oxygen measurements 1,3-Diphenylisobenzofuran (DPBF) (figure 82) was used as a singlet oxygen trap in organic solvent and was purchased from a supplier. 2,2'-(Anthracene-9,10-diylbis(methylene))dimalonic acid (ADMDA) was used a singlet oxygen trap in aqueous solvent and was synthesized according to the literature (figure 83).[1] In a typical procedure for the detection of singlet oxygen generation by using trap molecules, a photosensitizer (~1 μM) and a trap molecule (O.D ~ 1.0) were mixed in O_2 bubbled solvent. Initially several dark measurements were taken followed by irradiation of the mixture at absorption maximum of a sensitizer. Absorbance decrease of trap molecules was monitored suggesting singlet oxygen generation in

the presence of light and sensitizers.

Singlet oxygen quantum yields were calculated according to the literature.[201] The relative quantum yields were calculated with reference to Methylene Blue (MB) in dichloromethane as 0.57.[206] First, dichloromethane was bubbled with air for 5 minutes. In UV cuvette absorbance of DPBF was adjusted around 1.0 using air bubbled dichloromethane. Then, photosensitizer was added to cuvette and photosentizer's absorbance was adjusted around 0.2-0.3.

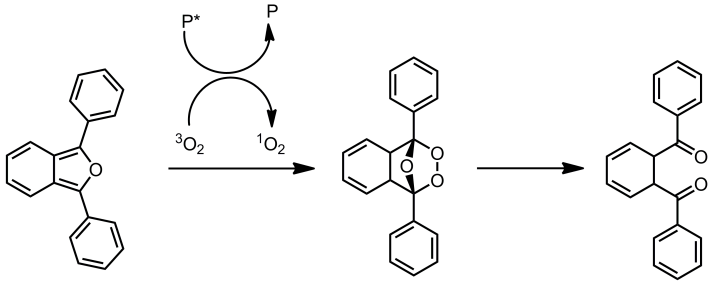

Figure 82. Reaction of singlet oxygen with 1,3-Diphenylisobenzofuran.

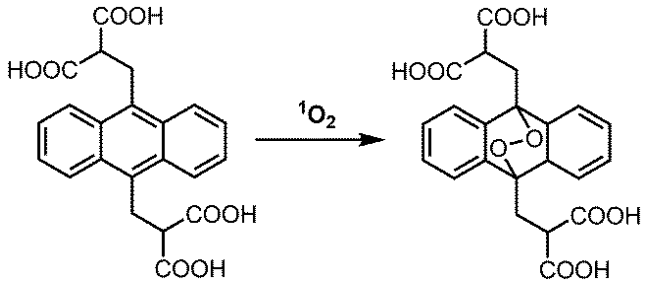

Figure 83. Reaction of singlet oxygen with 2,2'-(Anthracene-9,10-diylbis(methylene))dimalonic acid.

After, taking some measurements in dark, we took cuvette to monochromatic light system for irradiation at peak wavelength for 20 seconds. Absorbance was measured for several times after each irradiation. The graphics recorded are shown below; Figures 84 to 87. Then, slope of absorbance maxima of DPBF at 414 nm versus time graph for each photosensitizer were calculated. Singlet oxygen quantum yield were calculated according to the equation: where bod and ref designate the orthogonal BODIPY photosensitizer and MB respectively. m is the slope of difference in change in absorbance of DPBF (414 nm) with the irradiation time, F is the absorption correction factor, which is given by $F = 1 - 10^{-OD}$ (OD at the irradiation

wavelength), and PF is absorbed photonic flux (μEinstein dm^{-3} s^{-1}).

$$\phi_{\Delta}\,(\mathrm{bod}) = \phi_{\Delta}(\mathrm{ref}) \times \frac{\mathrm{m\ (bod)}}{\mathrm{m\ (ref)}} \times \frac{\mathrm{F\ (ref)}}{\mathrm{F\ (bod)}} \times \frac{\mathrm{PF\ (ref)}}{\mathrm{PF}\ (bod)}$$

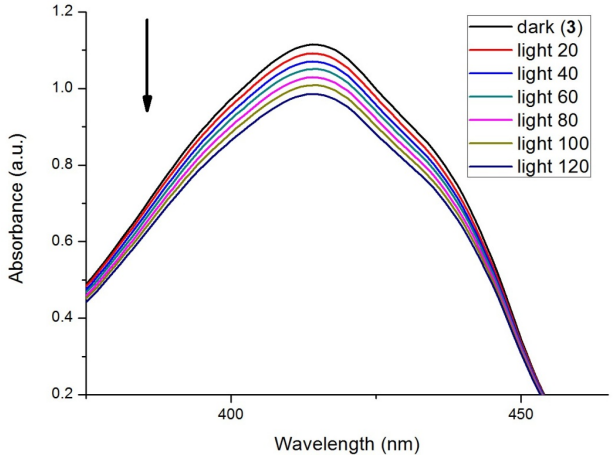

Figure 84. Decrease in absorbance of DPBF in dichloromethane in the presence of compound **(3)** in medium. Details are given in singlet oxygen measurements part. Copyright © 2011, John Wiley and Sons. Reprinted with permission from ref (121).

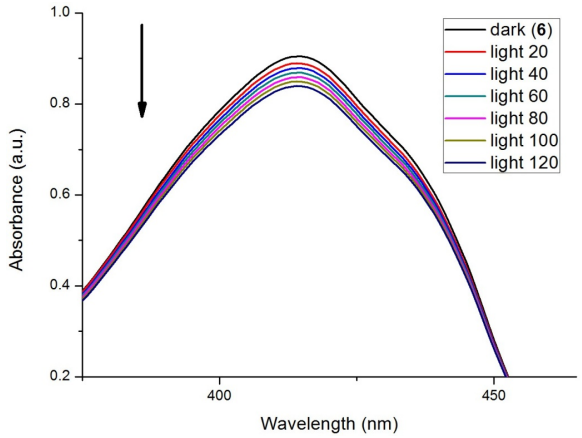

Figure 85. Decrease in absorbance of DPBF in dichloromethane in the presence of compound **(6)** in medium. Details are given in singlet oxygen measurements part. Copyright © 2011, John Wiley and Sons. Reprinted with permission from ref (121).

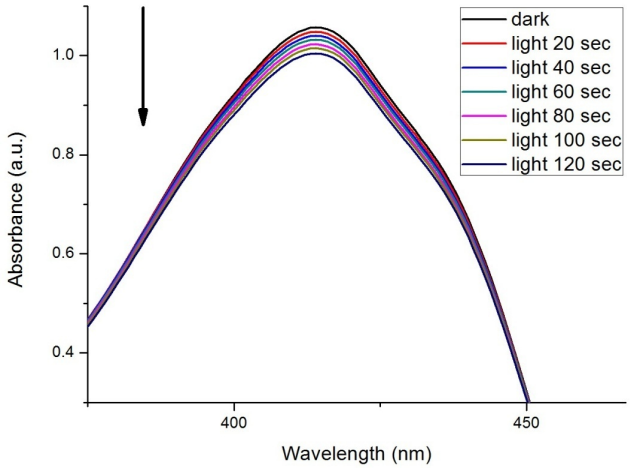

Figure 86. Decrease in absorbance of DPBF in dichloromethane in the presence of compound **(7)** in medium. Details are given in singlet oxygen measurements part. Copyright © 2011, John Wiley and Sons. Reprinted with permission from ref (121).

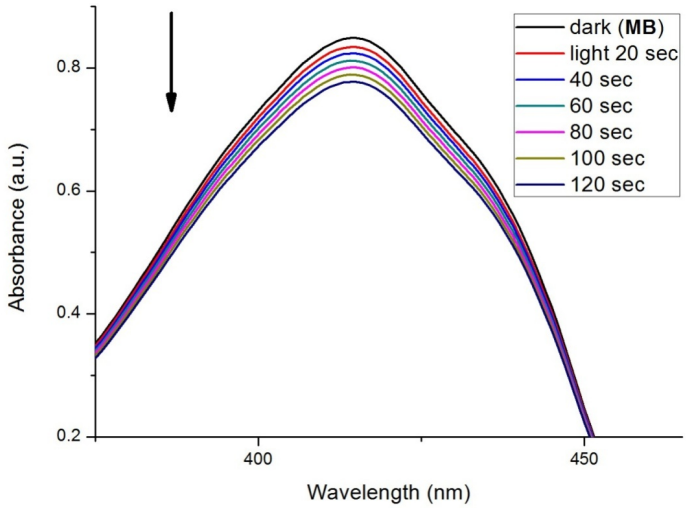

Figure 87. Decrease in absorbance of DPBF in dichloromethane in the presence of MB in medium. Details are given in singlet oxygen measurements part. Copyright © 2011, John Wiley and Sons. Reprinted with permission from ref (121).

X-ray Crystal Structure Determination: X-ray diffraction data were obtained on an Enraf-Nonius CAD4 (κ-geometry) diffractometer operating in ω/2θ scan mode using graphite-monochromated MoK_{α} radiation (λ = 0.71073 Å) at room temperature. The lattice parameters and their estimated standard deviations were determined by using CAD4 Express. Data reduction was carried out using XCAD4. The structures were solved by direct methods and refined by the full-matrix least-

squares refinement on F^2 using the programs SHELXS97 and SHELXL97, respectively, in the WinGX package. Atomic scattering factors were taken from the International Tables for X-ray Crystallography. Hydrogen atoms bonded to carbon were placed on ideal positions and refined with fixed isotropic displacement parameters using a riding model. The molecules are held together by weak van der Waals interactions. Hydrogen bond and molecular packing geometry of the title molecule was calculated with PLATON. The compound has one intermolecular and four intramolecular hydrogen bonds. Packing figure (figure 88) are prepared by MERCURY program.[217] **X-ray crystal structure of compound (3) was determined in Dr. Leyla Tatar Yildirim group, at Hacettepe University, Department of Physics Engineering, Ankara, Turkey.**

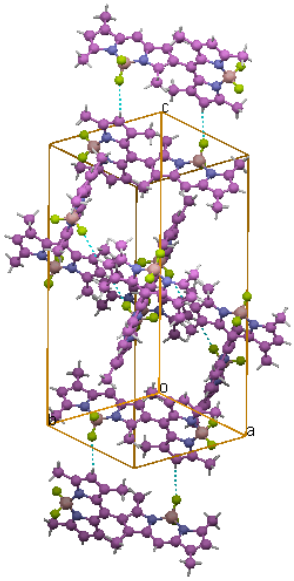

Figure 88. Packing diagrams of compound **(3)**. Dashed lines indicate inter H-bond between C2 and F4 atoms. Copyright © 2011, John Wiley and Sons. Reprinted with permission from ref (121).

Synthetic Details:

Synthesis of (1): 250 mL 1,2-dichloroethane was degassed with N_2. 2,4-dimethyl pyrrole (1 mL, 11.37 mmol), triethylorthoformate (0.95 mL, 5.69 mmol) and $POCl_3$ (0.58 mL, 6.25 mmol) were added to degassed solvent. Reaction was allowed to stir for 2 hours at room temperature. Then 11.55 mL NEt_3 and 11.55 mL $BF_3.OEt_2$ were added. After 1 hour the reaction was washed with water (3x250 mL), the organic

layer separated, dried on $NaSO_4$ and evaporated in vacuo. Column chromatography with $CHCl_3$ yielded the pure product as reddish solid (400 mg, 28 %). ^{1}H NMR (400 MHz, $CDCl_3$): δ_H 7.09 (1H, s, Ar*H*), 6.10 (2H, s, Ar*H*), 2.60 (6H, s, C*H*$_3$), 2.29 (6H, s, C*H*$_3$); ^{13}C NMR (100 MHz, $CDCl_3$): δ_C 156.8, 141.3, 133.5, 120.2, 119.1, 14.8, 11.2 ppm.

Synthesis of (2): 4 mL of DMF and 4 mL of $POCl_3$ was stirred in an ice bath for 5 min under argon. Then warmed to room temperature and waited for 30 minutes. To this mixture compound **(1)** (100 mg, 0.328 mmol) was added in dichloroethane (40 mL). The temperature is raised to 50 °C and stirred for 2 hours. The reaction medium was cooled and poured into 150 mL $NaHCO_3$ solution slowly under cool conditions. After cooling it was stirred for further 30 min, then washed with water 3 times. The organic layers was combined and dried over $NaSO_4$ and evaporated to dryness. The compound has been purified by column chromatography by using chloroform as an eluant and the compound has been got pure as reddish solid (95 %). ^{1}H NMR (400 MHz, $CDCl_3$): δ_H 10.02 (1H, s, C*H*O), 7.20 (1H, s, Ar*H*), 6.20 (1H, s, Ar*H*), 2.77 (3H, s, C*H*$_3$), 2.58 (3H, s, C*H*$_3$), 2.48 (3H, s, C*H*$_3$), 2.28 ppm (3H, s, C*H*$_3$); ^{13}C NMR (100 MHz, $CDCl_3$): δ_C 185.5, 163.5, 157.2, 145.4, 140.6, 136.4, 131.1, 125.8, 122.0, 121.5, 15.2, 12.9, 11.5, 10.4 ppm; MS HRMS (TOF- ESI): *m*/z calcd for $C_{14}H_{15}BF_2N_2O^+$: 275.1246 $[M+H]^+$; found: 275.1212$[M+H]^+$, Δ = 12.3 ppm.

Synthesis of (3): In N_2 bubbled 250 mL dichloromethane, 2,4-Dimethylpyrrole (50 µL, 0.478 mmol) and **(2)** (60 mg, 0.217 mmol) were mixed. 1 drop of trifluoroacetic acid has been added. The reaction mixture stirred at room temperature overnight. Then p-chloranil (49.2 mg, 0.217 mmol) was added to the reaction. After stirring 1 hours at room temperature, NEt_3 (2 mL) and $BF_3.OEt_2$ (2 mL) was added and stirred again for 1 hour. The reaction was finished by extracting with water (3x250 mL). Column chromatography with $CHCl_3$ yielded the pure product (20 %). ^{1}H NMR (400 MHz, $CDCl_3$): δ_H 7.18 (1H, s, Ar*H*), 6.15 (1H, s, Ar*H*), 6.02 (2H, s, Ar*H*), 2.61 (3H, s, C*H*$_3$), 2.59 (3H, s, C*H*$_3$), 2.57 (3H, s, C*H*$_3$), 2.54 (3H, s, C*H*$_3$), 2.40 (3H, s, C*H*$_3$), 2.30 (3H, s, C*H*$_3$), 2.12 (3H, s, C*H*$_3$), 1.72 ppm (3H, s, C*H*$_3$); ^{13}C NMR (100 MHz, $CDCl_3$): δ_C 160.3, 155.8, 151.5, 143.7, 142.5, 136.6, 134.7, 133.4, 132.3,

131.7, 124.2, 121.3, 120.7, 120.5, 14.9, 14.7, 13.9, 12.7, 9.8, 8.7 ppm; MS HRMS (TOF-ESI): *m*/z calcd for $C_{26}H_{28}B_2F_4N_4^+$: 493.2436 $[M+H]^+$; found: 493.2417 $[M+H]^+$, Δ = 3.9 ppm.

Synthesis of (6): In N_2 bubbled 100 mL dichloromethane 2,4-Dimethylpyrrole (16.2 µL, 0.12 mmol) and **(4)** (20 mg, 0.06 mmol) were mixed. 1 drop of trifluoroacetic acid has been added. The reaction mixture stirred at room temperature overnight. Then p-chloranil (14.8 mg, 0.06 mmol) was added to the reaction. After stirring 1 hour at room temperature, NEt_3 (1 mL) and $BF_3.OEt_2$ (1 mL) was added and stirred again for 1 hour. The reaction was finished by extracting with water (3x100 mL). Column chromatography with $CHCl_3$ yielded the pure product (16 %). ^{1}H NMR (400 MHz, $CDCl_3$): δ_H 6.05 (4H, s, Ar*H*), 2.61 (12H, s, C*H*$_3$), 1.60 (3H, s, C*H*$_3$); ^{13}C NMR (100 MHz, $CDCl_3$): δ_C 157.2, 142.6, 121.6, 14.8, 14.3 ppm; MS HRMS (TOF-APCI): *m*/z calcd for $C_{26}H_{28}B_2F_4N_4$: 493.2358 $[M-H]^-$; 493.2385 found: $[M-H]^-$, Δ = 5.5 ppm.

Synthesis of (7): In N_2 bubbled 100 mL dichloromethane 2,4-Dimethylpyrrole (14.8 µL, 0.143 mmol) and **(5)** (18 mg, 0.065 mmol) were mixed. 1 drop of trifluoroacetic acid has been added. The reaction mixture stirred at room temperature overnight. Then p-chloranil (16 mg, 0.065 mmol) was added to the reaction. After stirring 1 hour at room temperature, NEt_3 (1 mL) and $BF_3.OEt_2$ (1 mL) was added and stirred again for 1 hour. The reaction was finished by extracting with water (3x100 mL). Column chromatography with $CHCl_3$ yielded the pure product (9 %). ^{1}H NMR (400 MHz, $CDCl_3$): δ_H 2.54 (12H, s, C*H*$_3$), 2.36 (8H, q, J = 11.3 Hz, C*H*$_2$,), 1.82 (12H, s, C*H*$_3$), 1.10 (12H, s, C*H*$_3$); ^{13}C NMR (100 MHz, $CDCl_3$): δ_C 155.1, 137.8, 134.8, 133.2, 129.9, 17.1, 14.7, 12.8, 11.6 ppm; MS HRMS (TOF-APCI): *m*/z calcd for $C_{34}H_{43}B_2F_4N_4$: 605.3610 $[M-H]^-$; found: 605.3618 $[M-H]^-$, Δ = 1.3 ppm.

Synthesis of Bis-8,2'-distyryl-BODIPY Derivative, bis-10a': Compound **(3)** (0.121 mmol, 60.0 mg) and 4-methoxybenzaldehyde (0.728 mmol, 99.2 mg) were added to a 100 mL round-bottomed flask containing 50 mL of benzene, and to this solution were added piperidine (0.6 mL) and acetic acid (0.6 mL). The mixture was heated under reflux using a Dean−Stark trap, and the reaction was monitored by TLC

($CHCl_3$). When all of the starting material had been consumed, the mixture was cooled to room temperature and solvent was evaporated. Water (100 mL) was added to the residue, and the product was extracted into the chloroform. The organic phase dried over Na_2SO_4 and evaporated, and the residue was purified by silica gel column chromatography using $CHCl_3$ as the eluent. Product was separated as a blue solid in 30% yield (35 mg, 0.0363 mmol). ^{1}H NMR (400 MHz, CDCl3): δ_H 7.68 (3H, d, J = 18.8 Hz), 7.65−7.55 (m, 8H), 7.40 (d, 2H, J = 8.9 Hz), 7.35 (d, 1H, J = 15.2 Hz), 7.22 (d, 2H, J = 15.2 Hz), 7.10 (s, 1H), 7.02−6.93 (m, 6H), 6.86−6.77 (m, 3H), 6.66 (s, 2H), 3.95−3.85 (9H, m), 3.80 (3H, s), 2.37 (s, 3H), 2.16(s, 3H), 1.85 (s, 6H). ^{13}C NMR (100 MHz, CDCl3): δ_C 160.4, 153.0, 141.5, 141.3, 138.0, 137.2, 136.5, 136.1, 129.6, 129.5, 129.4, 129.3, 129.2, 129.1, 117.6, 117.3, 116.9, 116.5, 116.2, 114.5, 114.3, 114.2, 55.4, 55.3, 14.2, 11.5, 9.6 ppm. MS HRMS (TOF-ESI): m/z calcd for C58H53B2F4N4O4+ 967.41891 $[M+H]^+$, found 967.41898 [M+H]+, Δ = 0.1 ppm.

4.1.5. Conclusion

Our work demonstrated for the first time a practical example of excited state design leading to efficient cytotoxic singlet oxygen generation with a potential in photodynamic therapy. With a sound theoretical framework in design, it is only natural to expect other photosensitizers to emerge with similar line of reasoning. We performed detailed multireference quantum chemical analyses on several electronic states of orthogonal bis-BODIPYs. Essentially isolated monomeric states in the dimers dictated formation of a pair of (near) degenerate S_0 frontier orbitals, which yielded four SOMOs in the S_1 state. Domination of S_1 wave function by doubly substituted configurations was utilized as an electronic structure descriptor in assessing ISC efficiency. Formation of DS-TR S_1 states was not only tied to orthogonality but also to a certain degree of truncation in the π-framework of the substituents. Bis-BODIPYs with extended π-systems possess destabilized DS-TR states, as exchange coupling among unpaired electrons of same spin is significant only at small distances. Shifting the absorption wavelength to the red region is achieved with π-extension of bis-BODIPYs; however, ISC properties are adversely affected for such dimers. Modifications in the chromophore cores are likely to be a

more promising research direction.

4.2. Activatable Heavy Atom Free Sensitizers: Selective Enhancement of Photocytotoxicity

4.2.1. Objective

Photosensitized generation of reactive oxygen species, particularly singlet oxygen is at the core of photodynamic action leading to PDT. "On-off" switching of singlet oxygen generation would be highly valuable if it were to be linked to a cancer related cellular parameter. A favorite recipe for enhancing ISC in an organic sensitizer has been incorporation of heavy atoms. Unfortunately, this comes with price tag of increased "dark toxicity". Building on recent findings related to ISC efficiency, we designed dimeric BODIPY dyes with broken symmetry, which is inactive as a sensitizer, unless it is activated by a reaction with the intracellular GSH. Modulation of charge transfer and DS-TR excited state is an "off-on process" and most remarkably, the designed sensitizer can differentiate different concentrations of GSH in healthy (normal) and cancer cells, and thus remaining inefficient as a sensitizer inside a normal cell, while being transformed into a deadly singlet oxygen source inside the cancer cells. This is the first demonstration of such a difference in intracellular activity of a sensitizer.

4.2.2. Introduction

PDT that is based on the photosensitized generation of singlet oxygen by irradiation at the visible-near IR region of the spectrum, has been recognized as a non-invasive cancer treatment modality of great potential for some time, however the realization of that potential did not take place except for very limited cases of skin lesions and always at the initial stages of the diseases.[218] It should be in principle possible to localize irradiation to the area of the tumor, increasing spatial selectivity, but painful oedemia in the patient is a very common side-effect due to photosensitization in an unrelated locale inside the body. This situation prompted many in the field to propose so-called "activatable sensitizers", which are to be turned on only when

cancerous tissue or cell is uncounted, otherwise staying at a passive state, not-being capable of photosensitization, even if the molecule happens to absorb a photon of stray light.[219]

Earlier examples mostly made use of the pH difference between the tumor extracellular pH and the healthy tissues.[220] On the other hand, GSH concentration, which is reportedly higher in cancer cells,[79] was also exploited as a modulator,[135] however no difference in photosensitization activity in cancer cells were shown explicitly. Other modulators were caspase,[221] *this and that*, but in all these cases, differential sensitization in cancer versus normal cells was not demonstrated. The intracellular distinction is important because, extracellular singlet oxygen clearly is not as effective cytotoxic agent.

The other piece of the puzzle is the sensitizer itself. It is possible to attach quencher module,[130] which is removed by an external agent to restore photosensitization, but this bimodular approach makes the activatable sensitizer too large, in some cases making it cell impermeable, thus limiting any potential. Extracellular GSH/bio-thiol activation reaction is absolutely non-specific and does not really add anything to the selectivity of the photosensitization. With these considerations and by using the accumulated knowledge of excited state configurations and triplet photosensitization (section 4.1), we thus concluded that *de novo* design of a sensitizer, as opposed to tinkering with a porphyrin derivative, seemed more promising.

4.2.3. Results and Discussion

In this study, we designed a heavy atom free orthogonal-bis BODIPY sensitizer to get activatable, charge transfer (CT) mediated heavy atom free sensitization of PDT by modulating excited state characteristics of the sensitizer. Our sensitizer **(PS)** involves an unsubstituted Bodipy core (BOD-1, charge donor), which is linked orthogonally to another Bodipy (BOD-2, linker) that is substituted with a methyl pyridinium (MP, charge acceptor) moiety (figure 89). Incorporation of methylated pyridine unit has four major roles; i) suppressing the DS-TR nature of the BODIPY dimer's excited state via extension of conjugation ii) upon excitation, it is a potential

charge acceptor moiety, iii) forming a reaction site for bio-thiols (for instance GSH) (iii) improved water solubility. The electronic structure details of **(PS)** and **(actPS)** were investigated with a combination of DFT, TD-DFT, and CASSCF/CASPT2 methods before dealing with singlet oxygen generation experiments in order to validate our design strategies.

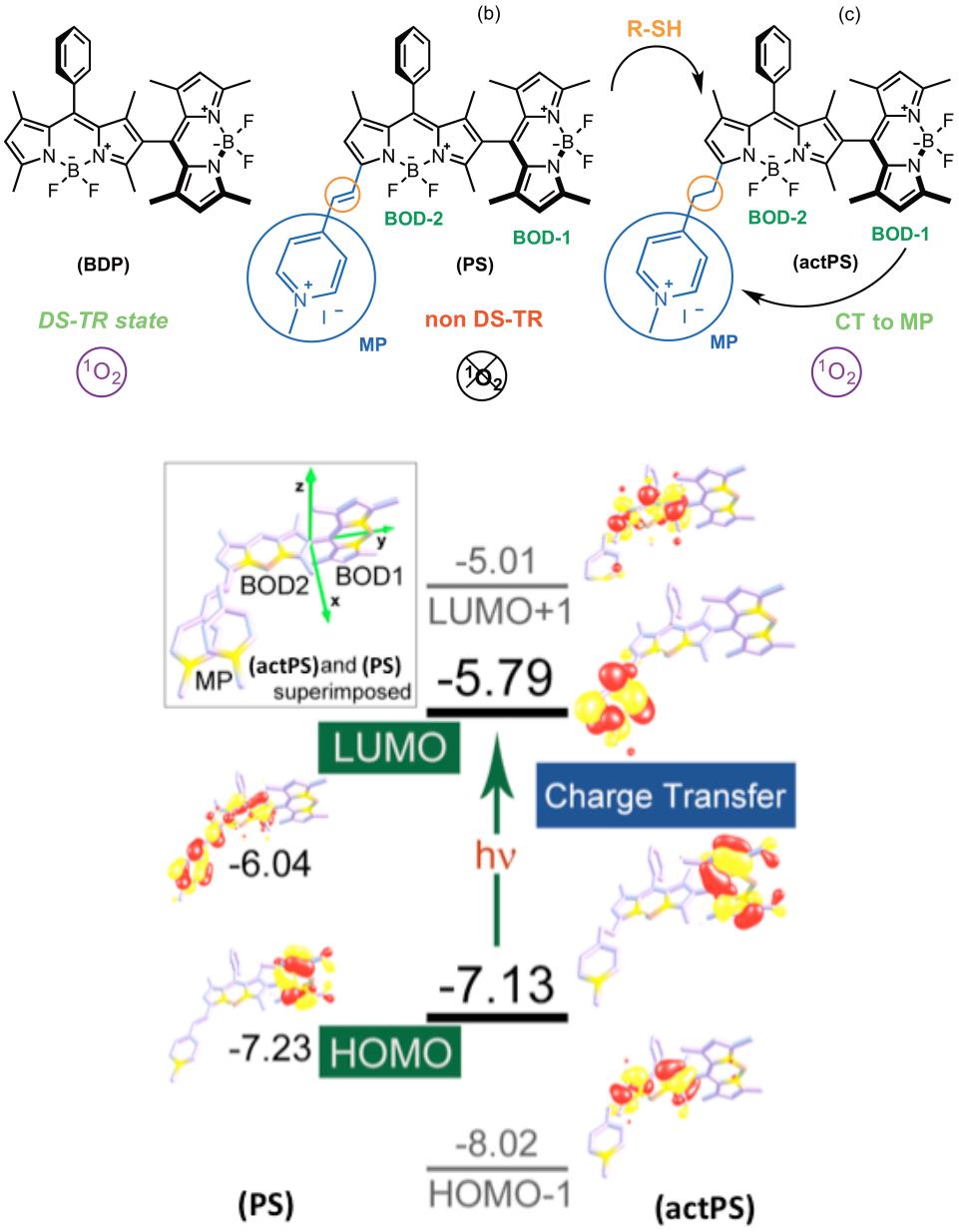

Figure 89. Design principles (top) and Orbital energies (eV) and plots of (**PS**) and **(actPS)** relevant to the CT excitation from BODIPY to methylpyridinium (bottom).

Initially our sensitizer **(PS)** is expected to be inactive due to the destabilized DS-TR

excited state and non-degenerate HOMO levels of individual BODIPY cores as a result of extended conjugation and asymmetric functionalization (section 4.1). In addition to that, theoretical calculations show that coplanar arrangement of MP on the xy-plane in **(PS)** generates a LUMO delocalized on the entire MP-BOD-2. On the other hand, when conjugation is broken like in the case of **(actPS)**, LUMO is clearly local to MP and acts as a spatially separated electron acceptor (figure 89). Frontier orbital plots and energies of **(PS)** and **(actPS)** are depicted in figure 89. As mentioned above, LUMO of **(actPS)** is mainly the LUMO of cationic methylpyridinium moiety. Therefore an $S_0 \rightarrow S_1$ excitation of the HOMO → LUMO type is a typical picture of a charge transfer (CT) transition from the unsubstituted BOD1 HOMO to the MP LUMO. This (through-space) CT transition is the key point in our design for achieving ISC in the case of **(actPS)**. Whenever orbitals taking place in a CT excitation are placed on orthogonal and separated donor – acceptor moieties (HOMO and LUMO of **(actPS)** in figure 89) the electronic transition is accompanied by a large change in orbital angular momentum that should be compensated by a change in the spin angular momentum, hence the reason of singlet-triplet hop. In line with the requirements on angular momentum change, the donor MO lies on the yz-plane and acceptor MO lies on the xy-plane for **(actPS)** (figure 89). Our calculations suggest that the 8-phenyl BODIPY is transformed into a spacer with the conversion of **(PS)** to **(actPS)**. The effect of structural spacers on the electronics of CT transitions was recently discussed[124] where absence of spacers was shown to diminish the CT nature of CT in twisted chromophores.

After obtaining promising theoretical insights, we firstly synthesized a *meso*-phenyl substituted BODIPY derivative according to well-established BODIPY chemistry. The formylation of the core at 2-position was performed followed by another BODIPY formation reaction to obtain an orthogonal dimer. Then, Knoevenagel condensation reaction was performed with 4-pyridine carboxyaldehyde. Finally we methylated the pyridine moiety by using excess iodomethane in ethyl acetate and methyl pyridinium salt of BODIPY was isolated successfully (figure 90).

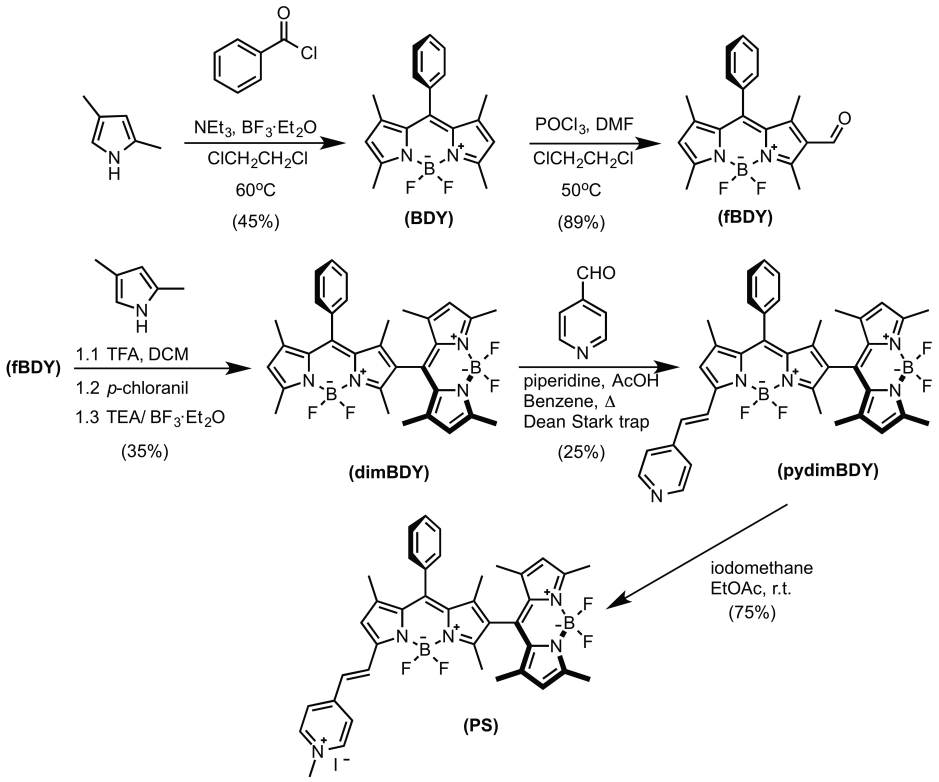

Figure 90. Synthesis of activatable sensitizer **(PS)**.

Later, in order to synthesize our activated sensitizer **(actPS)** by blocking the conjugation, we used a simple thiol mercaptoethanol in a proof of principle study. Reaction of **(PS)** with mercaptoethanol in DCM can possibly yield to products; i) addition of thiol to double bond or ii) reduction of the double bond under basic conditions.[222] Literature studies showed that latter product is obtained by a radicalic mechanism.[222] When we tried the reaction with catalytic amount of potassium carbonate in dichloromethane, we isolated the major product as a reduced form **(actPS)** (figure 91). ^{1}H NMR spectrum (figure 91) of **(actPS)** clearly shows the disappearance of the styryl peaks, which are observed at 7.9 and 7.4 ppm in the case of compound **(PS)**. Moreover appearance of a new peak at 3.4 ppm that corresponds to aliphatic hydrogens, (due to the reduction) can be interpreted as a direct proof of the desired adduct (figure 91). Further characterization of the adduct was done by mass spectrometry (figure 91) in which we observed a single BODIPY dimer pattern with 4.9 ppm precision.

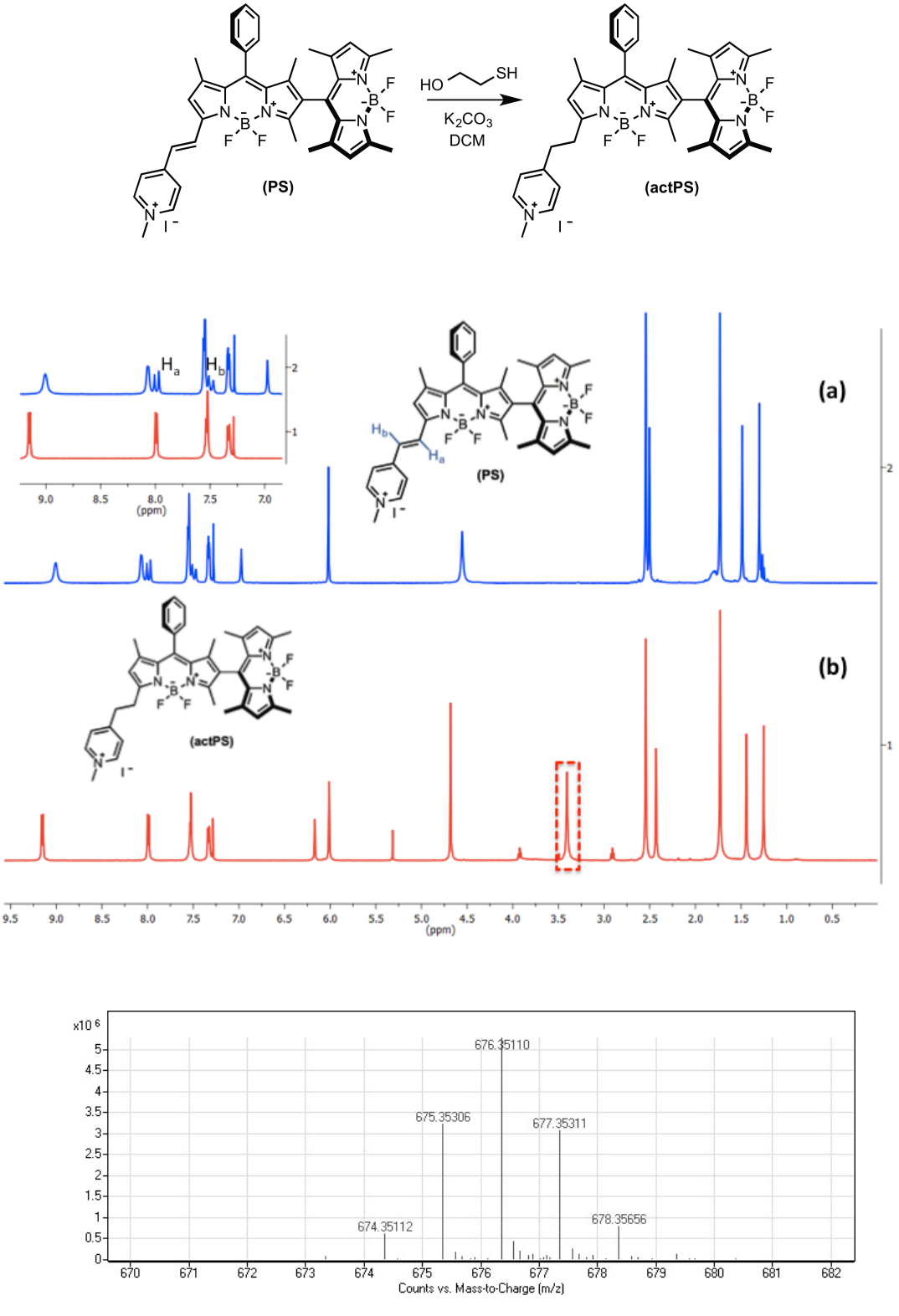

Figure 91. Reduction of compound **(PS)** in the presence of mercaptoethanol. ^{1}H NMR spectra of **(PS)** and **(actPS)**. HR-MS spectrum of **(actPS)** (Δ (ppm) = 4.9 ppm).

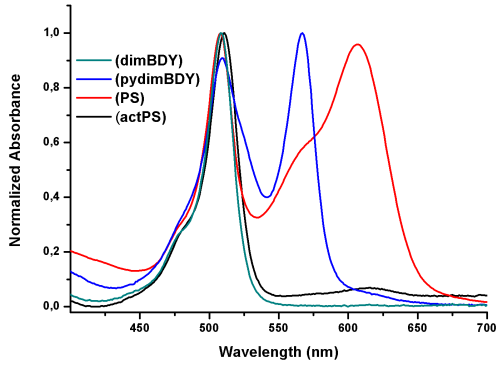

Figure 92. Normalized electronic absorption spectra of **(dimBDY)**, **(pydimBDY)**, **(PS)** and **(actPS)** in DCM.

Table 7. Photophysical characterization of sensitizers.

sensitizer	λ_{abs} [a] / nm	ε_{max} [a] / M^{-1} cm^{-1}	λ_{ems} [a] / nm
dimBDY	508	140000	530
pydimBDY	509	36000	522
	567	30000	573
PS	508	41000	522
	607	38000	645
	513[b]	34000[b]	520[b]
	590[b]	25000[b]	606[b]
actPS	511	119000	535
	508[b]	90000[b]	533[b]

[a]Values were obtained in DCM. [b]Values were obtained in 90/10 (HEPES Buffer/ MeCN). Fluorescence quantum yield measurements were acquired by using reference compounds Rhodamine 6G (water, ϕ_f = 0.95, ν = 1.333) and sulphorhodamine (ethanol, ϕ_f = 0.90, ν = 1.362). For all compounds fluorescence quantum yields were found to be almost zero.

After the synthesis of compounds **(PS)** and **(actPS)** and optical characterization, we performed series of singlet oxygen (SO) generation experiments by monitoring the singlet oxygen formation via 1,3-diphenylisobenzofuran as a SO trap molecule, when DCM was used as a solvent and 2,2'-(Anthracene-9,10-diyl)bis(methylene)dimalonic acid in the case of aqueous solutions (figure 93). First of all, we investigated the SO

generation capacity of compound **(dimBDY)** by observing the decrease in absorption of DPBF in DCM. As expected cytotoxic SO formation was highly efficient in the case of **(dimPDY)**. Then SO trap experiment was performed with **(PS)** in DCM and there was no change in absorbance indicating the formation of SS excited state and loss of DS-TR state due to the extended conjugation. After that, same experiment was repeated in 90:10 / HEPES buffer (pH 7.4):MeCN with water-soluble anthracene derivative trap in the presence of **(PS)**. Similarly SO generation could not be observed. There are two characteristic absorption peaks for **(PS)** due to the asymmetric arrangement of two different BODIPY cores.

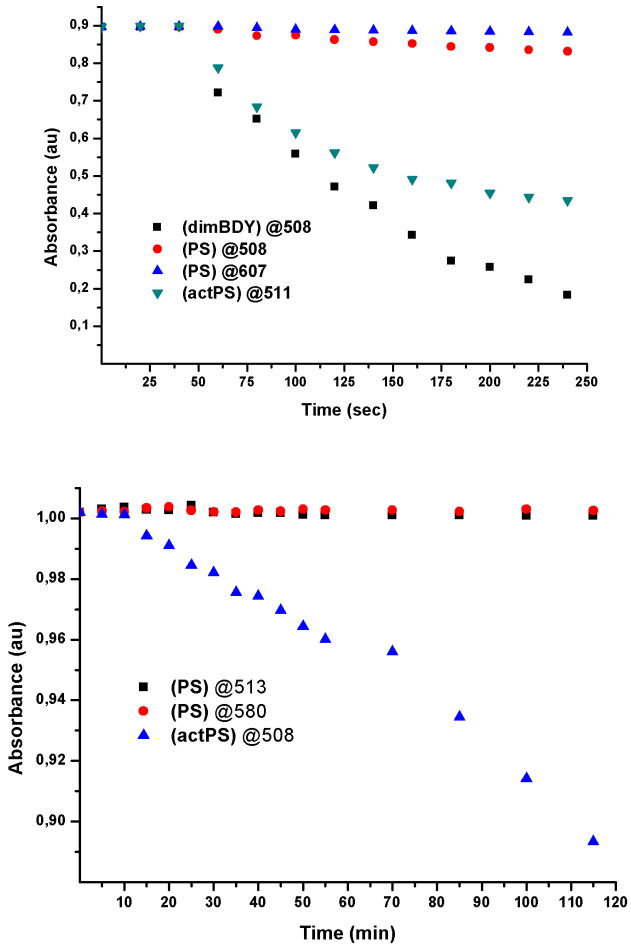

Figure 93. Relative $^1O_2$ generation efficiency of top: **(dimBDY)**, **(PS)** and **(actPS)** in DCM and bottom: **(PS)** and **(actPS)** in 90:10 (Hepes buffer, pH 7.2, 20mM : MeCN) detected by the absorbance decrease of DPBF at 414 nm and 2'-(Anthracene-9,10 diylbis(methylene))dimalonic acid (ADMDA) at 378 nm respectively with time. During first 60 seconds (right) and 15 minutes (left), the samples were kept in the dark.

It is important to note that, SO generation is only observed with compounds **(dimBDY)** and **(actPS)** in both solvents. In the case of **(dimBDY)**, SO generation can be detected due to the formation of doubly substituted tetra radical (DS-TR) excited state configuration as in the case of our previous studies (section 4.1). On the other hand, in **(actPS)**, charge transfer mediated ISC is the reason for SO generation. Moreover, remarkable SO generation difference is observed between **(PS)** and **(actPS)**, which is highly important for cancer related activation of sensitizers in PDT applications.

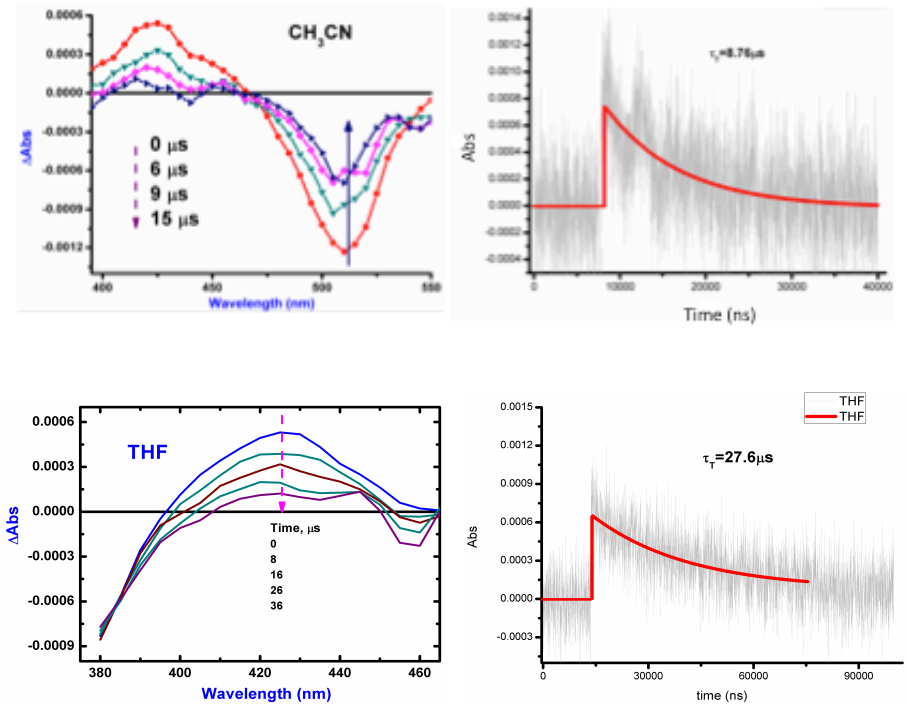

Figure 94. Left: The T_1-T_n transient absorption spectra of **(actPS)** in argon saturated THF and MeCN with laser excitation at 355 nm (the absorbance at 355 nm is 0.402). Right: The decay of triplet state T_1 of **(actPS)** at 425 nm in argon saturated THF and MeCN with laser excitation at 355 nm (the absorbance at 355 nm is 0.402). The triplet lifetimes are 8.7 µs (MeCN) and 27.6 µs (THF).

As another proof of singlet oxygen generation, we performed nanosecond transient absorption analysis of **(PS)** and **(actPS)** in MeCN and THF. Figure 94 shows the time evolution of the transient absorption (TA) spectra of **(actPS)**, which showed a positive peak with the maximum at 420 nm and a negative peak with the minimum at 510 nm (ground state bleaching) both in MeCN and THF. Both the shape and

position are very similar to the T_1-T_n absorption spectra of the well-known sensitizer iodo-Bodipy derivative.[223] This similarity indicates the positive signal of **(actPS)** is also T_1-T_n absorption. In the case of **(PS)**, additional peak at around 420 nm could not be detected. The following spectral behavior is also typical of the T_1-T_n absorption. The positive bands are separated from the ground state bleaching with well-defined isosbestic points. The triplet lifetime of **(actPS)** at 425 nm in argon saturated acetonitrile THF are 8.76 μs and 27.6 μs receptively, which are long enough for singlet oxygen generation reactions. In the case of **(PS)**, transient absorption peak at 425 nm cannot be detected in both solvents suggesting an "off" state for our sensitizer.

Table 8. The quantum yields for T_1 state formation of **(actPS)** in different solvents

Sample	**Solvent**	**Φ_T (quantum yield for T_1 state formation)***
actPS	Hexane-THF(5/1 v/v)	0.47
actPS	THF	0.14
actPS	acetonitrile	0.084

*Details are given in experimental part.

Triplet state quantum yield of **(actPS)** was calculated[224] by using a reference compound zinc phthalocyanine (ZnPc)[224] in different solvents (table 7). In a nonpolar solvent (Hexane-THF (5/1 v/v)) quantum yield was calculated as 0.47, when we moved to polar solvents triplet state quantum yield was decreased. This difference is due to the fact that the excited dimer undergoes very fast and effective intramolecular charge transfer (ICT) in polar solvents, which shutdowns ISC pathway, while ICT is almost negligible in nonpolar solvents.[223]

After obtaining promising results with SO generation experiments, we wanted to show that our sensitizer **(PS)** is preferentially reacting with GSH rather than other two major bio-thiols (Cys&Hcy) in intracellular conditions. To do so, we reacted **(PS)** with three bio-thiols. Thiols are introduced according to their intracellular concentrations (GSH: 5mM, Cys and Hcy: 25 μM). At the end of 12 hours, decrease in the absorption peak at 590 nm, which is the sign of thiol reaction, is only observed

with GSH (figure 95, left). No changes in absorption spectra were detected with other bio-thiols (figure 95, right).

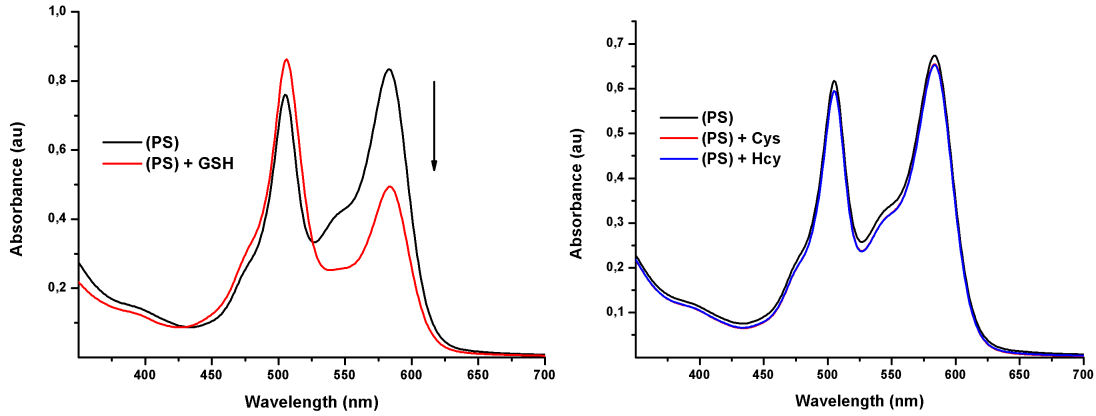

Figure 95. Comparison of electronic absorption spectrum of left: **(PS)** (30μM) and **(PS)** (30μM)+ GSH (5mM), right: **(PS)** (25μM) and **(PS)** (25μM) + Cys (25μM) & Hcy (25μM) in 90:10 (Hepes buffer, pH 7.2, 20mM : MeCN). Reaction time is 12 hours in all cases.

For further demonstration of the singlet oxygen generation capacity and photocytotoxicity of our dimers **(PS)** and **(actPS)**, we carried out a cell culture assay with HeLa cell lines. Experimental verification of photocytotoxicity was carried out as follows: varying concentrations of the dimeric dyes **(PS)** and **(actPS)** were incubated with HeLa cells within a standard culture medium at 37^{o}C in a humidified incubator containing 5% CO_2. Cells were irradiated with a green light-emitting diode (LED) source for 4 h, followed by 24 h of incubation in the dark. The control group was incubated in the dark under otherwise identical conditions. The cell viabilities were determined using a standard MTT assay (Figure 96). Even at very low concentrations of pre-activated **(actPS)**, a significant decrease of the cell viability was observed (red line in Figure 96, top). In the case of compound **(PS)**, cell death was also observed suggesting that **(PS)** can be activated intracellularly without any external stimuli (blue line in Figure 96, top). No statistically significant change was observed when the cells were kept in the dark, in the presence of the same concentration of the photosensitizers **(PS)** and **(actPS)** (Figure 96, bottom).

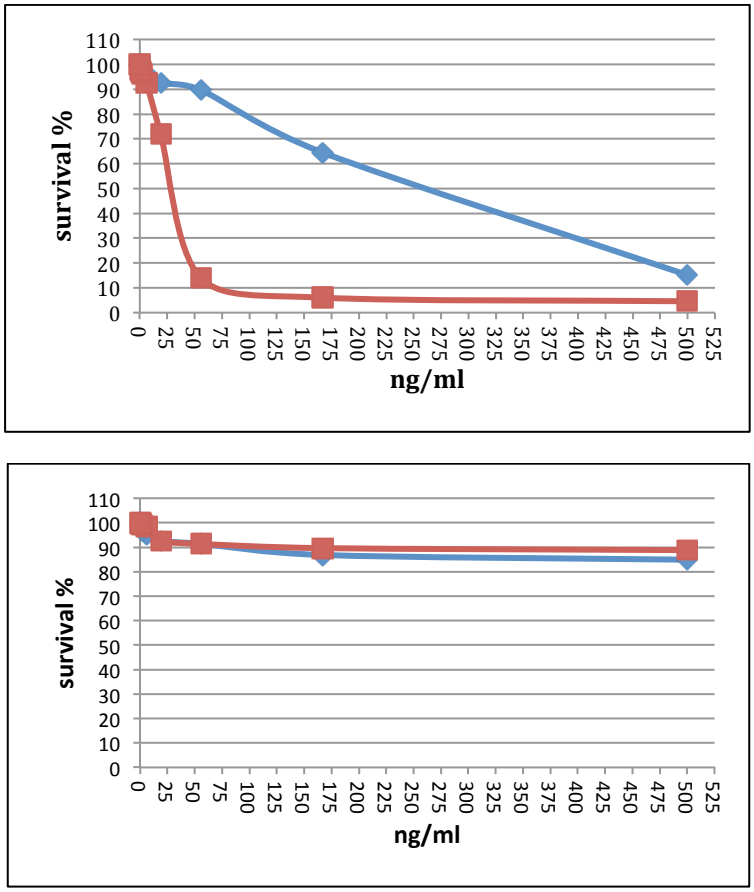

Figure 96. Photocytotoxicity of the sensitizer **(PS)** (blue) and **(actPS)** (red) as demonstrated by MTT assay. Cells were kept either in the dark (bottom), or under illumination with a green (520 nm) LED array (top).

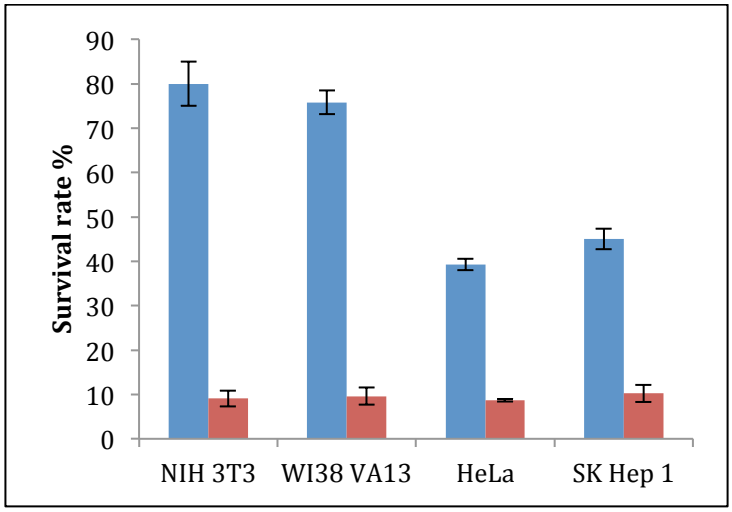

Figure 97. Cytotoxic effects of sample **(PS)** (blue), **(actPS)** (red). Cells were incubated with **(PS)**, **(actPS)** for 4 hr and irradiated with green LED. Cytotoxic effects were examined by MTT assay. Normal cell lines : NIH 3T3, WI38 VA13, cancer cell lines : HeLa, SK Hep 1.

We also conducted additional MTT assay tests to show that designed sensitizer **(PS)** can differentiate different concentrations of GSH in healthy (normal) and cancer cells (figure 97). Results were striking such that in the case of healthy cells (NIH 3T3 and WI38 VA13) survival rate was remained around 80%, however when **(PS)** is incubated with cancer cell lines (HeLa, SK Hep1) survival rate dropped to 40% after just 4 hours. These results clearly show that **(PS)** is able to differentiate intracellularly between healthy and cancer cells, which makes **(PS)** a good candidate as an activatable sensitizer. On the other hand, pre-activated **(actPS)** killed all healthy and cancer cells without any selectivity (survival rate is around 10% in all cell lines).

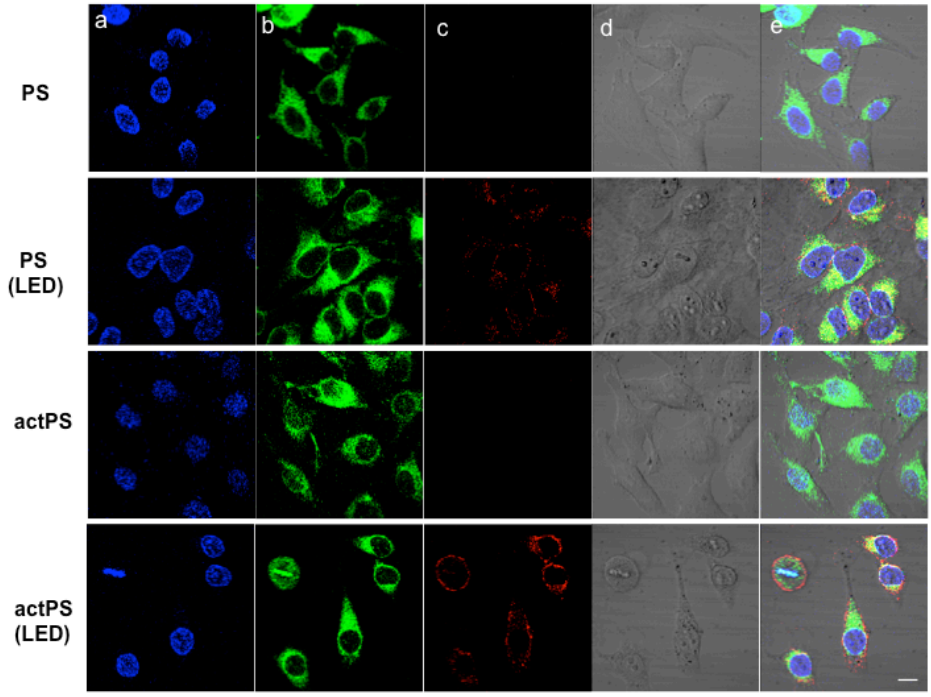

Figure 98. The HeLa cells were incubated with **(PS)**, **(actPS)** for 4 hrs. Cells were irradiated with green LED for 30 min and incubated another 3 hrs or kept under dark and stained with Annexin V-AF594 (apoptosis marker). Fluorescence images were acquired by confocal microscopy. For nucleus stain, 1 μg/ml DAPI costained for 30 min. (a) DAPI (ex. 405 nm, em. 430-455 nm), (b) **(PS)**, **(actPS)** (ex. 473 nm, em. 490-590 nm), (c) Annexin V-AF594 (ex. 559 nm, em. 575-675 nm), (d) DIC, (e) Merge. Scale bar: 10 μm

Confocal microscopy experiments were done in order to investigate the photocytotoxic effect and intracellular localization of **(PS)** and **(actPS)**. The HeLa cells were incubated with **(PS)** and **(actPS)** for 4 hours. After washing, the cells were

irradiated with green LED for 30 min and incubated for another 3 hours or kept under dark and stained with DAPI (nucleus stain, blue fluorescence) and Annexin V-AF594 (apoptosis marker, red fluorescence). Figure 98(b) clearly shows that both **(PS)** and **(actPS)** were located in the cytosol of the cells. Apoptotic cells were only detected upon irradiation (figure 98(c)). Confocal images proved once more that **(PS)** is getting activated intracellularly. Cells incubated with **(PS)** and **(actPS)** in the dark showed no Annexin V emission.

Finally, in order to elucidate the conjugation loss (activation) mechanism of **(PS)** in physiological medium (cell culture), we mimicked the **(PS)** – GSH reaction by reacting **(PS)** with excess mercaptoethanol (simple thiol analogue) in an aqueous solution 90:10 (HEPES buffer, pH 7.2, 20mM : MeCN) without adding any base. Color of the solution was changed with in a 20 minutes and mass spectrum (figure 99), which was acquired by taking an aliquot from a reaction mixture showed that predominantly Michael addition product was formed. Thus, it is possible to conclude that in cell culture medium, formation of Michael adduct is more favorable that blocks the conjugation and activates the charge transfer mediated ISC.

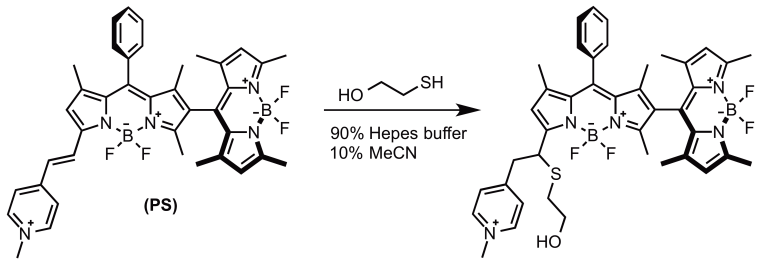

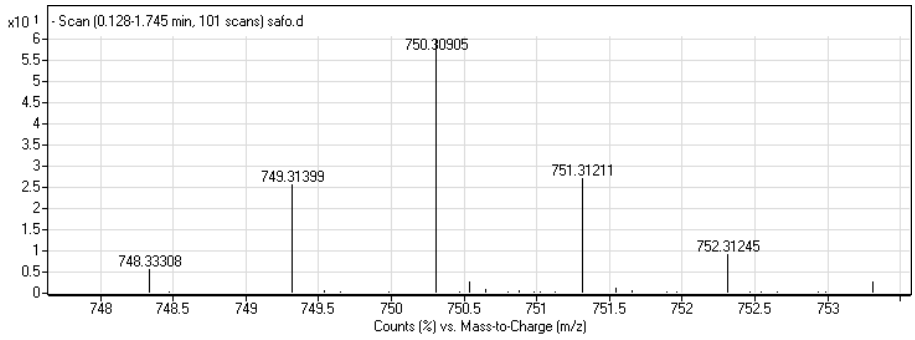

Figure 99. Michael addition of mercaptoethanol to compound **(PS)** in the absence of base in aqueous solution (90:10 (HEPES buffer, pH 7.2, 20mM : MeCN)). HR-MS spectrum of **(Michael adduct)** (Δ (ppm) = 31.8 ppm).

4.2.4. Experimental Details

General: All chemicals and solvents obtained from suppliers were used without further purification in the case of synthetic studies. During the photophysical characterizations, all solvents were dried and redistilled before use. Reactions were monitored by thin layer chromatography using Merck TLC Silica gel 60 F_{254}. Chromatography on silica gel was performed over Merck Silica gel 60 (particle size: 0.040-0.063 mm, 230-400 mesh ASTM).

^{1}H NMR and ^{13}C NMR spectra were recorded at room temperature on Bruker DPX-400 (operating at 400 MHz for ^{1}H NMR and 100 MHz for ^{13}C NMR) in $CDCl_3$ with tetramethylsilane (TMS) as internal standard. Coupling constants (*J values*) are given in Hz and chemical shifts are reported in parts per million (ppm). Splitting patterns are designated as s (singlet), d (doublet), t (triplet), q (quartet), m (multiplet), and p (pentet). Electronic absorption spectra in solution were acquired using a Varian Cary-100 spectrophotometer and a StellarNet BLACK Comet C-SR diode array miniature spectrophotometer connected to deuterium and halogen lamp by optical fiber using 1 cm matched quartz cuvettes at room temperature. Fluorescence spectra were determined on Varian Eclipse and Edinburgh Instruments FLS920 fluorospectrometer. Fluorescence lifetime of S_1 state was measured by time-correlated single photon counting method (Edinburgh FLS920 spectrophotometer) with excitation at 509 nm by a portable diode laser (150 ps FWHM) and emission was monitored at 520 nm. The lifetime values were computed by the F900 software. All spectra were corrected for the sensitivity of the photo-multiplier tube. Mass spectra were recorded on Agilent Technologies 6530 Accurate-Mass Q-TOF LC/MS.

Fluorescence Measurements: The fluorescence quantum yield (Φ_f) was computed by using;

$$\Phi_f = \Phi_f^0 \cdot \frac{F_s}{F_0} \cdot \frac{A_0}{A_s} \frac{n_s^2}{n_0^2}$$

in which F is the integrated fluorescence intensity, A is the absorbance at excitation wavelength, n is the refractive index of the solvent used, the subscript 0 stands for a

reference compound and s represents samples. A BODIPY monomer in CH_2Cl_2 was used as the reference (Φ_f=0.80).[121] The sample and reference solutions were prepared with the same absorbance (A_i) at the excitation wavelength (near 0.050 in a 1 cm quartz cell). All solutions were air saturated.

For **(actPS)**, Φ_f decreases with the increase of solvent polarity. The shape and emission maximum of fluorescence spectra is changed very slightly by solvent polarity. The decay curves are decreased with the increase of solvent polarity, indicating that the percentage of the short-lived emission component is increased with the increase of solvent polarity.

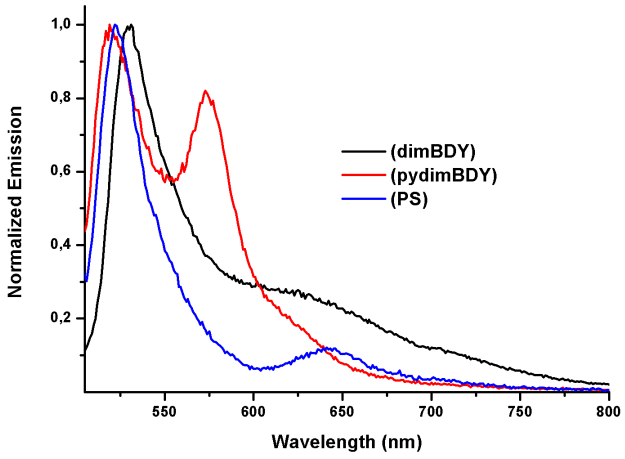

Figure 100. The normalized fluorescence emission spectra of **(dimBDY)**, **(pydimBDY)**, and **(PS)** in DCM.

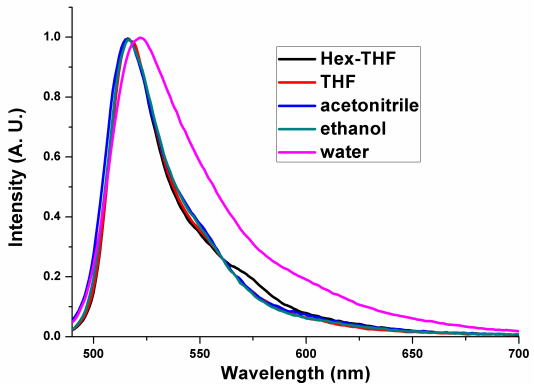

Figure 101. The normalized fluorescence emission spectra of **(actPS)** in different solvents with excitation at 418 nm (absorbance 0.090).

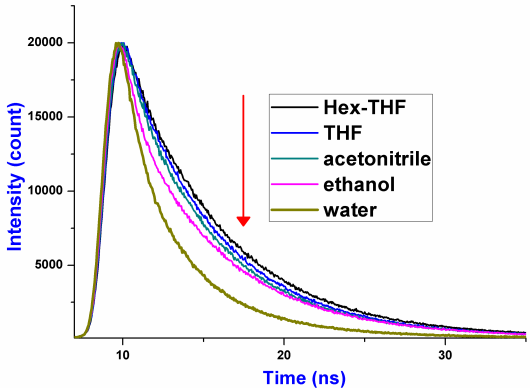

Figure 102. Fluorescence decay of **(actPS)** in EtOH with excitation at 509 nm diode laser (150 *ps*), the emission was monitored at 520 nm, the concentration of dyes is ca. 3.0 μM.

Table 9. Fluorescence quantum yield (F_f) and lifetime (t_f) of **(actPS)** in different solvents.

Sample	λ_{em}/nm	Φ_f	τ_f/ns	chi squared value	solvent
PS	517	0.088	1.60, 5.61(96%)	1.04	THF
actPS	516	0.19	0.92, 5.95(98%)	1.03	Hexane-THF(5:1 v/v)
actPS	517	0.15	1.35, 5.67(96%)	1.02	THF
actPS	517	0.089	0.93, 5.89(90%)	1.09	ethanol
actPS	516	0.073	2.11, 5.79(90%)	1.13	acetonitrile
actPS	522	0.035	0.77, 2.99(57%), 6.43(31%)	1.14	water

Excited Triplet State Studies: Nanosecond transient absorption measurements were obtained using LP920 (Edinburgh Instruments Ltd.). The excitation source was a Q-switched Nd/YAG laser (BRIO) of 4 ns full width at half maximum with third harmonic (355 nm) generation. The 355 nm beam was directed onto one side of a 1 cm square silica cell containing the sample (absorbance 0.40) after bubbling Ar gas during 20 min. The transient transmission variations were monitored at right angles to the excitation in a crossbeam arrangement using a 450W xenon flash lamp, a monochromator, a photomultiplier and a digitized oscilloscope interfaced with a

desktop computer. The power of the incident 355 nm laser pulse in the sample was about 5 mJ. The triplet quantum yield Φ_T was obtained by comparing the ΔA_T of the optically matched sample solution at peak maximum in a 1 cm cuvettes to that of the reference using the equation;[224]

$$\Phi_T = \Phi_T^{ZnPc} \cdot \frac{\Delta A_T}{\Delta A_T^{ZnPc}} \cdot \frac{\Delta \varepsilon_T^{ZnPc}}{\Delta \varepsilon_T}$$

Where the superscript represents the reference, ΔA_T is the absorbance of the triplet transient difference absorption spectrum at the selected wavelength, and ZnPc is the reference compound (Φ_T=0.65 in 1-propanol).[224] $\Delta\varepsilon_T$ is the triplet state molar absorption coefficient, which is obtained by equation given below;

$$\Delta\varepsilon_T = \varepsilon_S \frac{\Delta A_T}{\Delta A_S}$$

Where ΔA_S and ΔA_T are the absorbance change of the triplet transient difference absorption spectrum at the minimum of the bleaching band and the maximum of the positive band, respectively, and ε_S is the ground-state molar absorption coefficient at the UV-vis absorption band maximum. Both ΔA_S and ΔA_T were obtained from the triplet transient difference absorption spectra. **Excited triplet state quantum yield calculations were done in Xian-Fu Zhang group at Hebei Normal University of Science and Technology, Department of Chemistry, Qinhuangdao, China**

Singlet Oxygen Trap Experiments: In a typical procedure for the detection of singlet oxygen generation by using trap molecules, a photosensitizer (~1 μM) and a trap molecule (O.D ~ 1.0) were mixed in O_2 bubbled solvent. Initially several dark measurements were taken followed by irradiation of the mixture at absorption maximum of a sensitizer. Absorbance decreases of trap molecules (1,3-Diphenylisobenzofuran, 2,2'-(Anthracene-9,10-diylbis(methylene))dimalonic acid (ADMDA)) were monitored suggesting singlet oxygen generation in the presence of light and sensitizers. Irradiation of compounds was accomplished in Horiba Jobin-Yvon Time-Resolved Fluorometer, Fluorolog FL-1057 by using monochromatic

light system.

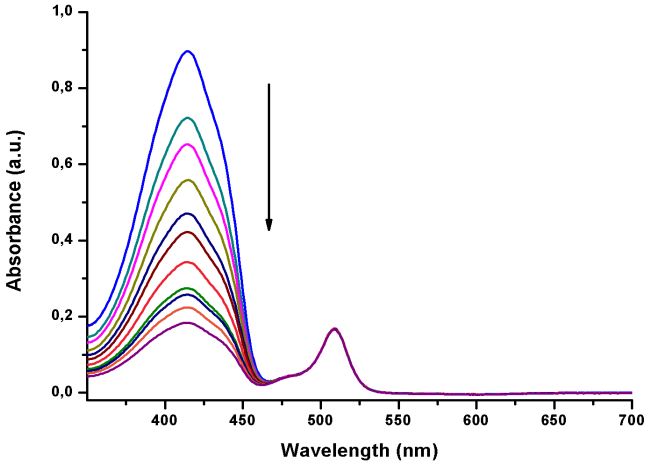

Figure 103. Decrease in absorbance of DPBF in DCM in the presence of **(dimBDY)** ($1X10^{-6}$ M). Excitation @508 nm.

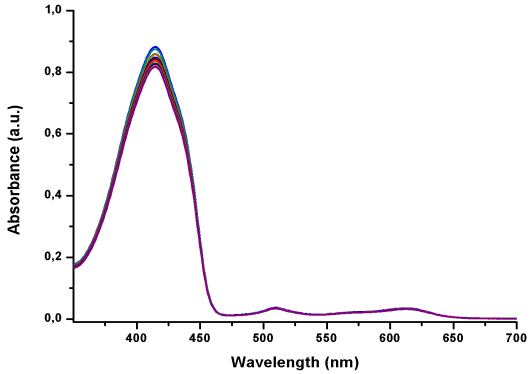

Figure 104. Decrease in absorbance of DPBF in DCM in the presence of **(PS)** ($1X10^{-6}$ M). Excitation @508 nm.

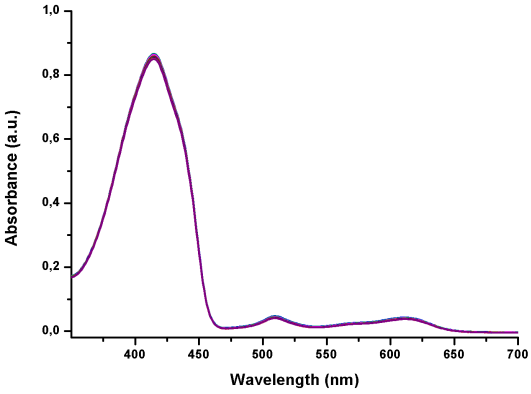

Figure 105. Decrease in absorbance of DPBF in DCM in the presence of **(PS)** ($1X10^{-6}$ M). Excitation @607 nm.

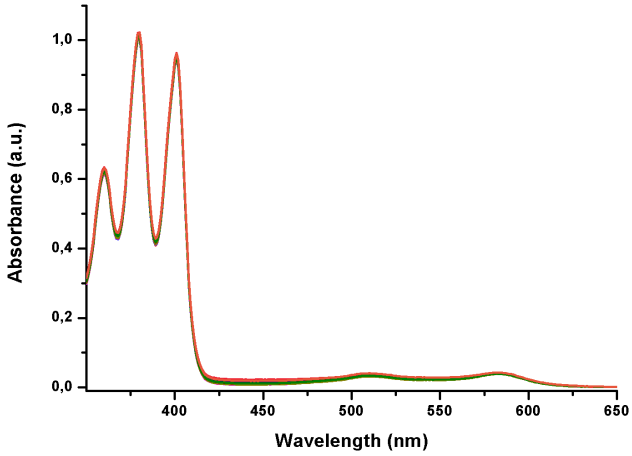

Figure 106. Decrease in absorbance of ADMDA in 90:10 (20 mM Hepes buffer:MeCN) in the presence of **(PS)** ($1X10^{-6}$ M). Excitation @513 nm.

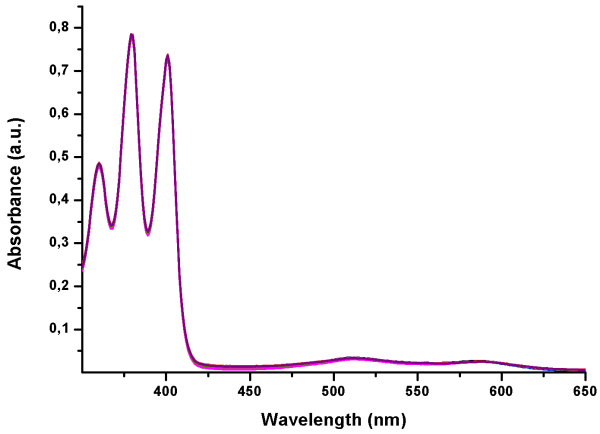

Figure 107. Decrease in absorbance of ADMDA in 90:10 (20 mM Hepes buffer:MeCN) in the presence of **(PS)** ($1X10^{-6}$ M). Excitation @590 nm.

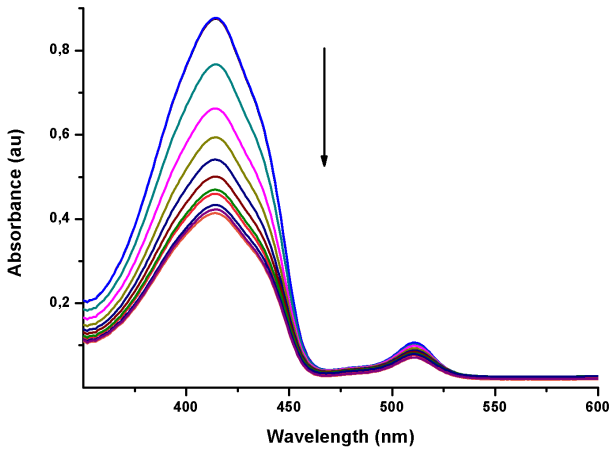

Figure 108. Decrease in absorbance of DPBF in DCM in the presence of **(actPS)** ($1X10^{-6}$ M). Excitation @511 nm.

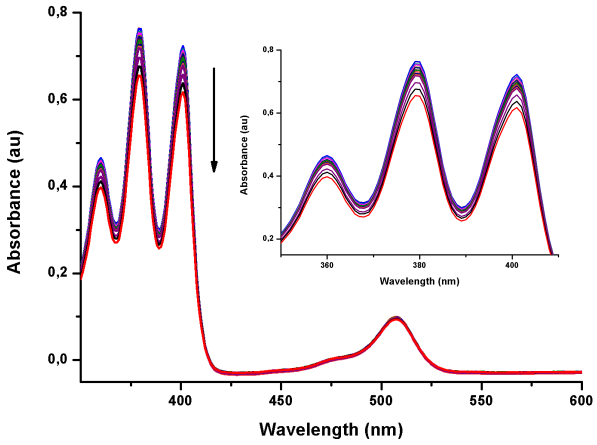

Figure 109. Decrease in absorbance of ADMDA in **90:10 (20 mM Hepes buffer:MeCN)** in the presence of **(5r) (1X10^{-6} M).** Excitation @508 nm.

Computational Details: Computational results are obtained using Density Functional Theory (DFT). Hybrid density functional calculations were carried out using Gaussian 09. Effective core potentials (ECP), where core electrons up to a given shell is treated with pseudopotentials and explicit treatment of the valence electrons employed, is used with Stevens-Basch-Krauss split valence, CEP-31G. Several other basis sets and various other functionals were previously tested, and this level of theory was confirmed to have reliable results compared with the experimental data. Spin contaminations were also checked and found to be negligible in all cases. Vibrational frequency calculations ensured that Hessian matrix does not contain any negative numbers and located geometries correspond to minimum points on the potential energy surface. **Computational studies were done in Dr. Yavuz Dede group at Gazi University, Department of Chemistry, Ankara, Turkey.**

Cell Culture Studies: In the case of MTT assay studies, cells were incubated with different concentrations of sensitizers for 4 hrs and irradiated with green LED or kept under dark. Cytotoxic effects were examined by MTT assay. NIH 3T3, WI38 VA13 were used as healthy cell lines and HeLa, SK Hep 1 were used as cancer cell lines. In the case of confocal microscopy imaging, HeLa cells were incubated with 5 μg/mL of each sensitizers for 3 hrs. After washing with DPBS, the cells were irradiated with green LED for 30 min or kept under dark and acquired the images by confocal microscopy. For nucleus staining, 1 g/mL DAPI was employed for 30 min. Annexin

V-AF594 was used as an apoptotic marker. Excitations were as follows; DAPI (ex. 405 nm, em. 430-455 nm), Annexin V-AF594 (ex. 559 nm, em. 575-675 nm) and **(PS)**, **(actPS)** (ex. 473 nm, em. 490-590 nm). **Cell studies were done in Dr. Yavuz Dede group at Gazi University, Department of Chemistry, Ankara, Turkey.**

Synthetic Details:

Synthesis of (BDY): To a 1 L round-bottomed flask containing 400 mL argon-degassed dichloroethane, 2,4-Dimethyl pyrrole (9.56 mmol, 0.924 g) and benzoyl chloride (4,34 mmol, 0.611 g) were added. The solution was refluxed for 1 day at 90^{o}C. After that, 5 mL of Et_3N and 5 mL of $BF_3.OEt_2$ were successively added and after 30 min, the reaction mixture was washed three times with water (3 x 100 mL), which was then extracted into the CH_2Cl_2 (3 x 100 mL) and dried over anhydrous Na_2SO_4. The solvent was evaporated and the residue was purified by silica gel column chromatography using (5 Hexane: 1 EtOAc) as the eluent. Red solid (0.631 g, 45%). ^{1}H NMR (400 MHz, $CDCl_3$): δ_H 7.51-7.49 (3H, m, Ar*H*), 7.30-7.28 (2H, m, Ar*H*), 6.00 (2H, s, Ar*H*), 2.58 (6H, s, CH_3), 1.39 (6H, s, CH_3). ^{13}C NMR (100 MHz, $CDCl_3$): δ_C 155.5, 143.3, 141.9, 135.1, 131.5, 129.1, 128.9, 127.9, 121.2, 14.6, 14.4 ppm. MS (TOF- ESI): m/z: Calcd: 324.1718, Found: 324.1795 $[M+H]^+$, Δ=23.6 ppm.

Synthesis of (fBDY): A mixture of DMF (2.5 mL) and $POCl_3$ (2.5 mL) was stirred under argon for 5 min in the ice bath. After warming solution up to room temperature, it was stirred for additional 30 min. **(BDY)** (1.24 mmol, 400.0 mg) in 60 mL dichloroethane was added to the solution and temperature raised to 50^{0}C. After stirring for 3 hrs, the mixture was cooled to room temperature and then poured in to iced cooled saturated aqueous solution of $NaHCO_3$ (150 mL). Then reaction mixture was stirred for 30 min after warming solution to rt. After 30 min. the mixture was washed with H_2O (2x100 mL). The product was extracted into the dichloromethane. Organic phase dried over Na_2SO_4. The solvent was evaporated and the residue was purified by silica gel column chromatography using CH_2Cl_2 as the eluent. Reddish-brown solid was obtained (388.0 mg, 89%). ^{1}H NMR (400 MHz, $CDCl_3$, 300K) : δ_H 10.02 (1H, s, C*H*O), 7.55-7.53 (3H, m, Ar*H*), 7.30-7.28 (2H, m,

Ar*H*), 6.12 (1H, s, Ar*H*), 2.83 (3H, s, C*H*$_3$), 2.62 (3H, s, C*H*$_3$), 1.66 (3H, s, C*H*$_3$), 1.43 (3H, s, C*H*$_3$). ^{13}C NMR (100 MHz, $CDCl_3$): δ_C 186.2, 161.7, 156.7, 147.6, 143.6, 142.9, 134.2, 129.9, 129.5, 127.7, 126.8, 124.0, 15.1, 14.8, 13.0, 11.6 ppm; MS (TOF- ESI): m/z: : Calcd: 352.1668, Found: 352.1710 $[M+H]^+$, Δ=11.9 ppm

Synthesis of (dimBDY): To a 500 mL round-bottomed flask containing 250 mL argon-degassed CH_2Cl_2, were 2,4-Dimethyl pyrrole (1.87 mmol, 178.3 mg) and **(fBDY)** (0.85 mmol, 0.300 g) were added. The solution was stirred under N_2 at room temperature for 1 day. After that, 1.5 mL of Et_3N and 2 mL of $BF_3.OEt_2$ were successively added and after 30 min, the reaction mixture was washed three times with water (3 x 100 mL), which was then extracted into the CH_2Cl_2 (3 x 100 mL) and dried over anhydrous Na_2SO_4. The solvent was evaporated and the residue was purified by silica gel column chromatography using CH_2Cl_2 as the eluent. Red solid (170.0 mg, 35%). ^{1}H NMR (400 MHz, $CDCl_3$): δ_H 7.52-7.49 (3H, m, Ar*H*), 7.32-7.30 (2H, m, Ar*H*), 6.10 (1H, s, Ar*H*), 6.00 (2H, s, Ar*H*), 2.61 (3H, s, C*H*$_3$), 2.54 (6H, s, C*H*$_3$), 2.43 (3H, s, C*H*$_3$), 1.73 (6H, s, C*H*$_3$), 1.43 (3H, s, C*H*$_3$), 1.23 (3H, s, C*H*$_3$). ^{13}C NMR (100 MHz, $CDCl_3$): δ_C 158.8, 155.7, 150.4, 145.6, 142.5, 142.4, 138.2, 134.5, 133.7, 132.5, 131.8, 130.9, 129.4, 127.8, 125.6, 122.5, 121.2, 46.6, 31.7, 22.7, 14.6, 14.1, 13.9, 12.7, 12.1 ppm. MS (TOF- ESI): m/z: Calcd: 568.2822, Found: 568.2698 $[M]^+$, Δ=21.8 ppm.

Synthesis of (pydimBDY): **(dimBDY)** (0.26 mmol, 150.0 mg) and 4-Pyridinecarboxaldehyde (0.79 mmol, 84.6 mg) were added to a 100 mL round-bottomed flask containing 50 mL benzene and to this solution piperidine (0.20 mL) and acetic acid (0.20 mL) were added. The mixture was heated under reflux by using a Dean Stark trap and reaction was monitored by TLC (CH_2Cl_2 : MeOH 95:5). When all the starting material had been consumed, the mixture was cooled to room temperature and solvent was evaporated. Water (100 mL) added to the residue and the product was extracted into the chloroform (3 x 100 mL). Organic phase dried over Na_2SO_4, evaporated and residue was purified by silica gel column chromatography using (CH_2Cl_2: MeOH 95:5) as the eluent. Purple solid was obtained (43.0 mg, 25%). ^{1}H NMR (400 MHz, $CDCl_3$): δ_H 8.69 (2H, s, Ar*H*), 7.92

(1H, d, *J* = 16.2, C*H*), 7.56-7.54 (5H, m, Ar*H*), 7.36-7.33 (2H, m, Ar*H*), 7.19 (1H, d, *J* = 16.2, C*H*), 6.73 (1H, s, Ar*H*), 6.02 (2H, s, Ar*H*), 2.55 (6H, s, CH_3), 2.50 (3H, s, CH_3), 1.74 (6H, s, CH_3), 1.50 (3H, s, CH_3), 1.28 (3H, s, CH_3). ^{13}C NMR (100 MHz, $CDCl_3$): δ_C 156.1, 153.9, 151.7, 148.4, 145.3, 143.8, 142.7, 142.2, 140.5, 134.2, 133.8, 132.7, 132.5, 131.6, 129.7, 129.5, 128.8, 127.7, 127.1, 124.4, 121.8, 121.4, 118.7, 25.1, 24.7, 14.7, 13.9, 13.1, 12.4. MS (TOF- ESI): m/z: Calcd: 658.3160, Found: 658.3164 $[M+H]^+$, Δ=0.6 ppm.

Synthesis of (PS): **(pydimBDY)** (0.061 mmol, 40.0 mg) and excess iodomethane (0.61 mmol, 87.0 mg) were dissolved in 5 mL ethyl acetate. The reaction mixture was stirred for 1 day at room temperature. When all the starting material had been consumed, solution was poured in to the cold diethyl ether. Precipitate was filtered and dried. Dark blue solid was obtained (36.7 mg, 75%). ^{1}H NMR (400 MHz, $CDCl_3$): δ_H 9.00 (2H, s, Ar*H*), 8.07 (2H, s, Ar*H*), 7.99 (1H, d, *J* = 16.2, C*H*), 7.56-7.54 (3H, m, Ar*H*), 7.49 (1H, d, *J* = 16.2, C*H*), 7.34-7.32 (2H, m, Ar*H*), 6.98 (1H, s, Ar*H*), 6.02 (2H, s, Ar*H*), 4.55 (3H, s, CH_3), 2.54 (6H, s, CH_3), 2.50 (3H, s, CH_3), 1.73 (6H, s, CH_3), 1.49 (3H, s, CH_3), 1.30 (3H, s, CH_3). ^{13}C NMR (100 MHz, $CDCl_3$): δ_C 156.1, 153.9, 151.7, 148.4, 145.3, 143.8, 142.7, 142.2, 140.5, 134.2, 133.8, 132.7, 132.5, 131.6, 129.7, 129.5, 128.8, 127.7, 127.1, 124.4, 121.8, 121.4, 118.7, 26.6, 25.1, 24.7, 14.7, 13.9, 13.1, 12.4. MS (TOF- ESI): m/z: Calcd: 672.3322, Found: 672.3236 $[M+H]^+$, Δ=12.8 ppm.

Synthesis of (actPS): Excess amount of mercaptoethanol (5.0 mmol) and catalytic amount of K_2CO_3 were added on to **(PS)** (0.024 mmol, 20 mg) in MeCN. Solution was stirred for 1 h. After that, the product was separated by silica gel column chromatography using (CH_2Cl_2: MeOH 90:10) as the eluent. Product was obtained as orange solid (17.3 mg, 90%). ^{1}H NMR (400 MHz, $CDCl_3$): δ_H 9.15 (2H, d, *J* = 6.6, Ar*H*), 7.99 (2H, d, *J* = 6.6, Ar*H*), 7.55-7.52 (3H, m, Ar*H*), 7.34-7.32 (2H, m, Ar*H*), 6.17 (1H, s, Ar*H*), 6.01 (2H, s, Ar*H*), 4.68 (3H, s, CH_3), 3.41 (4H, s, CH_2), 2.54 (6H, s, CH_3), 2.43 (3H, s, CH_3), 1.73 (6H, s, CH_3), 1.44 (3H, s, CH_3), 1.25 (3H, s, CH_3). ^{13}C NMR (100 MHz, $CDCl_3$): δ_C 161.5, 156.6, 156.0, 152.8, 145.4, 144.9, 143.9, 142.3, 140.4, 134.1, 132.9, 131.7, 129.6, 129.5, 128.2, 127.9, 126.7, 121.4, 120.8,

60.6, 49.0, 41.6, 34.7, 28.1, 14,7 14.6, 14.0, 12.9, 12.3. MS (TOF- ESI): m/z: Calcd: 674.3479, Found: 674.3511 $[M]^+$, Δ=4.9 ppm.

4.2.5. Conclusion

All in all, our work for the first time demonstrated an activatable heavy atom free BODIPY sensitizer as an efficient singlet oxygen generator for PDT applications. Modulations of excited state of the sensitizer through DS-TR and charge transfer configurations via cancer related input are the key for the selectivity of this therapeutic design. The electronic structure details are investigated with a combination of DFT, TD-DFT, and CASSCF/CASPT2 methods in order to validate our design principles. Chemical singlet oxygen trap experiments, transient absorption signals and detailed cell culture studies revealed that our sensitizer is getting activated only in the presence of high amount of GSH. Further investigations showed that we are able to differentiate healthy and cancer cells during the PDT action. This study is the first example of such differentiation.

CHAPTER 5

Axially Chiral BODIPY Derivatives

This work is partially described in the following publication:

Kolemen, S.; Cakmak, Y.; Kostereli, Z.; Akkaya, E. U. *Org. Lett.*, **2014**, *16*, 660.

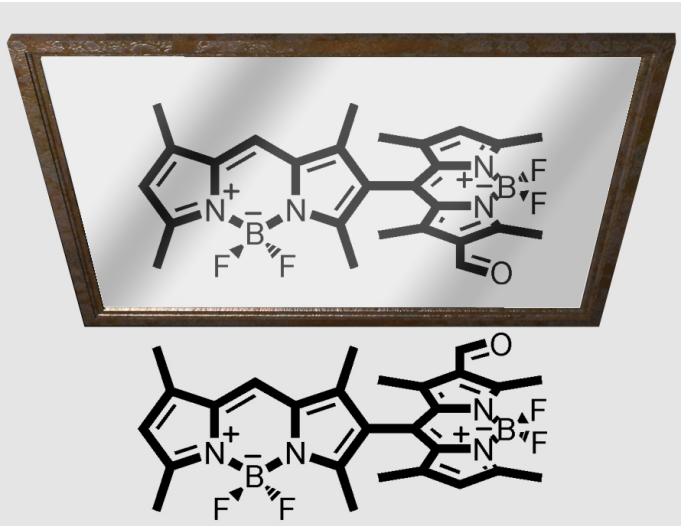

5.1. Objective

A dissymetrically substituted orthogonal BODIPY dimer and an orthogonal BODIPY trimer exist as two stable conformers, which are in fact atropisomeric enantiomers. The racemic mixture can be separated by HPLC using a chiral stationary phase. These enantiomeric derivatives hold great potential as chiral agents in asymmetric synthesis, fluorogenic/chromogenic sensing and biological applications.

5.2. Introduction

BODIPY dyes, once considered to be yet another class of fluorophores with applications limited to laser dyes and biological labeling, continue to flourish as their rich chemistry[24,29] unravels and a multitude of new potential applications keep pouring in.[54,85,225,226] It is remarkable that all positions on the parent boradiazaindacene ring including the boron bridge can be functionalized using straightforward procedures, resulting in a large family of chromophores with impressive diversity of photophysical and photochemical properties. Case in point, the parent compound has a very small intersystem crossing rate,[202] but on heavy atom functionalization of the 3,5-positions, BODIPY derivatives are transformed into effective singlet oxygen generators with a potential in photodynamic therapy.[123] In our attempts to find an alternative to heavy atom substitution protocol, we discovered that orthogonal BODIPY dimers have a remarkable excited state feature, which makes them very efficient in intersystem crossing.[227]

At that point, we recognized the potential of this compound for atropisomerism. Axial chirality in atropisomeric compounds is the result of non-planar arrangement of different groups on both sides of the chiral plane and enantiopure products can be isolated because of the restricted rotation of a single bond on that chiral axis. Most extensively used and studied atropisomeric molecules are bi-naphthyl derivatives with various applications.[146] On the other hand, chiral BODIPY derivatives were also previously reported in a few, chirality is generated by the tethered chiral prosthetic groups,[23,149,151,228-230] and in one recent example, by the asymmetrically substituted

boron bridge.[148] Nevertheless, chirality based on rotationally hindered BODIPY cores was not previously proposed or explored.

5.3. Results and Discussion

In the case of dimer **(3)**, there is still a symmetry plane, however a single dissymmetric substitution would remove that. To carry out that operation chemically, we formylated the dimer **(3)**. The reaction takes place essentially exclusively in the *meso*-functionalized ring. To further increase the complexity, we wanted to generate another BODIPY unit, where the formyl carbon would then supply the *meso*-carbon for the nascent third BODIPY ring. The latter reaction was carried out following highly established procedures for BODIPY synthesis while the pyrrole rings were supplied by 2,4-dimethylpyrrole (figure 110).

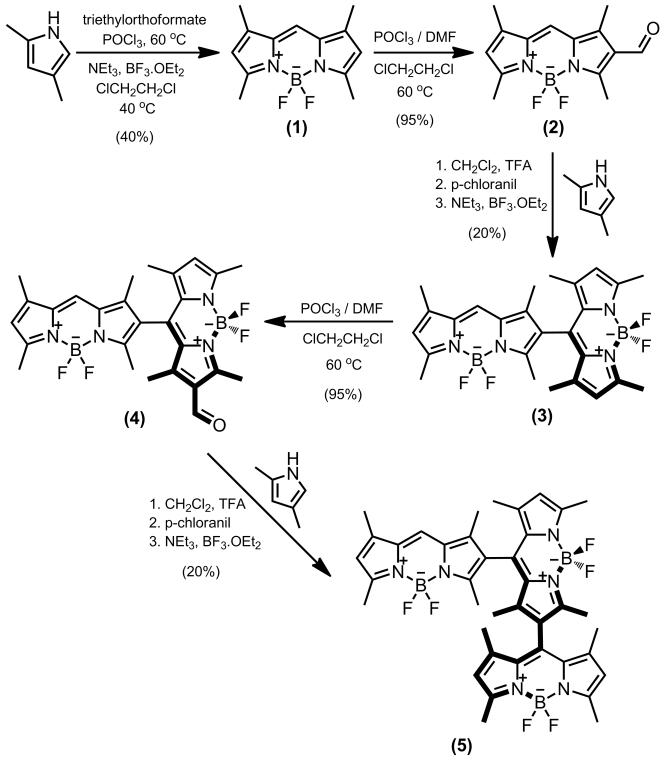

Figure 110. Synthesis of the atropisomeric BODIPY derivative **(4)** and **(5)**. As expected, **(4)** and **(5)** are produced as racemates. For both **(4)** and **(5)** (*R*) enantiomers are depicted. Copyright © 2014, American Chemical Society. Reprinted with permission from ref (150).

It should be also noted here that the formyl group is highly useful precursor for other functionalities. For both the formyl derivative **(4)** and the trimer **(5)**, purification (as

the racemic mixture) was through silica gel chromatography using dichloromethane / methanol (95% / 5%) and only dichloromethane as the eluent solvents, respectively. The racemates were then subjected to chiral HPLC purification. The conditions had to be carefully optimized to affect efficient separation of the both enantiomeric couples.

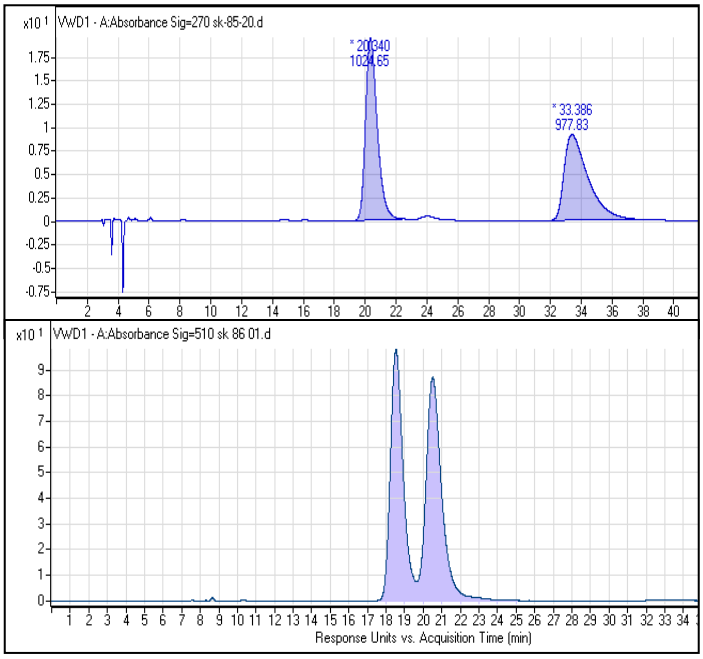

Figure 111. HPLC separation of compound **(4)** to **(4a)** (20.3 min) and **(4b)** (33.4 min), (95% / 5 %, heptane / IPA, detection @270 nm) (top), and compound **(5)** to **(5a)** (18.5 min) and **(5b)** (20.6 min), (98% / 2%, heptane / ethanol, detection @510 nm) (bottom). Copyright © 2014, American Chemical Society. Reprinted with permission from ref (150).

Analytical and preparative HPLC separations of racemic mixtures of compound **(4)** and **(5)** were performed using cellulose based Chiralcel-OD columns. For analytical and preparative resolutions, racemic mixture of the compounds were dissolved in an isocratic eluent of isopropyl alcohol or ethanol/heptane, filtered and injected to the column. HPLC chromatograms are shown in figure 111. Racemic compound **(4)** yielded easily resolvable peaks under these conditions, but the resolution for **(5)** was somewhat more challenging. Separated enantiomers were checked for their optical spectra (figure 112, 113, 114) / mass / NMR (see experimental details) and were found to be identical as expected.

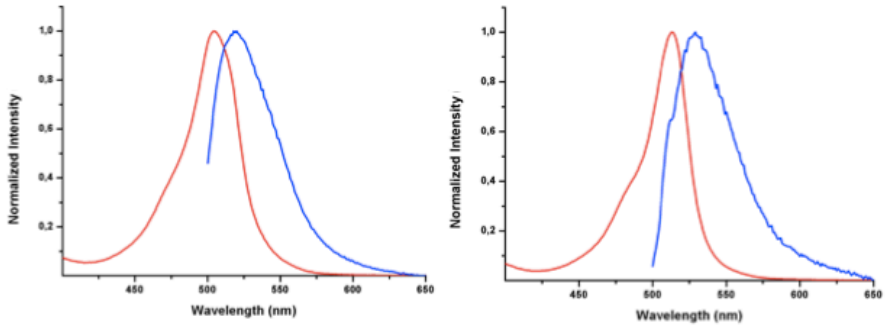

Figure 112. Electronic absorption (red) and emission (blue) spectra of **(4)** (left) and **(5)** (right). Ext @ 500 nm for **(4)** and 510 nm for **(5)**. Copyright © 2014, American Chemical Society. Reprinted with permission from ref (150).

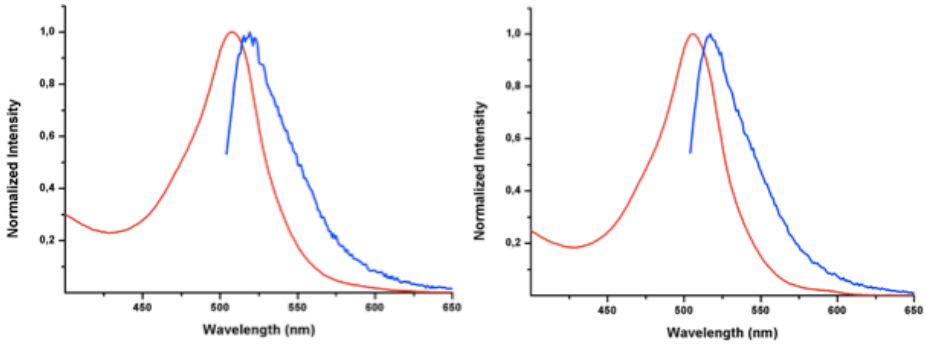

Figure 113. Electronic absorption (red) and emission (blue) spectra of **(4a)**(left) and **(4b)** (right). Ext @ 500 nm. Copyright © 2014, American Chemical Society. Reprinted with permission from ref (150).

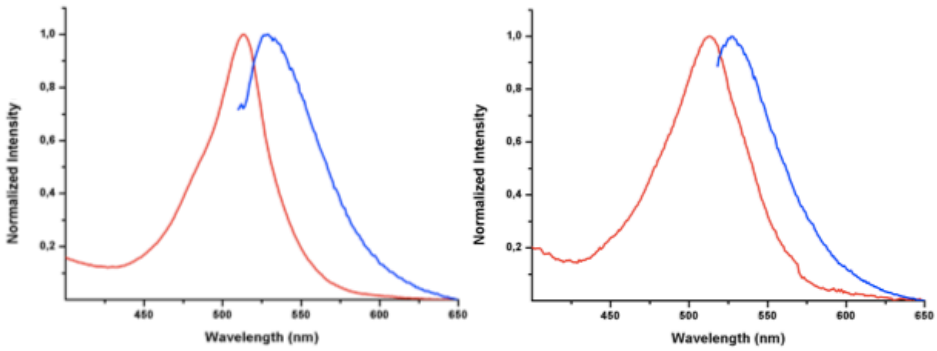

Figure 114. Electronic absorption (red) and emission (blue) spectra of **(5a)** (left) and **(5b)** (right). Ext @ 510 nm. Copyright © 2014, American Chemical Society. Reprinted with permission from ref (150).

Circular dichroism data (Figures 115 and 116) clearly demonstrate successful separation of the two enantiomers. While the racemic mixture **(4)** resulted in an

essentially flat line indicative of achirality, enantiomer **(4a)** and the enantiomer **(4b)** show the mirror image spectra. Same is true for **(5)**, **(5a)** and **(5b)**. The peaks on the visible region are related to sharp S_0-S_1 transition of the BODIPY core.

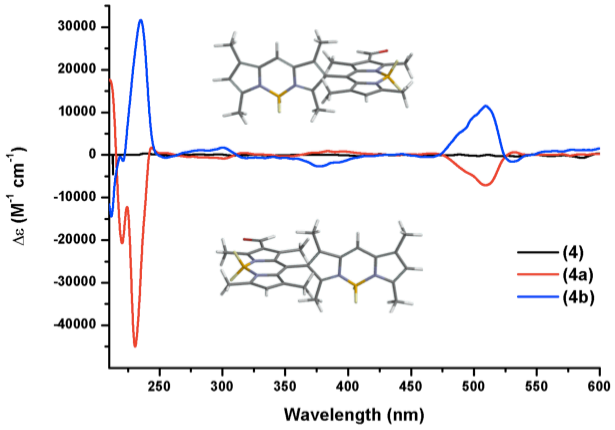

Figure 115. Circular dichroism spectra of racemic mixture **(4)** and the two enantiomers following resolution using Chiralcel-OD columns via preparative HPLC. The structures shown on the figure are the energy-minimized structures (employing the MM method as implemented in Spartan 08) and the assignment is arbitrary. Copyright © 2014, American Chemical Society. Reprinted with permission from ref (150).

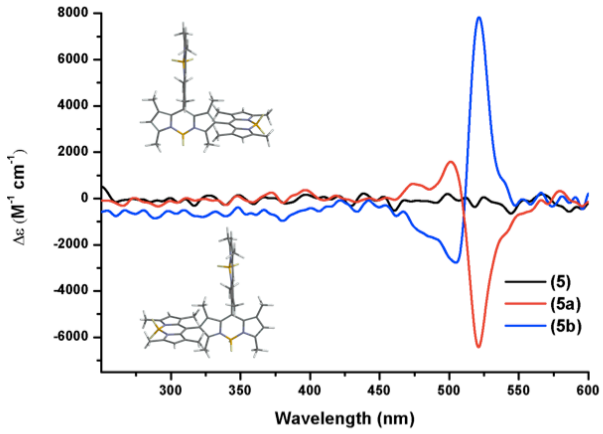

Figure 116. Circular dichroism spectra of racemic mixture **(5)** and the two enantiomers following resolution using Chiralcel-OD columns via preparative HPLC. The structures shown on the figure are the energy-minimized (employing the MM method as implemented in Spartan 08) structures and the assignment is arbitrary. Copyright © 2014, American Chemical Society. Reprinted with permission from ref (150).

The compound **(4)** has a major absorption band in the visible region (λ_{max}=505 nm, ε = 78000 $M^{-1}cm^{-1}$). Only weak fluorescence emission (quantum yield < 1%) is observed with a peak at 520 nm. The trimer on the other hand, has a stronger

absorption at 514 nm (ε= 162000 $M^{-1}cm^{-1}$). This compound also has a low quantum yield of emission (quantum yield < 1%) (Figure 117, Table 9).

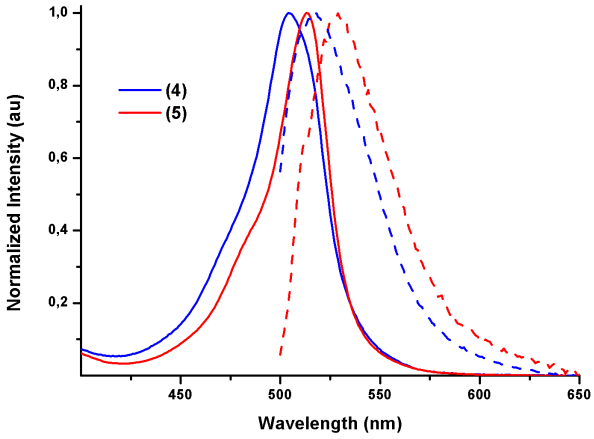

Figure 117. Electronic absorption (solid line) and emission (dashed line) spectra of compounds **(4)** and **(5)**. Copyright © 2014, American Chemical Society. Reprinted with permission from ref (150).

Table 10. Photophysical characterization of compound **(4)** and **(5)**.

dye	λ_{abs}[a]/nm	$\varepsilon_{max}/M^{-1}\ cm^{-1}$	λ_{ems}[a]/nm	Φ_f[b]	τ_f[a]/ns
4	505	78000	520	0.0078	3.14
5	514	162000	528	0.0075	3.72

[a] Data acquired in CH_2Cl_2. [b] in reference to fluorescein in 0.1 M NaOH solution, excited at 495 nm.

5.4. Experimental Details

General: ^1H NMR and ^{13}C NMR spectra were recorded on Bruker DPX-400 (operating at 400 MHz for ^1H NMR and 100 MHz for ^{13}C NMR) in $CDCl_3$ with tetramethylsilane (TMS) as internal standard. All spectra were recorded at 25°C and coupling constants (*J values*) are given in *Hz*. Chemical shifts were reported in parts per million (ppm). Absorption spectra were performed by using a Varian Cary-100. Fluorescence measurements were conducted on a Varian Eclipse Spectrofluometer. The fluorescence decay measurements were carried out with the Horiba Jobin-Yvon

Time-Resolved Fluorometer, Fluorolog FL-1057. The instrument response function was measured with an aqueous ludox solution. Mass spectra were recorded with Agilent Technologies 6224 TOF LC/MS and 6530 Accurate Mass Q-TOF LC/MS. High performance liquid chromatography (HPLC) separations were performed by using Agilent Technologies HPLC-1200 Series with multi-wavelength detector (MWD) and Agilent Technologies Preparative HPLC-1200 Series with diode array detector (DAD). Circular dichroism (CD) measurements were conducted with Jasco J-815 CD Spectrometer. Reactions were monitored by thin layer chromatography using Merck TLC Silica gel 60 F_{254}. Silica gel column chromatography was performed over Merck Silica gel 60 (particle size: 0.040-0.063 mm, 230-400 mesh ASTM). Compounds (**1**), (**2**), and (**3**) were synthesized according to our pervious study.[121] All other reagents and solvents were purchased from suppliers and used without further purification.

HPLC Separation: Analytical and preparative HPLC separation of racemic mixtures of compound **(4)** and **(5)** were performed on Agilent Technologies HPLC-1200 Series with multi-wavelength detector (MWD) and Agilent Technologies Preparative HPLC-1200 Series with diode array detector (DAD). In both cases, cellulose based Chiralcel-OD columns were used.

For analytical resolution, racemic mixture of compound **(4)** was dissolved in an isocratic eluent of (5%/95% isopropyl alcohol/heptane), filtered and injected to the column. The flow rate was 1 mL/min and UV detection wavelength was 270 nm. This separation was performed on a 250 x 4.6 mm column. One injection was done (10µL). In the case of preparative resolution of **(4)**, again it was dissolved in an isocratic eluent of (5%/95% isopropyl alcohol/hexane), filtered and injected to the column. The flow rate was adjusted as 12 mL/min and UV detection wavelength was 270 nm. This separation was performed on a 250 x 10 mm column. In preparative separation 5 injections were done (5 mg/injections, 2000µL/injections), in order to get reasonable amounts of **(4a)** (12.0 mg) and **(4b)** (8.0 mg).

For analytical resolution, racemic mixture of compound **(5)** was dissolved in an isocratic eluent of (2%/98% ethanol/heptane), filtered and injected to the column.

The flow rate was 0.8 mL/min and UV detection wavelength was 510 nm. This separation was performed on a 250 x 4.6 mm column. One injection was done (10µL). In the case of preparative resolution of **(5)**, again it was dissolved in an isocratic eluent of (2%/98% ethanol/hexane), filtered and injected to the column. The flow rate was adjusted as 8 mL/min and UV detection wavelength was 510 nm. This separation was performed on a 250 x 10 mm column. In preparative separation 5 injections were done (2 mg/injections, 2000µL/injections), in order to get reasonable amounts of **(5a)** (4.3 mg) and **(5b)** (2.6 mg).

Synthetic Details:

Synthesis of (4): 1 mL of DMF and 1 mL of $POCl_3$ was stirred in an ice bath for 5 min under argon. Then warmed to room temperature and waited for 30 minutes. To this mixture compound (**3)** (200 mg, 0.405 mmol) was added in dichloroethane (60 mL). The temperature was raised to 50^0C and stirred for 2 hours. The reaction medium was cooled and poured into 150 mL of ice cooled $NaHCO_3$ solution slowly. After that it was stirred for further 30 min, then washed with water 3 times. The organic layers was combined and dried over Na_2SO_4 and evaporated to dryness. The compound has been purified by column chromatography by using DCM / MeOH (95%/5%) as an eluent and the compound has been got pure as reddish solid (95 %). ^{1}H NMR (400 MHz, $CDCl_3$): δH 10.05 (1H, s, C*H*O), 7.21 (1H, s, Ar*H*), 6.20 (1H, d, *J*= 3.64 Hz, Ar*H*), 2.83 (3H, s, CH_3), 2.62 (3H, s, CH_3), 2.60 (3H, s, CH_3), 2.41 (3H, s, CH_3), 2.35 (3H, s, CH_3), 2.12 (3H, s, CH_3), 2.02 (3H, s, CH_3), 1.75 (3H, s, CH_3); ^{13}C NMR (100 MHz, $CDCl_3$): δC 185.8, 161.9, 161.6, 156.7, 150.1, 146.6, 144.5, 142.2, 135.8, 135.6, 135.2, 134.7, 132.1, 129.9, 126.4, 124.2, 122.9, 121.0, 120.8, 15.1, 14.9, 14.4, 13.1, 12.6, 11.2, 10.8, 9.8 ppm. MS HRMS (TOF-ESI): *m/z* calcd: 522.239; found: 522.237 $[M-H]^-$, Δ = 3.8 ppm. Retention time of **(4a)** and **(4b)** are 20.3 min and 33.4 min respectively.

*^{1}H NMR and HRMS results for compound **(4a)***: (400 MHz, $CDCl_3$): δH 10.05 (1H, s, C*H*O), 7.20 (1H, s, Ar*H*), 6.18 (1H, d, *J*= 3.72 Hz, Ar*H*), 2.81 (3H, s, CH_3), 2.62 (3H, s, CH_3), 2.58 (3H, s, CH_3), 2.40 (3H, s, CH_3), 2.32 (3H, s, CH_3), 2.12 (3H, s, CH_3), 2.02 (3H, s, CH_3), 1.75 (3H, s, CH_3). MS HRMS (TOF-ESI): *m/z* calcd:

522.239; found: 522.236 $[M+H]^-$, Δ = 5.7 ppm.

*^{1}H NMR and HRMS results for compound **(4b)***: (400 MHz, $CDCl_3$): δH 10.03 (1H, s, C*H*O), 7.19 (1H, s, Ar*H*), 6.20 (1H, d, *J*= 3.48 Hz, Ar*H*), 2.80 (3H, s, CH_3), 2.62 (3H, s, CH_3), 2.58 (3H, s, CH_3), 2.39 (3H, s, CH_3), 2.31 (3H, s, CH_3), 2.11 (3H, s, CH_3), 2.02 (3H, s, CH_3), 1.75 (3H, s, CH_3). MS HRMS (TOF-ESI): *m/z* calcd: 522.239; found: 522.247 $[M+H]^-$, Δ = 15.3 ppm.

*CD result for compound **(4a)***: [λ, nm] {Δε, M^{-1} cm^{-1}}: [510] {-7298.56}, [378] {785.52}, [300] {-821.75}, [235] {-44751.24}.

*CD result for compound **(4b)***: [λ, nm] {Δε, M^{-1} cm^{-1}}: [510] {11592.04}, [378] {-2686.81}, [300] {2039.80}, [235] {31716.42}.

Synthesis of (5): In N_2 bubbled 250 mL dichloromethane, 2,4-Dimethylpyrrole (145 μL, 1.408 mmol) and **(4)** (336.6 mg, 0.646 mmol) were mixed. 2 drops of trifluoroacetic acid has been added. The reaction mixture stirred at room temperature overnight. Then p-chloranil (159 mg, 0.646 mmol) was added to the reaction. After stirring 1 hour at room temperature, NEt_3 (5 mL) and $BF_3.OEt_2$ (5 mL) were added and stirred again for additional 1 hour. The reaction was finished by extracting with water (3x250 mL). Column chromatography with CH_2Cl_2 yielded the pure product (20 %). ^{1}H NMR (400 MHz, $CDCl_3$): δH 7.18 (1H, s, Ar*H*), 6.18 (1H, s, Ar*H*), 6.12 (1H, s, Ar*H*), 6.01 (2H, d, *J*= 12.04 Hz, Ar*H*), 2.53 (3H, s, CH_3), 2.52 (3H, s, CH_3), 2.51 (6H, s, CH_3), 2.41 (3H, s, CH_3), 2.38 (3H, s, CH_3), 2.25 (3H, s, CH_3), 2.13 (3H, s, CH_3), 1.75 (3H, s, CH_3), 1.71 (6H, s, CH_3), 1.53 (3H, s, CH_3); ^{13}C NMR (100 MHz, $CDCl_3$): δC 161.4, 159.0, 156.1, 155.5, 150.9, 150.3, 144.8, 144.2, 142.5, 142.0, 137.6, 135.6, 135.1, 134.4, 133.5, 133.0, 132.1, 131.9, 131.7, 131.0, 130.8, 128.8, 125.7, 123.4, 122.6, 121.5, 121.1, 120.8, 120.7, 31.9, 29.7, 22.7, 15.0, 14.8, 14.6, 14.1, 13.8, 13.7, 12.7, 12.5, 11.5, 11.3, 9.7 ppm; MS HRMS (TOF-ESI): *m/z* calcd: 740.358; found: 740.3585 $[M-H]^-$, Δ = 0.68 ppm. Retention time of **(5a)** and **(5b)** are 18.5 min and 20.6 min respectively.

*^{1}H NMR and HRMS results for compound **(5a)***: (400 MHz, $CDCl_3$): δH 7.19 (1H, s,

Ar*H*), 6.18 (1H, s, Ar*H*), 6.11 (1H, s, Ar*H*), 6.02 (2H, d, *J*= 12.04 Hz, Ar*H*), 2.55 (3H, s, CH_3), 2.53 (3H, s, CH_3), 2.51 (6H, s, CH_3), 2.41 (3H, s, CH_3), 2.38 (3H, s, CH_3), 2.25 (3H, s, CH_3), 2.11 (3H, s, CH_3), 1.74 (3H, s, CH_3), 1.71 (6H, s, CH_3), 1.54 (3H, s, CH_3); MS HRMS (TOF-ESI): *m/z* calcd: 740.358; found: 740.366 $[M+H]^-$, Δ = 10.8 ppm.

^{1}H NMR and HRMS results for compound ***(5b)***: (400 MHz, $CDCl_3$): δH 7.18 (1H, s, Ar*H*), 6.19 (1H, s, Ar*H*), 6.12 (1H, s, Ar*H*), 6.03 (2H, d, *J*= 12.04 Hz, Ar*H*), 2.56 (3H, s, CH_3), 2.52 (3H, s, CH_3), 2.51 (6H, s, CH_3), 2.41 (3H, s, CH_3), 2.38 (3H, s, CH_3), 2.25 (3H, s, CH_3), 2.13 (3H, s, CH_3), 1.75 (3H, s, CH_3), 1.71 (6H, s, CH_3), 1.53 (3H, s, CH_3); MS HRMS (TOF-ESI): *m/z* calcd: 740.358; found: 740.367 $[M+H]^-$, Δ = 12.2 ppm.

CD result for compound ***(5a)***: [λ, nm] {Δε, M^{-1} cm^{-1}}: [521] {-6402.25}, [505] {1617.65}, [474] {674.13}.

CD result for compound ***(5b)***: [λ, nm] {Δε, M^{-1} cm^{-1}}: [521] {7900.20}, [505] {-2768.80}, [474] {-1212.90}.

5.5. Conclusion

In summary, we present the first example of atropisomeric BODIPY derivatives with persistent chirality due to multiple methyl group clashes. The orthogonally linked BODIPY compounds have been demonstrated to have interesting photophysical properties but now, we show that they can be isolated as atropisomeric chiral compounds. Their large extinction coefficients and large anisotropy factors (g> $5x10^{-3}$) would mean that similar compounds may find practical applications as chiroptical fluorogenic/chromogenic sensors, and as highly selective chiral photosensitizers in a therapeutic context, among other potential fields.

CHAPTER 6

Controlled Singlet Oxygen Generation on Gold Nanorods: Advancing Photodynamic Therapy

Kolemen, S.; Ozdemir, T.; Karatas, T.; Akkaya, E. U

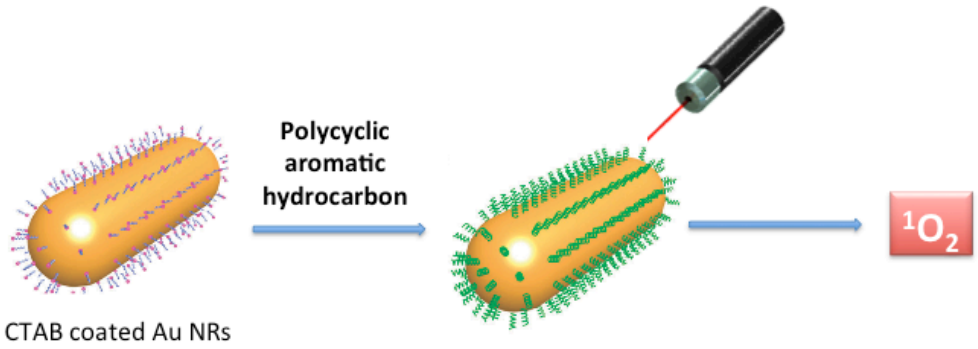

6.1. Objective

In this project, our primary goal is to deliver the principal cytotoxic agent of photodynamic therapy, singlet oxygen, directly by thermal decomposition of otherwise stable endoperoxides. To that end, endoperoxide derivative is conjugated to the gold nanorod. Irradiation of gold nanorod with near-IR laser light causes temperature increase on the surface of nanoparticle, which triggers the thermal decomposition of the endoperoxide that yield singlet and molecular oxygen. This project, which is a radical rewriting of the photodynamic therapy concept, is poised to revamp photodynamic therapy, offering potential solutions for major problems (light penetration depth and hypoxia) hitherto blocking broader clinical application.

6.2. Introduction

Photodynamic therapy is a useful methodology for the treatment of various cancers.[112] However, its applicability is severely limited by two factors, the requirement for external excitation of the photosensitizer, and hypoxia (low oxygen concentration) in tumor tissues. Mammalian tissue is transparent only in the optimal spectral region, the so-called therapeutic window (600-950 nm). This means that a photosensitizer in living organism will be excited efficiently only if it has absorption maximum at this interval. Most tumor tissues and cells, as a result rapid outgrowth of their blood supply, are hypoxic. The other major requirement is the presence of dissolved molecular oxygen for sensitization. This reduced oxygen concentration not only inhibits efficiency of photodynamic therapy, but also reduces responsiveness of the cancer cells to traditional chemotherapy, allowing further progression of the cancer. Thus, it is highly desired to design PDT agents, which can produce both molecular and cytotoxic singlet oxygen upon near-IR irradiation. Traditional PDT sensitizers are only capable of generating singlet after series of photophysical steps including ISC. It is also possible to deliver singlet oxygen chemically at sufficient concentrations to induce apoptotic and/or necrotic cell deaths.

It is very well known that the chemical reactivity of singlet oxygen is different than the triplet ground state oxygen. It can undergo addition reactions to form

endoperoxides.[152] Most endoperoxides (EPOs) are not stable; they thermally (or photochemically) decompose, in some cases generating singlet oxygen. Many polycyclic aromatic compounds can trap singlet oxygen, and some of these resulting endoperoxides exhibit an interesting feature, which is the release of oxygen in the excited state on warming. Most of these endoperoxides themselves are prepared by photosensitized oxygenation, which involves [4+2] cycloaddition of $^1O_2$. In the dissociation of EPOs, in principle there are two primary pathways, cycloreversion, leading to the substrate and O_2 (in either triplet or singlet state) and homolytic cleavage of the peroxide bond, which is often accompanied by rearrangements or decomposition to hydroxyketones or quinones.

Gold nanoparticles attracted considerable attention in recent years mostly due to their plasmonic properties.[165] Surface plasmon confers absorption properties to the nanoparticles depending on their size, state of aggregation, and surrounding dielectric medium. Absorption of light causes heating, and this was once considered an undesirable property, a nuisance, which has to be minimized in applications such as imaging. Within the last decade however, this nanoscale heating proved to be valuable in the therapeutic context.[182] Typical gold nanospheres have absorption bands in the visible region of the spectrum, but gold nanorods (GNRs) may have strong absorptions in the therapeutically relevant red to near IR region, depending on their aspect ratios. Since the absorption peak can be pushed into near IR in the case of gold nanorods, plasmonic heating can be obtained by relatively more penetrating red-to-near IR light sources. Cell death in tissues heated to 41-47^{o}C displays signs of apoptosis, but at temperatures above 50^{o}C, it is mostly due to necrosis.[182] While hyperthermia induced in this way is interesting and getting the attention that it deserves in many research groups worldwide, the therapeutic potential *in vivo* and in clinical studies needs to be further evaluated.

Once appropriate EPOs are synthesized and characterized chemically, the delivery of the singlet oxygen to the targeted tumor region can be reduced to a problem of safe systemic transport of an endoperoxide, followed by decomposition (cycloreversion) at the target region. However, the temperature inside the human body is very well

regulated by homeostasis, it wouldn't be reasonable to expect significant temperature differences in any part of the body to yield differential decomposition rates. At that point, gold nanorods are quite useful to achieve this goal, as they have strong and tunable absorption peaks in their absorption spectra, and this phenomenon is being exploited to generate localized heating in the vicinity of these particles. Combination of gold nanoparticles with aromatic endoperoxides has not been utilized for PDT action until very recently. During the preparation of this thesis Branda *et al.* reported an anthracene endoperoxide derivative, which is conjugated to gold nanospheres (organic solvent soluble) for the purpose of singlet oxygen generation on gold nanoparticles. In their design excitation of gold nanospheres at 500 nm increase the temperature on nanoparticles that triggers the thermal decomposition of conjugated anthracene derivative to yield singlet oxygen. However, near-IR irradiation and water dispersion of the conjugate, which are highly significant for therapeutic applications, could not be introduced.

In this study, we are introducing PEGlyated anthracene endoperoxide derivative, which is conjugated to gold nanorods with SPR peak around 800 nm in order to realize the control singlet and molecular oxygen generation by irradiating the nanorods with near-IR laser (figure 118). Once laser irradiation is applied on to the nanorod-EPO conjugate, local temperature increases on the nanorods trigger the thermal decomposition of EPO and produce both singlet (cytotoxic) and molecular oxygen.

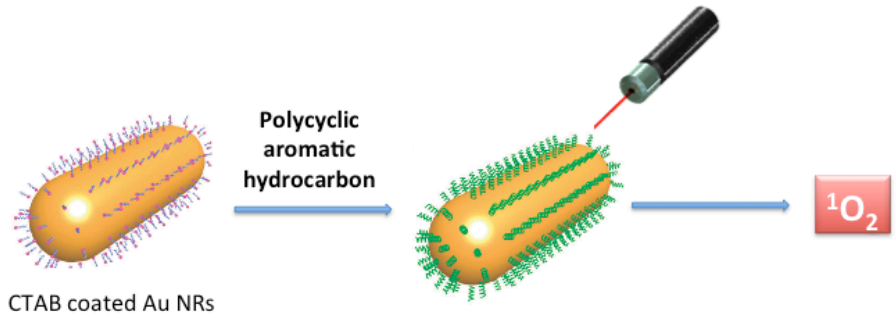

Figure 118. Therapeutic design.

6.3. Results and Discussion

The shape of gold nanoparticles has critical role in governing their optical and chemical properties. Dramatic changes can be seen in many characteristics of gold nanocrystals when you shift from spherical to nonspherical nanoparticles. Among the nonspherical gold NPs, gold nanorods have attracted much interest. They have been widely used in optical devices, biochemical sensors and nanomedicine applications. Most featured property of Au nanorods is their tunable and intense localized surface plasmon resonance (LSPR) bands at visible and near-IR region of the electromagnetic spectrum. Also, GNRs have the ability of converting absorbed light to heat (photothermal conversion). In addition to that there are many well-established growth methods for this rod-like NPs, which all of them offering high yields, improved aspect ratios, shape and uniformity control. With all these advantages, we thought that Au nanorods might be a good candidate for our design. Our first attempt was to synthesize GNRs with LSPR peak at longer wavelengths (around 800 nm). Various studies in literature show that short rods (~40 nm) with aspect ratio of 4 satisfy our needs.[173] We synthesized the GNRs with seed-mediated growth technique according to El-Sayed procedure.[173] It is the most applied wet chemical, bottom-up method. In a typical procedure, first of all small Au nanoparticle seed (~1-2 nm) were prepared by the reduction of $HAuCl_4$ with borohydride in cetyltrimethylammonium bromide (CTAB) solution. CTAB is a surfactant and is used to prevent the aggregation and more importantly it directs the longitudinal growth of the Au nanoparticles by forming micelles around the Au NPs. After the preparation of so-called seed solution, growth was accomplished by the reduction of additional $HAuCl_4$ (Au (III)) by ascorbic acid to Au (I) and further reduction of Au (I) to Au (0) with the help of gold seeds synthesized in the previous step. One of the important contributors to the growth is the $AgNO_3$. Detailed studies reveal that Ag (I) ions selectively bind to energetic {110} sides of Au NPs and diminish the growth rate at that position. Thus Au atoms choose to deposit on {100} sides that results in longitudinal growth of Au NPs to form rod-like shapes.

Figure 119 shows the TEM images of gold nanorods that were synthesized with

respect to El-Sayed seed-mediated growth technique. TEM images (Figure 119) clearly represents the highly uniform rods with acceptable yield. Size of the rods is 40 nm with an aspect ratio of 4. Surface plasmon resonance peaks were observed by acquiring the electronic absorption spectrum (Figure 119).

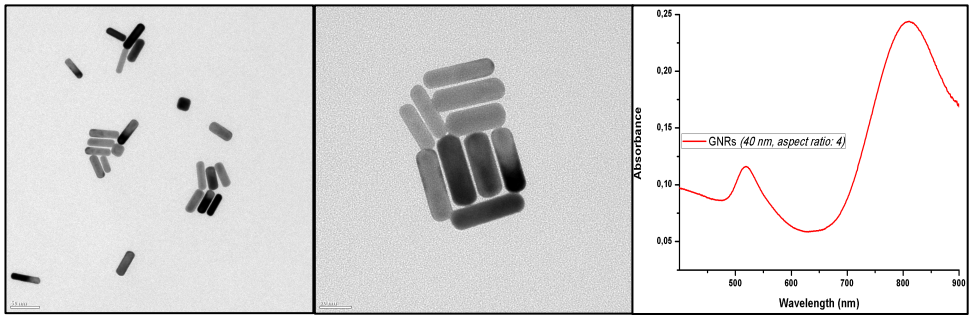

Figure 119. TEM images of gold nanorods (~40 nm) and electronic absorption spectrum of GNRs in HEPES buffer (pH 7.2, 20 mM).

GNRs exhibit mainly two surface plasmon modes; (i) *longitudinal mode* corresponds to electron oscillations along the length direction and the (ii) *transverse mode* associated with the transverse electron oscillations. In our spectrum we observed these two well-known modes at around 500 nm (transverse) and 800 nm (longitudinal). Since the path of the electron movements is longer at length direction, the longitudinal peak is red-shifted. One should note that aspect ratio could be varied from 2.4 to 8.5 in GNRs that directly affects the longitudinal plasmon wavelength.

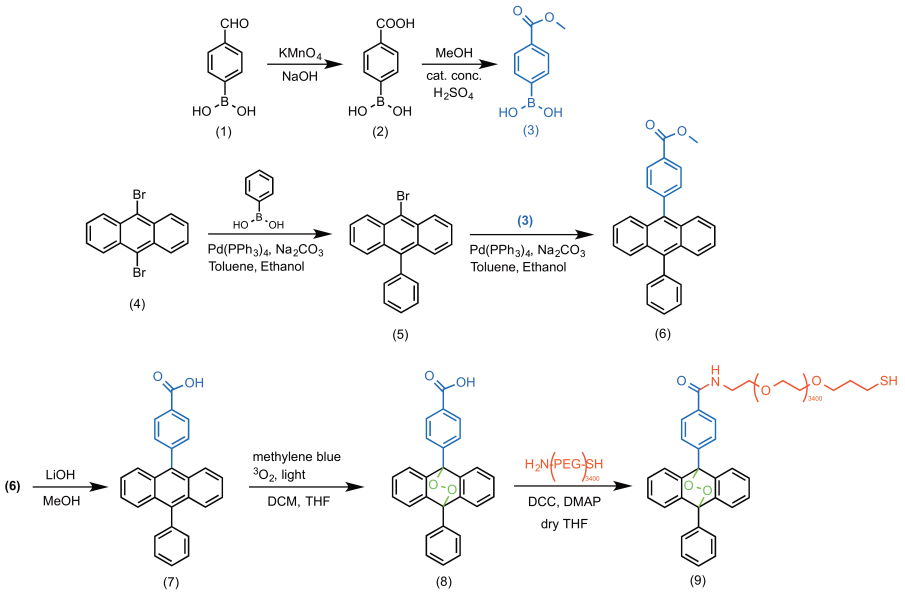

Figure 120. Reaction scheme for the target compound.

After obtaining GNRs, the next step was to synthesize a water-soluble anthracene endoperoxide derivative with thiolated end group for GNRs conjugation (figure 120). We started with 4-formylboronic acid and oxidized it to carboxylic acid with $KMnO_4$. Then methyl ester derivative was synthesized in MeOH with catalytic amount of concentrated sulfuric acid. This esterification was crucial because Suzuki coupling could not be done with 4-carboxyphenylboronic acid, most probably due to the de-activation of the palladium catalyst. On the other hand, we did mono Suzuki coupling between commercial 9,10-dibromoanthracene and phenylboronic acid. After that we repeated the coupling with compound **(5)** and methyl ester derivative of boronic acid **(3)** successfully. Hydrolysis of ester to acid was achieved by LiOH in MeOH. At that point, we synthesized the endoperoxide. Methylene blue and our anthracene derivative were irradiated with a water-cooled 400W Hg arc lamp by bubbling $^3O_2$ in cosolvent (DCM/dry THF). Finally DCC coupling was applied in dry THF with NH_2-$(PEG)_{3400}$-SH and the carboxylated anthracene endoperoxide **(8)** to get the water-soluble, thiolated target endoperoxide **(9)**.

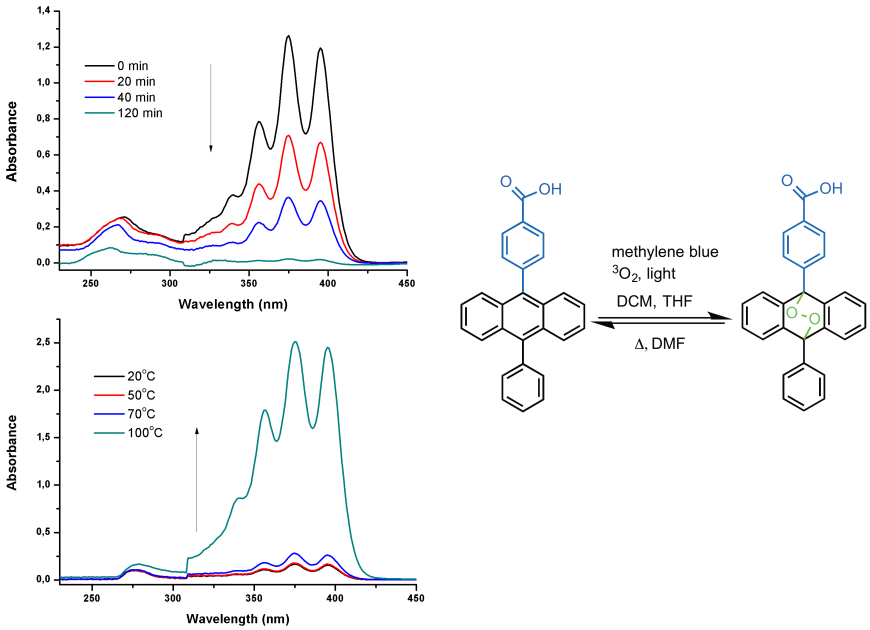

Figure 121. Top: Absorption spectra that is taken during the endoperoxide formation reaction. Bottom: Thermolysis of endoperoxide **(8)** to parent compound **(7)**.

Endoperoxide formation (compound **(8)**) was further observed and followed by the electronic absorption spectrum during the reaction (Figure 121, top). As the reaction precedes absorption peaks at 352, 375, and 395 nm of the parent anthracene

decreases due to the disturbed aromaticity, which is the result of reaction with $^1O_2$, produced by methylene blue.

It is a typical [4+2] cycloaddition reaction. At the end of two hours, reaction was completed with almost no absorbance at corresponding wavelengths as expected. On the other hand, we also checked the reappearance of absorbance bands (regained aromaticity) of the parent anthracene upon heating in DMF solution. Figure 121, bottom clearly confirms the release of oxygen followed by thermal decomposition of our compound **(8)**.

Next we tried to show thermal decomposition of our target compound **(9)**. For that purpose, **(9)** in DMSO solution was heated in a closed system. The time of heating was 1 hour for all selected temperatures. As in the case of compound **(8)**, reappearance of absorbance bands was followed at 352, 375, and 395 nm. Release was finished after 9 hours at 140°C (Figure 122). Additionally **(9)** was heated at 95°C for six hours, which resulted in efficient thermolysis. On the other hand, when we heated **(9)** at 37°C (body temperature), anthracene absorption cannot be detected, suggesting that our singlet oxygen carrier is stable under physiological conditions (figure 123). We also studied the oxygen release from compound **(9)** in aqueous solution (Figure 124). Thermolysis in aqueous medium is important for practical applications such as cell culture studies. **(9)** was heated in double-distilled water for 1 hour at 100°C in a closed system. Reappearance of absorbance was observed indicating the decomposition of endoperoxide.

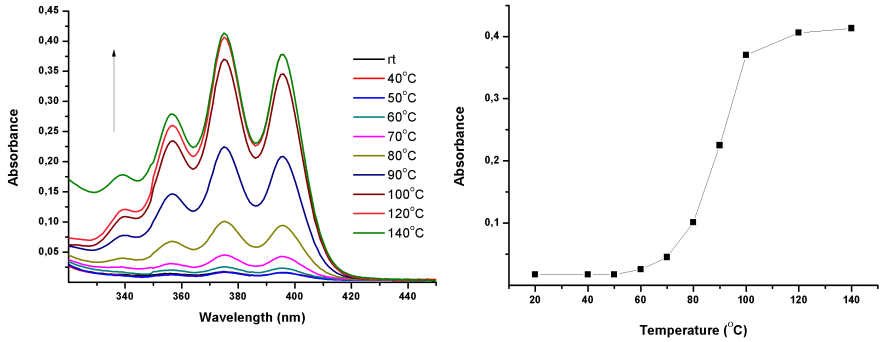

Figure 122. Left: Thermolysis of $5x10^{-5}$ M **(9)** in DMSO at different temperature. Right: Absorbance vs. temperature graph of the thermolysis. The time of heating was 30 min for all selected temperatures.

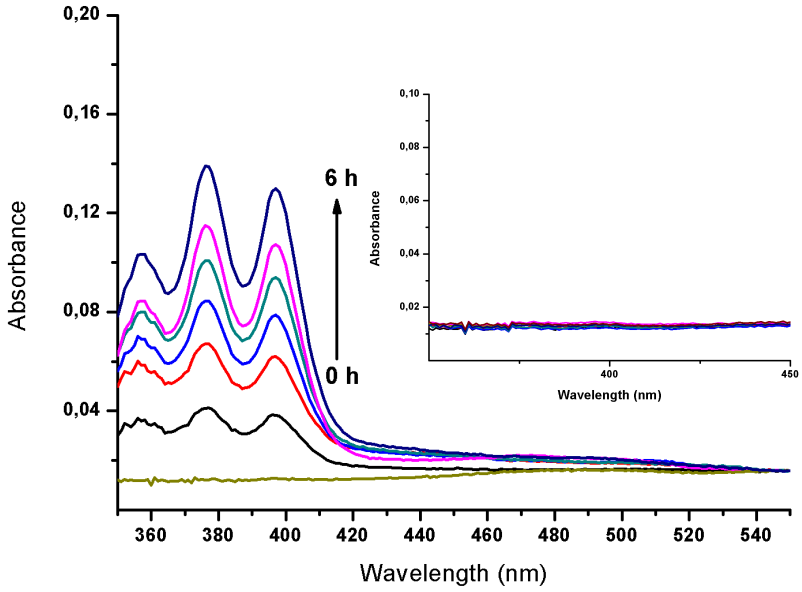

Figure 123. Thermolysis of $5x10^{-5}$ M **(9)** in DMSO at 95°C for 6 hours. Inset: Absorbance of $5x10^{-5}$ M **(9)** in DMSO at 37°C. Sample was heated for 6 hours.

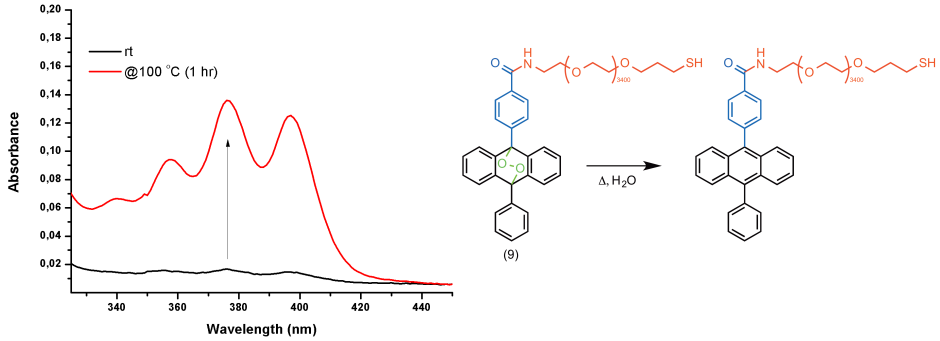

Figure 124. Thermolysis of $1x10^{-5}$ M **(9)** at 100°C for 1 hr in HEPES buffer (pH 7.2, 20 mM).

It is known that thermolysis of polycyclic aromatic endoperoxides yield both molecular ($^3O_2$) and singlet oxygen ($^1O_2$). So, remaining important task is to show the presence of singlet oxygen. In order to prove that, we used a singlet oxygen trap molecule, diphenyl*iso*benzofuran (DPBF). Upon production of $^1O_2$, it reacts with DPBF and decomposes the trap molecule that causes a decrease in absorbance at 414 nm. Thus, we arranged the absorbance of DPBF to around O.D~1 and mixed it with $1x10^{-5}$ M **(9)** in DMSO. Then mixture was heated at 70°C for 150 minutes. In every 30 minutes, aliquots were taken and electronic absorption spectra acquired. In the first 30 min, dramatic decrease in DPBF absorbance was seen indicating the effective production of singlet oxygen. After 90 min, we started to see reappearance absorbance bands of anthracene. Decrease in trap absorbance was observed in the

course of 150 minutes heating (Figure 125).

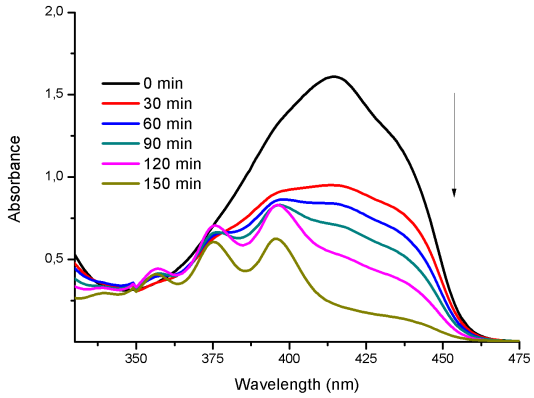

Figure 125. Decrease in absorbance of DPBF in DMSO in the presence of $1x10^{-5}$ M upon heating at 70°C **(9)** and the reappearance of parent anthracene absorbance bands.

After obtaining promising results, we conjugated the compound **(9)** with GNRs. TEM images of GNRs after conjugation are given in figure 126. LSPR maximum of the GNRs are slightly red shifted prior to conjugation both in buffer and DMSO (figure 126).

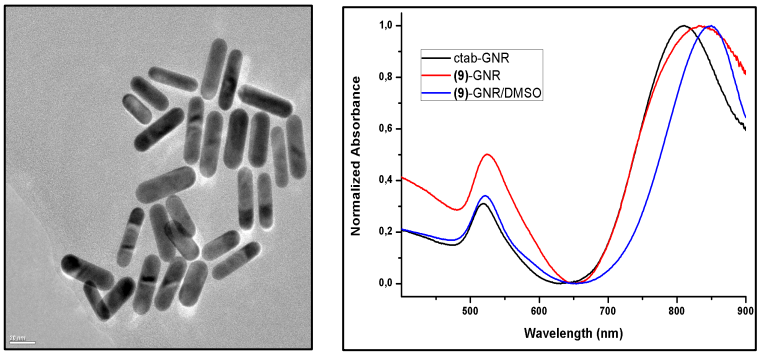

Figure 126. Left: TEM image of GNR-**(9)** conjugate. Right: Normalized electronic absorption spectra of CTAB-GNR, **(9)-GNR**(in HEPES (pH 7.2, 20 mM) and **(9)-GNR** in DMSO.

Following the conjugation, we mixed the conjugate with trap molecule in DMSO and heated the mixture in an oil bath. Decrease in absorption of trap clearly showed the singlet oxygen generation as well as successful conjugation of gold nanorods and **(9)** (figure 127). We further conducted several singlet oxygen generation experiments with our gold nanorod-**(9)** conjugate (**GNR-(9)**) via laser irradiation. We dispersed the **GNR-(9)** in DMSO and irradiated the conjugate with laser light (830 nm) in the

presence of singlet oxygen trap (DPBF).

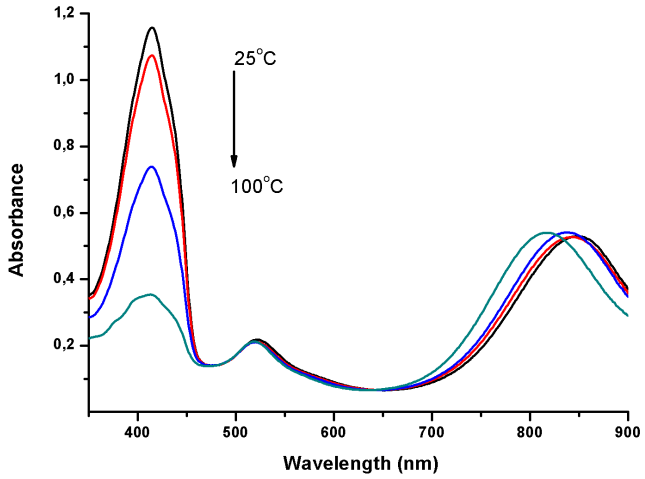

Figure 127. Decrease in absorbance of DPBF at 414 nm in DMSO in the presence of **(9)-GNR** upon heating in oil bath.

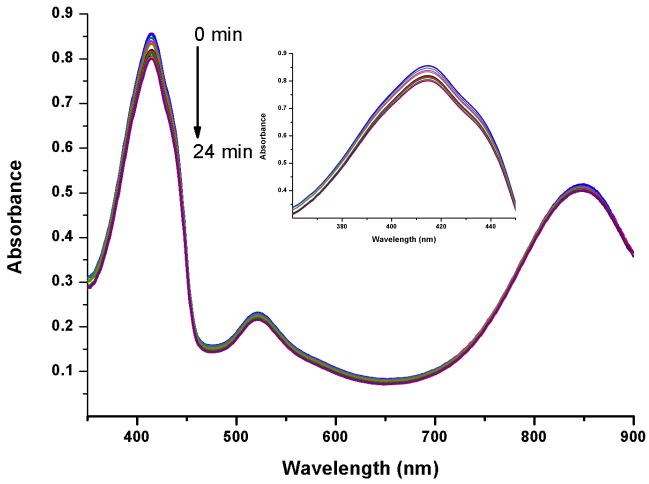

Figure 128. Decrease in absorbance of DPBF at 414 nm in DMSO in the presence of **(9)-GNR**. Excitation @830 nm.

Decrease in the absorption spectrum of DPBF clearly showed that our conjugate is generating singlet oxygen (figure 128). This is the result of local temperature increase on the surface of gold nanorod upon excitation at its surface plasmon peak (830 nm), which triggers the thermal decomposition of compound **(9)**. On the other hand, when we irradiated the solution, which contains gold nanorod only, there was no decrease in trap absorbance (figure 129). Relative absorbance decrease difference of GNR-EPO and GNR with respect to time is given in figure 130.

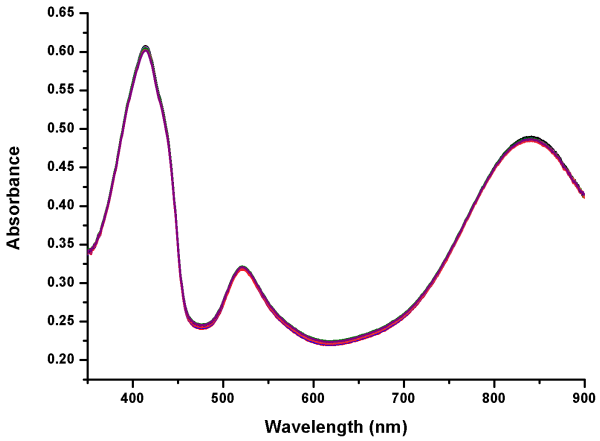

Figure 129. Absorbance of DPBF in DMSO in the presence of **GNRs only** (0.125 nM). Excitation @830 nm.

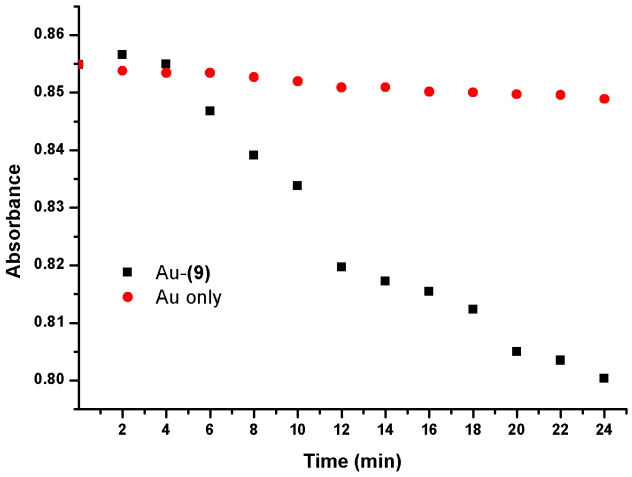

Figure 130. Relative $^1O_2$ generation efficiency of **(9)-GNR** and **GNR only** in DMSO detected by the absorbance decrease of DPBF @414 nm with time. During first 4 min the samples were kept in the dark.

6.4. Experimental Details

General: ^{1}H NMR and ^{13}C NMR spectra were recorded on Bruker DPX-400 (operating at 400 MHz for ^{1}H NMR and 100 MHz for ^{13}C NMR) in $CDCl_3$ with tetramethylsilane (TMS) as internal standard. All spectra were recorded at 25°C and coupling constants (*J values*) are given in *Hz*. Chemical shifts were reported in parts per million (ppm). Absorption spectra were performed by using a Varian Cary-100. Mass spectra were recorded with Agilent Technologies 6224 TOF LC/MS and 6530 Accurate Mass Q-TOF LC/MS. TEM images were acquired by using FEI Technai

G2 F30 high-resolution transmission electron microscope and carbon grid. Reactions were monitored by thin layer chromatography using Merck TLC Silica gel 60 F_{254}. Silica gel column chromatography was performed over Merck Silica gel 60 (particle size: 0.040-0.063 mm, 230-400 mesh ASTM). All other reagents and solvents were purchased from suppliers and used without further purification.

Singlet Oxygen Trap Experiments: In singlet oxygen measurements 1,3-Diphenylisobenzofuran (DPBF) was used as a singlet oxygen trap in DMSO. In a typical procedure for the detection of singlet oxygen generation by using trap molecules, **(9)-GNR** conjugate and a trap molecule were mixed in DMSO. Initially several dark measurements were taken followed by irradiation of the conjugate at absorption maximum of GNR. Absorbance decrease of trap molecules was monitored suggesting singlet oxygen generation in the presence of light and conjugate. Irradiation of the conjugate was accomplished by using Tsunami, SpectraPhysics, USA laser system in combination with Spectrum Analyzer, SpectraSuite, Ocean Optics, USA. Excitation wavelength was adjusted to 830 nm ($1W/cm^2$) and 11 mm lens (Thorlabs) was used in order to focus the incoming light. **Laser irradiation was performed in Dr. Bulend Ortac group at UNAM, Bilkent University, Ankara, Turkey.**

Synthetic Details:

Synthesis of (2): A solution of 4-formylboronic acid (1.0 g, 6.67 mmol) in aqueous sodium hydroxide solution (5.4 mL of a 2.5 M solution) was diluted with distilled water (40 mL) just before the addition of a freshly prepared solution of $KMnO_4$ (246 mg, 1.56 mmol, 0.23 eq.) in water (7.5 mL). This addition was repeated twice at 1-hour intervals. After stirring over night, ethanol (3 mL) was added and the mixture stirred at 50^oC for 10 min. After cooling and filtrating over celite, the filtrate was acidified to pH 2.5 with 0.5 M HCl. Finally filtration of the precipitate gave the pure product as a white solid (90%). ^1H NMR (400 MHz, DMSO-d_6): δH 8.30 (2H, s), 7.80 (4H, s); ^{13}C NMR (100 MHz, DMSO-*d6*): δC 194.0, 167.9, 134.9, 134.5, 132.4, 128.7, 128.5 ppm. MS HRMS (TOF-ESI): *m*/*z* calcd: 164.040; found: 164.037 $[M-H]^-$, Δ = 17.0 ppm.

Synthesis of (3): **(2)** (1.0 gr, 6.02 mmol) was dissolved in 25 mL MeOH, then 5 drops of conc. H_2SO_4 was added. The mixture was stirred at reflux for 1 day. After that solvent was evaporated under vacuum. Then aqueous Na_2CO_3 was added and the mixture was extracted in to the ethyl acetate. Organic phase was washed with water and the solvent was removed. Recrystallization from toluene gave the pure product as a white solid (60%). ^{1}H NMR (400 MHz, DMSO-d_6): δH 8.20 (2H, s), 7.80 (4H, s), 3.75 (3H, s); ^{13}C NMR (100 MHz, DMSO-*d6*): δC 164.8, 132.6, 129.1, 126.3, 50.4 ppm. MS HRMS (TOF-ESI): *m*/*z* calcd: 178.056; found: 178.053 $[M-H]^-$, Δ = 13.2 ppm.

Synthesis of (5): 9,10-Dibromoanthracene (1.68 g, 5 mmol), phenylboronic acid (0.61 g, 5 mmol), $Pd(PPh_3)_4$ (0.58 mg, 0.5 mmol) and 2 M Na_2CO_3 were mixed in degassed toluene (30 mL), ethanol (10 mL) and distilled water (12 mL). Reaction was heated for 3 hours at 100^{o}C. The mixture is extracted with ethyl acetate and the organic phase dried over anhydrous Na_2SO_4. Solvent was evaporated in vacuo and compound was purified by silica gel FCC using hexane as the eluent. A white solid was obtained (35%). ^{1}H NMR (400 MHz, $CDCl_3$): δH 8.61 (2H, d, *J* = 8.8 Hz), 7.71-7.62 (2H, m), 7.60-7.53 (5H, m), 7.45-7.30 (4H, m); ^{13}C NMR (100 MHz, $CDCl_3$): δC 138.4, 137.8, 131.1, 131.0, 130.0, 128.4, 127.8, 127.7, 127.4, 126.9, 125.5 ppm. MS HRMS (TOF-ESI): *m*/*z* calcd: 332.020; found: 332.022 [M], Δ = 5.7 ppm.

Synthesis of (6): **(5)** (0.15 g, 0.44 mmol), **(3)** (0.080 g, 0.44 mmol), $Pd(PPh_3)_4$ (0.061 g, 0.044 mmol) and 2 M Na_2CO_3 were mixed in degassed toluene (6 mL), ethanol (2 mL) and distilled water (3 mL). Reaction was heated for 3 hours at 100^{o}C. The mixture is extracted with ethyl acetate and the organic phase dried over anhydrous Na_2SO_4. Solvent was evaporated in vacuo and compound was purified by silica gel FCC using 3:1 (DCM: hexane) as the eluent. A white solid was obtained (53%). ^{1}H NMR (400 MHz, $CDCl_3$): δH 8.32 (2H, d, *J* = 1.8 Hz), 7.78-7.73 (2H, m), 7.69-7.60 (7H, m), 7.55 (2H, d, *J* = 1.3 Hz), 7.39-7.32 (4H, m), 4.05 (3H, s); ^{13}C NMR (100 MHz, $CDCl_3$): δC 167.1, 144.4, 138.9, 137.8, 135.8, 131.6, 131.5, 131.3, 129.9, 129.7, 129.5, 128.5, 127.6, 127.1, 126.5, 125.4, 125.1, 52.3 ppm. MS HRMS (TOF-ESI): *m*/*z* calcd: 388.146; found: 388.149 [M], Δ = 6.1 ppm.

Synthesis of (7): **(6)** (80 mg, 0.21 mmol) was dissolved in 5 mL MeOH. To this solution 2M LiOH in 1 mL water was added. The mixture was stirred for 3 hours at 60°C then the solution was acidified to pH 2.0 followed by precipitation in water. Filtrate was collected and dried (48%). ^{1}H NMR (400 MHz, $CDCl_3$): δH 8.22 (2H, d, *J* = 8.0 Hz), 7.71-7.62 (2H, m), 7.60-7.55 (5H, m), 7.53-7.48 (2H, m), 7.47-7.37 (6H, m); ^{13}C NMR (100 MHz, $CDCl_3$): δC 167.8, 143.5, 138.5, 137.8, 136.1, 131.8, 131.3, 130.7, 130.1, 129.6, 129.4, 129.2, 128.3, 126.9, 126.5, 126.3, 126.0 ppm. MS HRMS (TOF-ESI): *m/z* calcd: 373.123; found: 373.121 $[M-H]^-$, Δ = 5.6 ppm.

Synthesis of (8): **(7)** (50 mg, 0.13 mmol) was dissolved in co-solvent DCM-THF (10 mL-5mL) and cooled to -78°C. Methylene blue (0.013 mmol) was added to the solution. The mixture was stirred under O_2 atmosphere for 3 hours. Water-cooled 400W Hg arc lamp (white light) irradiation was performed during the reaction. Solvent was evaporated in vacuo, and compound was purified by silica gel FCC using 95:5 (DCM: MeOH) as the eluent (55%). ^{1}H NMR (400 MHz, $CDCl_3$): δH 8.25 (2H, d, *J* = 1.5 Hz), 7.78 (2H, d, *J* = 1.7 Hz), 7.71 (2H, d, *J* = 1.5 Hz), 7.68-7.59 (3H, m), 7.35-7.29 (4H, m), 7.11-7.02 (4H, m); ^{13}C NMR (100 MHz, $CDCl_3$): δC 140.1, 139.8, 139.5, 132.6, 130.1, 129.1, 128.5, 127.9, 127.5, 127.2, 123.6, 123.4 ppm. MS HRMS (TOF-ESI): *m/z* calcd: 407.129; found: 407.118 $[M-H]^-$, Δ = 25.7 ppm.

Synthesis of (9): **(8)** (50 mg, 0.12 mmol), H_2N-PEG-SH (292 mg, 0.086 mmol, MW: 3400 g/mol) were dissolved in 5 mL dry THF. DCC (26 mg, 0.12 mmol) and DMAP (11 mg, 0.15 mmol) were added to the solution. Reaction mixture was stirred for 2 hours and precipitate formation was observed. Precipitate was filtered and cold diethyl ether was added to the solution in order to precipitate the product. Pure product was filtered (42%). ^{1}H NMR (400 MHz, $CDCl_3$): δH 8.12 (2H, d, *J* = 8.2 Hz), 7.78 (2H, d, *J* = 8.2 Hz), 7.71-7.60 (5H, m), 7.21-7.12 (6H, m), 7.11-7.07 (2H, m), 3.78-3.49 (m, PEG), 2.90 (2H, t, *J* = 6.5), 1.22 (2H, s), 0.90 (1H, s). ^{13}C NMR (100 MHz, $CDCl_3$): δC 167.0, 157.2, 140.9, 140.4, 140.1, 139.9, 136.0, 134.5, 132.9, 128.3, 127.7, 127.3, 127.2, 123.5, 123.2, 70.4, 70.3, 70.2, 70.0, 69.9, 69.5, 66.9, 38.5, 33.8, 25.6, 24.9 ppm.

Synthesis of Gold Nanorod:

Preparation of Seed Solution: Firstly CTAB solution (5.0 mL, 0.20 M) was mixed with $HAuCl_4$ solution (5.0 mL, 0.00050 M). To the stirred solution, ice-cold $NaBH_4$ (0.60 mL, 0.010 M) was added, which yields brownish yellow solution. The mixture was vigorously stirred for 2 min. It was stored at room temperature.

Growth of Nanorods with LSPR band around 800 nm: CTAB solution (5.0 mL, 0.20 M) was added to $AgNO_3$ (0.20 mL, 0.0040 M) solution at 25ºC. To this mixture, $HAuCl_4$ (5.0 mL, 0.0010 M) was added and after gently mixing, ascorbic acid (70.0 µL, 0.0788 M) was added. Addition of ascorbic acid changed the color of solution from dark yellow to colorless. Finally, 12.0 mL of the seed solution was added to the growth solution at 27-30ºC. The color of the solution changed to purple within 10-20 min. The temperature of the growth medium was kept at 27-30ºC for 12 hours. In order to remove excess CTAB, the solution was centrifuged at 6000 rpm for 10 min and dispersed in distilled water. With this experimental method, 1.8E+10 nps/mL, 0.060 mg/mL GNRs were obtained.

Synthesis of EPO decorated GNRs: GNR solution was centrifuged at 14000 rpm just before the conjugation for further removal of CTAB. Then, equi-volume solutions of GNR (O.D~1.0, ~0.25 nM) and **(9)** are mixed under vigorous stirring and sonicated for 1 min. After that the mixture was left to react for 2 hours. Excess, unreacted **(9)** were removed by centrifugation at 7000 rpm for 10 min and **(9)-GNR** was dispersed in buffer or DMSO.

6.5. Conclusion

To sum up, in this study water-soluble anthracene endoperoxide derivative was combined with gold nanorod in order to achieve light induced thermal decomposition of endoperoxide that yields cytotoxic singlet oxygen. Thermal decomposition and singlet oxygen generation were observed in detail. Since this project is addressing major problems of PDT, we are confident that, this new approach will definitely be a breakthrough in PDT designs.

CHAPTER 7

CONCLUSION

This thesis covers mainly three topics, which are selective fluorescence sensing of GSH, finding out alternative pathways for the generation of cytotoxic singlet oxygen for PDT applications and synthesis of axially chiral BODIPY fluorophores. Almost all of these studies gave novel and/or interesting results such as (i) use of two modulation sides for the fluorescent detection of the glutathione for the first time and selective intracellular GSH detection and monitoring (ii) first example of an orthogonal, heavy atom-free BODIPY designs that generate singlet oxygen efficiently (iii) detailed computational studies about heavy atom-free sensitization of PDT (iv) first example of an activatable heavy atom free BODIPY sensitizer for targeted PDT action (v) first synthesis of atropisomeric Bodipy derivatives and (v) addressing long-standing issues related to PDT by utilization of nanoparticles.

In the first part (chapter 3), we performed the selective fluorescent detection of one of the most significant bio-thiol, glutathione. The main obstacle in designing GSH selective chemosensor is that; conventional reactions that are mostly used for the detection of other bio-thiols (Cys and Hcy) namely Michael addition, cyclization and disulfide bond breakage are not well suited for GSH due to its different, larger and bulkier chemical structure. Thus some additional approaches were needed. In this study, we thought that selectivity towards GSH could be achieved by incorporating an additional recognition site, such as azacrown ethers for the terminal ammonium group found in GSH in addition to Michael acceptor site for thiol end. In addition to that remarkable turn-on response upon addition of GSH was detected at pH 6.0, mimicking the pH of cancer cells where GSH concentration is elevated. This was obtained by judicious modulation of PeT process. Cancer cell culture studies and

GSH inhibition experiments were revealed that our novel probe is able to detect intracellular level of GSH in cancer cells selectively. The design principle represented here, which includes two binding sides approach, will pave the way for similar design methodologies.

In chapter 4, we addressed the heavy atom mediated dark toxicity conflict of PDT sensitizers by designing and introducing a new concept on BODIPY dyes. This was achieved by engineering the excited state of the BODIPY leading to efficient cytotoxic singlet oxygen generation. We synthesized series of orthogonal BODIPY dimers without incorporating any heavy atoms. In the light of computational studies we defined a new excited state configuration for our dimers named as doubly substituted tetra radical state (DS-TR), which was shown to be essential for obtaining ISC. Chemical singlet oxygen trap experiments, singlet oxygen phosphorescence signals and cell culture studies proved the formation of SO. For further investigation of this novel excited state configuration and in order to check its applicability in near-IR absorbing BODIPY dimers, we conducted additional detailed computational studies. Shifting the absorption wavelength to the red region is achieved with π-extension of bis-BODIPYs; however, ISC properties are adversely affected for such dimers. Modifications in the chromophore cores are likely to be a more promising research direction rather than simple π-extension. In the second part of chapter 4, we enlarged the excited state modulation by combining DS-TR and charge transfer concepts in order to get an activatable heavy atom free sensitizer. Singlet oxygen trap experiments, transient absorption signals and detailed cell culture studies revealed that our sensitizer is getting activated only in the presence of high amount of GSH, which is a well known cancer marker. Further investigations showed that we are able to differentiate healthy and cancer cells during the PDT action. This is the first example of such differentiation, where GSH is used as a targeting agent.

In chapter 5, we recognized the potential of our dimeric BODIPY derivatives for atropisomerism, while dealing with them for PDT applications. In this manner, we introduced the axially chiral BODIPY derivatives for the first time in this chapter. Analytical and preparative HPLC separations of racemic mixtures of target

compounds were performed using cellulose based Chiralcel-OD columns and circular dichroism studies clearly demonstrated successful separation of the two enantiomers. In summary, we presented the first example of atropisomeric BODIPY derivatives with persistent chirality due to multiple methyl group clashes. The orthogonally linked BODIPY compounds have been demonstrated to have interesting photophysical properties (chapter 4) but also we showed that they could be isolated as atropisomeric chiral compounds. Similar compounds may find practical applications and hold great promise as chiroptical fluorogenic/chromogenic sensors, and as highly selective chiral photosensitizers in a therapeutic context, among other potential applications.

In chapter 6, we addressed the major problems of PDT concept hitherto blocking broader clinical application. These restrictions are mainly incorporation of heavy atoms, which was mentioned in chapter 4, restricted light penetration depth through tissues and hypoxia (molecular oxygen deficiency). To do so, we combined water-soluble anthracene derivative endoperoxide with near-IR absorbing gold nanorods. In this study heating itself is not the therapeutic action as in the case of photothermal therapy, but it is a trigger. On the other hand hypoxia is not an issue; generation of singlet oxygen in current practice of PDT is dependent on the presence of dissolved oxygen. As mentioned previously, the process of singlet oxygen generation through photosensitization itself depletes cellular oxygen very fast, so that the dose of irradiation has to be carefully adjusted and the light has to be introduced in pulses. Endoperoxides decompose along a few different pathways, but in any case for cycloreversion, the product is either triplet molecular oxygen ($^3O_2$) or singlet oxygen ($^1O_2$). Singlet oxygen generation capacity of our conjugate was observed upon irradiation with laser light via singlet oxygen trap experiments.

There is no doubt that today interdisciplinary research efforts are the key in solving complicated problems. As a chemist our starting point is the design of intelligent molecular structures with multiple properties. Accordingly, in this thesis, I combined organic&nanoparticle synthesis with supramolecular chemistry, photochemistry, biochemistry and materials science in order to touch on the challenges in the field of

fluorescence sensing, PDT and chiral fluorophores.

BIBLIOGRAPHY

(1) Czarnik, A. W.; American Chemical Society. Division of Organic Chemistry.; American Chemical Society. Meeting: *Fluorescent chemosensors for ion and molecule recognition*; American Chemical Society: Washington, DC, **1993**.

(2) Kim, J. S.; Quang, D. T. Calixarene-derived fluorescent probes. *Chem. Rev.* **2007**, *107*, 3780-3799.

(3) Santos-Figueroa, L. E.; Moragues, M. E.; Climent, E.; Agostini, A.; Martinez-Manez, R.; Sancenon, F. Chromogenic and fluorogenic chemosensors and reagents for anions. A comprehensive review of the years 2010-2011. *Chem. Soc. Rev.* **2013**, *42*, 3489-3613.

(4) Tsien, R. Y. New Calcium Indicators and Buffers with High Selectivity against Magnesium and Protons - Design, Synthesis, and Properties of Prototype Structures. *Biochemistry-Us* **1980**, *19*, 2396-2404.

(5) Wu, J. S.; Liu, W. M.; Ge, J. C.; Zhang, H. Y.; Wang, P. F. New sensing mechanisms for design of fluorescent chemosensors emerging in recent years. *Chem. Soc. Rev.* **2011**, *40*, 3483-3495.

(6) Chan, J.; Dodani, S. C.; Chang, C. J. Reaction-based small-molecule fluorescent probes for chemoselective bioimaging. *Nat Chem* **2012**, *4*, 973-984.

(7) Lakowicz, J. R.: *Principles of Fulorescence Spectroscopy*; Springer: New York, **1999**.

(8) Haugland, R. P.: *Handbook of Fluorescent probes and research products*; Molecular Probes, **2002**.

(9) Coleman, M. D.: *Human Drug Metabolism: An Introduction*; Wiley-Blackwell, **2010**.

(10) Teale, F. W. W., G. Ultraviolet fluorescence of the aromatic amino acids. *Biochem. J.* **1957**, *65*, 476-482.

(11) Demchenko, A. P.: *Ultraviolet Spectroscopy of Proteins*; Springer-Verlag: Berlin, **1986**.

(12) Sapsford, K. E.; Berti, L.; Medintz, I. L. Materials for fluorescence resonance energy transfer analysis: Beyond traditional donor-acceptor combinations. *Angew. Chem. Int. Ed.* **2006**, *45*, 4562-4588.

(13) Marme, N.; Knemeyer, J. P.; Wolfrum, J.; Sauer, M. Highly sensitive protease assay using fluorescence quenching of peptide probes based on photoinduced electron transfer. *Angew. Chem. Int. Ed.* **2004**, *43*, 3798-3801.

(14) Li, X. H.; Gao, X. H.; Shi, W.; Ma, H. M. Design Strategies for Water-Soluble Small Molecular Chromogenic and Fluorogenic Probes. *Chem. Rev.* **2014**, *114*, 590-659.

(15) Baeyer, A. Ueber eine neue Klasse von Farbstoffen. *Ber. Dtsch. Chem. Ges.* **1871**, *4*, 555-558.

(16) Beija, M.; Afonso, C. A. M.; Martinho, J. M. G. Synthesis and applications of Rhodamine derivatives as fluorescent probes. *Chem. Soc. Rev.* **2009**, *38*, 2410-2433.

(17) Cosa, G.; Focsaneanu, K. S.; McLean, J. R. N.; McNamee, J. P.; Scaiano, J. C. Photophysical properties of fluorescent DNA-dyes bound to single- and double-stranded DNA in aqueous buffered solution. *Photochem. Photobiol.*

2001, *73*, 585-599.

(18) Soh, N.; Ueda, T. Perylene bisimide as a versatile fluorescent tool for environmental and biological analysis: A review. *Talanta* **2011**, *85*, 1233-1237.

(19) Wood, T. E.; Thompson, A. Advances in the chemistry of dipyrrins and their complexes. *Chem. Rev.* **2007**, *107*, 1831-1861.

(20) Sathyamoorthi, G.; Wolford, L. T.; Haag, A. M.; Boyer, J. H. Selective Side-Chain Oxidation of Peralkylated Pyrromethene-Bf2 Complexes. *Heteroat. Chem* **1994**, *5*, 245-249.

(21) Domaille, D. W.; Zeng, L.; Chang, C. J. Visualizing Ascorbate-Triggered Release of Labile Copper within Living Cells using a Ratiometric Fluorescent Sensor. *J. Am. Chem. Soc.* **2010**, *132*, 1194-1195.

(22) Yin, S. C.; Leen, V.; Van Snick, S.; Boens, N.; Dehaen, W. A highly sensitive, selective, colorimetric and near-infrared fluorescent turn-on chemosensor for Cu2+ based on BODIPY. *Chem. Commun.* **2010**, *46*, 6329-6331.

(23) Moczar, I.; Huszthy, P.; Maidics, Z.; Kadar, M.; Toth, K. Synthesis and optical characterization of novel enantiopure BODIPY linked azacrown ethers as potential fluorescent chemosensors. *Tetrahedron* **2009**, *65*, 8250-8258.

(24) Loudet, A.; Burgess, K. BODIPY dyes and their derivatives: Syntheses and spectroscopic properties. *Chem. Rev.* **2007**, *107*, 4891-4932.

(25) Tram, K.; Yan, H. B.; Jenkins, H. A.; Vassiliev, S.; Brucec, D. The synthesis and crystal structure of unsubstituted 4,4-difluoro-4-bora-3a, 4a-diaza-s-indacene (BODIPY). *Dyes Pigments* **2009**, *82*, 392-395.

(26) Schmitt, A.; Hinkeldey, B.; Wild, M.; Jung, G. Synthesis of the Core Compound of the BODIPY Dye Class: 4,4'-Difluoro-4-bora-(3a,4a)-diaza-s-indacene. *J. Fluoresc.* **2009**, *19*, 755-758.

(27) Arroyo, I. J.; Hu, R. R.; Merino, G.; Tang, B. Z.; Pena-Cabrera, E. The Smallest and One of the Brightest. Efficient Preparation and Optical Description of the Parent Borondipyrromethene System. *J. Org. Chem.* **2009**, *74*, 5719-5722.

(28) Ulrich, G.; Ziessel, R.; Harriman, A. The chemistry of fluorescent bodipy dyes: Versatility unsurpassed. *Angew. Chem. Int. Ed.* **2008**, *47*, 1184-1201.

(29) Ziessel, R.; Ulrich, G.; Harriman, A. The chemistry of Bodipy: a new El Dorado for fluorescence tools. *New J. Chem.* **2007**, *31*, 496-501.

(30) Yakubovskyi, V. P.; Shandura, M. P.; Kovtun, Y. P. Boradipyrromethenecyanines. *Eur. J. Org. Chem.* **2009**, 3237-3243.

(31) Jackson, A. H.; Pandey, R. K.; Rao, K. R. N.; Roberts, E. Reactions on Solid Supports .2. A Convenient Method for Synthesis of Pyrromethanes Using a Montmorillonite Clay as Catalyst. *Tetrahedron Lett.* **1985**, *26*, 793-796.

(32) Boens, N.; Leen, V.; Dehaen, W. Fluorescent indicators based on BODIPY. *Chem. Soc. Rev.* **2012**, *41*, 1130-1172.

(33) Qin, W. W.; Baruah, M.; De Borggraeve, W. M.; Boens, N. Photophysical properties of an on/off fluorescent pH indicator excitable with visible light based on a borondipyrromethene-linked phenol. *J. Photoch. Photobio. A* **2006**, *183*, 190-197.

(34) Yogo, T.; Urano, Y.; Ishitsuka, Y.; Maniwa, F.; Nagano, T. Highly efficient and photostable photosensitizer based on BODIPY chromophore. *J. Am. Chem. Soc.* **2005**, *127*, 12162-12163.

(35) Jiao, L. J.; Yu, C. J.; Li, J. L.; Wang, Z. Y.; Wu, M.; Hao, E. H. beta-

Formyl-BODIPYs from the Vilsmeier-Haack Reaction. *J. Org. Chem.* **2009**, *74*, 7525-7528.

(36) Loudet, A.; Bandichhor, R.; Wu, L. X.; Burgess, K. Functionalized BF(2) chelated azadipyrromethene dyes. *Tetrahedron* **2008**, *64*, 3642-3654.

(37) Wories, H. J. K., J. H.; Lodder, G.; Lugtenburg, J.; Fokkens, R.; Driessen, O.; Mohn, G. R. A novel water-soluble fluorescent probe: Synthesis, luminescence and biological properties of the sodium salt of the 4-sulfonato-3,3′ ,5,5′ -tetramethyl-2,2′ -pyrromethen-1,1′ -BF2 complex. *Recl. Trav. Chim. Pays-Bas.* **1985**, *104*, 288-291.

(38) Li, L. L.; Han, J. Y.; Nguyen, B.; Burgess, K. Syntheses and spectral properties of functionalized, water-soluble BODIPY derivatives. *J. Org. Chem.* **2008**, *73*, 1963-1970.

(39) Uppal, T.; Hu, X. K.; Fronczek, F. R.; Maschek, S.; Bobadova-Parvanova, P.; Vicente, M. G. H. Synthesis, Computational Modeling, and Properties of Benzo-Appended BODIPYs. *Chem-Eur. J.* **2012**, *18*, 3893-3905.

(40) Zhou, C. Z.; Nagy, G.; Walker, A. V. Toward molecular electronic circuitry: Selective deposition of metals on patterned self-assembled monolayer surfaces. *J. Am. Chem. Soc.* **2005**, *127*, 12160-12161.

(41) Buyukcakir, O.; Bozdemir, O. A.; Kolemen, S.; Erbas, S.; Akkaya, E. U. Tetrastyryl-Bodipy Dyes: Convenient Synthesis and Characterization of Elusive Near IR Fluorophores. *Org. Lett.* **2009**, *11*, 4644-4647.

(42) Liu, J. Y.; Ermilov, E. A.; Roder, B.; Ng, D. K. P. Switching the photo-induced energy and electron-transfer processes in BODIPY-phthalocyanine conjugates. *Chem. Commun.* **2009**, 1517-1519.

(43) Niu, S. L.; Ulrich, G.; Ziessel, R.; Kiss, A.; Renard, P. Y.; Romieu, A. Water-Soluble BODIPY Derivatives. *Org. Lett.* **2009**, *11*, 2049-2052.

(44) Qin, W. W.; Baruah, M.; Sliwa, M.; Van der Auweraer, M.; De Borggraeve, W. M.; Beljonne, D.; Van Averbeke, B.; Boens, N. Ratiometric, fluorescent BODIPY dye with aza crown ether functionality: Synthesis, solvatochromism, and metal ion complex formation. *J. Phys. Chem. A* **2008**, *112*, 6104-6114.

(45) Diring, S.; Puntoriero, F.; Nastasi, F.; Campagna, S.; Ziessel, R. Star-Shaped Multichromophoric Arrays from Bodipy Dyes Grafted on Truxene Core. *J. Am. Chem. Soc.* **2009**, *131*, 6108-6110.

(46) Coskun, A.; Akkaya, E. U. Signal ratio amplification via modulation of resonance energy transfer: Proof of principle in an emission ratiometric Hg(II) sensor. *J. Am. Chem. Soc.* **2006**, *128*, 14474-14475.

(47) Yuan, M. J.; Zhou, W. D.; Liu, X. F.; Zhu, M.; Li, J. B.; Yin, X. D.; Zheng, H. Y.; Zuo, Z. C.; Ouyang, C.; Liu, H. B.; Li, Y. L.; Zhu, D. B. A multianalyte chemosensor on a single molecule: Promising structure for an integrated logic gate. *J. Org. Chem.* **2008**, *73*, 5008-5014.

(48) Rohand, T.; Baruah, M.; Qin, W. W.; Boens, N.; Dehaen, W. Functionalisation of fluorescent BODIPY dyes by nucleophilic substitution. *Chem. Commun.* **2006**, 266-268.

(49) Harriman, A.; Izzet, G.; Ziessel, R. Rapid energy transfer in cascade-type bodipy dyes. *J. Am. Chem. Soc.* **2006**, *128*, 10868-10875.

(50) Zhao, W. L.; Carreira, E. M. Conformationally restricted aza-bodipy:

A highly fluorescent, stable, near-infrared-absorbing dye. *Angew. Chem. Int. Ed.* **2005**, *44*, 1677-1679.

(51) Umezawa, K.; Nakamura, Y.; Makino, H.; Citterio, D.; Suzuki, K. Bright, color-tunable fluorescent dyes in the visible-near-infrared region. *J. Am. Chem. Soc.* **2008**, *130*, 1550-1551.

(52) Barin, G.; Yilmaz, M. D.; Akkaya, E. U. Boradiazaindacene (Bodipy)-based building blocks for the construction of energy transfer cassettes. *Tetrahedron Lett.* **2009**, *50*, 1738-1740.

(53) Bozdemir, O. A.; Cakmak, Y.; Sozmen, F.; Ozdemir, T.; Siemiarczuk, A.; Akkaya, E. U. Synthesis of Symmetrical Multichromophoric Bodipy Dyes and Their Facile Transformation into Energy Transfer Cassettes. *Chem-Eur. J.* **2010**, *16*, 6346-6351.

(54) Kolemen, S.; Bozdemir, O. A.; Cakmak, Y.; Barin, G.; Erten-Ela, S.; Marszalek, M.; Yum, J. H.; Zakeeruddin, S. M.; Nazeeruddin, M. K.; Gratzel, M.; Akkaya, E. U. Optimization of distyryl-Bodipy chromophores for efficient panchromatic sensitization in dye sensitized solar cells. *Chem. Sci.* **2011**, *2*, 949-954.

(55) Rousseau, T.; Cravino, A.; Bura, T.; Ulrich, G.; Ziessel, R.; Roncali, J. BODIPY derivatives as donor materials for bulk heterojunction solar cells. *Chem. Commun.* **2009**, 1673-1675.

(56) Gorman, A.; Killoran, J.; O'Shea, C.; Kenna, T.; Gallagher, W. M.; O'Shea, D. F. In vitro demonstration of the heavy-atom effect for photodynamic therapy. *J. Am. Chem. Soc.* **2004**, *126*, 10619-10631.

(57) Atilgan, S.; Ekmekci, Z.; Dogan, A. L.; Guc, D.; Akkaya, E. U. Water soluble distyryl-boradiazaindacenes as efficient photosensitizers for photodynamic therapy. *Chem. Commun.* **2006**, 4398-4400.

(58) Singh-Rachford, T. N.; Haefele, A.; Ziessel, R.; Castellano, F. N. Boron Dipyrromethene Chromophores: Next Generation Triplet Acceptors/Annihilators for Low Power Upconversion Schemes. *J. Am. Chem. Soc.* **2008**, *130*, 16164-16165.

(59) Camerel, F.; Bonardi, L.; Schmutz, M.; Ziessel, R. Highly luminescent gels and mesogens based on elaborated borondipyrromethenes. *J. Am. Chem. Soc.* **2006**, *128*, 4548-4549.

(60) Bozdemir, O. A.; Buyukcakir, O.; Akkaya, E. U. Novel Molecular Building Blocks Based on the Boradiazaindacene Chromophore: Applications in Fluorescent Metallosupramolecular Coordination Polymers. *Chem-Eur. J.* **2009**, *15*, 3830-3838.

(61) Ozlem, S.; Akkaya, E. U. Thinking Outside the Silicon Box: Molecular AND Logic As an Additional Layer of Selectivity in Singlet Oxygen Generation for Photodynamic Therapy. *J. Am. Chem. Soc.* **2009**, *131*, 48-49.

(62) de Silva, A. P.; Moody, T. S.; Wright, G. D. Fluorescent PET (Photoinduced Electron Transfer) sensors as potent analytical tools. *Analyst* **2009**, *134*, 2385-2393.

(63) Matsumoto, T.; Urano, Y.; Shoda, T.; Kojima, H.; Nagano, T. A thiol-reactive fluorescence probe based on donor-excited photoinduced electron transfer: Key role of ortho substitution. *Org. Lett.* **2007**, *9*, 3375-3377.

(64) De Silva, A. P. G., H.Q.N.; Gunnlaugsson, T.; Huxley, A.J.M.; Rademacher, J.T; Rice, T.E.: *Chemosensors for Ion and Molecule Recognition*;

Kluwer Academic, **1997**.

(65) Baki, C. N.; Akkaya, E. U. Boradiazaindacene-appended calix[4]arene: Fluorescence sensing of pH near neutrality. *J. Org. Chem.* **2001**, *66*, 1512-1513.

(66) de Silva, A. P.; Gunnlaugsson, T.; Rice, T. E. Recent evolution of luminescent photoinduced electron transfer sensors - A review. *Analyst* **1996**, *121*, 1759-1762.

(67) Akkaya, E. U.; Huston, M. E.; Czarnik, A. W. Chelation-Enhanced Fluorescence of Anthrylazamacrocycle Conjugate Probes in Aqueous-Solution. *J. Am. Chem. Soc.* **1990**, *112*, 3590-3593.

(68) Diebler, H. E., M.; Ilgenfritz, G.; Maass, G.; Winkler, R. Kinetics and mechanism of reactions of main group metal ions with biological carriers. *Pure Appl. Chem.* **1969**, *20*, 93-115.

(69) Valeur, B. L., I. Design principles of fluorescent molecular sensors for cation recognition. *Coordin. Chem. Rev.* **2000**, *205*, 3-40.

(70) Deniz, E.; Isbasar, G. C.; Bozdemir, O. A.; Yildirim, L. T.; Siemiarczuk, A.; Akkaya, E. U. Bidirectional switching of near IR emitting boradiazaindacene fluorophores. *Org. Lett.* **2008**, *10*, 3401-3403.

(71) Luo, J. D.; Xie, Z. L.; Lam, J. W. Y.; Cheng, L.; Chen, H. Y.; Qiu, C. F.; Kwok, H. S.; Zhan, X. W.; Liu, Y. Q.; Zhu, D. B.; Tang, B. Z. Aggregation-induced emission of 1-methyl-1,2,3,4,5-pentaphenylsilole. *Chem. Commun.* **2001**, 1740-1741.

(72) Liu, L.; Zhang, G. X.; Xiang, J. F.; Zhang, D. Q.; Zhu, D. B. Fluorescence "Turn On" Chemosensors for Ag+ and Hg2+ Based on Tetraphenylethylene Motif Featuring Adenine and Thymine Moieties. *Org. Lett.* **2008**, *10*, 4581-4584.

(73) Shahrokhian, S. Lead phthalocyanine as a selective carrier for preparation of a cysteine-selective electrode. *Anal. Chem.* **2001**, *73*, 5972-5978.

(74) Zhang, S.; Ong, C. N.; Shen, H. M. Critical roles of intracellular thiols and calcium in parthenolide-induced apoptosis in human colorectal cancer cells. *Cancer Lett.* **2004**, *208*, 143-153.

(75) Seshadri, S.; Beiser, A.; Selhub, J.; Jacques, P. F.; Rosenberg, I. H.; D'Agostino, R. B.; Wilson, P. W. F.; Wolf, P. A. Plasma homocysteine as a risk factor for dementia and Alzheimer's disease. *New Engl. J. Med.* **2002**, *346*, 476-483.

(76) Jung, H. S.; Chen, X. Q.; Kim, J. S.; Yoon, J. Recent progress in luminescent and colorimetric chemosensors for detection of thiols. *Chem. Soc. Rev.* **2013**, *42*, 6019-6031.

(77) Dalton, T. D.; Shertzer, H. G.; Puga, A. Regulation of gene expression by reactive oxygen. *Annu. Rev. Pharmacool. Toxicol.* **1999**, *39*, 67-101.

(78) Kleinman, W. A.; Richie, J. P. Status of glutathione and other thiols and disulfides in human plasma. *Biochem. Pharmacol.* **2000**, *60*, 19-29.

(79) Zheng, Z. B.; Zhu, G. Z.; Tak, H.; Joseph, E.; Eiseman, J. L.; Creighton, D. J. N-(2-hydroxypropyl)methaerylamide copolymers of a glutathione (GSH)-activated glyoxalase I inhibitor and DNA alkylating agent: Synthesis, reaction kinetics with GSH, and in vitro antitumor activities. *Bioconjugate Chem.* **2005**, *16*, 598-607.

(80) Chen, X.; Zhou, Y.; Peng, X. J.; Yoon, J. Fluorescent and colorimetric

probes for detection of thiols. *Chem. Soc. Rev.* **2010**, *39*, 2120-2135.

(81) de Silva, A. P.; Gunaratne, H. Q. N.; Gunnlaugsson, T. Fluorescent PET (photoinduced electron transfer) reagents for thiols. *Tetrahedron Lett.* **1998**, *39*, 5077-5080.

(82) Sun, Y. Q.; Chen, M. L.; Liu, J.; Lv, X.; Li, J. F.; Guo, W. Nitroolefin-based coumarin as a colorimetric and fluorescent dual probe for biothiols. *Chem. Commun.* **2011**, *47*, 11029-11031.

(83) Wang, H. L.; Zhou, G. D.; Mao, C.; Chen, X. Q. A fluorescent sensor bearing nitroolefin moiety for the detection of thiols and its biological imaging. *Dyes Pigments* **2013**, *96*, 232-236.

(84) Jung, H. S.; Han, J. H.; Pradhan, T.; Kim, S.; Lee, S. W.; Sessler, J. L.; Kim, T. W.; Kang, C.; Kim, J. S. A cysteine-selective fluorescent probe for the cellular detection of cysteine. *Biomaterials* **2012**, *33*, 945-953.

(85) Isik, M.; Ozdemir, T.; Turan, I. S.; Kolemen, S.; Akkaya, E. U. Chromogenic and Fluorogenic Sensing of Biological Thiols in Aqueous Solutions Using BODIPY-Based Reagents. *Org. Lett.* **2013**, *15*, 216-219.

(86) Shiu, H. Y.; Wong, M. K.; Che, C. M. "Turn-on" FRET-based luminescent iridium(III) probes for the detection of cysteine and homocysteine. *Chem. Commun.* **2011**, *47*, 4367-4369.

(87) Hu, M. M.; Fan, J. L.; Li, H. L.; Song, K. D.; Wang, S.; Cheng, G. H.; Peng, X. J. Fluorescent chemodosimeter for Cys/Hcy with a large absorption shift and imaging in living cells. *Org. Biomol. Chem.* **2011**, *9*, 980-983.

(88) Wang, H. L.; Zhou, G. D.; Gai, H. W.; Chen, X. Q. A fluorescein-based probe with high selectivity to cysteine over homocysteine and glutathione. *Chem. Commun.* **2012**, *48*, 8341-8343.

(89) Yuan, L.; Lin, W. Y.; Zhao, S.; Gao, W. S.; Chen, B.; He, L. W.; Zhu, S. S. A Unique Approach to Development of Near-Infrared Fluorescent Sensors for in Vivo Imaging. *J. Am. Chem. Soc.* **2012**, *134*, 13510-13523.

(90) Niu, L. Y.; Guan, Y. S.; Chen, Y. Z.; Wu, L. Z.; Tung, C. H.; Yang, Q. Z. BODIPY-Based Ratiometric Fluorescent Sensor for Highly Selective Detection of Glutathione over Cysteine and Homocysteine. *J. Am. Chem. Soc.* **2012**, *134*, 18928-18931.

(91) Zhu, B. C.; Zhang, X. L.; Li, Y. M.; Wang, P. F.; Zhang, H. Y.; Zhuang, X. Q. A colorimetric and ratiometric fluorescent probe for thiols and its bioimaging applications. *Chem. Commun.* **2010**, *46*, 5710-5712.

(92) Yang, Y. K.; Shim, S.; Tae, J. Rhodamine-sugar based turn-on fluorescent probe for the detection of cysteine and homocysteine in water. *Chem. Commun.* **2010**, *46*, 7766-7768.

(93) Dolmans, D. E. J. G. J.; Fukumura, D.; Jain, R. K. Photodynamic therapy for cancer. *Nat. Rev. Cancer* **2003**, *3*, 380-387.

(94) Daniell, M. D.; Hill, J. S. A History of Photodynamic Therapy. *Aust. Nz. J. Surg.* **1991**, *61*, 340-348.

(95) Ackroyd, R.; Kelty, C.; Brown, N.; Reed, M. The history of photodetection and photodynamic therapy. *Photochem. Photobiol.* **2001**, *74*, 656-669.

(96) Spikes, J. D.: *Primary Photoprocesses in Biology and Medicine*; Plenum Press: New York, **1985**.

(97) Raab, O. Uber die Wirkung fluoreszierender Stoffe auf Infusorien. *Zeitung Biol.* **1900**, *39*, 524-526.

(98) Finsen, N. R.: *Phototherapy*; Edward Arnold: London, **1901**.

(99) von Tappeiner, H.; Jodlbauer, A.: *Die sensiblilisierende Wirkung fluoreszierender Substanzer Gesammte Untersuchungen uber die photodynamische Erscheinerung*; Voger, F. C.: Leipzig, **1907**.

(100) Hausmann, W. Die sensiblisierende Wirkung des Hematoporphyrins. *Biochem. Zeitung* **1911**, *30*, 276-316.

(101) Meyer–Betz, F. Untersuchungen uber die biologische photodynamische Wirkung des Hematoporphyrins und anderer Derivative des Blut und Galenafarbstoffs. *Dtsch. Arch. Klin.* **1913**, *112*, 476-503.

(102) Lipson, R. L.; Baldes, E. J. The photodynamic properties of a particular hematoporphyrin derivative. *Arch. Dermatol.* **1960**, *82*, 508-516.

(103) Diamond, I. Photodynamic therapy of malignant tumours. *Lancet* **1972**, *2*, 1175-1177.

(104) Dougherty, T. J.; Grindey, G. B.; Fiel, R.; Weishaupt, K. R.; Boyle, D. G. Photoradiation therapy. II. Cure of animal tumors with hematoporphyrin and light. *J. Natl. Cancer Inst.* **1975**, *55*, 115–121.

(105) Dougherty, T. J. Photoradiation therapy for the treatment of malignant tumors. *Cancer Res.* **1978**, *38*, 2628-2635.

(106) Hayata, Y.; Kato, H.; Konaka, C.; Ono, J.; Takizawa, N. Hematoporphyrin derivative and laser photoradiation in the treatment of lung cancer. *Chest*. **1982**, *81*, 269–277.

(107) Agostinis, P.; Berg, K.; Cengel, K. A.; Foster, T. H.; Girotti, A. W.; Gollnick, S. O.; Hahn, S. M.; Hamblin, M. R.; Juzeniene, A.; Kessel, D.; Korbelik, M.; Moan, J.; Mroz, P.; Nowis, D.; Piette, J.; Wilson, B. C.; Golab, J. Photodynamic Therapy of Cancer: An Update. *Ca-Cancer J. Clin.* **2011**, *61*, 250-281.

(108) Zhao, J. Z.; Wu, W. H.; Sun, J. F.; Guo, S. Triplet photosensitizers: from molecular design to applications. *Chem. Soc. Rev.* **2013**, *42*, 5323-5351.

(109) Moan, J.; Berg, K. The Photodegradation of Porphyrins in Cells Can Be Used to Estimate the Lifetime of Singlet Oxygen. *Photochem. Photobiol.* **1991**, *53*, 549-553.

(110) Ogilby, P. R. Singlet oxygen: there is still something new under the sun, and it is better than ever. *Photoch. Photobio. Sci.* **2010**, *9*, 1543-1560.

(111) Juzeniene, A.; Nielsen, K. P.; Moan, J. Biophysical aspects of photodynamic therapy. *J. Environ. Pathol. Tox.* **2006**, *25*, 7-28.

(112) Castano, A. P.; Mroz, P.; Hamblin, M. R. Photodynamic therapy and anti-tumour immunity. *Nat. Rev. Cancer* **2006**, *6*, 535-545.

(113) Henderson, B. W.; Waldow, S. M.; Mang, T. S.; Potter, W. R.; Malone, P. B.; Dougherty, T. J. Tumor Destruction and Kinetics of Tumor-Cell Death in 2 Experimental Mouse-Tumors Following Photodynamic Therapy. *Cancer Res* **1985**, *45*, 572-576.

(114) Tromberg, B. J.; Orenstein, A.; Kimel, S.; Barker, S. J.; Hyatt, J.; Nelson, J. S.; Berns, M. W. Invivo Tumor Oxygen-Tension Measurements for the Evaluation of the Efficiency of Photodynamic Therapy. *Photochem. Photobiol.* **1990**, *52*, 375-385.

(115) Henderson, B. W.; Fingar, V. H. Oxygen Limitation of Direct Tumor-

Cell Kill during Photodynamic Treatment of a Murine Tumor-Model. *Photochem. Photobiol.* **1989**, *49*, 299-304.

(116) Dolmans, D. E. J. G. J.; Kadambi, A.; Hill, J. S.; Waters, C. A.; Robinson, B. C.; Walker, J. P.; Fukumura, D.; Jain, R. K. Vascular accumulation of a novel photosensitizer, MV6401, causes selective thrombosis in tumor vessels after photodynamic therapy. *Cancer Re.s* **2002**, *62*, 2151-2156.

(117) Ferrario, A.; von Tiehl, K. F.; Rucker, N.; Schwarz, M. A.; Gill, P. S.; Gomer, C. J. Antiangiogenic treatment enhances photodynamic therapy responsiveness in a mouse mammary carcinoma. *Cancer Res.* **2000**, *60*, 4066-4069.

(118) Henderson, B. W.; Dougherty, T. J. How Does Photodynamic Therapy Work. *Photochem. Photobiol.* **1992**, *55*, 145-157.

(119) deVree, W. J. A.; Essers, M. C.; deBruijn, H. S.; Star, W. M.; Koster, J. F.; Sluiter, W. Evidence for an important role of neutrophils in the efficacy of photodynamic therapy in vivo. *Cancer Res.* **1996**, *56*, 2908-2911.

(120) Turro, N. J.; Ramamurthy, V.; Scaiano, J. C.: *Principles of Molecular Photochemistry: An Introduction*; University Science Books: Sausalito, **2009**.

(121) Cakmak, Y.; Kolemen, S.; Duman, S.; Dede, Y.; Dolen, Y.; Kilic, B.; Kostereli, Z.; Yildirim, L. T.; Dogan, A. L.; Guc, D.; Akkaya, E. U. Designing Excited States: Theory-Guided Access to Efficient Photosensitizers for Photodynamic Action. *Angew. Chem. Int. Ed.* **2011**, *50*, 11937-11941.

(122) Chou, P. T.; Chi, Y.; Chung, M. W.; Lin, C. C. Harvesting luminescence via harnessing the photophysical properties of transition metal complexes. *Coord. Chem. Rev.* **2011**, *255*, 2653-2665.

(123) Kamkaew, A.; Lim, S. H.; Lee, H. B.; Kiew, L. V.; Chung, L. Y.; Burgess, K. BODIPY dyes in photodynamic therapy. *Chem. Soc. Rev.* **2013**, *42*, 77-88.

(124) Yalcin, S.; Thomas, L.; Tian, M. Q.; Seferoglu, N.; Ihmels, H.; Dede, Y. Switching Off the Charge Transfer and Closing the S-1-T-1 ISC Channel in Excited States of Quinolizinium Derivatives: A Theoretical Study. *J. Org. Chem.* **2014**, *79*, 3799-3808.

(125) Broring, M.; Kruger, R.; Link, S.; Kleeberg, C.; Kohler, S.; Xie, X.; Ventura, B.; Flamigni, L. Bis(BF(2))-2,2 '-bidipyrrins (BisBODIPYs): Highly fluorescent BODIPY dimers with large Stokes shifts. *Chem-Eur. J.* **2008**, *14*, 2976-2983.

(126) Ventura, B.; Marconi, G.; Broring, M.; Krugerb, R.; Flamigni, L. Bis(BF2)-2,2 '-bidipyrrins, a class of BODIPY dyes with new spectroscopic and photophysical properties. *New J. Chem.* **2009**, *33*, 428-438.

(127) Huang, L.; Yu, X. R.; Wu, W. H.; Zhao, J. Z. Styryl Bodipy-C-60 Dyads as Efficient Heavy-Atom-Free Organic Triplet Photosensitizers. *Org. Lett.* **2012**, *14*, 2594-2597.

(128) Shirasu, N.; Nam, S. O.; Kuroki, M. Tumor-targeted Photodynamic Therapy. *Anticancer Res.* **2013**, *33*, 2823-2831.

(129) Choi, Y.; Weissleder, R.; Tung, C. H. Selective antitumor effect of novel protease-mediated photodynamic agent. *Cancer Res.* **2006**, *66*, 7225-7229.

(130) McDonnell, S. O.; Hall, M. J.; Allen, L. T.; Byrne, A.; Gallagher, W. M.; O'Shea, D. F. Supramolecular photonic therapeutic agents. *J. Am. Chem. Soc.* **2005**, *127*, 16360-16361.

(131) Lovell, J. F.; Chen, J.; Jarvi, M. T.; Cao, W. G.; Allen, A. D.; Liu, Y.; Tidwell, T. T.; Wilson, B. C.; Zheng, G. FRET Quenching of Photosensitizer Singlet Oxygen Generation. *J. Phys. Chem. B* **2009**, *113*, 3203-3211.

(132) Chen, J.; Jarvi, M.; Lo, P. C.; Stefflova, K.; Wilson, B. C.; Zheng, G. Using the singlet oxygen scavenging property of carotenoid in photodynamic molecular beacons to minimize photodamage to non-targeted cells. *Photoch. Photobio. Sci.* **2007**, *6*, 1311-1317.

(133) Chaiswing, L.; Oberley, T. D. Extracellular/Microenvironmental Redox State. *Antioxid. Redox Sign.* **2010**, *13*, 449-465.

(134) Yeh, C. C.; Hou, M. F.; Wu, S. H.; Tsai, S. M.; Lin, S. K.; Hou, L. A.; Ma, H.; Tsai, L. Y. A study of glutathione status in the blood and tissues of patients with breast cancer. *Cell Biochem. Funct.* **2006**, *24*, 555-559.

(135) He, H.; Lo, P. C.; Ng, D. K. P. A Glutathione-Activated Phthalocyanine-Based Photosensitizer for Photodynamic Therapy. *Chem-Eur. J.* **2014**, *20*, 6241-6245.

(136) Cho, Y.; Choi, Y. Graphene oxide-photosensitizer conjugate as a redox-responsive theranostic agent. *Chem. Commun.* **2012**, *48*, 9912-9914.

(137) Warburg, O. On the origin of cancer cells. *Science* **1956**, *123*, 309-314.

(138) Cahn, R. S.; Ingold, C.; Prelog, V. Specification of Molecular Chirality. *Angew. Chem. Int. Ed.* **1966**, *5*, 385-415.

(139) Eliel, E. L.; Wilen, S. H.; Mander, L. N.: *Stereochemistry of organic compounds*; Wiley: New York, **1994**.

(140) Kobayashi, N.; Muranaka, A.; Mack, J.: *Circular Dichroism and Magnetic Circular Dichroism Spectroscopy for Organic Chemists*; The Royal Society of Chemistry: United Kingdom, **2012**.

(141) Moss, G. P. Basic terminology of stereochemistry. *Pure Appl. Chem.* **1996**, *68*, 2193-2222.

(142) Baker, R. W.; Brkic, Z.; Sargent, M. V.; Skelton, B. W.; White, A. H. Atropisomerism of 2,2 '-binaphthalenes. *Aust. J. Chem.* **2000**, *53*, 925-938.

(143) Kuhn, R.: *Stereochemie*; Franz Deuticke: Leipzig, **1933**.

(144) Oki, M.: *Topics in Sterochemistry*; Wiley Interscience: New York, **1983**.

(145) Lin, J.; Zhang, H. C.; Pu, L. Bisbinaphthyl macrocycle-based highly enantioselective fluorescent sensors for alpha-hydroxycarboxylic acids. *Org. Lett.* **2002**, *4*, 3297-3300.

(146) Pu, L. Fluorescence of organic molecules in chiral recognition. *Chem. Rev.* **2004**, *104*, 1687-1716.

(147) Liu, H. L.; Peng, Q.; Wu, Y. D.; Chen, D.; Hou, X. L.; Sabat, M.; Pu, L. Highly Enantioselective Recognition of Structurally Diverse alpha-Hydroxycarboxylic Acids using a Fluorescent Sensor. *Angew. Chem. Int. Ed.* **2010**, *49*, 602-606.

(148) Haefele, A.; Zedde, C.; Retailleau, P.; Ulrich, G.; Ziessel, R. Boron Asymmetry in a BODIPY Derivative. *Org. Lett.* **2010**, *12*, 1672-1675.

(149) Beer, G.; Rurack, K.; Daub, J. Chiral discrimination with a fluorescent boron-dipyrromethene dye. *Chem. Commun.* **2001**, 1138-1139.

(150) Kolemen, S.; Cakmak, Y.; Kostereli, Z.; Akkaya, E. U. Atropisomeric

Dyes: Axial Chirality in Orthogonal BODIPY Oligomers. *Org. Lett.* **2014**, *16*, 660-663.

(151) Lerrick, R. I.; Winstanley, T. P. L.; Haggerty, K.; Wills, C.; Clegg, W.; Harrington, R. W.; Bultinck, P.; Herrebout, W.; Benniston, A. C.; Hall, M. J. Axially chiral BODIPYs. *Chem. Commun.* **2014**, *50*, 4714-4716.

(152) Aubry, J. M.; Pierlot, C.; Rigaudy, J.; Schmidt, R. Reversible binding of oxygen to aromatic compounds. *Acc. Chem. Res.* **2003**, *36*, 668-675.

(153) Saito, I.; Matsuura, T.; Inoue, K. Formation of Superoxide Ion from Singlet Oxygen - on the Use of a Water-Soluble Singlet Oxygen Source. *J. Am. Chem. Soc.* **1981**, *103*, 188-190.

(154) Bloodworth, A. J.; J., E. H.: *Endoperoxides In Singlet O2*; Boca Raton: Florida, **1985**.

(155) Stevens, B.; Perez, S. R.; Ors, J. A. Photoperoxidation of unsaturated organic molecules. XIV. 1O2 acceptor properties and reactivity. *J. Am. Chem. Soc.* **1974**, *96*, 6846-6850.

(156) Erden, I.; Golitz, P.; Nader, R.; Demeijere, A. Novel Molecules of the Phane-Type with Para-Benzoquinone and Oxahomobenzene Moieties. *Angew. Chem. Int. Ed.* **1981**, *20*, 583-585.

(157) Bobrowski, M.; Liwo, A.; Oldziej, S.; Jeziorek, D.; Ossowski, T. CAS MCSCF/CAS MCQDPT2 study of the mechanism of singlet oxygen addition to 1,3-butadiene and benzene. *J. Am. Chem. Soc.* **2000**, *122*, 8112-8119.

(158) Turro, N. J.; Chow, M. F.; Rigaudy, J. Mechanism of Thermolysis of Endoperoxides of Aromatic-Compounds - Activation Parameters, Magnetic-Field, and Magnetic Isotope Effects. *J. Am. Chem. Soc.* **1981**, *103*, 7218-7224.

(159) Saito, I.; Nagata, R.; Nakagawa, H.; Moriyama, H.; Matsuura, T.; Inoue, K. New singlet oxygen source and trapping reagent for peroxide intermediates. *Free Radical Res. Com.* **1987**, *2*, 327-336.

(160) Slavetinska, L.; Mosinger, J.; Kubat, P. Supramolecular carriers of singlet oxygen: Photosensitized formation and thermal decomposition of endoperoxides in the presence of cyclodextrins. *J. Photoch. Photobio. A* **2008**, *195*, 1-9.

(161) Drexler, K. E.: *Nanosystems: molecular machinery, manufacturing, and computation*; Wiley, **1992**.

(162) Haberlen, O. D.; Chung, S. C.; Stener, M.; Rosch, N. From clusters to bulk: A relativistic density functional investigation on a series of gold clusters Au-n, n=6, ..., 147. *J. Chem. Phys.* **1997**, *106*, 5189-5201.

(163) de Abajo, F. J. G. Nonlocal Effects in the Plasmons of Strongly Interacting Nanoparticles, Dimers, and Waveguides. *J. Phys. Chem. C* **2008**, *112*, 17983-17987.

(164) Huang, X. H.; Neretina, S.; El-Sayed, M. A. Gold Nanorods: From Synthesis and Properties to Biological and Biomedical Applications. *Adv. Mater.* **2009**, *21*, 4880-4910.

(165) Chen, H. J.; Shao, L.; Li, Q.; Wang, J. F. Gold nanorods and their plasmonic properties. *Chem. Soc. Rev.* **2013**, *42*, 2679-2724.

(166) Minelli, C.; Lowe, S. B.; Stevens, M. M. Engineering Nanocomposite Materials for Cancer Therapy. *Small* **2010**, *6*, 2336-2357.

(167) Gole, A.; Murphy, C. J. Seed-mediated synthesis of gold nanorods:

Role of the size and nature of the seed. *Chem. Mater.* **2004**, *16*, 3633-3640.

(168) Yu, Y. Y.; Chang, S. S.; Lee, C. L.; Wang, C. R. C. Gold nanorods: Electrochemical synthesis and optical properties. *J. Phys. Chem. B* **1997**, *101*, 6661-6664.

(169) Cao, J. M.; Ma, X. J.; Zheng, M. B.; Liu, J. S.; Ji, H. M. Solvothermal preparation of single-crystalline gold nanorods in novel nonaqueous microemulsions. *Chem. Lett.* **2005**, *34*, 730-731.

(170) Zhu, Y. J.; Hu, X. L. Microwave-polyol preparation of single-crystalline gold nanorods and nanowires. *Chem. Lett.* **2003**, *32*, 1140-1141.

(171) Kim, F.; Song, J. H.; Yang, P. D. Photochemical synthesis of gold nanorods. *J. Am. Chem. Soc.* **2002**, *124*, 14316-14317.

(172) Jana, N. R.; Gearheart, L.; Murphy, C. J. Seed-mediated growth approach for shape-controlled synthesis of spheroidal and rod-like gold nanoparticles using a surfactant template. *Adv. Mater.* **2001**, *13*, 1389-1393.

(173) Nikoobakht, B.; El-Sayed, M. A. Preparation and growth mechanism of gold nanorods (NRs) using seed-mediated growth method. *Chem. Mater.* **2003**, *15*, 1957-1962.

(174) Vigderman, L.; Khanal, B. P.; Zubarev, E. R. Functional Gold Nanorods: Synthesis, Self-Assembly, and Sensing Applications. *Adv. Mater.* **2012**, *24*, 4811-4841.

(175) Gomez-Grana, S.; Hubert, F.; Testard, F.; Guerrero-Martinez, A.; Grillo, I.; Liz-Marzan, L. M.; Spalla, O. Surfactant (Bi)Layers on Gold Nanorods. *Langmuir* **2012**, *28*, 1453-1459.

(176) Kou, X. S.; Zhang, S. Z.; Yang, Z.; Tsung, C. K.; Stucky, G. D.; Sun, L. D.; Wang, J. F.; Yan, C. H. Glutathione- and cysteine-induced transverse overgrowth on gold nanorods. *J. Am. Chem. Soc.* **2007**, *129*, 6402-6404.

(177) Caswell, K. K.; Wilson, J. N.; Bunz, U. H. F.; Murphy, C. J. Preferential end-to-end assembly of gold nanorods by biotin-streptavidin connectors. *J. Am. Chem. Soc.* **2003**, *125*, 13914-13915.

(178) Gole, A.; Murphy, C. J. Polyelectrolyte-coated gold nanorods: Synthesis, characterization and immobilization. *Chem. Mater.* **2005**, *17*, 1325-1330.

(179) Chen, H. J.; Shao, L.; Ming, T. A.; Sun, Z. H.; Zhao, C. M.; Yang, B. C.; Wang, J. F. Understanding the Photothermal Conversion Efficiency of Gold Nanocrystals. *Small* **2010**, *6*, 2272-2280.

(180) Jang, B.; Kim, Y. S.; Choi, Y. Effects of gold nanorod concentration on the depth-related temperature increase during hyperthermic ablation. *Small* **2011**, *7*, 265-270.

(181) Baffou, G.; Girard, C.; Quidant, R. Mapping Heat Origin in Plasmonic Structures. *Phys. Rev. Lett.* **2010**, *104*.

(182) Jaque, D.; Martinez Maestro, L.; Del Rosal, B.; Haro-Gonzalez, P.; Benayas, A.; Plaza, J. L.; Martin Rodriguez, E.; Garcia Sole, J. Nanoparticles for photothermal therapies. *Nanoscale* **2014**, *6*, 9494-9530.

(183) Huang, X. H.; El-Sayed, I. H.; Qian, W.; El-Sayed, M. A. Cancer cell imaging and photothermal therapy in the near-infrared region by using gold nanorods. *J. Am. Chem. Soc.* **2006**, *128*, 2115-2120.

(184) Jang, B.; Park, J. Y.; Tung, C. H.; Kim, I. H.; Choi, Y. Gold Nanorod-Photosensitizer Complex for Near-Infrared Fluorescence Imaging and

Photodynamic/Photothermal Therapy In Vivo. *ACS Nano* **2011**, *5*, 1086-1094.

(185) Isik, M.; Guliyev, R.; Kolemen, S.; Altay, Y.; Senturk, B.; Tekinay, T.; Akkaya, E. U. Designing an Intracellular Fluorescent Probe for Glutathione: Two Modulation Sites for Selective Signal Transduction. *Org. Lett.* **2014**, *16*, 3260-3263.

(186) Xu, Z. C.; Yoon, J.; Spring, D. R. Fluorescent chemosensors for Zn2+. *Chem. Soc. Rev.* **2010**, *39*, 1996-2006.

(187) Sessler, J. L.; Lawrence, C. M.; Jayawickramarajah, J. Molecular recognition via base-pairing. *Chem. Soc. Rev.* **2007**, *36*, 314-325.

(188) Domaille, D. W.; Que, E. L.; Chang, C. J. Synthetic fluorescent sensors for studying the cell biology of metals. *Nat. Chem. Biol.* **2008**, *4*, 168-175.

(189) Guo, Y.; Yang, X.; Hakuna, L.; Barve, A.; Escobedo, J. O.; Lowry, M.; Strongin, R. M. A fast response highly selective probe for the detection of glutathione in human blood plasma. *Sensors* **2012**, *12*, 5940-5950.

(190) Bozdemir, O. A.; Guliyev, R.; Buyukcakir, O.; Selcuk, S.; Kolemen, S.; Gulseren, G.; Nalbantoglu, T.; Boyaci, H.; Akkaya, E. U. Selective Manipulation of ICT and PET Processes in Styryl-Bodipy Derivatives: Applications in Molecular Logic and Fluorescence Sensing of Metal Ions. *J. Am. Chem. Soc.* **2010**, *132*, 8029-8036.

(191) Bozdemir, O. A.; Sozmen, F.; Buyukcakir, O.; Guliyev, R.; Cakmak, Y.; Akkaya, E. U. Reaction-Based Sensing of Fluoride Ions Using Built-in Triggers for Intramolecular Charge Transfer and Photoinduced Electron Transfer. *Org. Lett.* **2010**, *12*, 1400-1403.

(192) Gotor, R.; Costero, A. M.; Gavina, P.; Gil, S.; Parra, M. Binding and Fluorescent Sensing of Dicarboxylates by a Bis(calix[4]pyrrole)-Substituted BODIPY Dye. *Eur. J. Org. Chem.* **2013**, 1515-1520.

(193) Niu, L. Y.; Guan, Y. S.; Chen, Y. Z.; Wu, L. Z.; Tung, C. H.; Yang, Q. Z. A turn-on fluorescent sensor for the discrimination of cystein from homocystein and glutathione. *Chem. Commun.* **2013**, *49*, 1294-1296.

(194) Gabe, Y.; Urano, Y.; Kikuchi, K.; Kojima, H.; Nagano, T. Highly sensitive fluorescence probes for nitric oxide based on boron dipyrromethene chromophore-rational design of potentially useful bioimaging fluorescence probe. *J. Am. Chem. Soc.* **2004**, *126*, 3357-3367.

(195) Kobayashi, T.; Komatsu, T.; Kamiya, M.; Campos, C.; Gonzalez-Gaitan, M.; Terai, T.; Hanaoka, K.; Nagano, T.; Urano, Y. Highly Activatable and Environment-Insensitive Optical Highlighters for Selective Spatiotemporal Imaging of Target Proteins. *J. Am. Chem. Soc.* **2012**, *134*, 11153-11160.

(196) Jacques, P. F.; Selhub, J.; Bostom, A. G.; Wilson, P. W. F.; Rosenberg, I. H. The effect of folic acid fortification on plasma folate and total homocysteine concentrations. *New Engl. J. Med.* **1999**, *340*, 1449-1454.

(197) Droge, W.; Eck, H. P.; Mihm, S. Hiv-Induced Cysteine Deficiency and T-Cell Dysfunction - a Rationale for Treatment with N-Acetylcysteine. *Immunol. Today* **1992**, *13*, 211-214.

(198) Drew, R.; Miners, J. O. The Effects of Buthionine Sulfoximine (Bso) on Glutathione Depletion and Xenobiotic Biotransformation. *Biochem. Pharmacol.* **1984**, *33*, 2989-2994.

(199) Wang, Y. W.; Yu, M. X.; Yu, Y. H.; Bai, Z. P.; Shen, Z.; Li, F. Y.; You, X. Z. A colorimetric and fluorescent turn-on chemosensor for Al3+ and its

application in bioimaging. *Tetrahedron Lett.* **2009**, *50*, 6169-6172.

(200) Lovell, J. F.; Liu, T. W. B.; Chen, J.; Zheng, G. Activatable Photosensitizers for Imaging and Therapy. *Chem. Rev.* **2010**, *110*, 2839-2857.

(201) Adarsh, N.; Avirah, R. R.; Ramaiah, D. Tuning Photosensitized Singlet Oxygen Generation Efficiency of Novel Aza-BODIPY Dyes. *Org. Lett.* **2010**, *12*, 5720-5723.

(202) Lim, S. H.; Thivierge, C.; Nowak-Sliwinska, P.; Han, J. Y.; van den Bergh, H.; Wagnieres, G.; Burgess, K.; Lee, H. B. In Vitro and In Vivo Photocytotoxicity of Boron Dipyrromethene Derivatives for Photodynamic Therapy. *J. Med. Chem.* **2010**, *53*, 2865-2874.

(203) Salem, L.; Rowland, C. The Electronic Properties of Diradicals. *Angew. Chem. Int. Ed.* **1972**, *11*, 92-111.

(204) Michl, J. Spin-orbit coupling in biradicals .1. The 2-electrons-in-2-orbitals model revisited. *J. Am. Chem. Soc.* **1996**, *118*, 3568-3579.

(205) Krumova, K.; Cosa, G. Bodipy Dyes with Tunable Redox Potentials and Functional Groups for Further Tethering: Preparation, Electrochemical, and Spectroscopic Characterization. *J. Am. Chem. Soc.* **2010**, *132*, 17560-17569.

(206) Mirenda, M.; Strassert, C. A.; Dicelio, L. E.; Roman, E. S. Dye-Polyelectrolyte Layer-by-Layer Self-Assembled Materials: Molecular Aggregation, Structural Stability, and Singlet Oxygen Photogeneration. *ACS Appl. Mater. Inter.* **2010**, *2*, 1556-1560.

(207) Hanson, K.; Roskop, L.; Djurovich, P. I.; Zahariev, F.; Gordon, M. S.; Thompson, M. E. A Paradigm for Blue- or Red-Shifted Absorption of Small Molecules Depending on the Site of pi-Extension. *J. Am. Chem. Soc.* **2010**, *132*, 16247-16255.

(208) Chen, L. X.; Jager, W. J. H.; Niemczyk, M. P.; Wasielewski, M. R. Effects of pi-conjugation attenuation on the photophysics and exciton dynamics of poly(p-phenylenevinylene) polymers incorporating 2,2 '-bipyridines. *J. Phys. Chem. A* **1999**, *103*, 4341-4351.

(209) Larson, J. R.; Epiotis, N. D.; Mcmurchie, L. E.; Shaik, S. S. On the Role of Spin Inversion in the Triplet Photochemistry of Benzyl Halides and Benzylammonium Salts. *J. Org. Chem.* **1980**, *45*, 1388-1393.

(210) Saebo, S.; Pulay, P. Local Treatment of Electron Correlation. *Annu. Rev. Phys. Chem.* **1993**, *44*, 213-236.

(211) Martinez, G. R.; Garcia, F.; Catalani, L. H.; Cadet, J.; Oliveira, M. C. B.; Ronsein, G. E.; Miyarnoto, S.; Medeiros, M. H. G.; Di Mascio, P. Synthesis of a hydrophilic and non-ionic anthracene derivative, the N,N '-di-(2,3-dihydroxypropyl)-9,10-anthracenedipropanamide as a chemical trap for singlet molecular oxygen detection in biological systems. *Tetrahedron* **2006**, *62*, 10762-10770.

(212) Becke, A. D. Density-Functional Thermochemistry .3. The Role of Exact Exchange. *J. Chem. Phys.* **1993**, *98*, 5648-5652.

(213) Stevens, W. J.; Basch, H.; Krauss, M. Compact Effective Potentials and Efficient Shared-Exponent Basis-Sets for the 1st-Row and 2nd-Row Atoms. *J. Chem. Phys.* **1984**, *81*, 6026-6033.

(214) Frisch, M. J. e. a.: Gaussian03. Gaussian Inc.: Wallingford, **2004**.

(215) Aquilante, F.; De Vico, L.; Ferre, N.; Ghigo, G.; Malmqvist, P. A.; Neogrady, P.; Pedersen, T. B.; Pitonak, M.; Reiher, M.; Roos, B. O.; Serrano-

Andres, L.; Urban, M.; Veryazov, V.; Lindh, R. Software News and Update MOLCAS 7: The Next Generation. *J. Comput. Chem.* **2010**, *31*, 224-247.

(216) Schmidt, M. W.; Baldridge, K. K.; Boatz, J. A.; Elbert, S. T.; Gordon, M. S.; Jensen, J. H.; Koseki, S.; Matsunaga, N.; Nguyen, K. A.; Su, S. J.; Windus, T. L.; Dupuis, M.; Montgomery, J. A. General Atomic and Molecular Electronic-Structure System. *J. Comput. Chem.* **1993**, *14*, 1347-1363.

(217) Macrae, C. F.; Edgington, P. R.; McCabe, P.; Pidcock, E.; Shields, G. P.; Taylor, R.; Towler, M.; van De Streek, J. Mercury: visualization and analysis of crystal structures. *J. Appl. Crystallogr.* **2006**, *39*, 453-457.

(218) Huang, Z. A review of progress in clinical photodynamic therapy. *Technol. Cancer Res. T.* **2005**, *4*, 283-293.

(219) Majumdar, P.; Nomula, R.; Zhao, J. Z. Activatable triplet photosensitizers: magic bullets for targeted photodynamic therapy. *J. Mater. Chem. C* **2014**, *2*, 5982-5997.

(220) Erbas-Cakmak, S.; Bozdemir, O. A.; Cakmak, Y.; Akkaya, E. U. Proof of principle for a molecular 1:2 demultiplexer to function as an autonomously switching theranostic device. *Chem. Sci.* **2013**, *4*, 858-862.

(221) Liu, T. C.; Wu, L. Y.; Choi, J. K.; Berkman, C. E. Targeted photodynamic therapy for prostate cancer: Inducing apoptosis via activation of the caspase-8/-3 cascade pathway. *Int. J. Oncol.* **2010**, *36*, 777-784.

(222) Meissner, J. W. G.; Vanderlaan, A. C.; Pandit, U. K. Reduction of 5-Arylidenebarbiturate Derivatives by Thiols. *Tetrahedron Lett.* **1994**, *35*, 2757-2760.

(223) Zhang, X. F.; Yang, X. D. Photosensitizer That Selectively Generates Singlet Oxygen in Nonpolar Environments: Photophysical Mechanism and Efficiency for a Covalent BODIPY Dimer. *J. Phys. Chem. B* **2013**, *117*, 9050-9055.

(224) Carmichael, I.; Hug, G. L. Triplet-Triplet Absorption-Spectra of Organic-Molecules in Condensed Phases. *J. Phys. Chem. Ref. Data* **1986**, *15*, 1-250.

(225) Baglan, M.; Ozturk, S.; Gur, B.; Meral, K.; Bozkaya, U.; Bozdemir, O. A.; Atilgan, S. Novel phenomena for aggregation induced emission enhancement: highly fluorescent hydrophobic TPE-BODIPY couples in both organic and aqueous media. *Rsc. Adv.* **2013**, *3*, 15866-15874.

(226) Sunahara, H.; Urano, Y.; Kojima, H.; Nagano, T. Design and synthesis of a library of BODIPY-based environmental polarity sensors utilizing photoinduced electron-transfer-controlled fluorescence ON/OFF switching. *J. Am. Chem. Soc.* **2007**, *129*, 5597-5604.

(227) Duman, S.; Cakmak, Y.; Kolemen, S.; Akkaya, E. U.; Dede, Y. Heavy Atom Free Singlet Oxygen Generation: Doubly Substituted Configurations Dominate S-1 States of Bis-BODIPYs. *J. Org. Chem.* **2012**, *77*, 4516-4527.

(228) Gossauer, A.; Nydegger, F.; Kiss, T.; Sleziak, R.; Stoeckli-Evans, H. Synthesis, chiroptical properties, and solid-state structure determination of two new chiral dipyrrin difluoroboryl chelates. *J. Am. Chem. Soc.* **2004**, *126*, 1772-1780.

(229) Ikeda, C.; Maruyama, T.; Nabeshima, T. Convenient and highly efficient synthesis of boron-dipyrrins bearing an arylboronate center. *Tetrahedron Lett.* **2009**, *50*, 3349-3351.

(230) Kim, H.; Burghart, A.; Welch, M. B.; Reibenspies, J.; Burgess, K. Synthesis and spectroscopic properties of a new 4-bora-3a,4a-diaza-s-indacene (BODIPY (R)) dye. *Chem. Commun.* **1999**, 1889-1890.

APPENDIX

A.1. Selective Fluorescence Sensing of Glutathione Using a Bifunctional Probe

A.1.1. ^{1}H and ^{13}C NMR Spectra

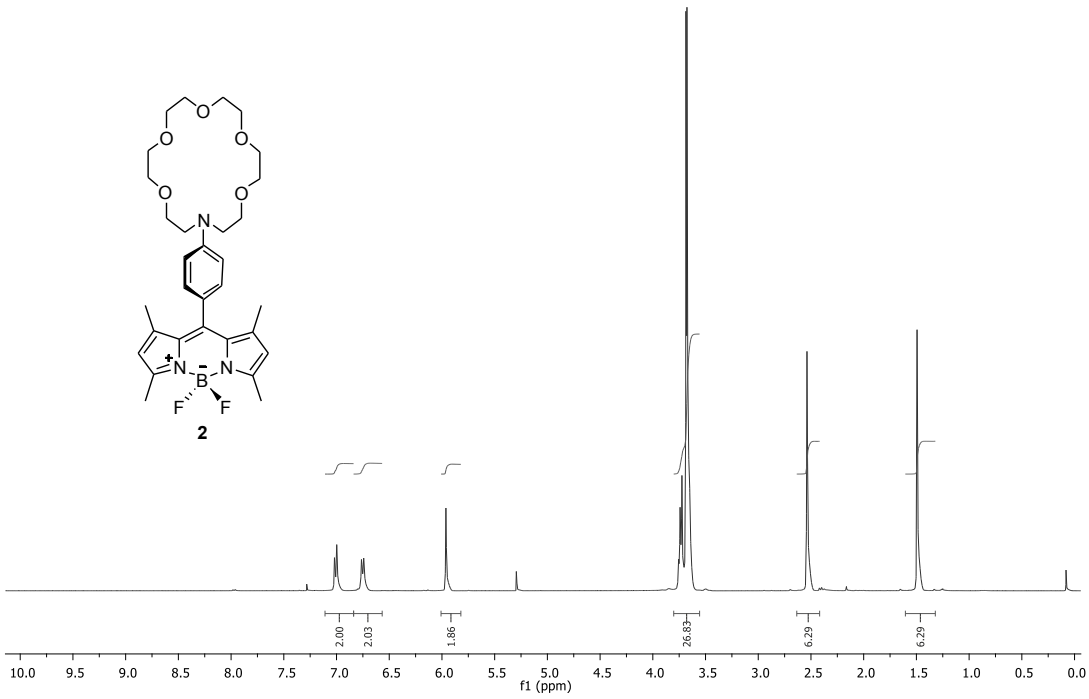

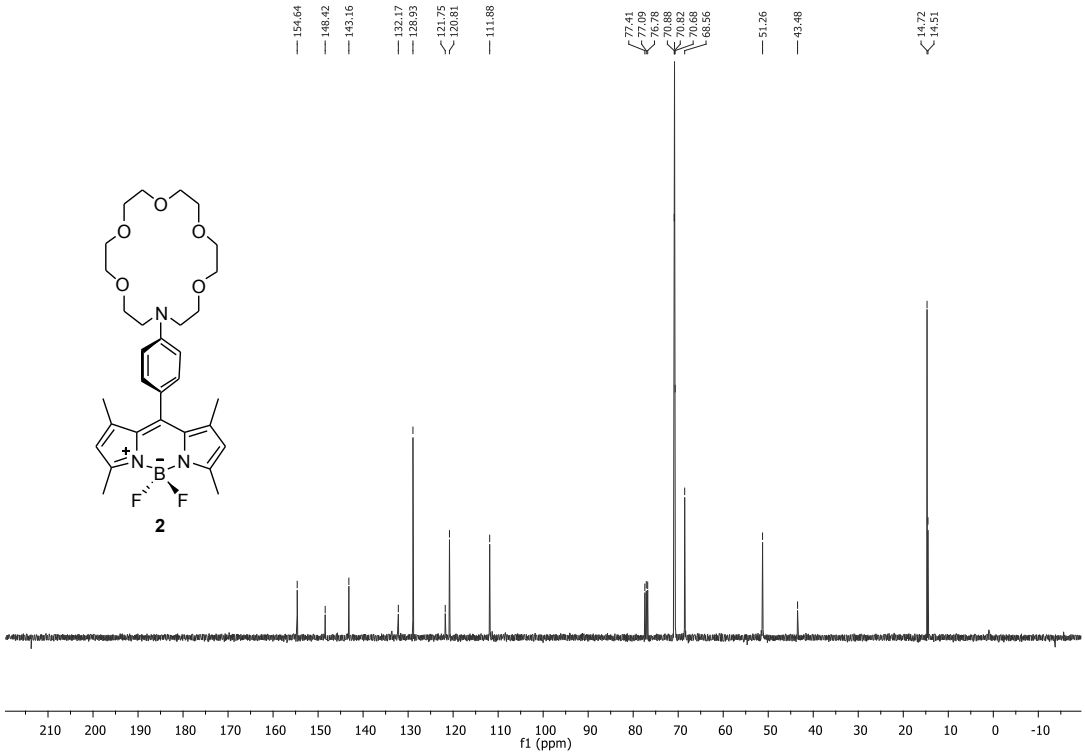
154.64
148.42
143.16
132.17
128.93
121.75
120.81
111.88
77.41
77.09
76.78
70.88
70.82
70.68
68.56
51.26
43.48
14.72
14.51
2
f1 (ppm)

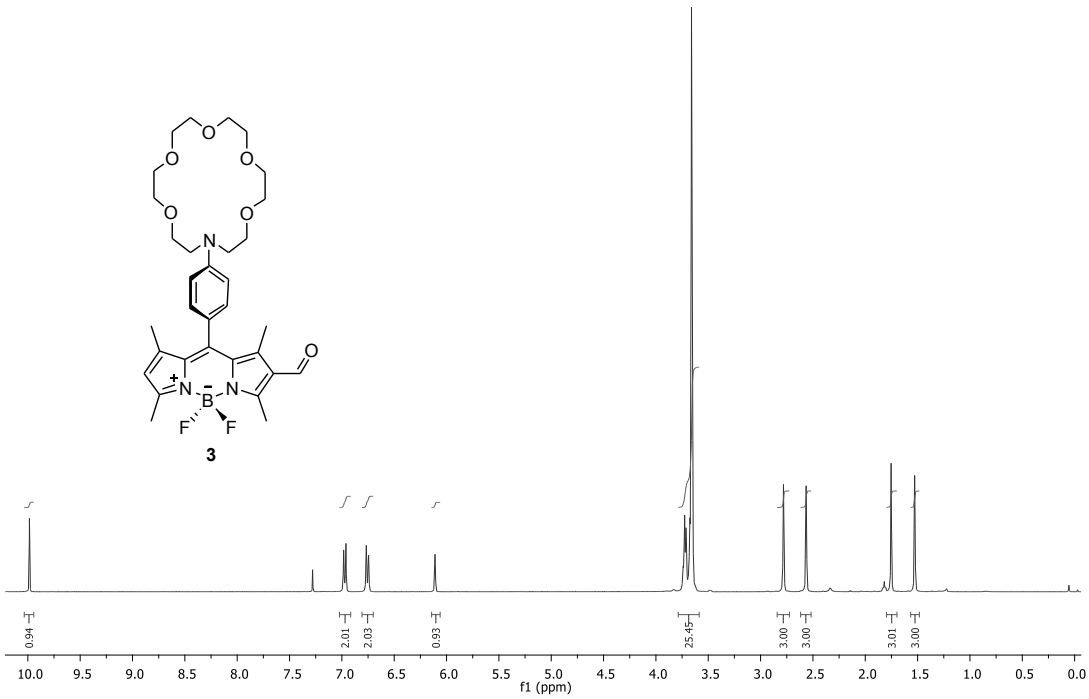
3
0.94
2.01
2.03
0.93
25.45
3.00
3.00
3.01
3.00
f1 (ppm)

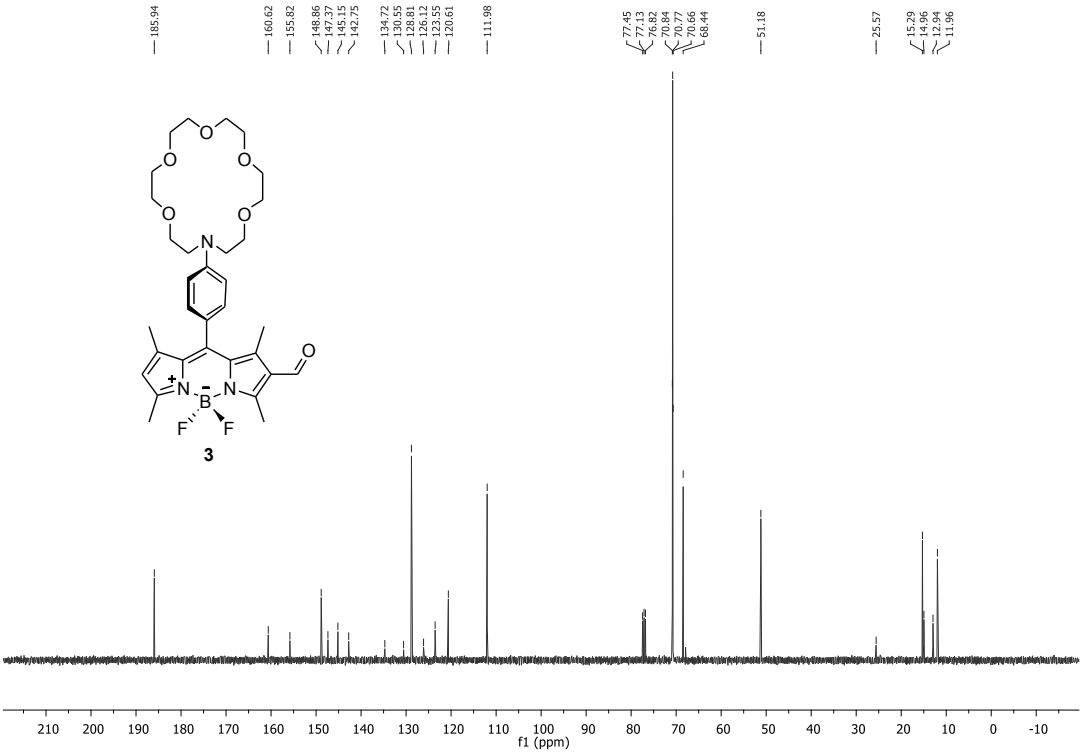
185.94
160.62
155.82
148.86
147.37
145.15
142.75
134.72
130.55
128.81
126.12
123.55
120.61
111.98
77.45
77.13
76.82
70.84
70.77
70.66
68.44
51.18
25.57
15.29
14.96
13.94
11.96
O
N
B
F
F
3
f1 (ppm)

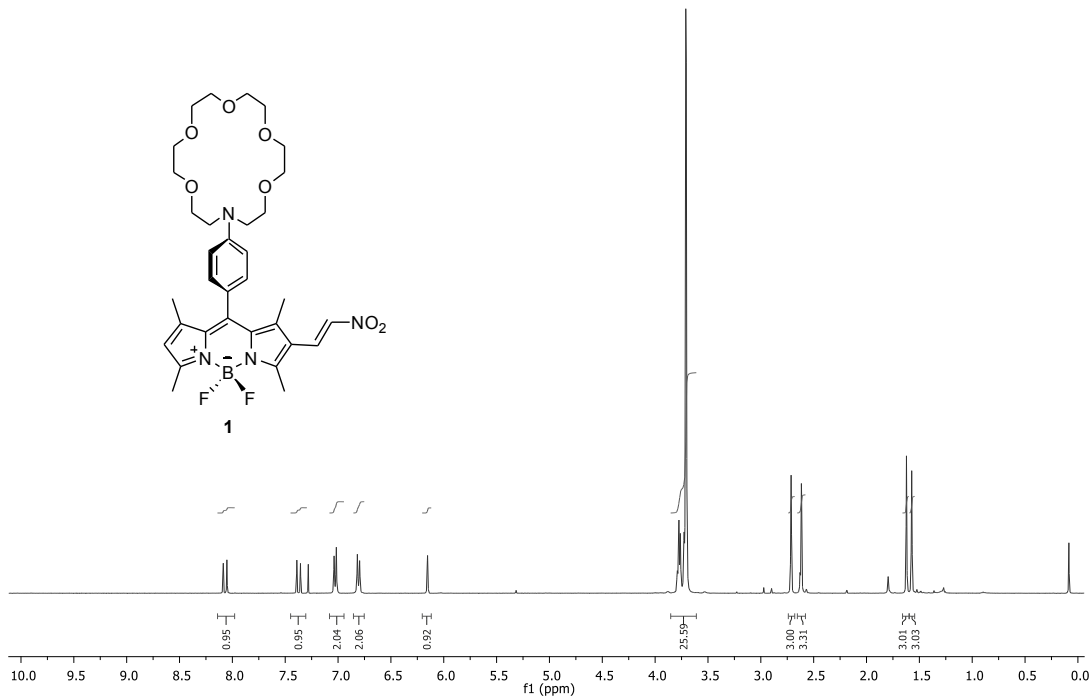
NO2
1
0.95
0.95
2.04
2.06
0.92
25.59
3.00
3.31
3.01
3.03
f1 (ppm)

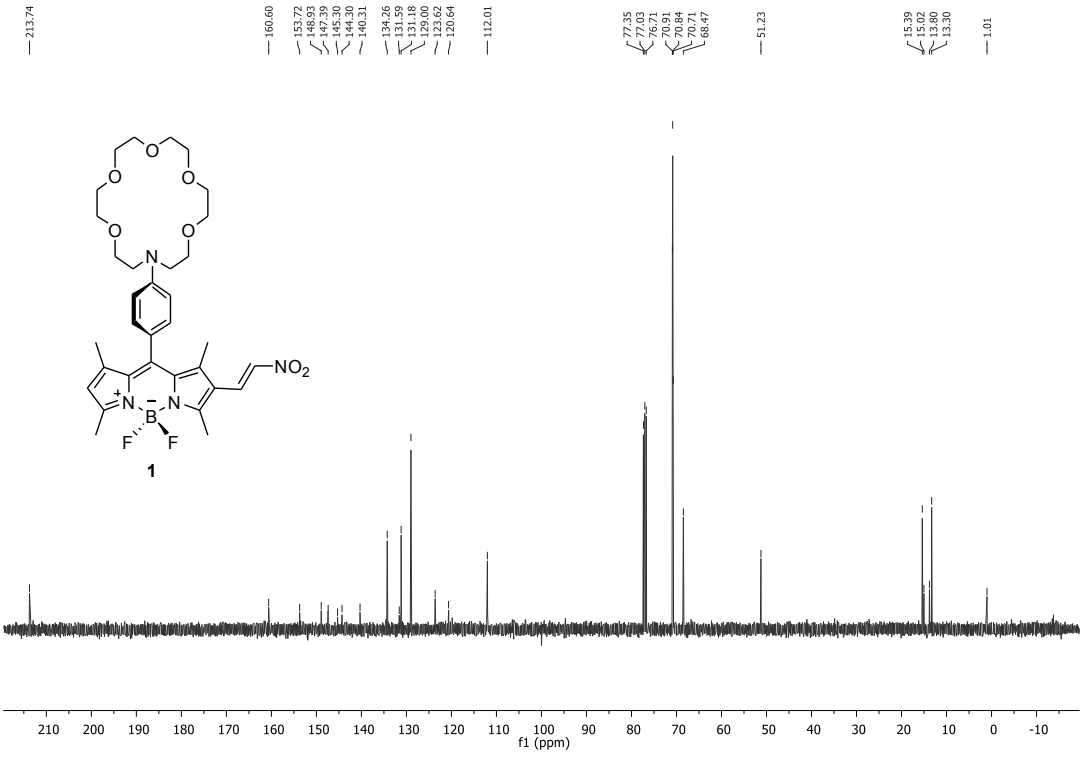
213.74
160.60
153.72
148.93
147.39
145.30
144.30
140.31
134.26
131.59
131.18
129.00
123.62
120.64
112.01
77.35
77.03
76.71
70.91
70.84
70.71
68.47
51.23
15.39
15.02
13.80
13.30
1.01
NO2
1
f1 (ppm)

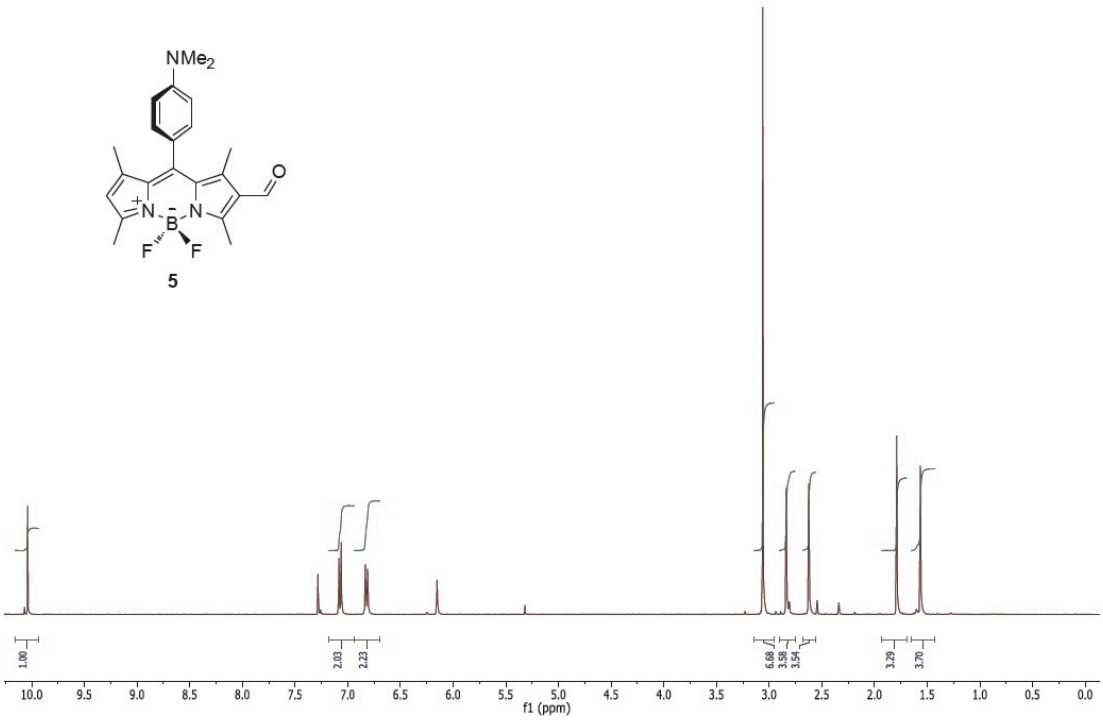
NMe2
O
5
1.00
2.03
2.23
6.68
3.58
3.54
3.29
3.70
f1 (ppm)

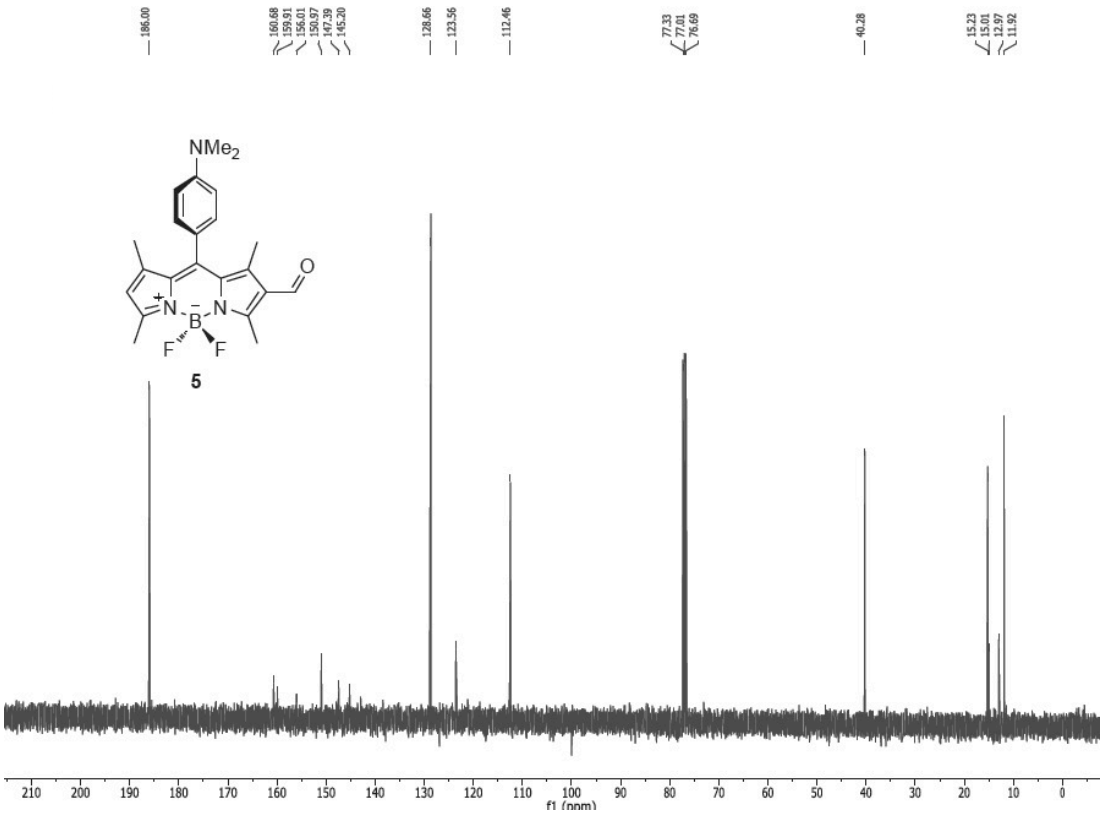
186.00
160.68
159.91
156.01
150.97
147.39
145.20
128.66
123.56
112.46
77.33
77.01
76.69
40.28
15.23
15.01
12.97
11.92
NMe2
O
N
B
N
F
F
5
210 200 190 180 170 160 150 140 130 120 110 100 90 80 70 60 50 40 30 20 10 0
f1 (ppm)

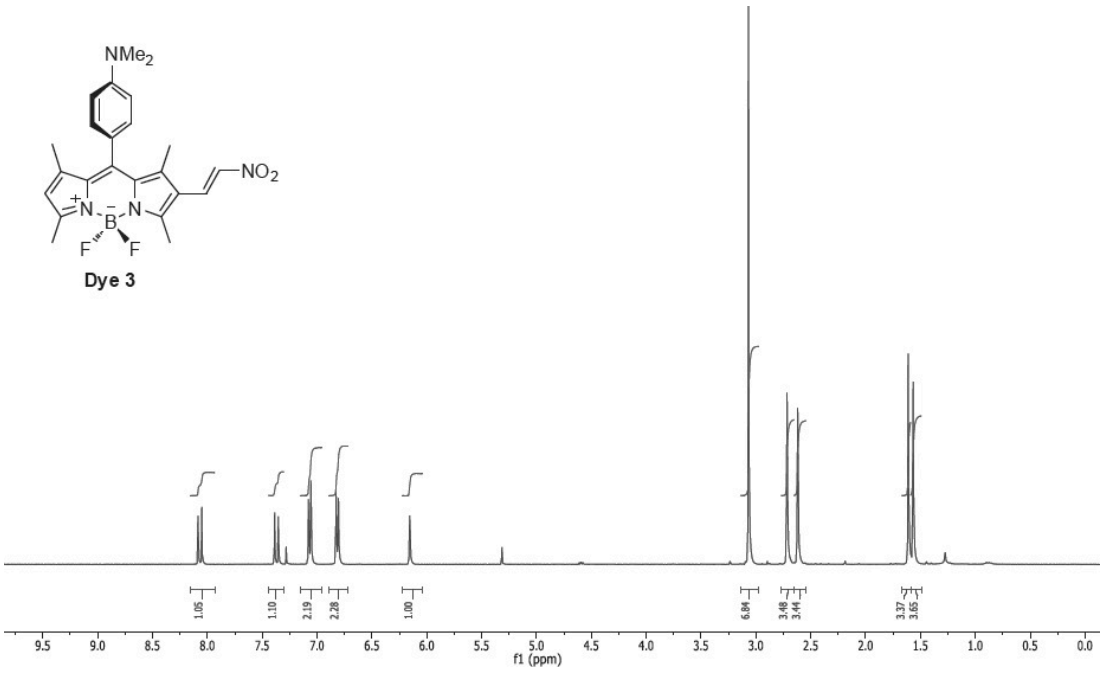
NMe2
NO2
N
B
N
F
F
Dye 3
1.05
1.10
2.19
2.28
1.00
6.84
3.48
3.44
3.37
3.65
9.5 9.0 8.5 8.0 7.5 7.0 6.5 6.0 5.5 5.0 4.5 4.0 3.5 3.0 2.5 2.0 1.5 1.0 0.5 0.0
f1 (ppm)

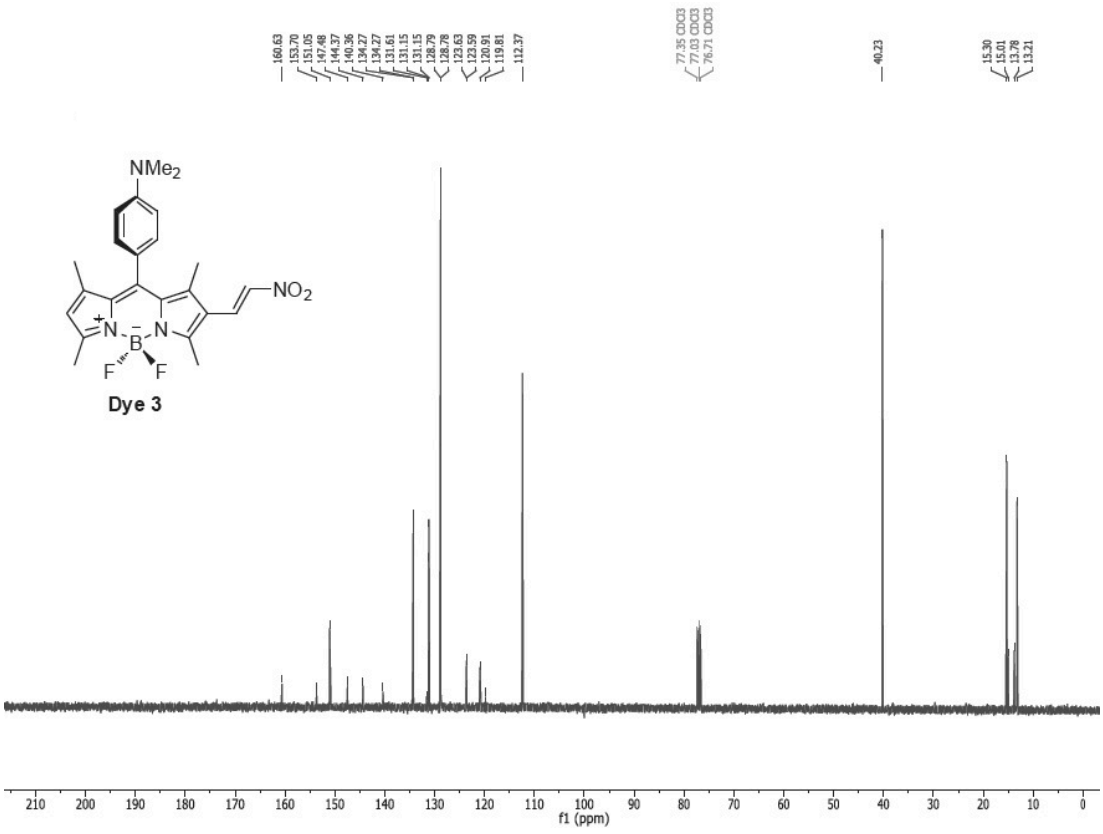

A.1.2. Mass Spectra

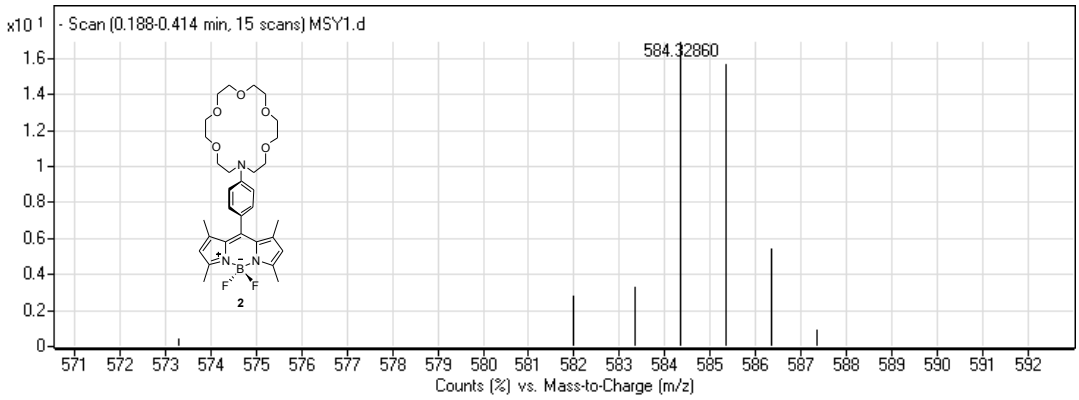

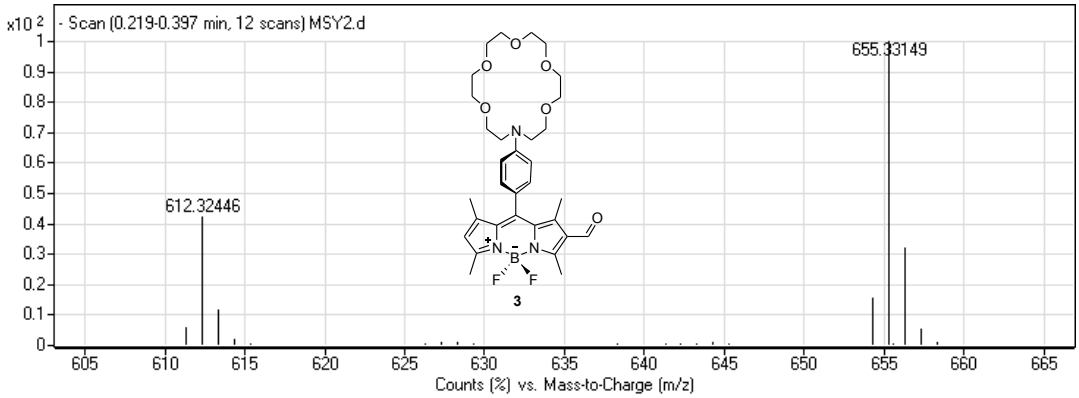
x10 2
- Scan (0.219-0.397 min, 12 scans) MSY2.d
655.33149
612.32446
3
Counts (%) vs. Mass-to-Charge (m/z)

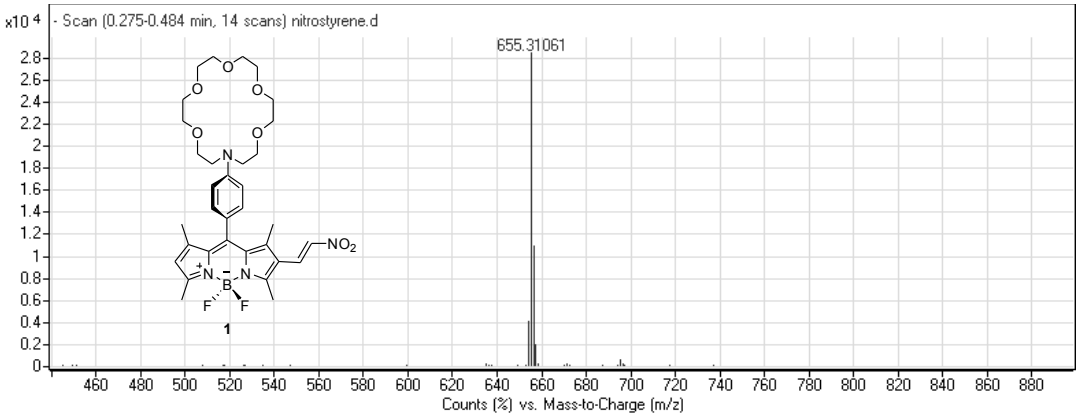
x10 4
- Scan (0.275-0.484 min, 14 scans) nitrostyrene.d
655.31061
NO2
1
Counts (%) vs. Mass-to-Charge (m/z)

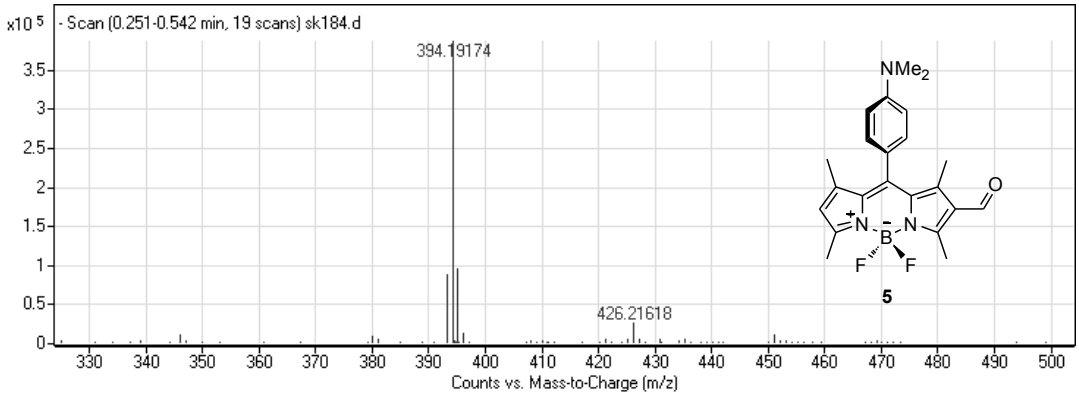
x10 5
- Scan (0.251-0.542 min, 19 scans) sk184.d
394.19174
426.21618
NMe2
5
Counts vs. Mass-to-Charge (m/z)

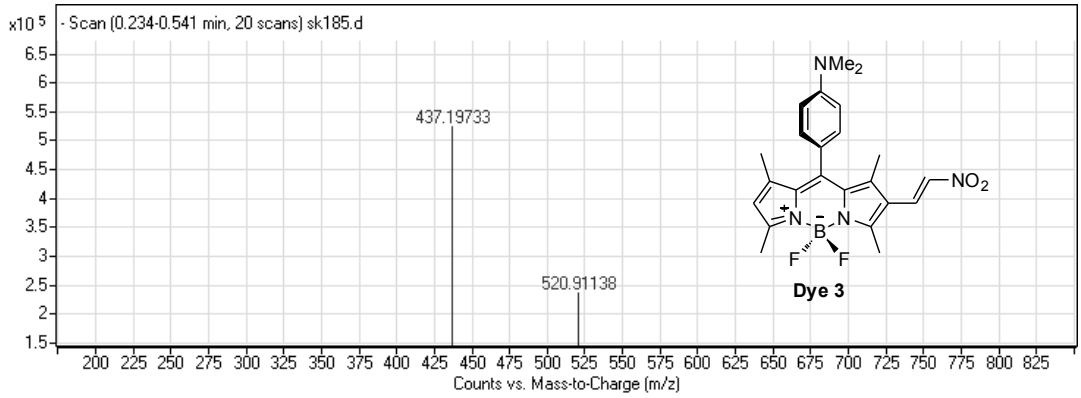

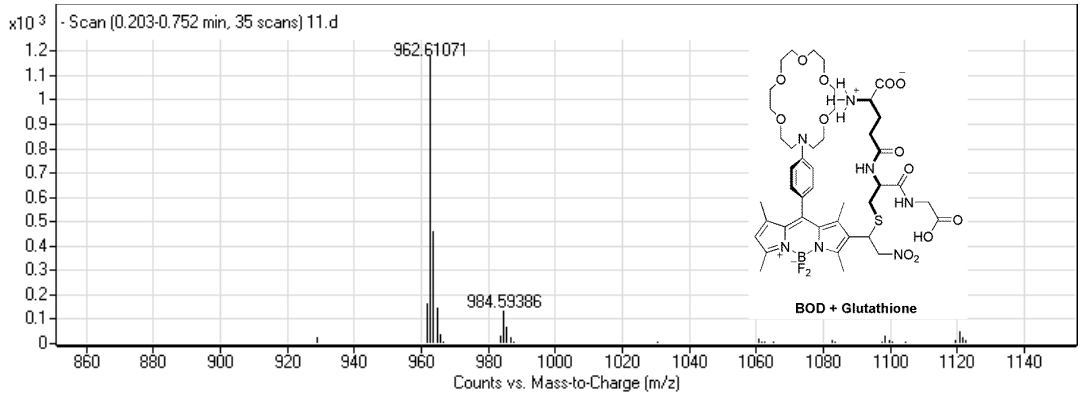

A.2. Activatable Heavy Atom Free Sensitizers for Photodynamic Therapy Application

A.2.1. Singlet Oxygen Generation by Using Heavy Atom Free Orthogonal BODIPY Derivatives

A.2.1.1. ^{1}H NMR and ^{13}C NMR Spectra

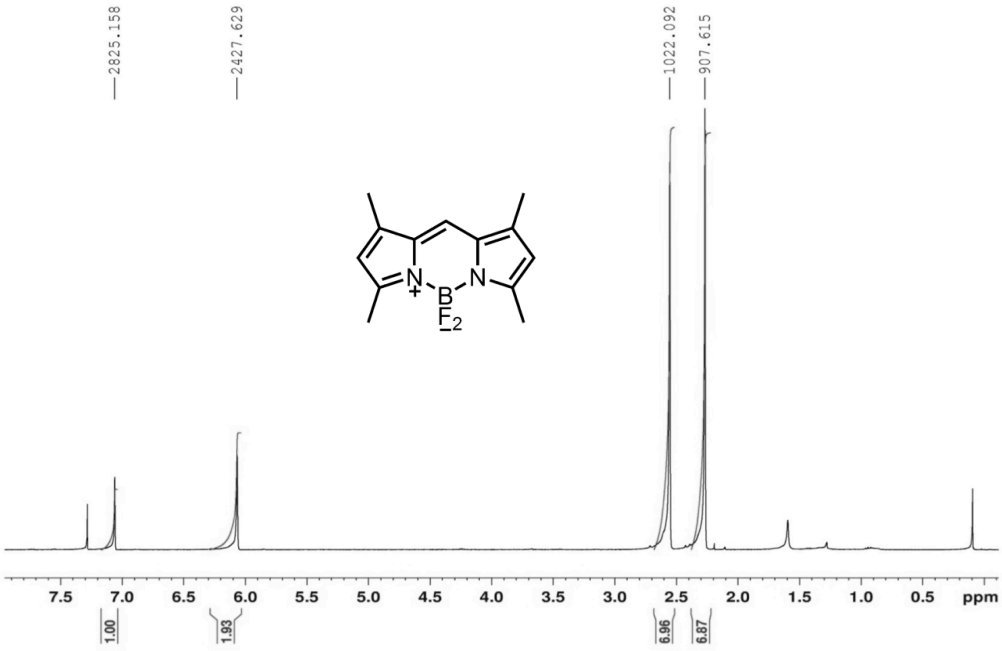
2825.158
2427.629
1022.092
907.615
7.5 7.0 6.5 6.0 5.5 5.0 4.5 4.0 3.5 3.0 2.5 2.0 1.5 1.0 0.5 ppm
1.00
1.93
6.96
6.87

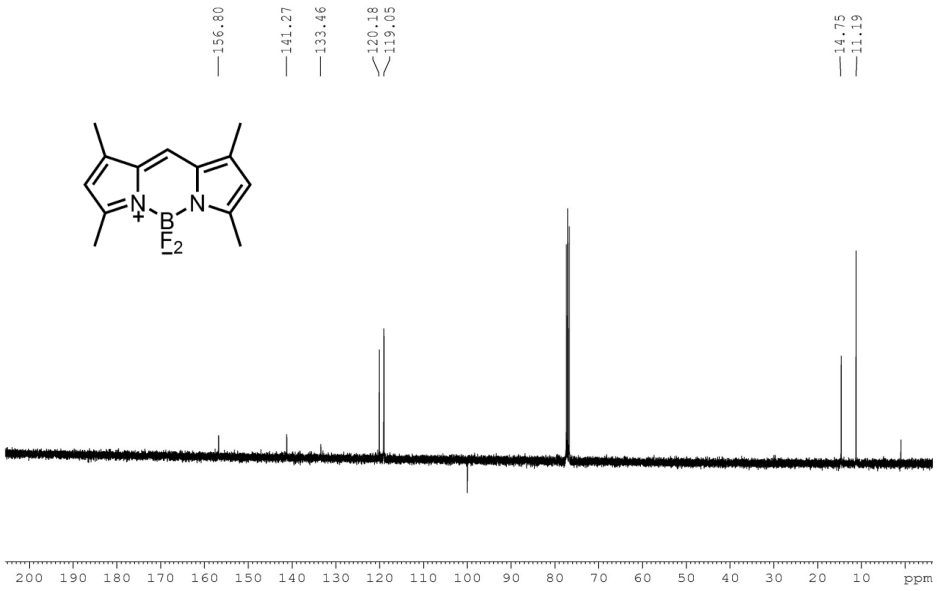
156.80
141.27
133.46
120.18
119.05
14.75
11.19
200 190 180 170 160 150 140 130 120 110 100 90 80 70 60 50 40 30 20 10 ppm

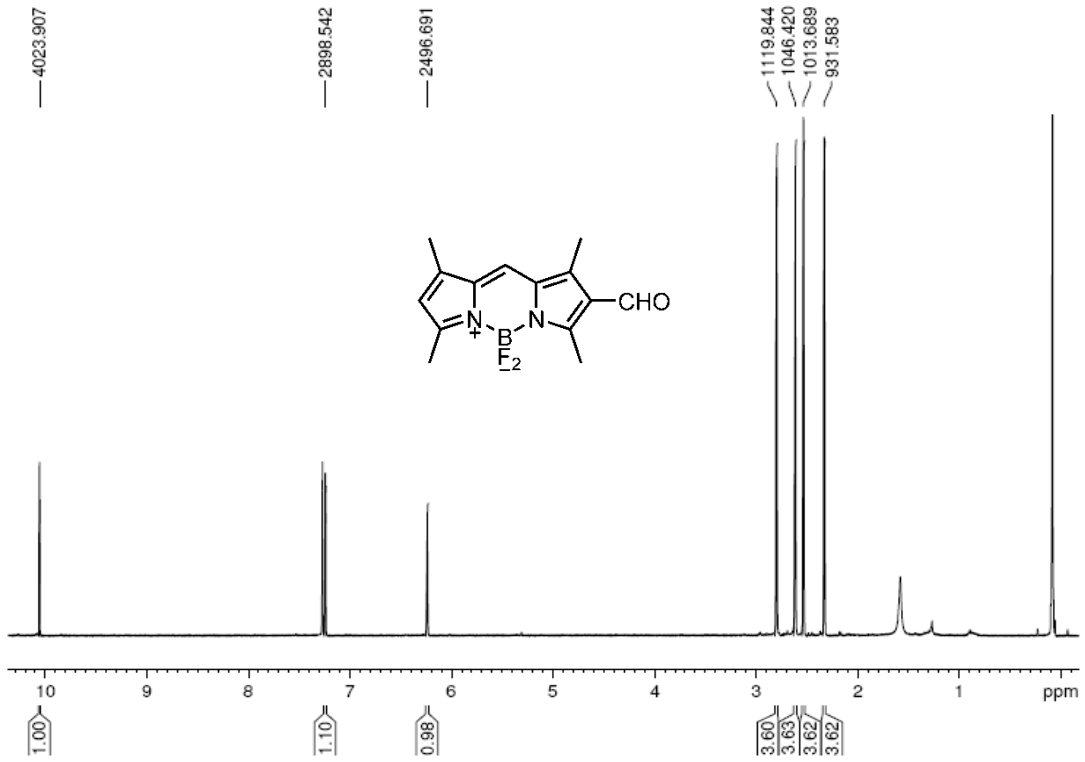
4023.907
2898.542
2496.691
1119.844
1046.420
1013.689
931.583
CHO
N
B
F2
10
9
8
7
6
5
4
3
2
1
ppm
1.00
1.10
0.98
3.60
3.63
3.62
3.62

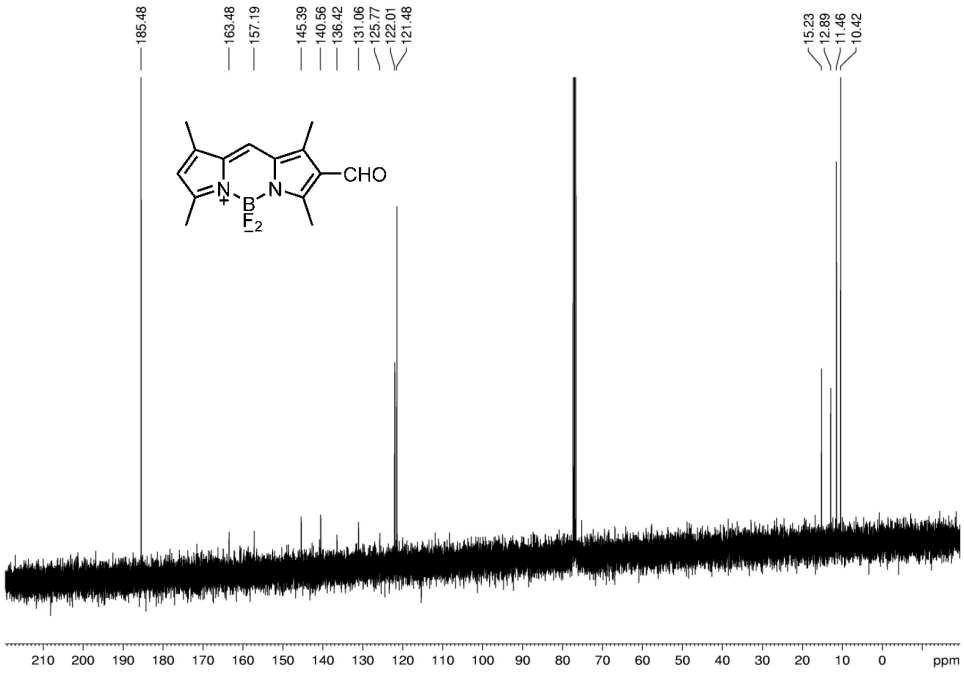
185.48
163.48
157.19
145.39
140.56
136.42
131.06
125.77
122.01
121.48
15.23
12.89
11.46
10.42
CHO
N
B
F2
210
200
190
180
170
160
150
140
130
120
110
100
90
80
70
60
50
40
30
20
10
0
ppm

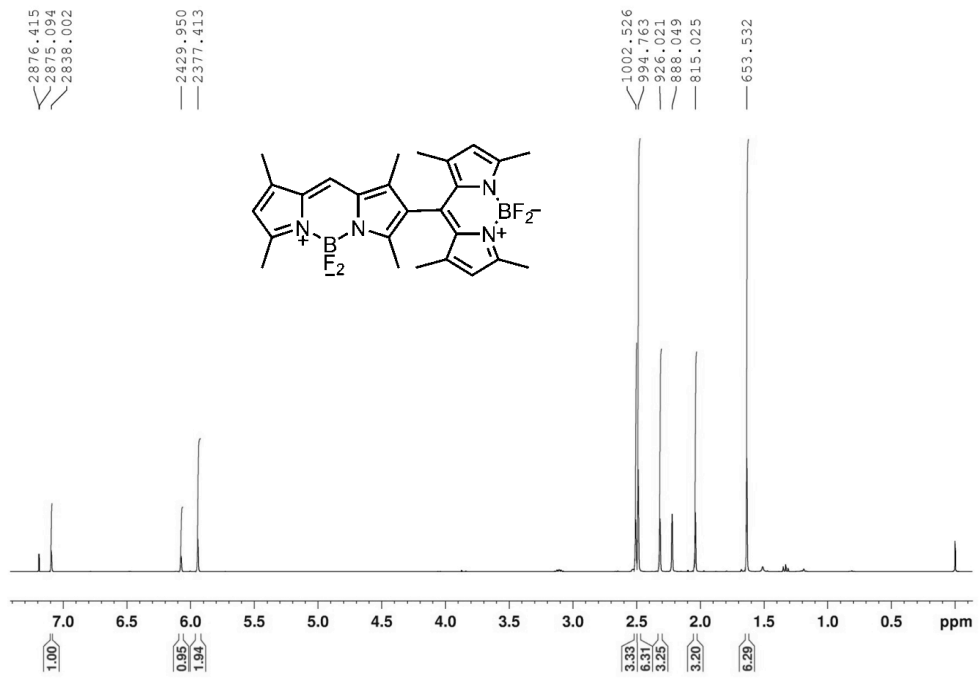
2876.415
2875.094
2838.002
2429.950
2377.413
1002.526
994.763
926.021
888.049
815.025
653.532
7.0
6.5
6.0
5.5
5.0
4.5
4.0
3.5
3.0
2.5
2.0
1.5
1.0
0.5
ppm
1.00
0.95
1.94
3.33
6.31
3.25
3.20
6.29

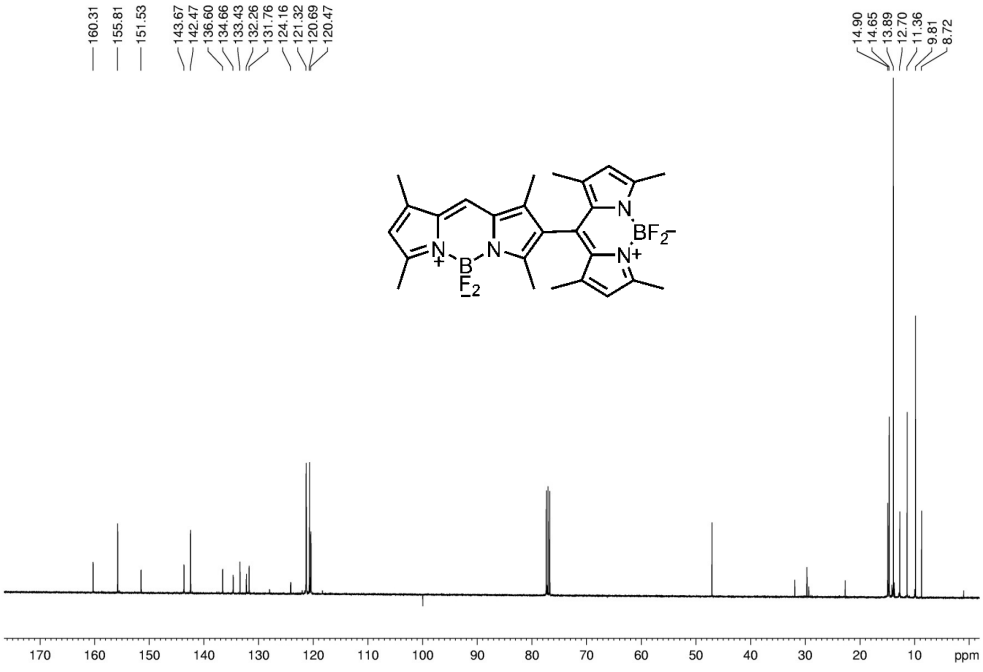
160.31
155.81
151.53
143.67
142.47
136.60
134.66
133.43
132.26
131.76
124.16
121.32
120.69
120.47
14.90
14.65
13.89
12.70
11.36
9.81
8.72
170
160
150
140
130
120
110
100
90
80
70
60
50
40
30
20
10
ppm

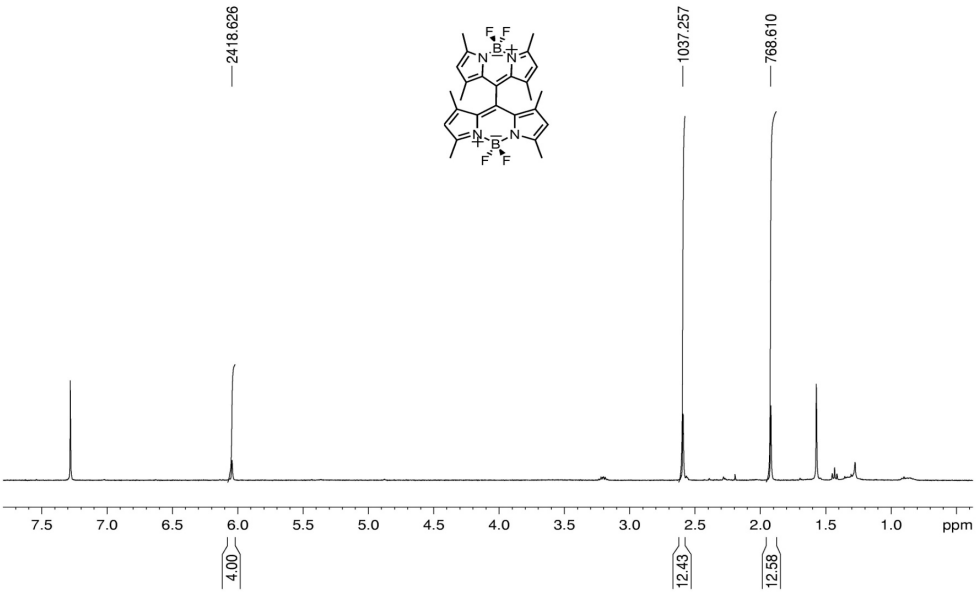
2418.626
1037.257
768.610
7.5
7.0
6.5
6.0
5.5
5.0
4.5
4.0
3.5
3.0
2.5
2.0
1.5
1.0
ppm
4.00
12.43
12.58

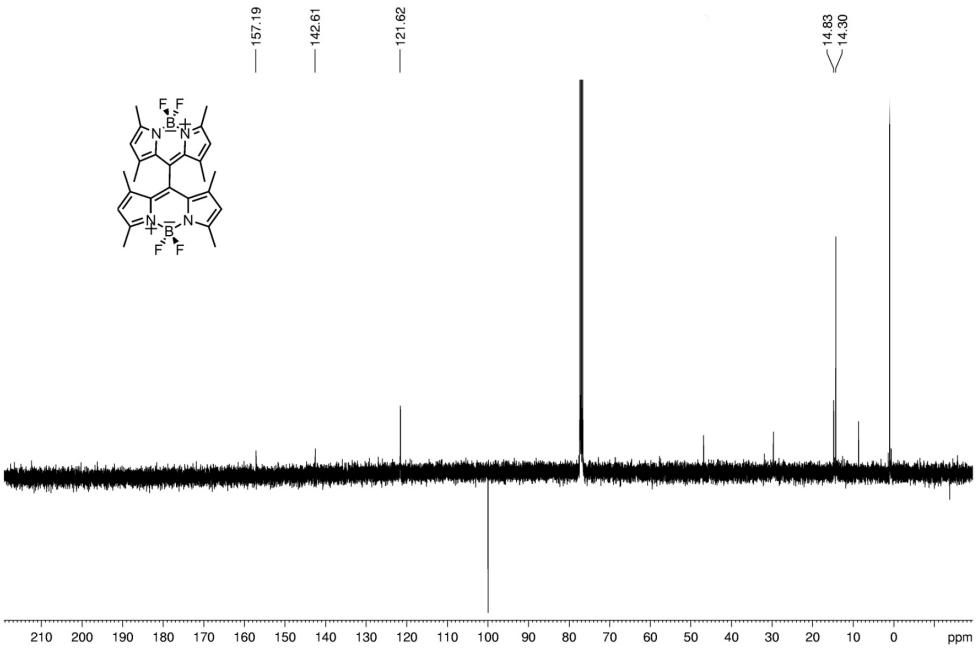
157.19
142.61
121.62
14.83
14.30
210
200
190
180
170
160
150
140
130
120
110
100
90
80
70
60
50
40
30
20
10
0
ppm

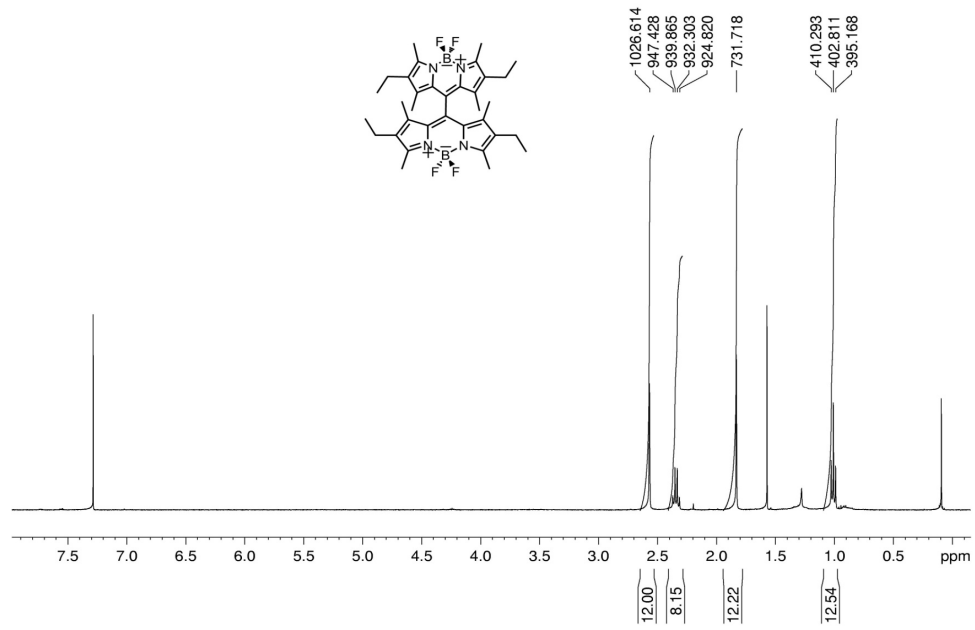
1026.614
947.428
939.865
932.303
924.820
731.718
410.293
402.811
395.168
7.5 7.0 6.5 6.0 5.5 5.0 4.5 4.0 3.5 3.0 2.5 2.0 1.5 1.0 0.5 ppm
12.00
8.15
12.22
12.54

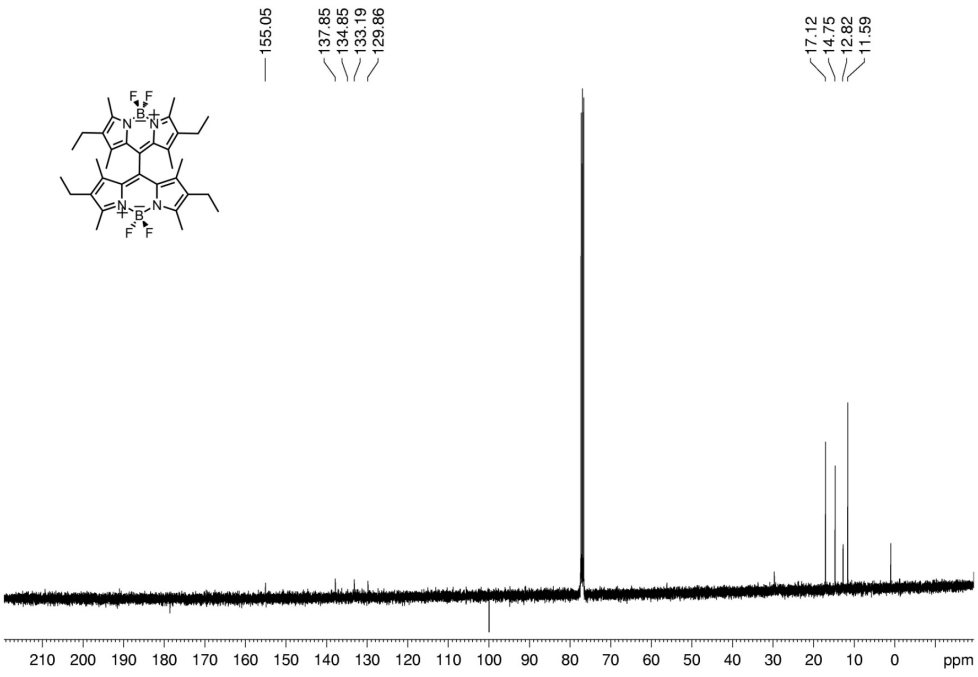
155.05
137.85
134.85
133.19
129.86
17.12
14.75
12.82
11.59
210 200 190 180 170 160 150 140 130 120 110 100 90 80 70 60 50 40 30 20 10 0 ppm

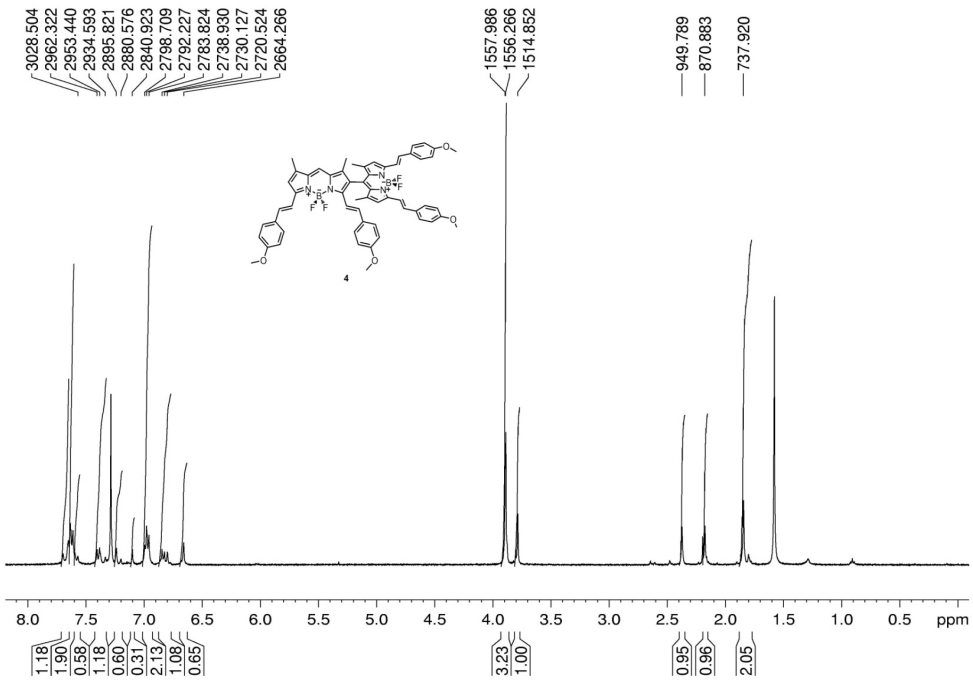
3028.504
2962.322
2953.440
2934.593
2895.821
2880.576
2840.923
2798.709
2792.227
2783.824
2738.930
2730.127
2720.524
2664.266
1557.986
1556.266
1514.852
949.789
870.883
737.920
4
8.0 7.5 7.0 6.5 6.0 5.5 5.0 4.5 4.0 3.5 3.0 2.5 2.0 1.5 1.0 0.5 ppm
1.18 1.90 0.58 1.18 0.60 0.31 2.13 1.08 0.65
3.23 1.00
0.95 0.96 2.05

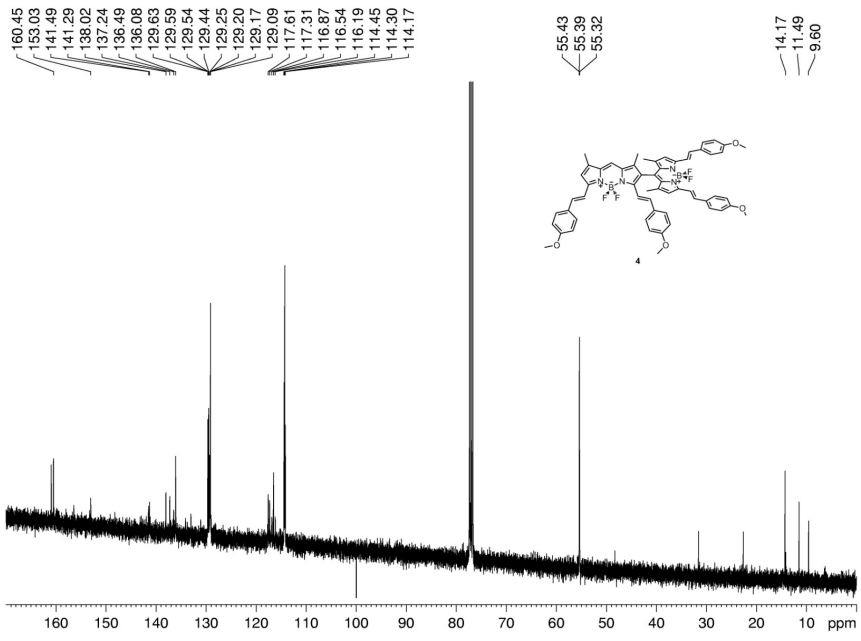
160.45
153.03
141.49
141.29
138.02
137.24
136.49
136.08
129.63
129.59
129.54
129.44
129.25
129.20
129.17
129.09
117.61
117.31
116.87
116.54
116.19
114.45
114.30
114.17
55.43
55.39
55.32
14.17
11.49
9.60
4
160 150 140 130 120 110 100 90 80 70 60 50 40 30 20 10 ppm

A.2.1.2. Mass Spectra

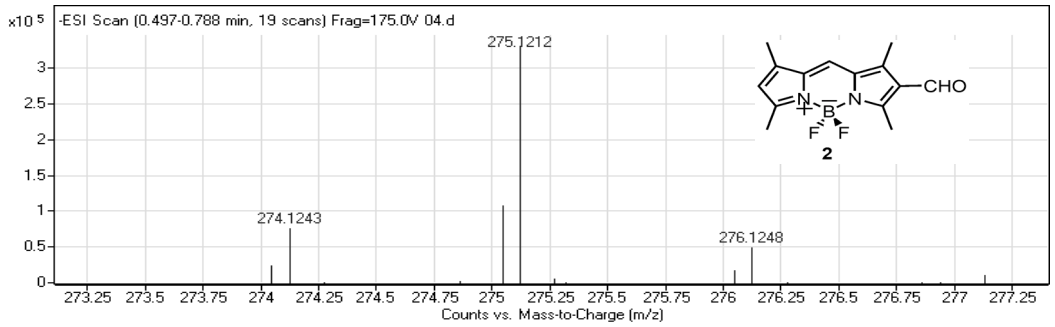

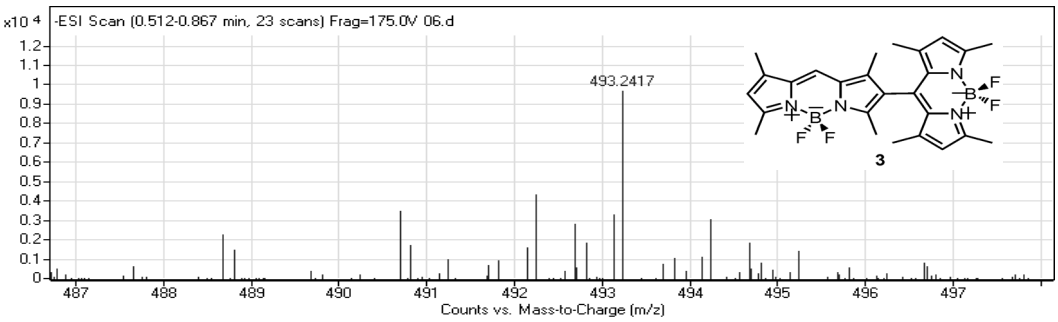

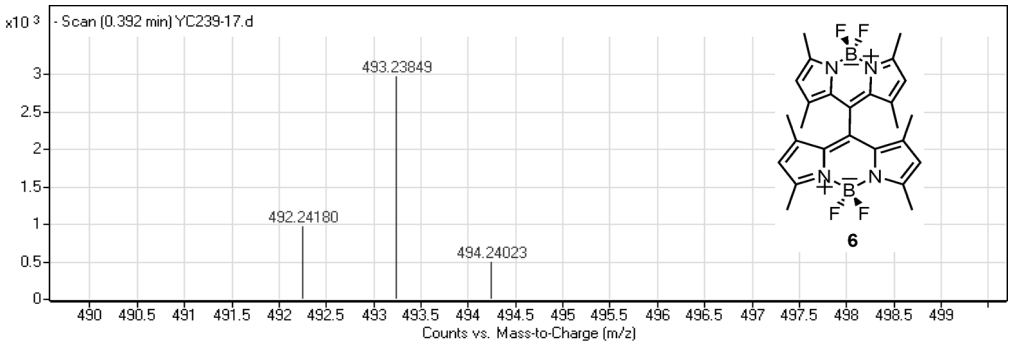

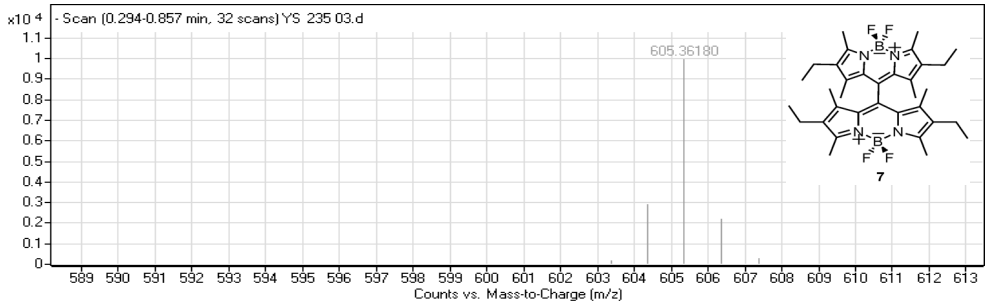

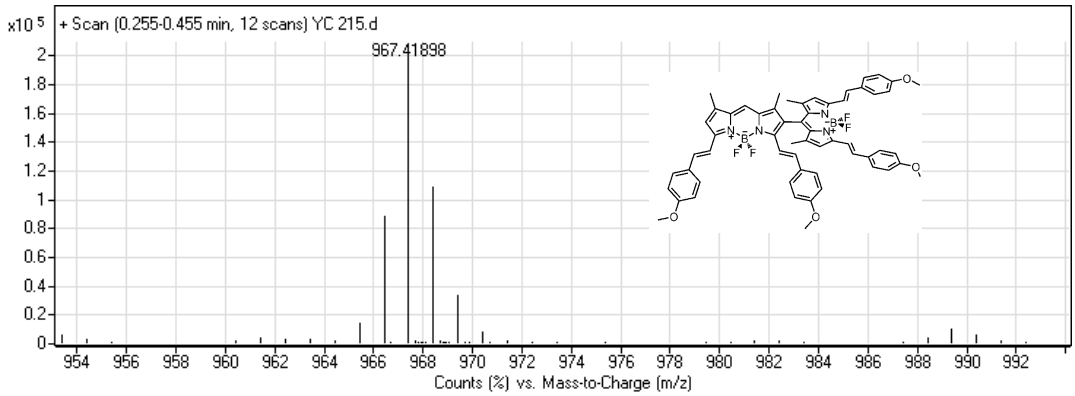

A.2.2. Singlet Oxygen Generation by Using Heavy Atom Free Orthogonal BODIPY Derivatives

A.2.2.1. ^{1}H NMR and ^{13}C NMR Spectra

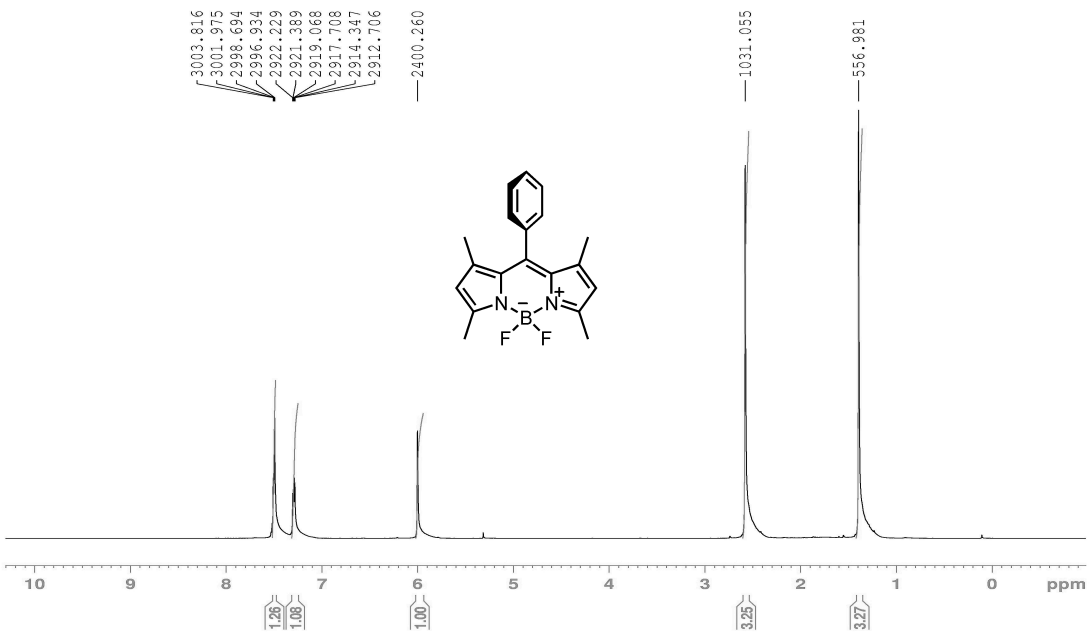
3003.816
3001.975
2998.694
2996.934
2922.229
2921.389
2919.068
2917.708
2914.347
2912.706
2400.260
1031.055
556.981
10
9
8
7
6
5
4
3
2
1
0
ppm
1.26
1.08
1.00
3.25
3.27

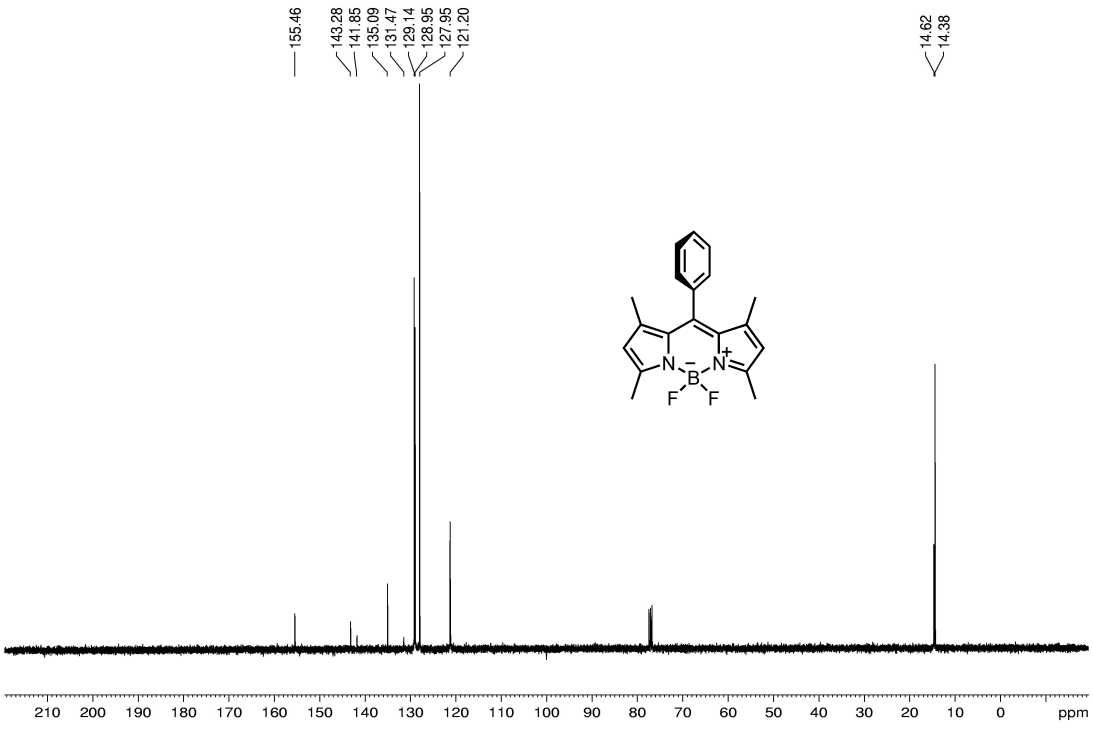
155.46
143.28
141.85
135.09
131.47
129.14
128.95
127.95
121.20
14.62
14.38
210
200
190
180
170
160
150
140
130
120
110
100
90
80
70
60
50
40
30
20
10
0
ppm

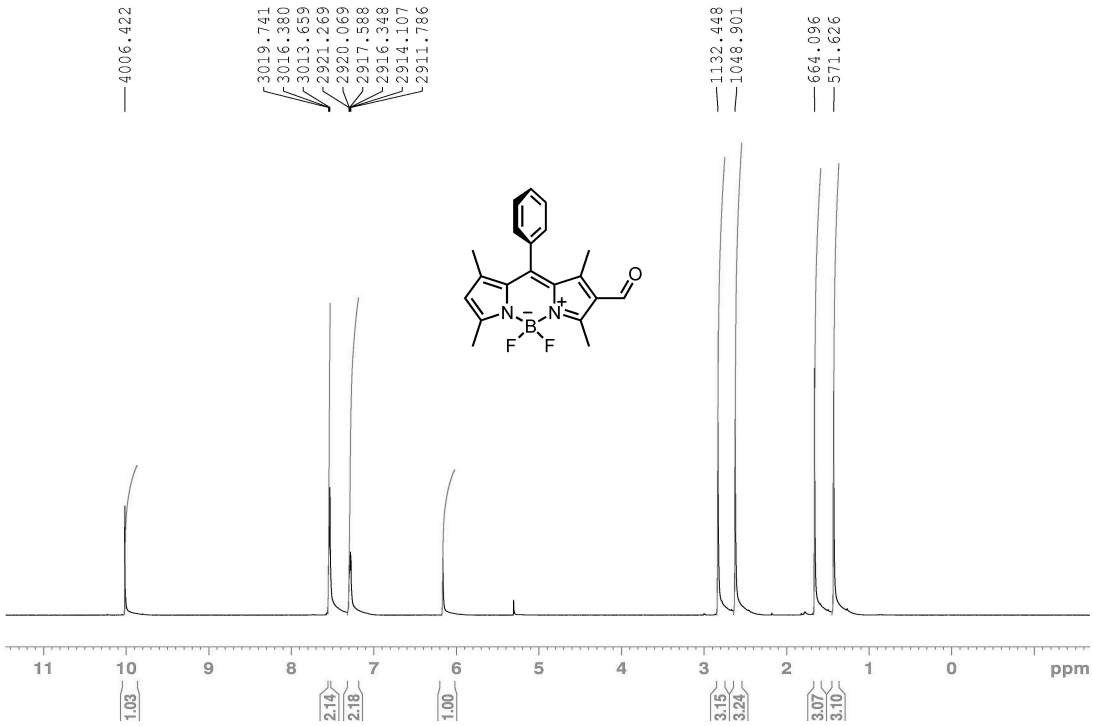
4006.422
3019.741
3016.380
3013.659
2921.269
2920.069
2917.588
2916.348
2914.107
2911.786
1132.448
1048.901
664.096
571.626
11
10
9
8
7
6
5
4
3
2
1
0
ppm
1.03
2.14
2.18
1.00
3.15
3.24
3.07
3.10

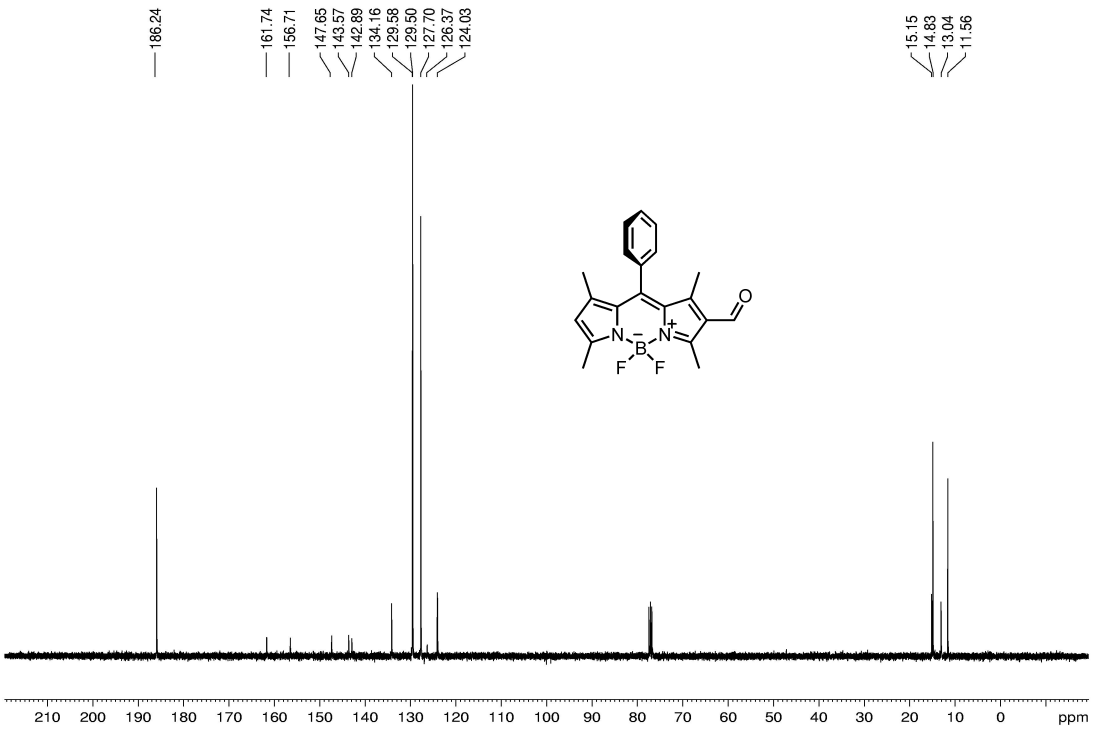
186.24
161.74
156.71
147.65
143.57
142.89
134.16
129.58
129.50
127.70
126.37
124.03
15.15
14.83
13.04
11.56
210
200
190
180
170
160
150
140
130
120
110
100
90
80
70
60
50
40
30
20
10
0
ppm

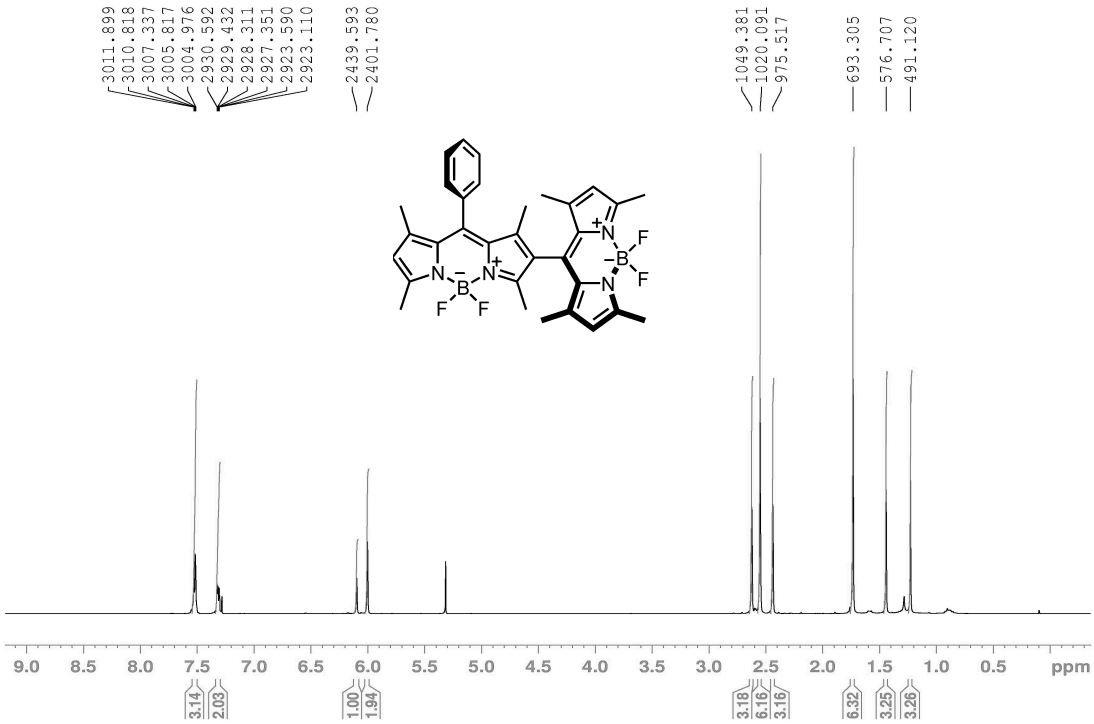
3011.899
3010.818
3007.337
3005.817
3004.976
2930.592
2929.432
2928.311
2927.351
2923.590
2923.110
2439.593
2401.780
1049.381
1020.091
975.517
693.305
576.707
491.120
9.0 8.5 8.0 7.5 7.0 6.5 6.0 5.5 5.0 4.5 4.0 3.5 3.0 2.5 2.0 1.5 1.0 0.5 ppm
3.14
2.03
1.00
1.94
3.18
6.16
3.16
6.32
3.25
3.26

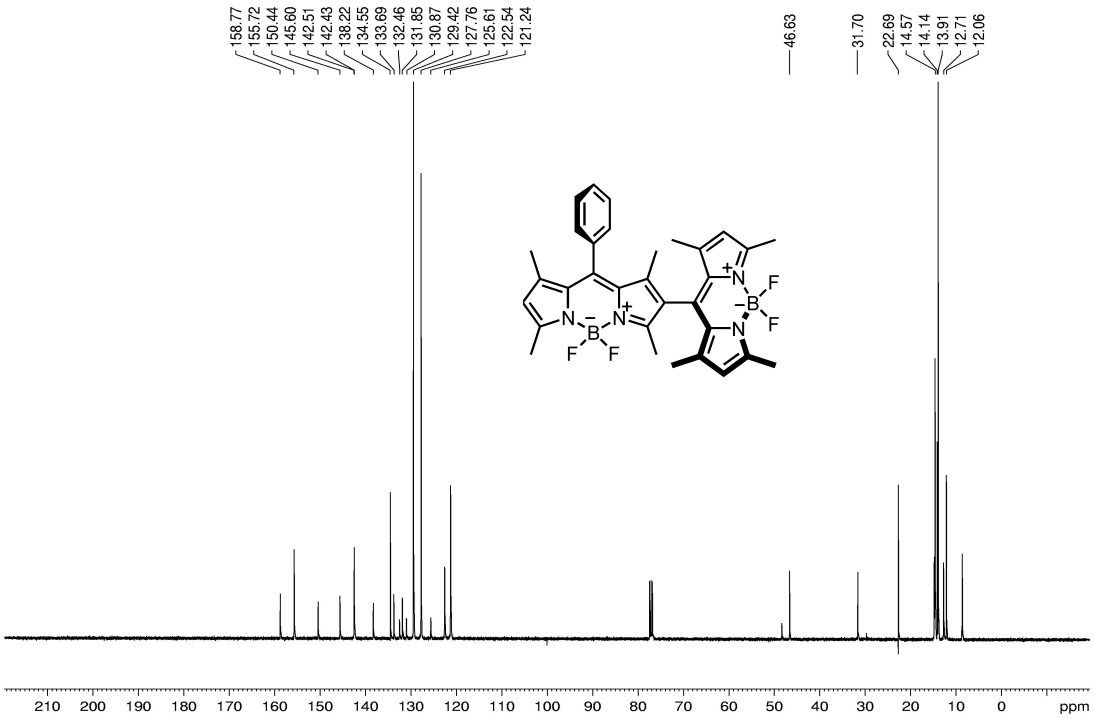
158.77
155.72
150.44
145.60
142.51
142.43
138.22
134.55
133.69
132.46
131.85
130.87
129.42
127.76
125.61
122.54
121.24
46.63
31.70
22.69
14.57
14.14
13.91
12.71
12.06
210 200 190 180 170 160 150 140 130 120 110 100 90 80 70 60 50 40 30 20 10 0 ppm

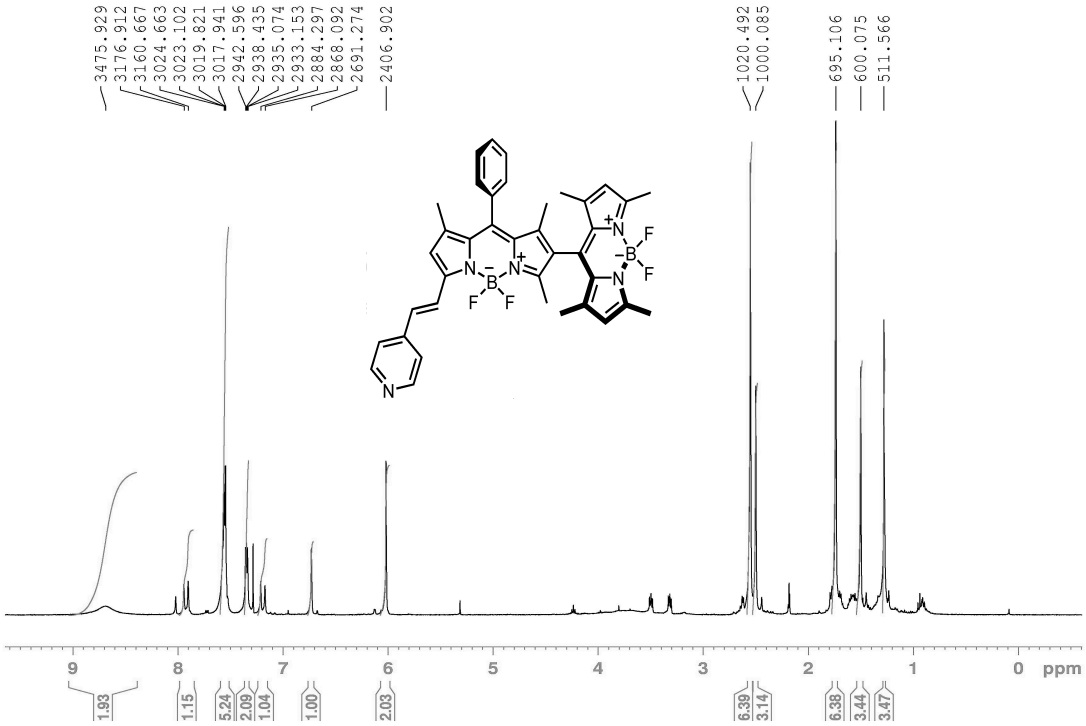
3475.929
3176.912
3160.667
3024.663
3023.102
3019.821
3017.941
2942.596
2938.435
2935.074
2933.153
2884.297
2868.092
2691.274
2406.902
1020.492
1000.085
695.106
600.075
511.566
9
8
7
6
5
4
3
2
1
0
ppm
1.93
1.15
5.24
2.09
1.04
1.00
2.03
6.39
3.14
6.38
3.44
3.47

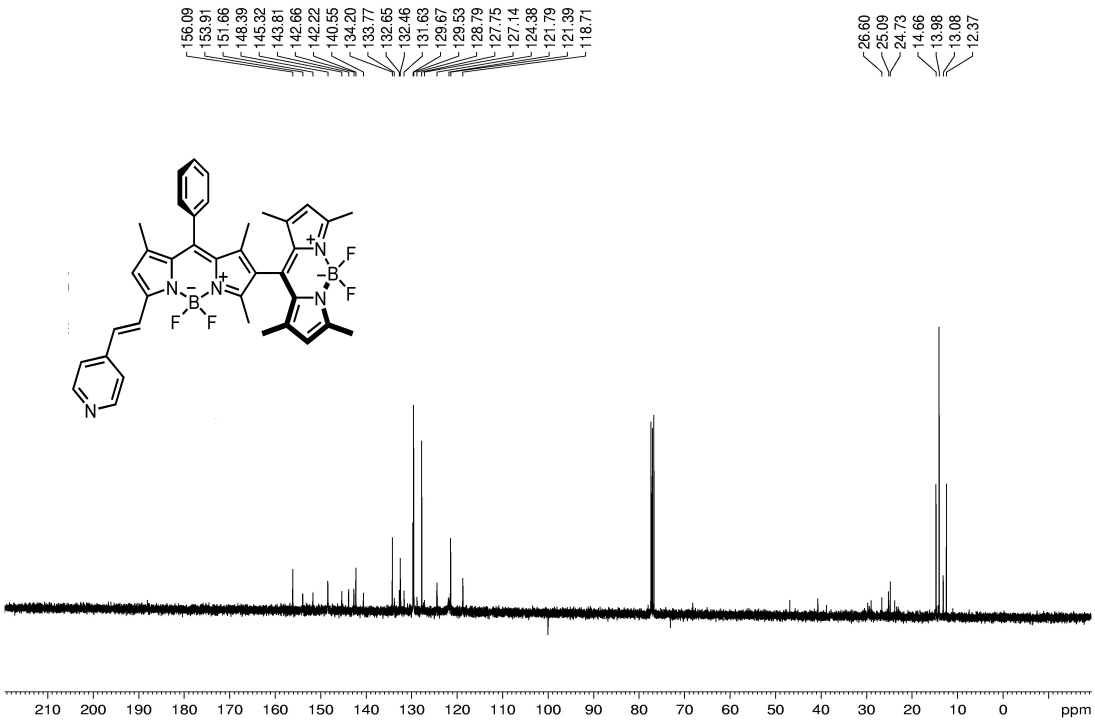
156.09
153.91
151.66
148.39
145.32
143.81
142.66
142.22
140.55
134.20
133.77
132.65
132.46
131.63
129.67
129.53
128.79
127.75
127.14
124.38
121.79
121.39
118.71
26.60
25.09
24.73
14.66
13.98
13.08
12.37
210
200
190
180
170
160
150
140
130
120
110
100
90
80
70
60
50
40
30
20
10
0
ppm

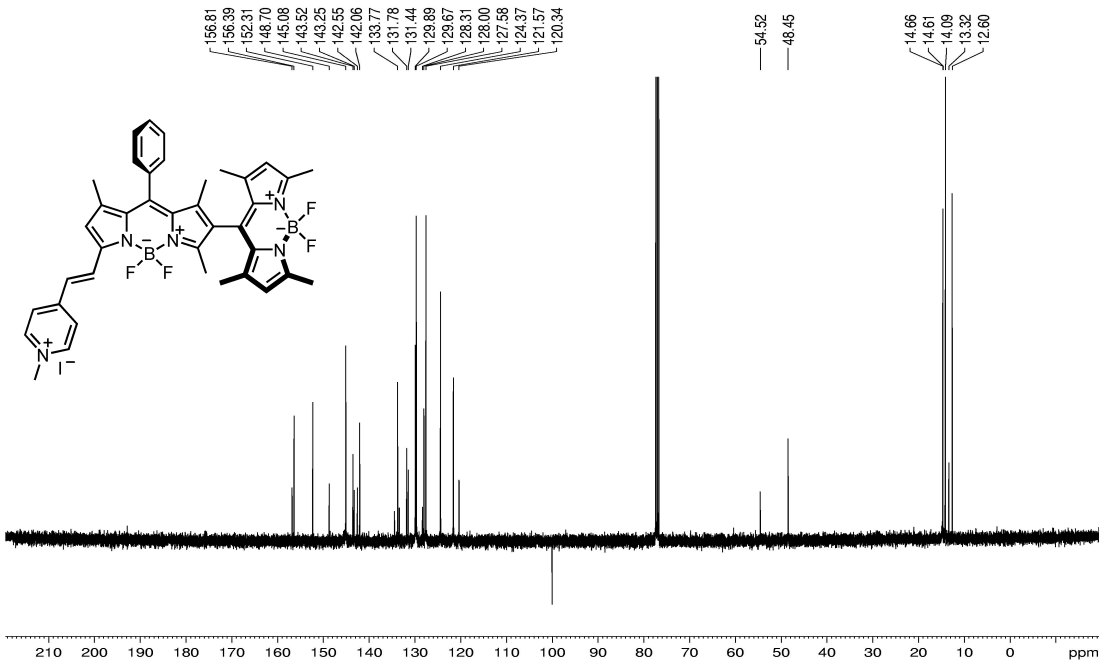
156.81
156.39
152.31
148.70
145.08
143.52
143.25
142.55
142.06
133.77
131.78
131.44
129.89
129.67
128.31
128.00
127.58
124.37
121.57
120.34
54.52
48.45
14.66
14.61
14.09
13.32
12.60
210 200 190 180 170 160 150 140 130 120 110 100 90 80 70 60 50 40 30 20 10 0 ppm

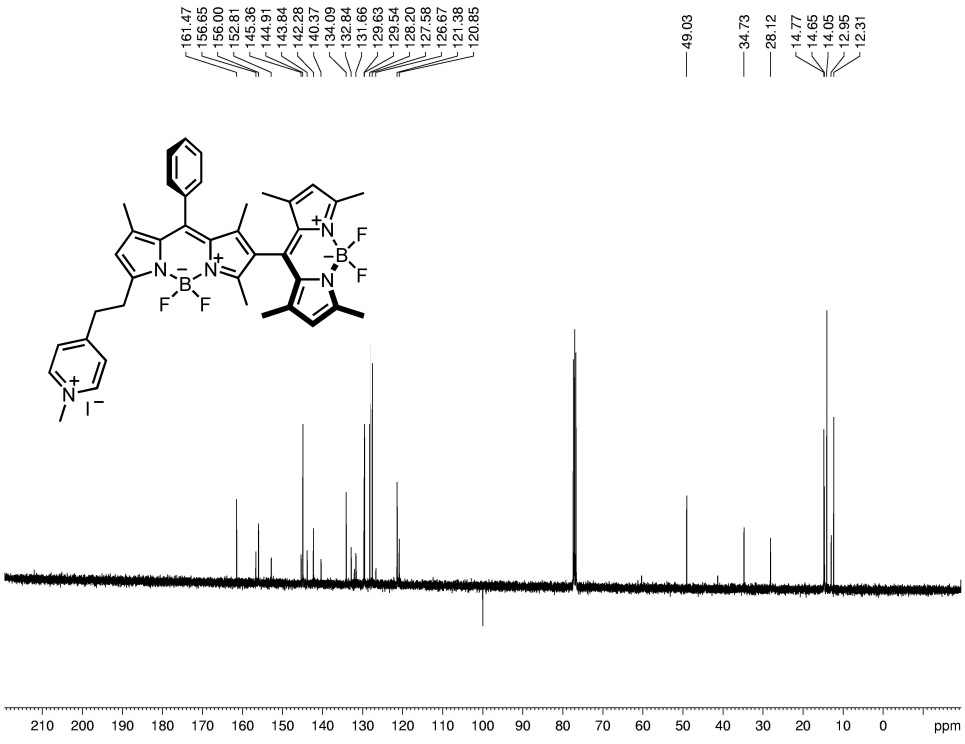
161.47
156.65
156.00
152.81
145.36
144.91
143.84
142.28
140.37
134.09
132.84
131.66
129.63
129.54
128.20
127.58
126.67
121.38
120.85
49.03
34.73
28.12
14.77
14.65
14.05
12.95
12.31
210 200 190 180 170 160 150 140 130 120 110 100 90 80 70 60 50 40 30 20 10 0 ppm

A.2.2.2. Mass Spectra

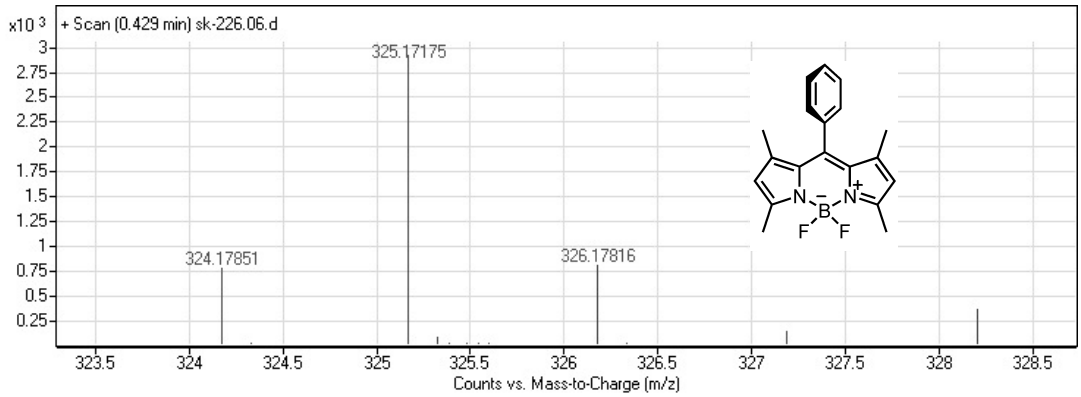

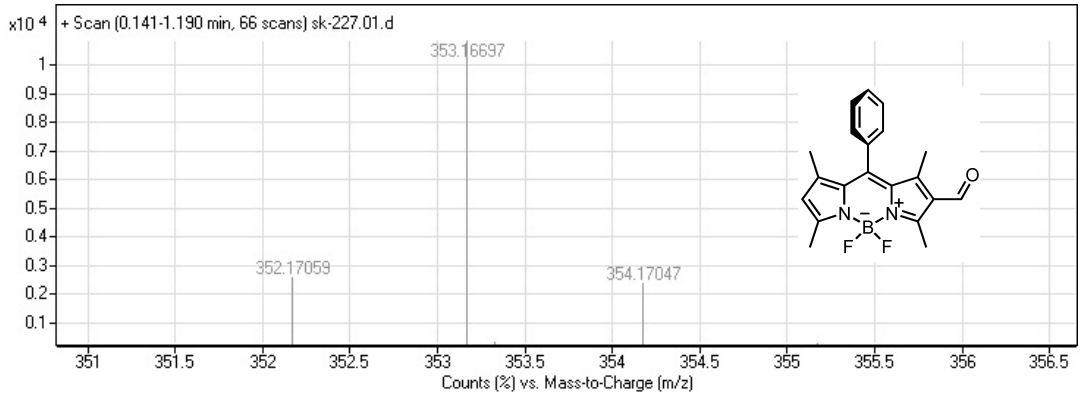

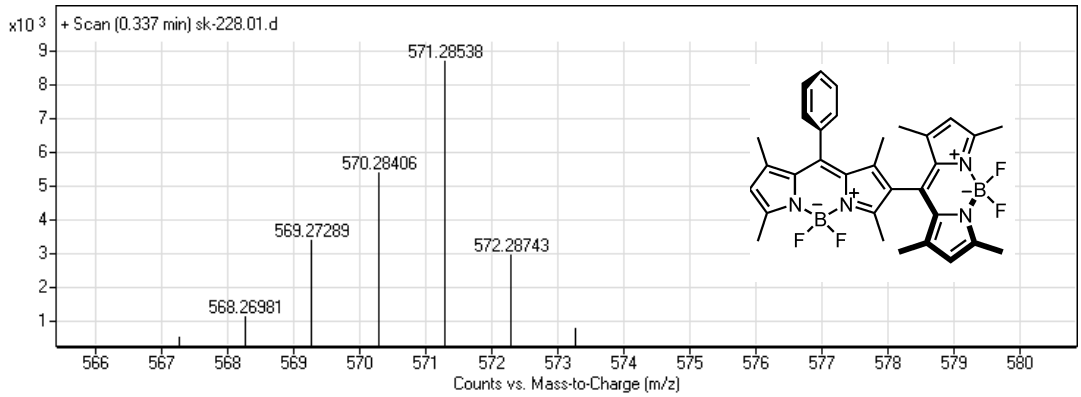

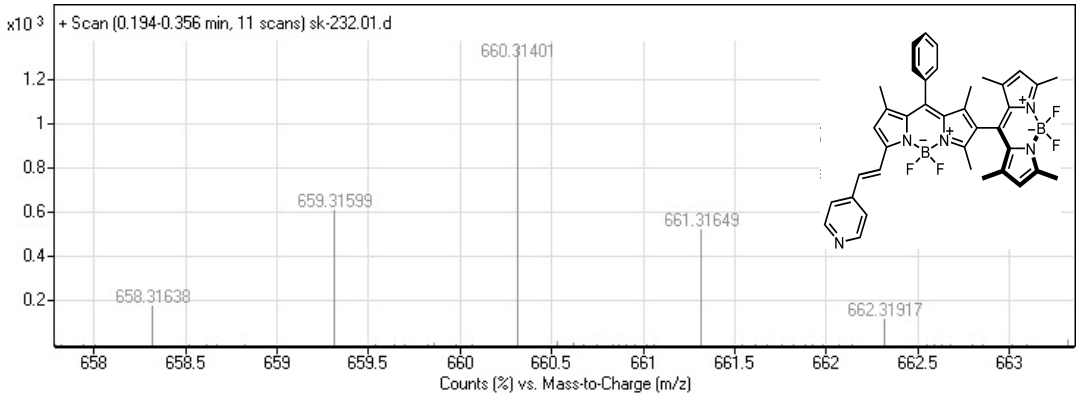
x10 3
+ Scan (0.194-0.356 min, 11 scans) sk-232.01.d
660.31401
659.31599
661.31649
658.31638
662.31917
Counts (%) vs. Mass-to-Charge (m/z)

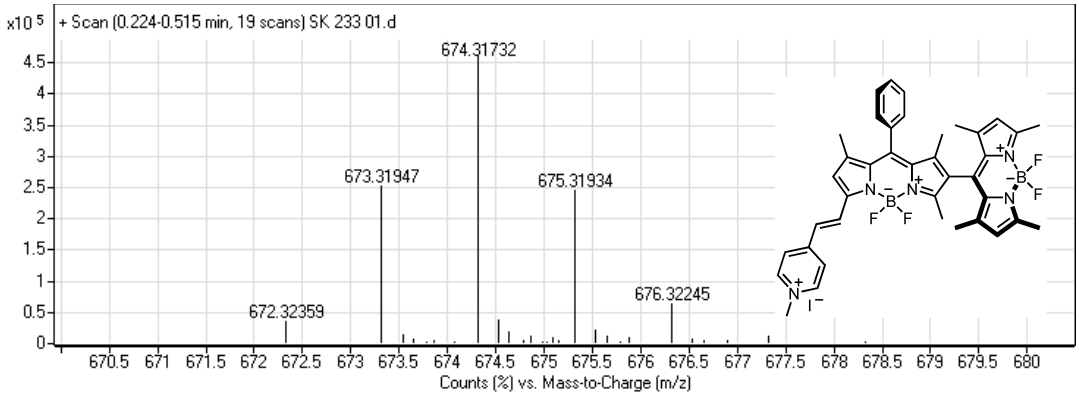
x10 5
+ Scan (0.224-0.515 min, 19 scans) SK 233 01.d
674.31732
673.31947
675.31934
672.32359
676.32245
Counts (%) vs. Mass-to-Charge (m/z)

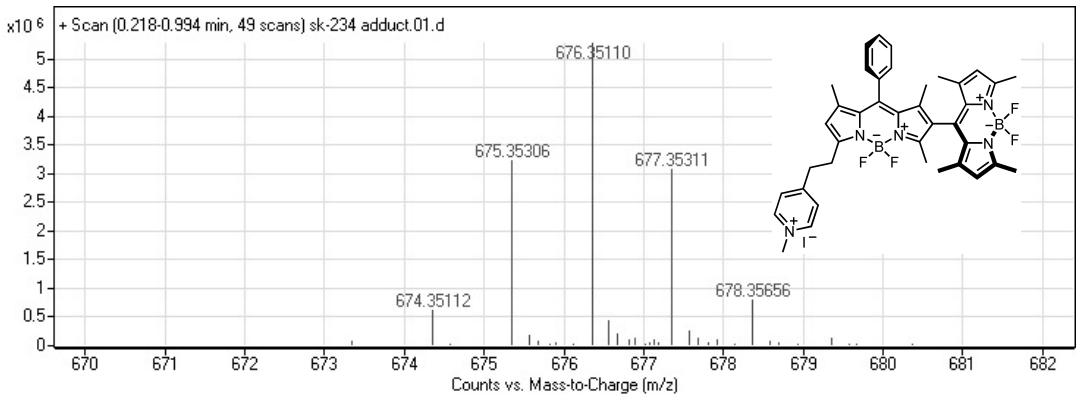
x10 6
+ Scan (0.218-0.994 min, 49 scans) sk-234 adduct.01.d
676.35110
675.35306
677.35311
674.35112
678.35656
Counts vs. Mass-to-Charge (m/z)

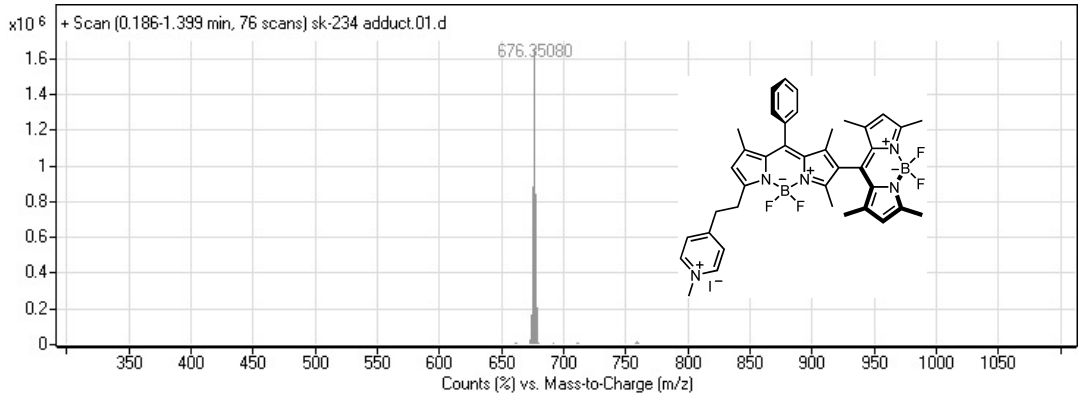

A.3. Axially Chiral BODIPY Derivatives

A.3.1. ^{1}H and ^{13}C NMR Spectra

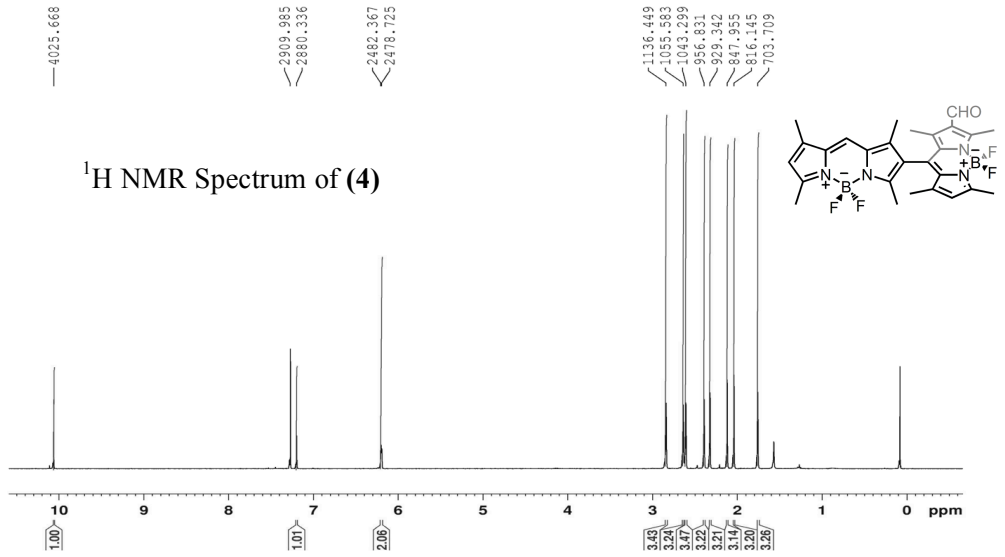

^{1}H NMR Spectrum of **(4)**

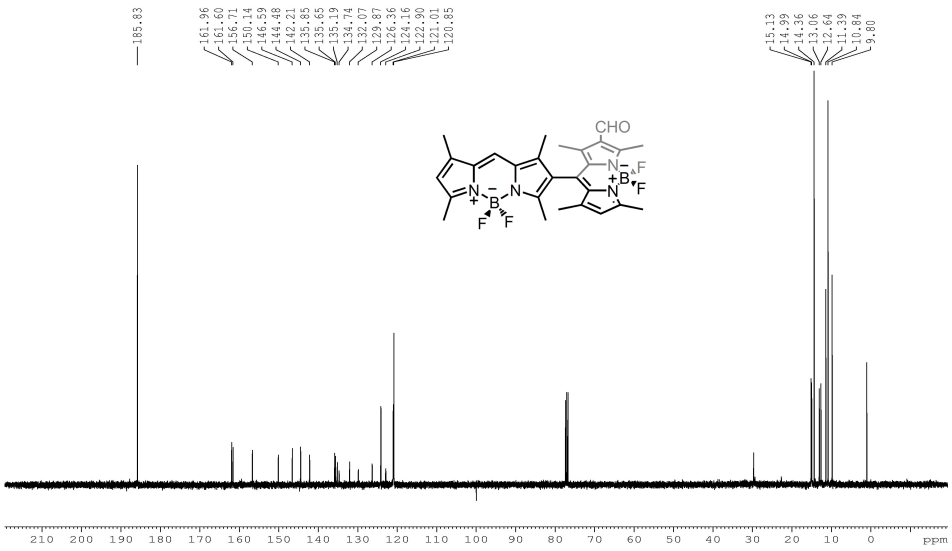

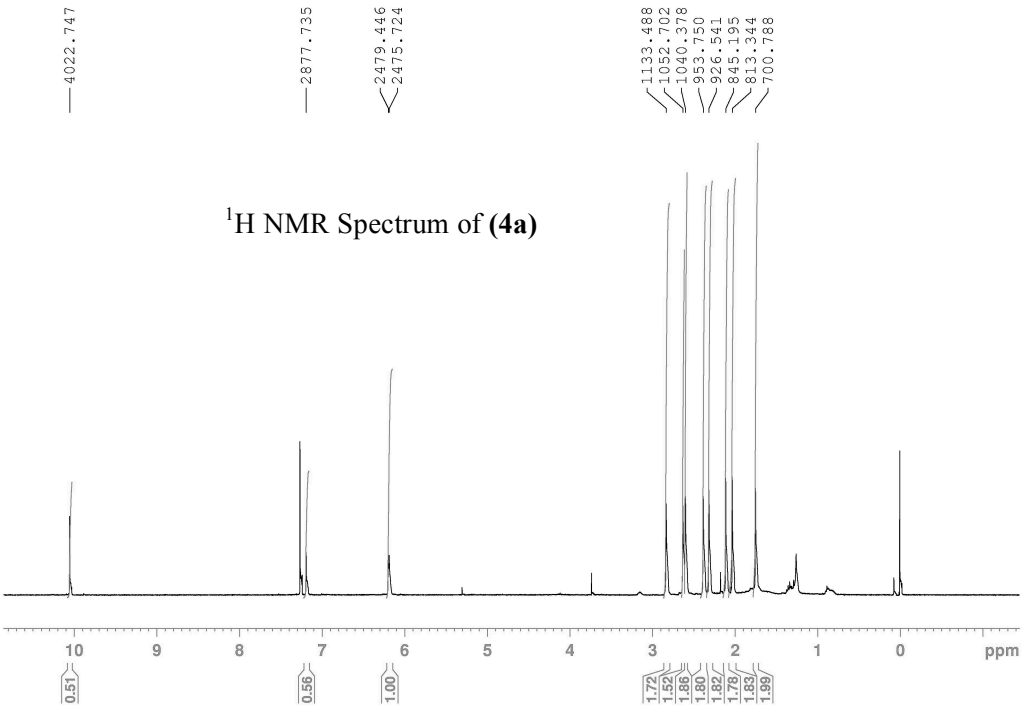

^{1}H NMR Spectrum of **(4a)**

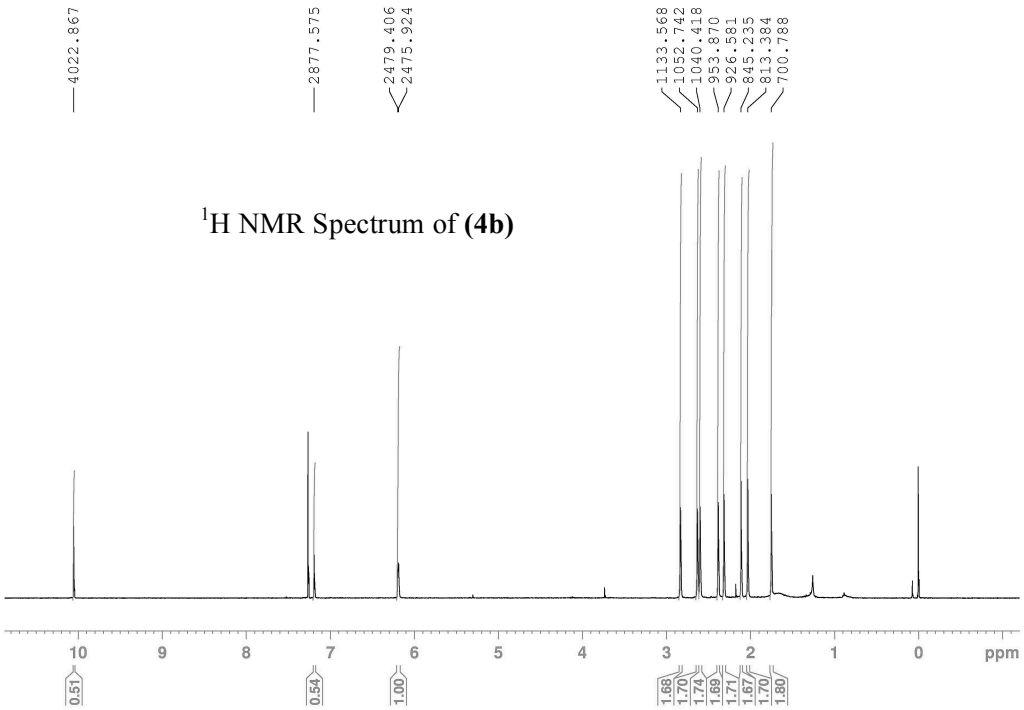

^{1}H NMR Spectrum of **(4b)**

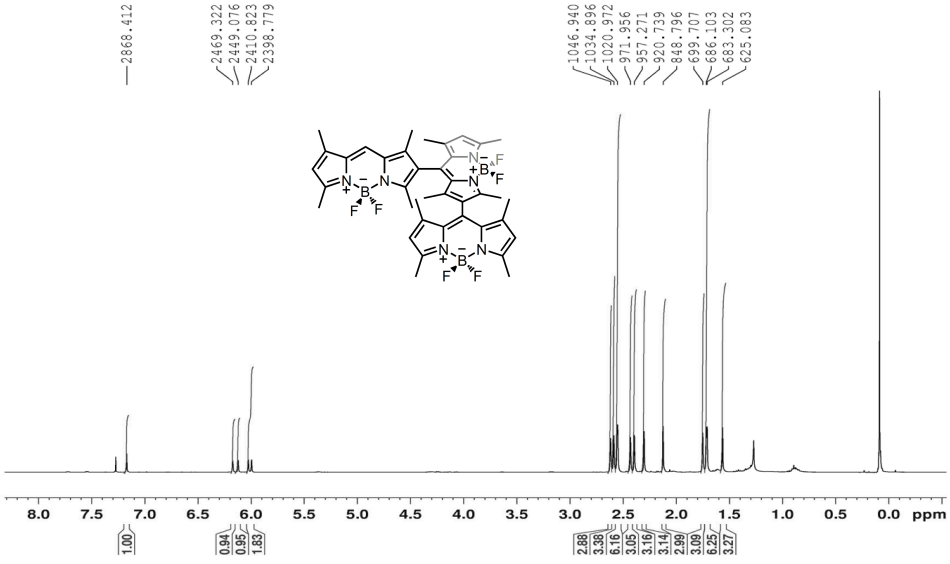

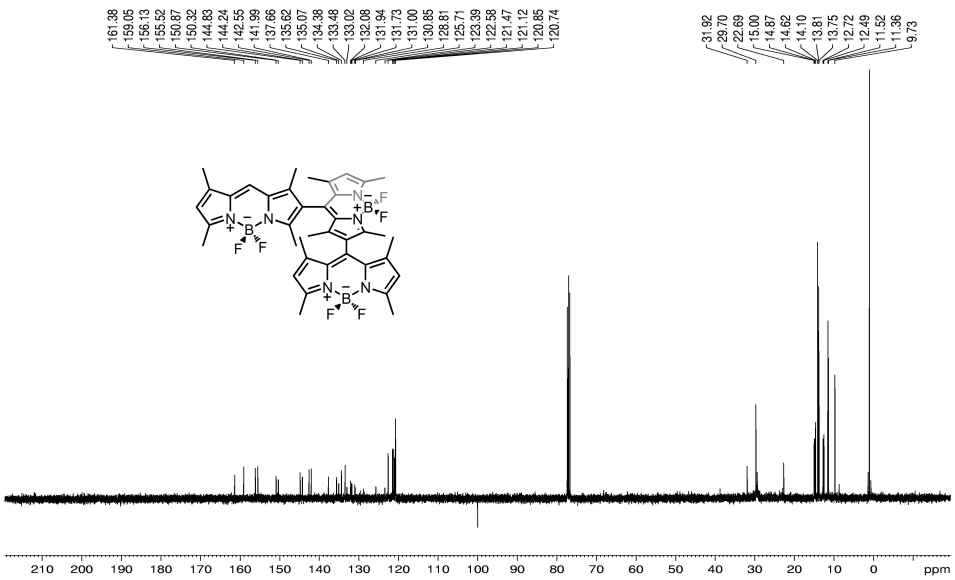

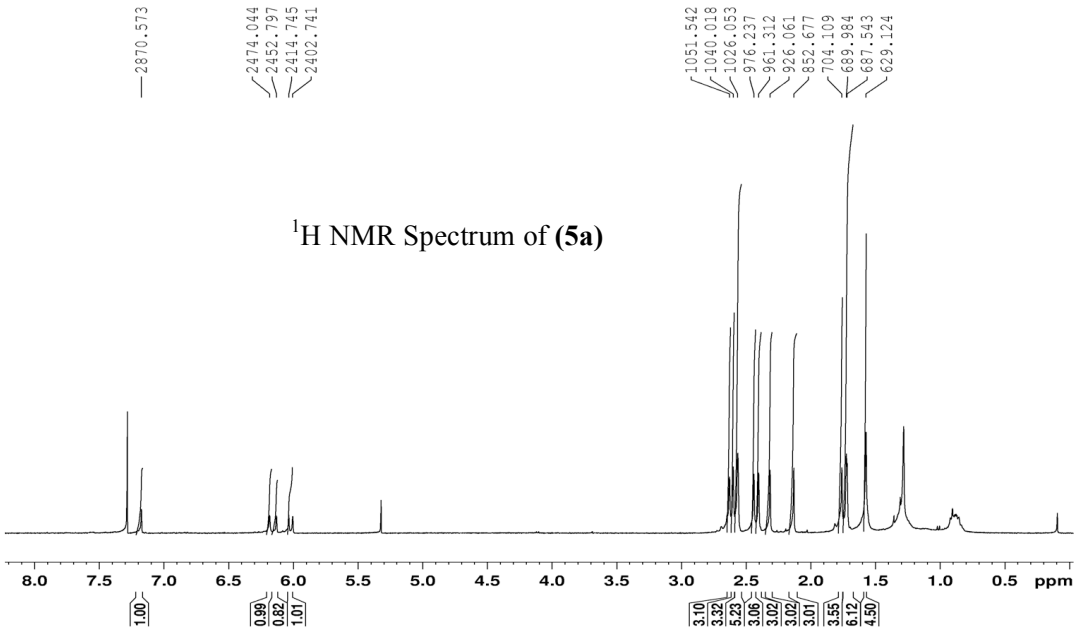

^{1}H NMR Spectrum of **(5a)**

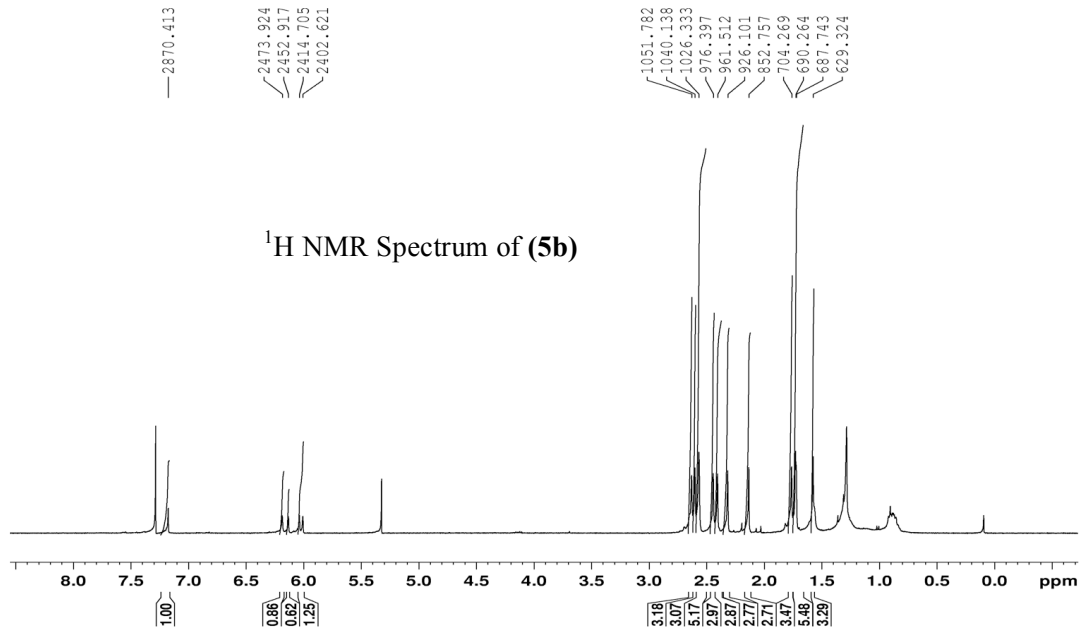

^{1}H NMR Spectrum of **(5b)**

A.3.2. Mass Spectra

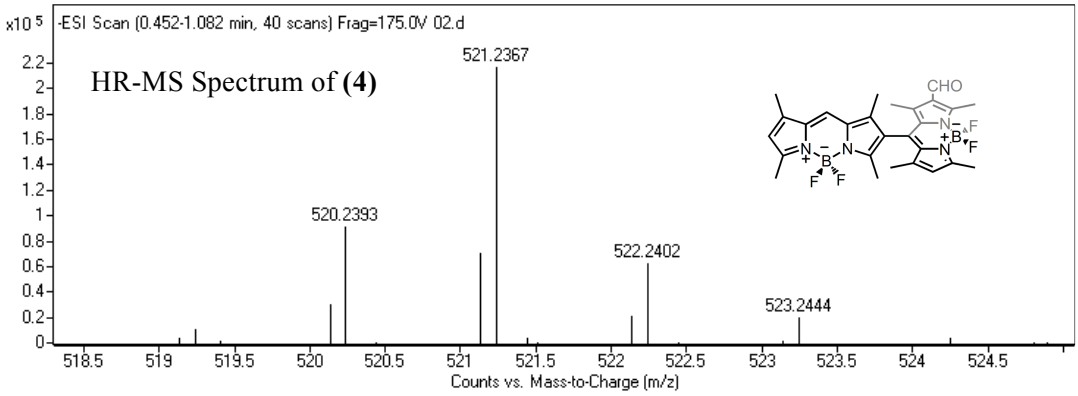

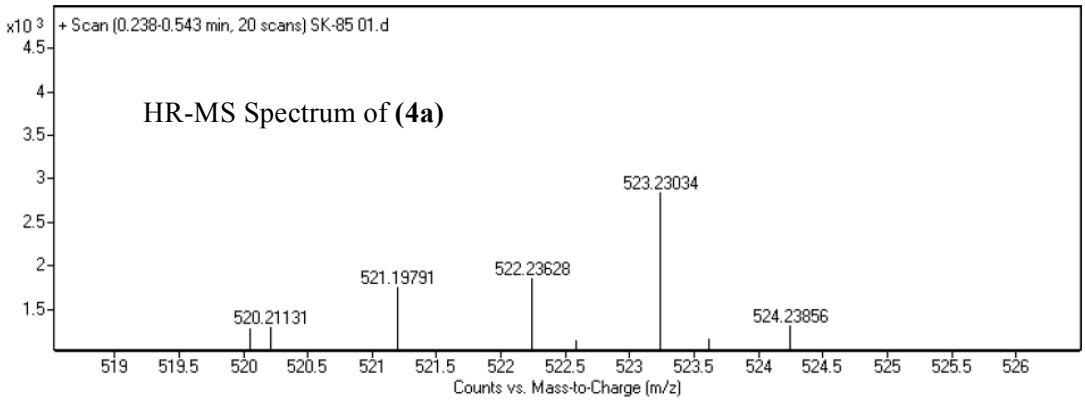
x10 3
+ Scan (0.238-0.543 min, 20 scans) SK-85 01.d
HR-MS Spectrum of (4a)
523.23034
521.19791
522.23628
520.21131
524.23856
Counts vs. Mass-to-Charge (m/z)

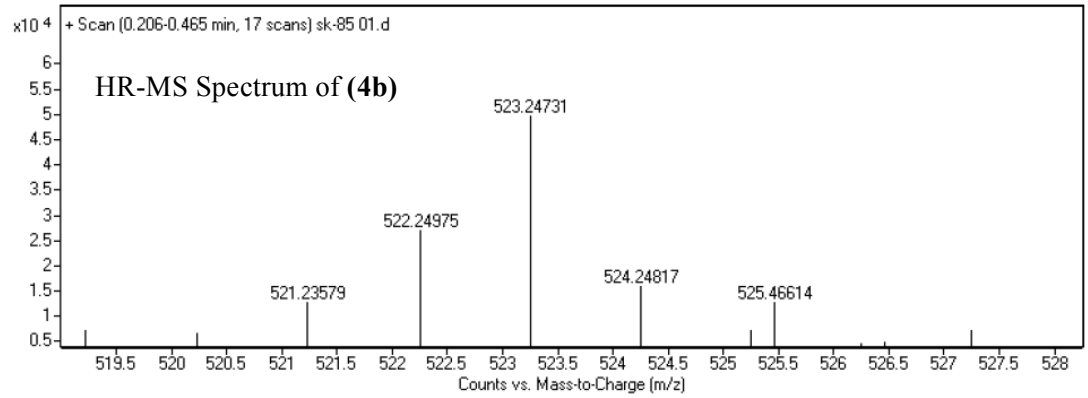
x10 4
+ Scan (0.206-0.465 min, 17 scans) sk-85 01.d
HR-MS Spectrum of (4b)
523.24731
522.24975
524.24817
521.23579
525.46614
Counts vs. Mass-to-Charge (m/z)

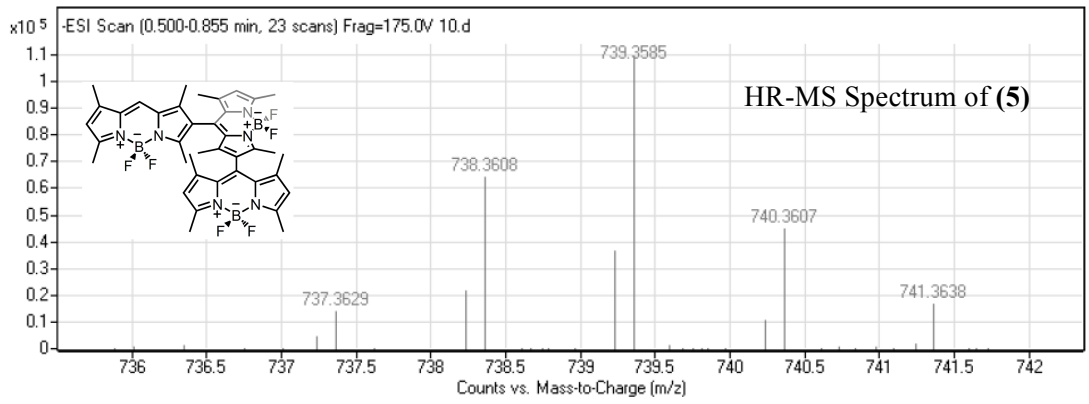
x10 5
-ESI Scan (0.500-0.855 min, 23 scans) Frag=175.0V 10.d
HR-MS Spectrum of (5)
739.3585
738.3608
740.3607
737.3629
741.3638
Counts vs. Mass-to-Charge (m/z)

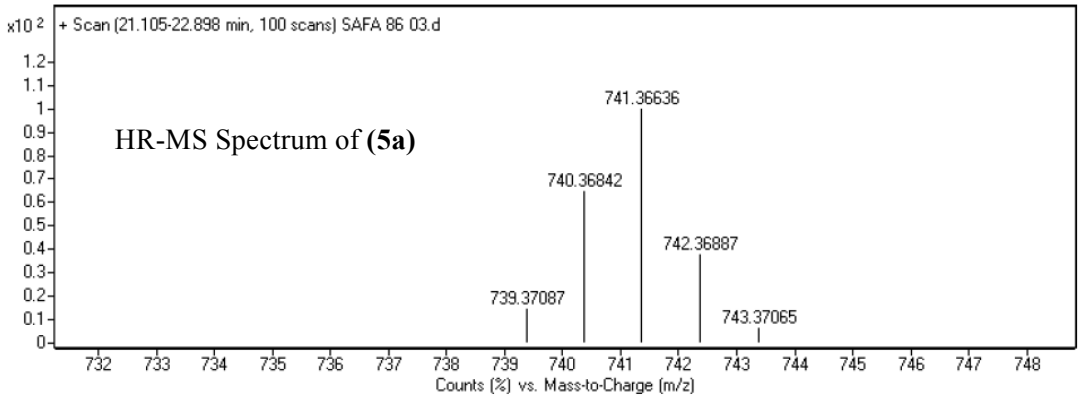

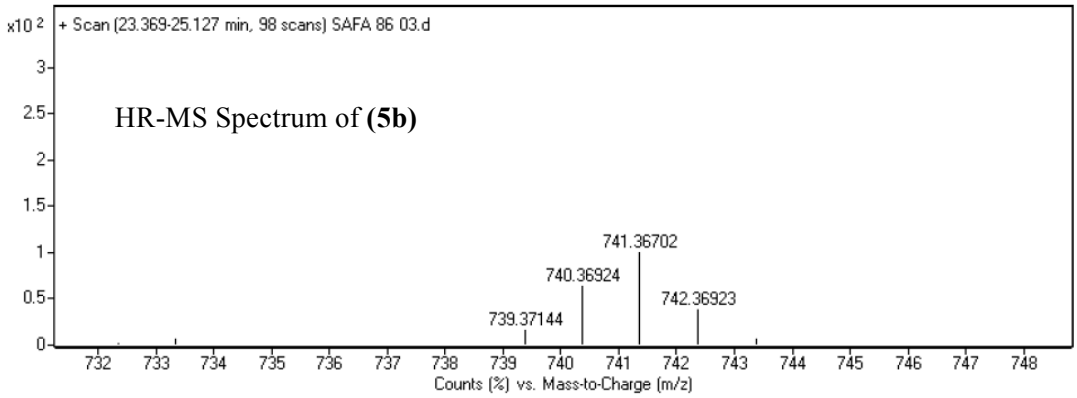

A.4. Controlled Singlet Oxygen Generation on Gold Nanorods: Advancing Photodynamic Therapy

A.4.1. ^{1}H and ^{13}C NMR Spectra

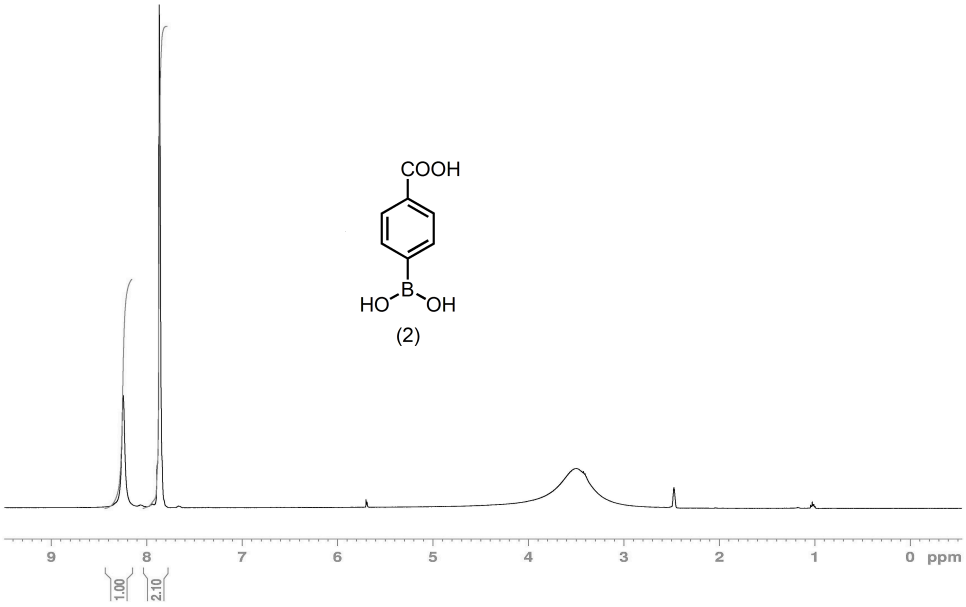
COOH
HO
B
OH
(2)
9
8
7
6
5
4
3
2
1
0 ppm
1.00
2.10

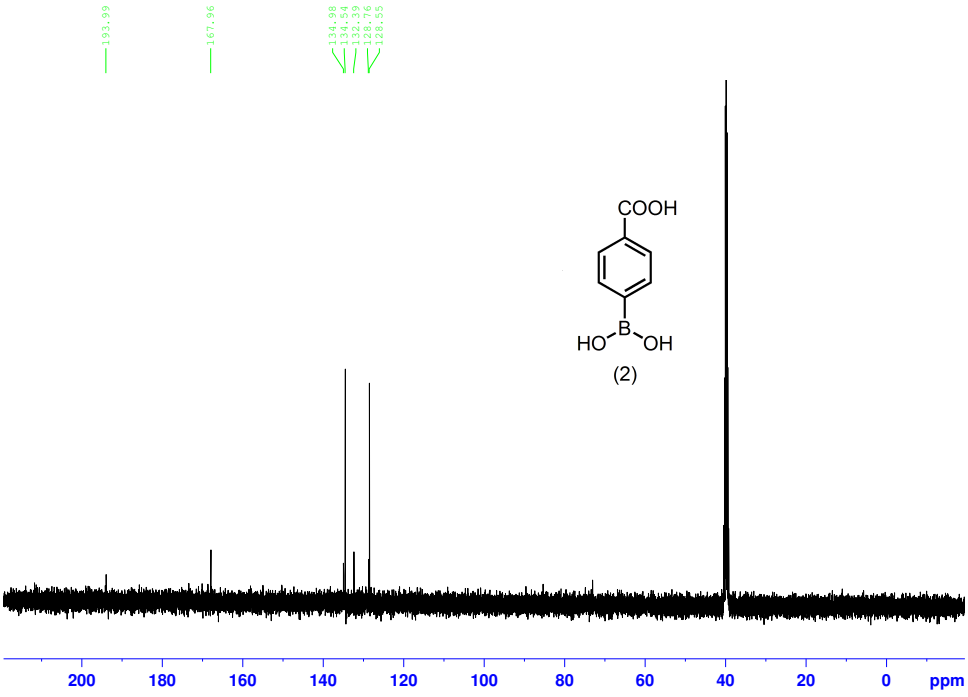
193.99
167.96
134.98
134.54
132.39
128.76
128.55
COOH
HO
B
OH
(2)
200
180
160
140
120
100
80
60
40
20
0
ppm

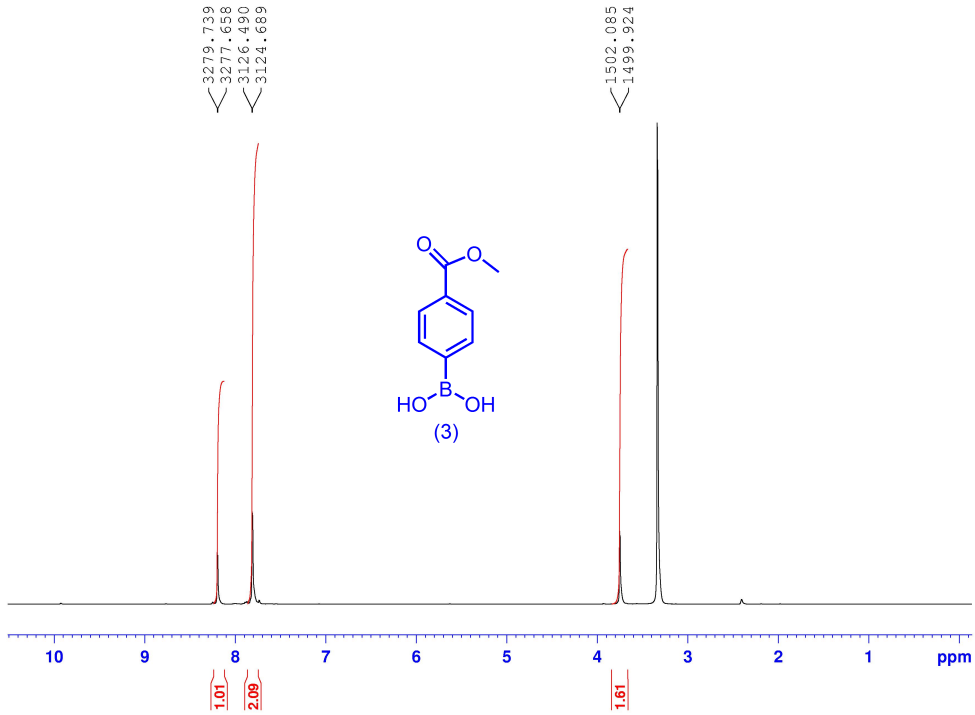
3279.739
3277.658
3126.490
3124.689
1502.085
1499.924
HO
B
OH
O
O
(3)
10
9
8
7
6
5
4
3
2
1
ppm
1.01
2.09
1.61

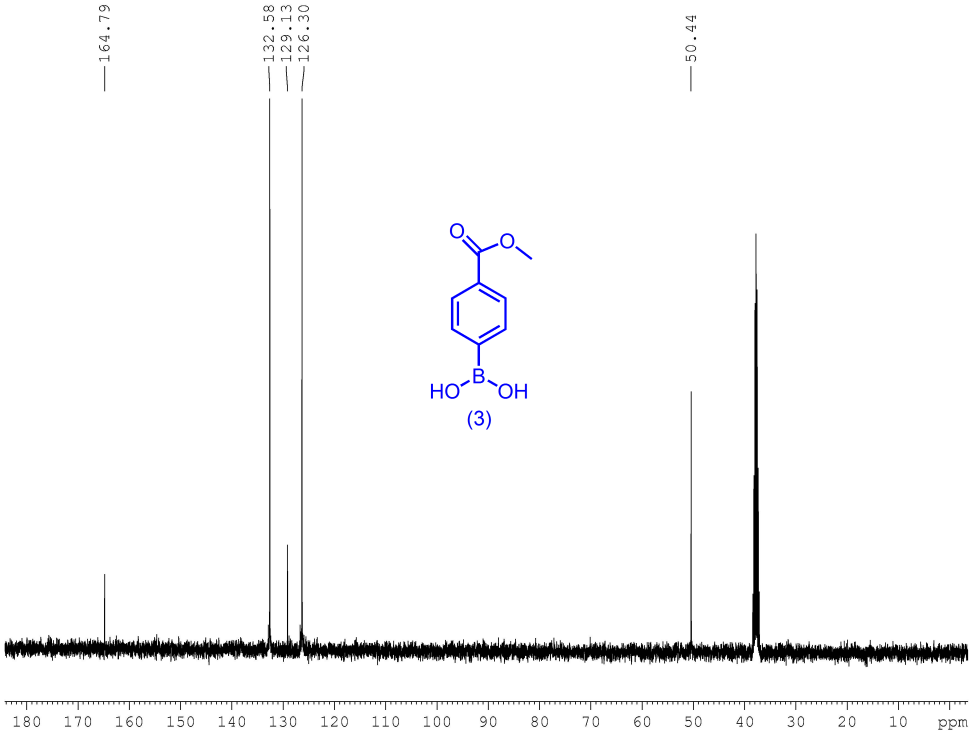
164.79
132.58
129.13
126.30
50.44
HO
B
OH
O
O
(3)
180
170
160
150
140
130
120
110
100
90
80
70
60
50
40
30
20
10
ppm

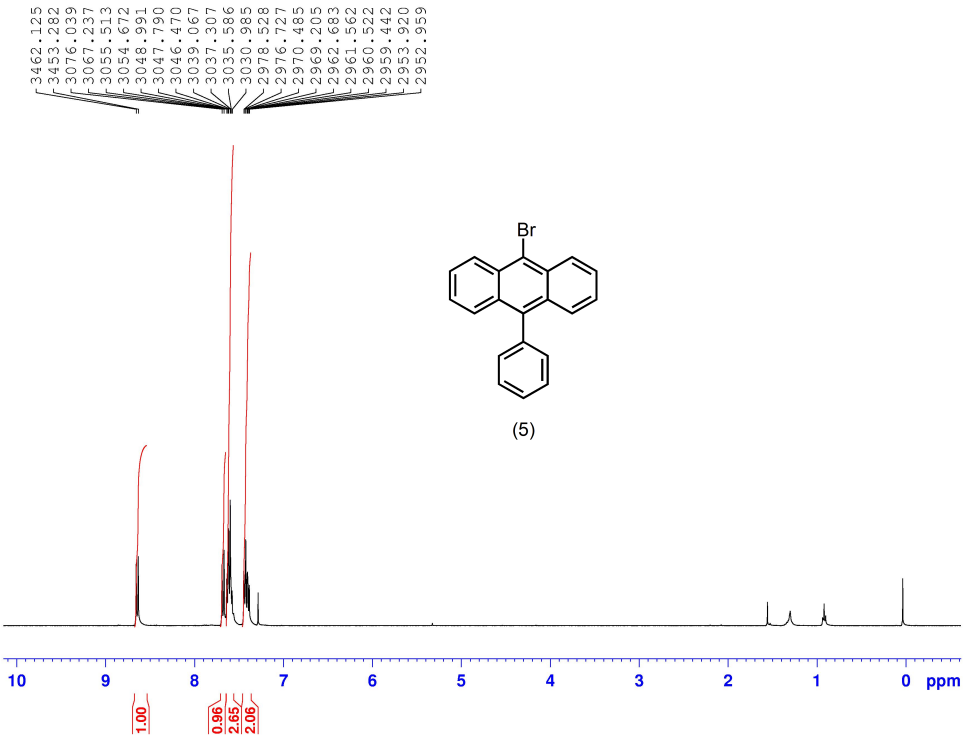
3462.125
3453.282
3076.039
3067.237
3055.513
3054.672
3048.991
3047.790
3046.470
3039.067
3037.307
3035.586
3030.985
2978.528
2976.727
2970.485
2969.205
2962.683
2961.562
2960.522
2959.442
2953.920
2952.959
Br
(5)
10
9
8
7
6
5
4
3
2
1
0
ppm
1.00
0.96
2.65
2.06

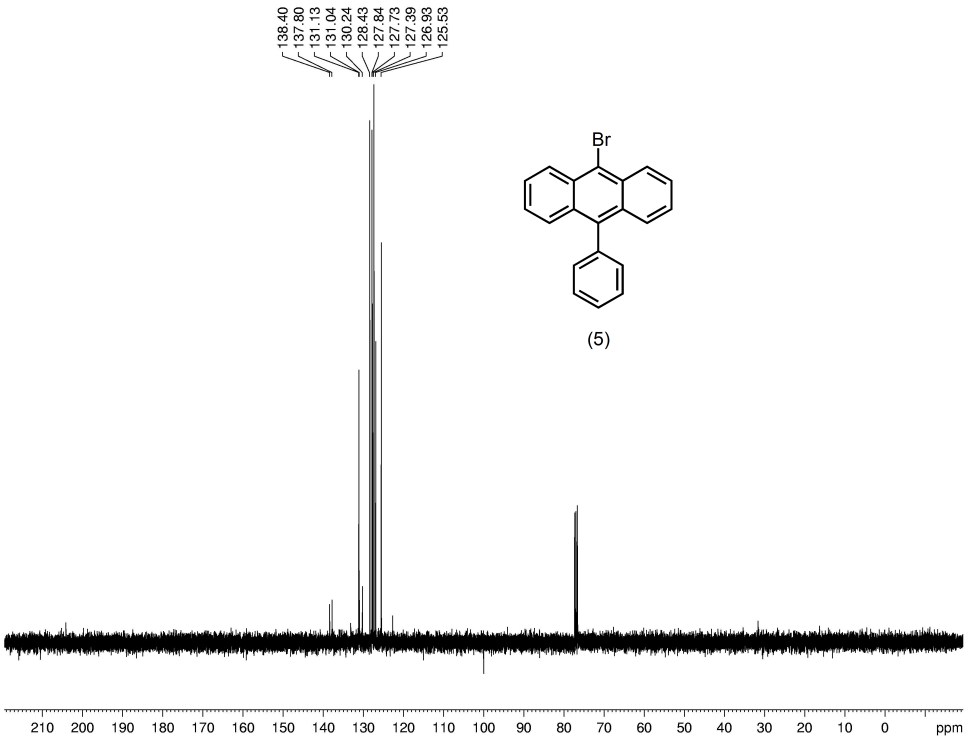
138.40
137.80
131.13
131.04
130.24
128.43
127.84
127.73
127.39
126.93
125.53
Br
(5)
210
200
190
180
170
160
150
140
130
120
110
100
90
80
70
60
50
40
30
20
10
0
ppm

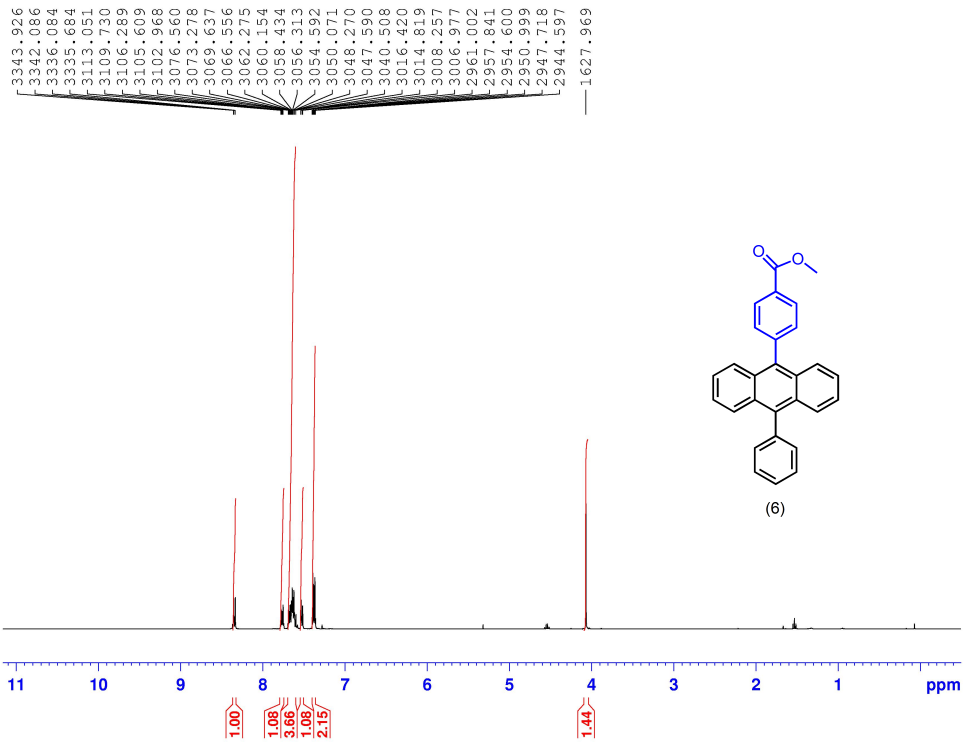
3343.926
3342.086
3336.084
3335.684
3113.051
3109.730
3106.289
3105.609
3102.968
3076.560
3073.278
3069.637
3066.556
3062.275
3060.154
3058.434
3056.313
3054.592
3050.071
3048.270
3047.590
3040.508
3016.420
3014.819
3008.257
3006.977
2961.002
2957.841
2954.600
2950.999
2947.718
2944.597
1627.969
(6)
11
10
9
8
7
6
5
4
3
2
1
ppm
1.00
1.08
3.66
1.08
2.15
1.44

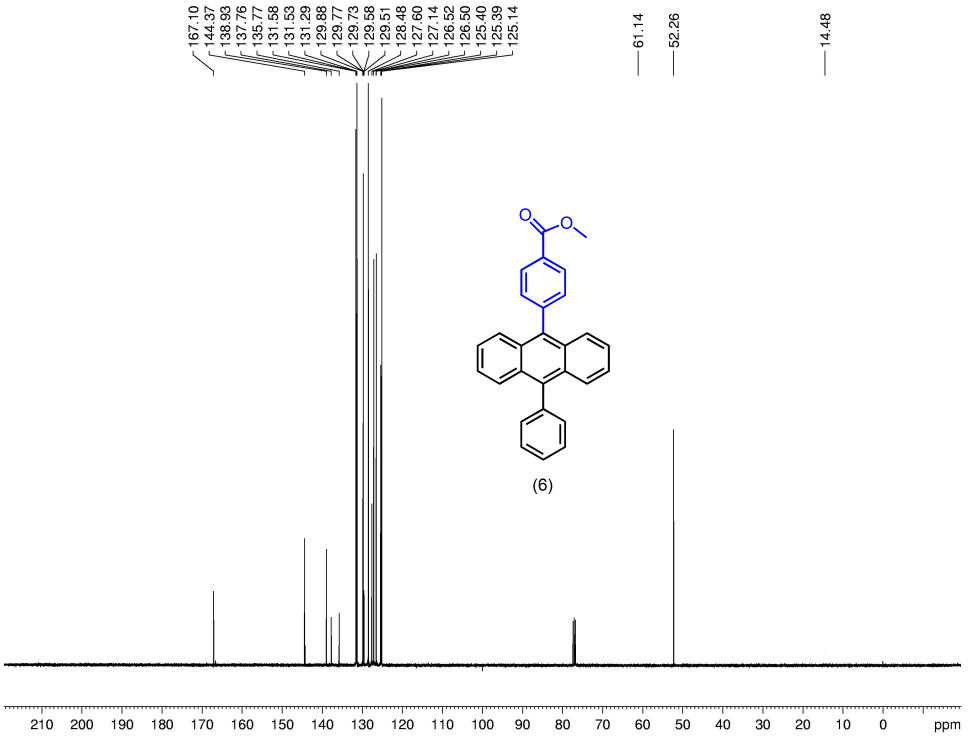
167.10
144.37
138.93
137.76
135.77
131.58
131.53
131.29
129.88
129.77
129.73
129.58
129.51
128.48
127.60
127.14
126.52
126.50
125.40
125.39
125.14
61.14
52.26
14.48
(6)
210
200
190
180
170
160
150
140
130
120
110
100
90
80
70
60
50
40
30
20
10
0
ppm

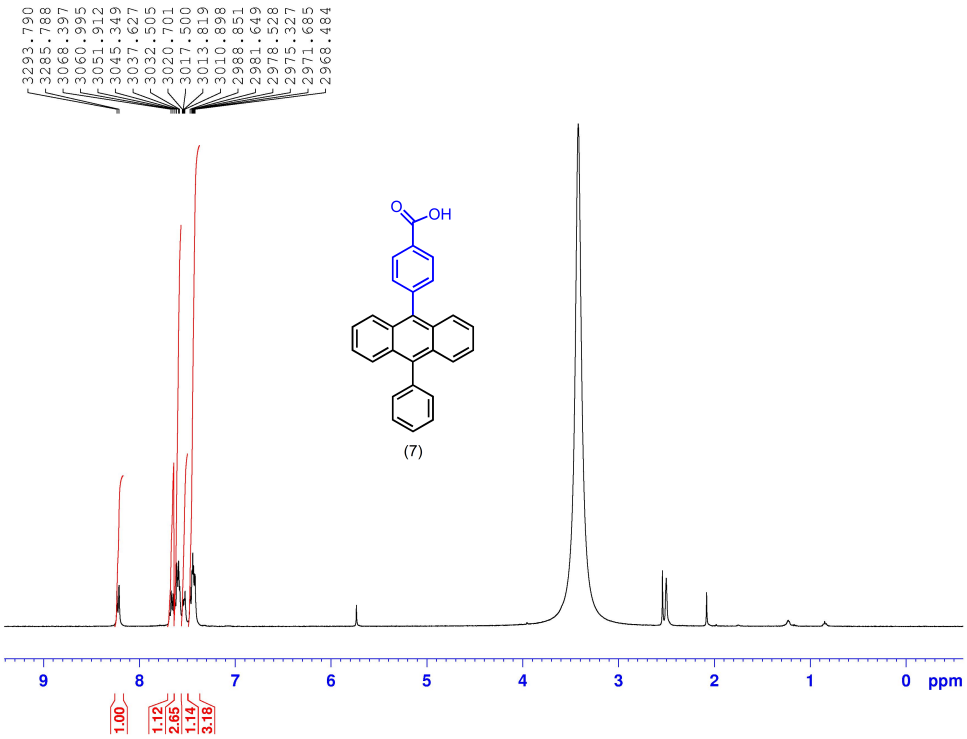
3293.790
3285.788
3068.397
3060.995
3051.912
3045.349
3037.627
3032.505
3020.701
3017.500
3013.819
3010.898
2988.851
2981.649
2978.528
2975.327
2971.685
2968.484
OH
O
(7)
9
8
7
6
5
4
3
2
1
0
ppm
1.00
1.12
2.65
1.14
3.18

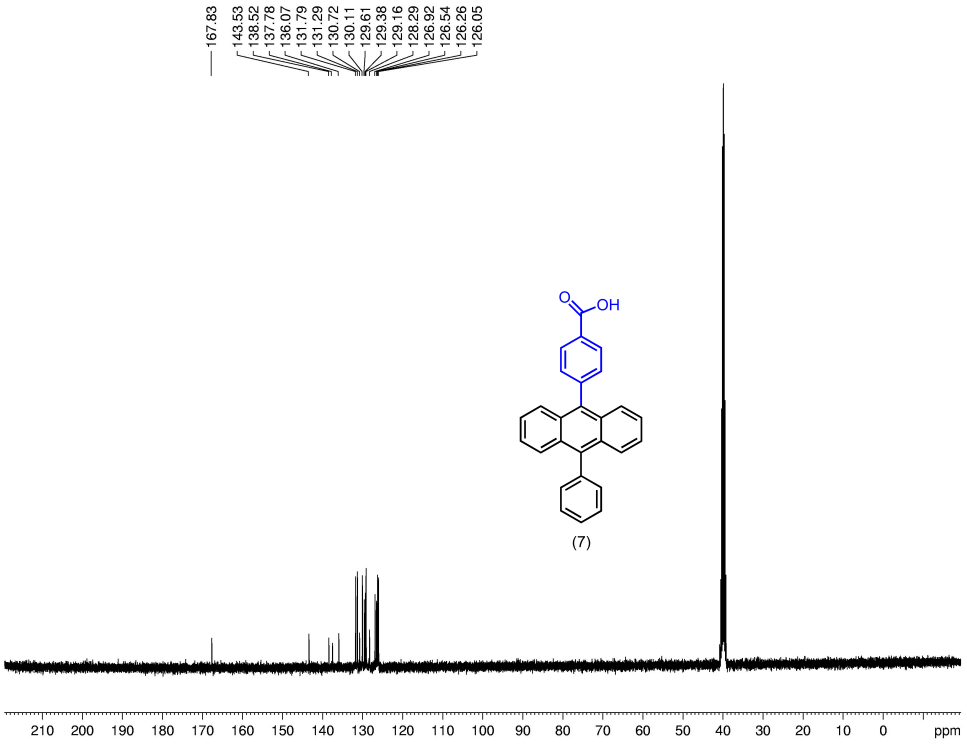
167.83
143.53
138.52
137.78
136.07
131.79
131.29
130.72
130.11
129.61
129.38
129.16
128.29
126.92
126.54
126.26
126.05
OH
O
(7)
210
200
190
180
170
160
150
140
130
120
110
100
90
80
70
60
50
40
30
20
10
0
ppm

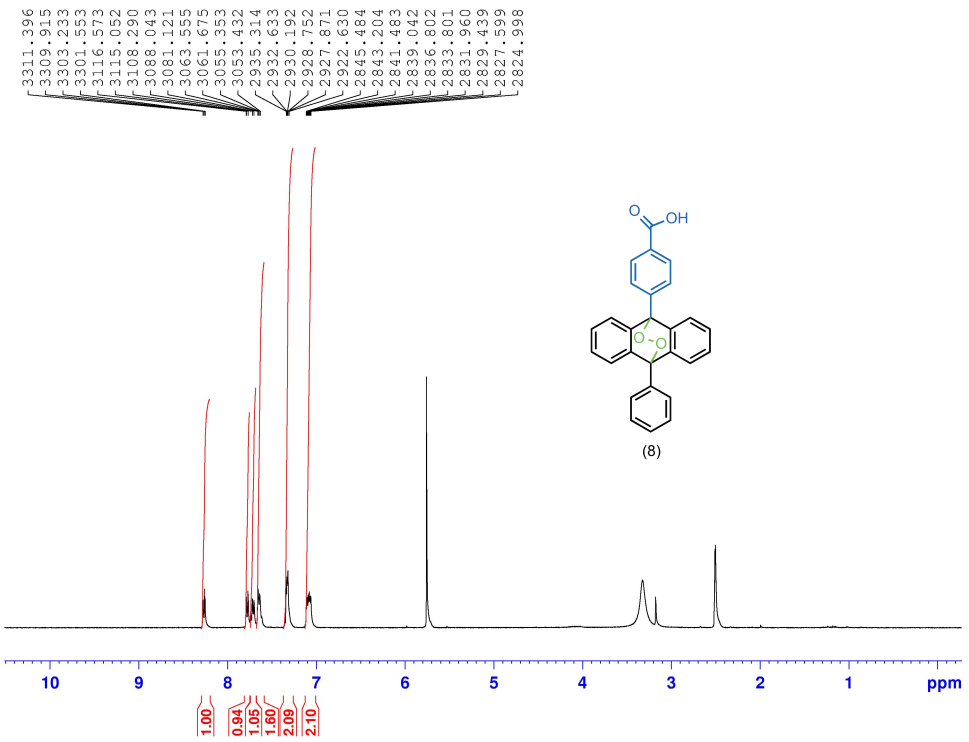
3311.396
3309.915
3303.233
3301.553
3116.573
3115.052
3108.290
3088.043
3081.121
3063.555
3061.675
3055.353
3053.432
2935.314
2932.633
2930.192
2928.752
2927.871
2922.630
2845.484
2843.204
2841.483
2839.042
2836.802
2833.801
2831.960
2829.439
2827.599
2824.998
O
OH
O
O
(8)
10
9
8
7
6
5
4
3
2
1
ppm
1.00
0.94
1.05
1.60
2.09
2.10

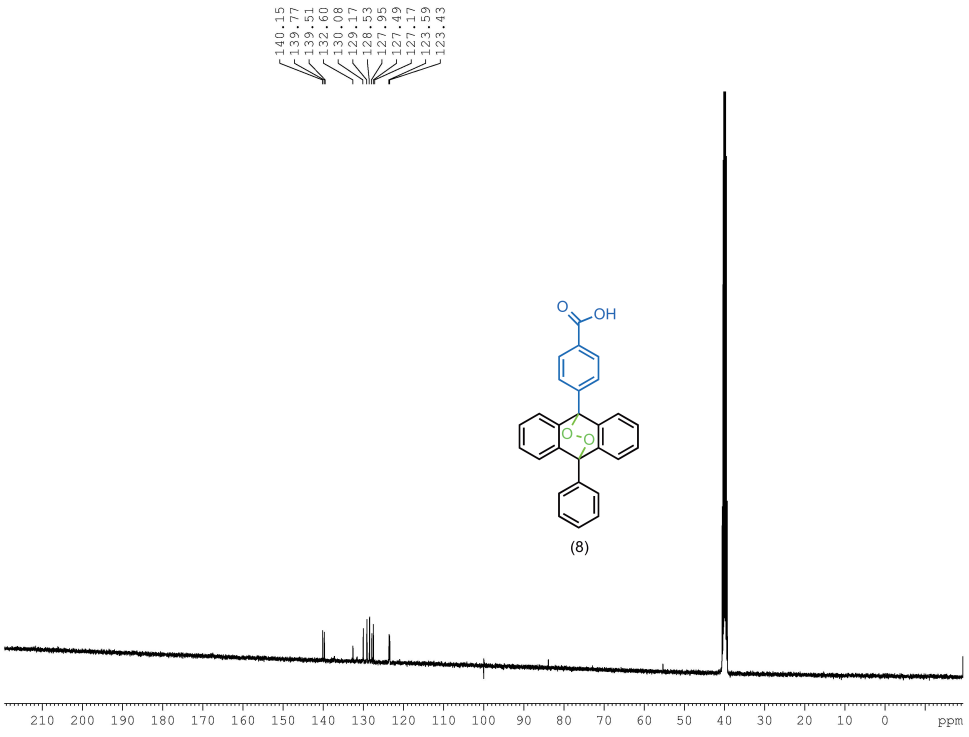
140.15
139.77
139.51
132.60
130.08
129.17
128.53
127.95
127.49
127.17
123.59
123.43
O
OH
O
O
(8)
210
200
190
180
170
160
150
140
130
120
110
100
90
80
70
60
50
40
30
20
10
0
ppm

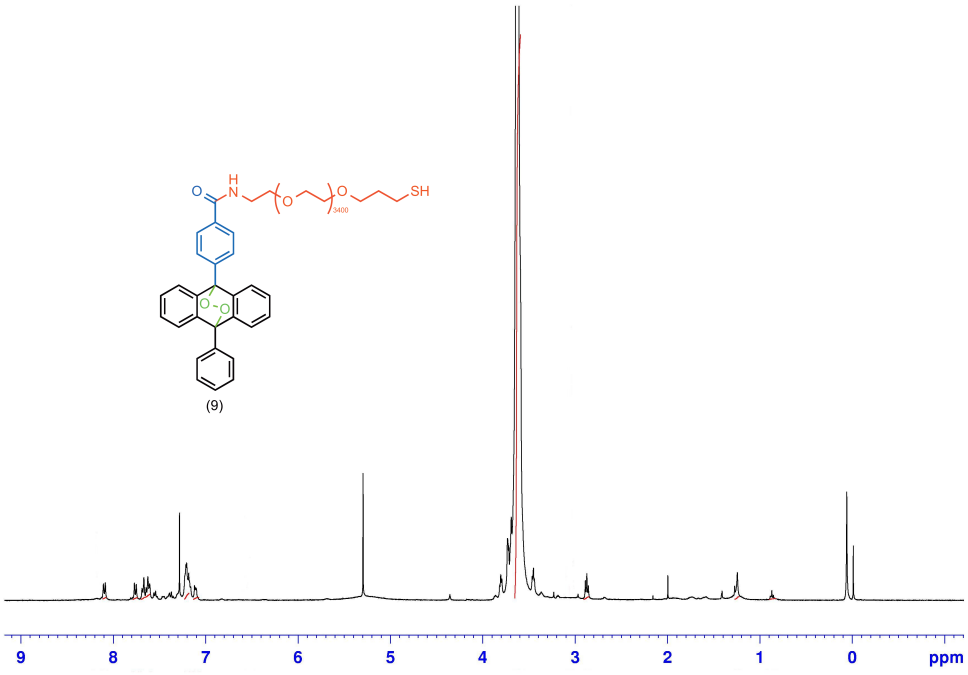
(9)
9
8
7
6
5
4
3
2
1
0
ppm

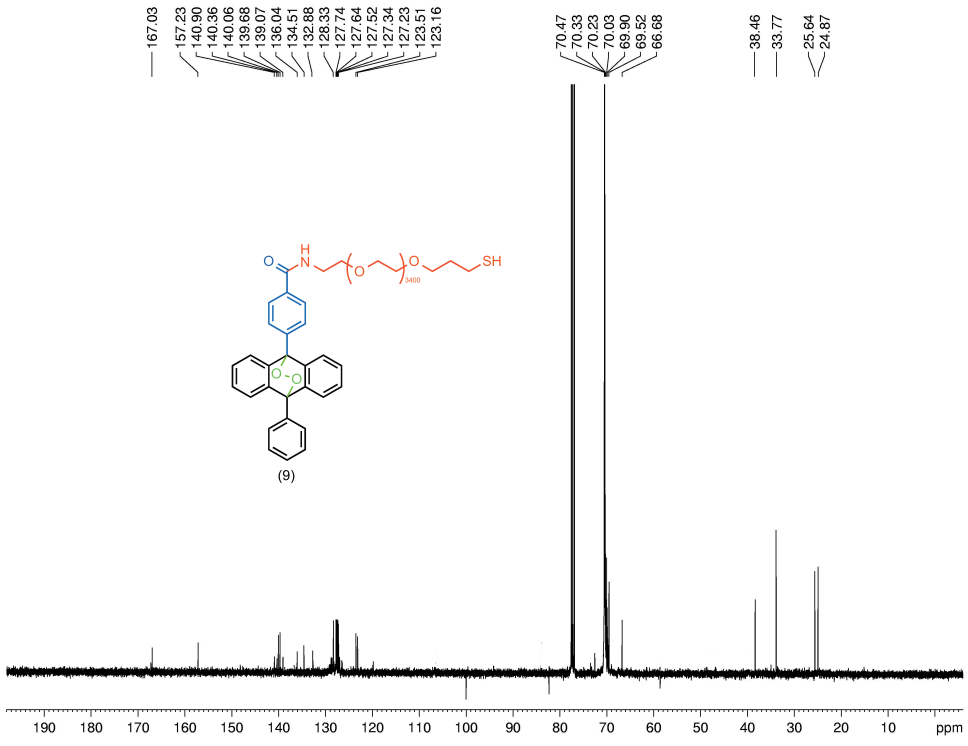
167.03
157.23
140.90
140.36
140.06
139.68
139.07
136.04
134.51
132.88
128.33
127.74
127.64
127.52
127.34
127.23
123.51
123.16
70.47
70.33
70.23
70.03
69.90
69.52
66.68
38.46
33.77
25.64
24.87
(9)
190
180
170
160
150
140
130
120
110
100
90
80
70
60
50
40
30
20
10
ppm

A.4.1. Mass Spectra

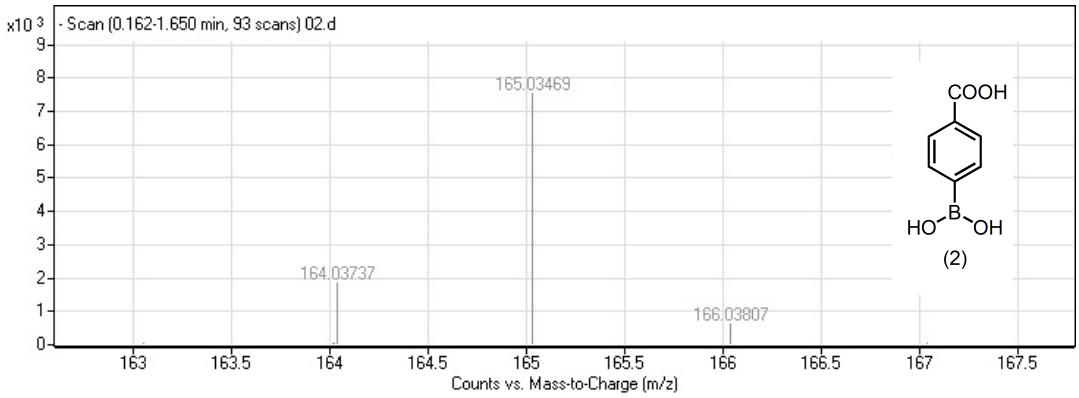

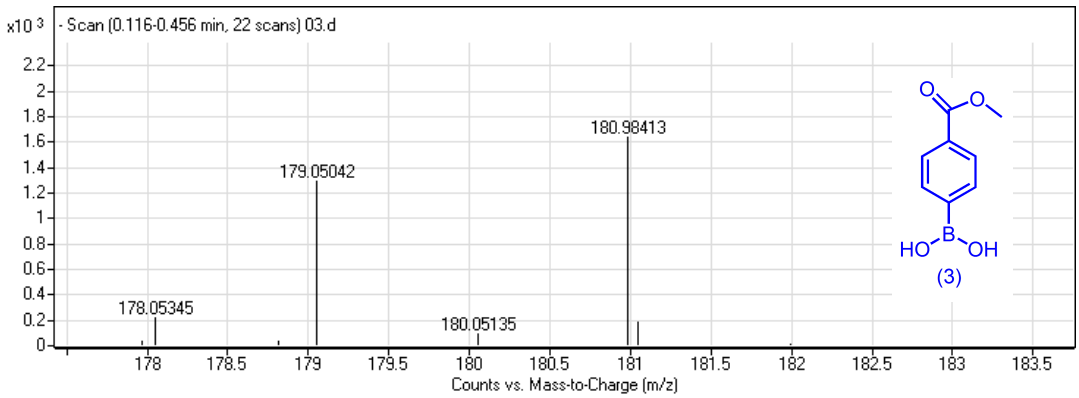

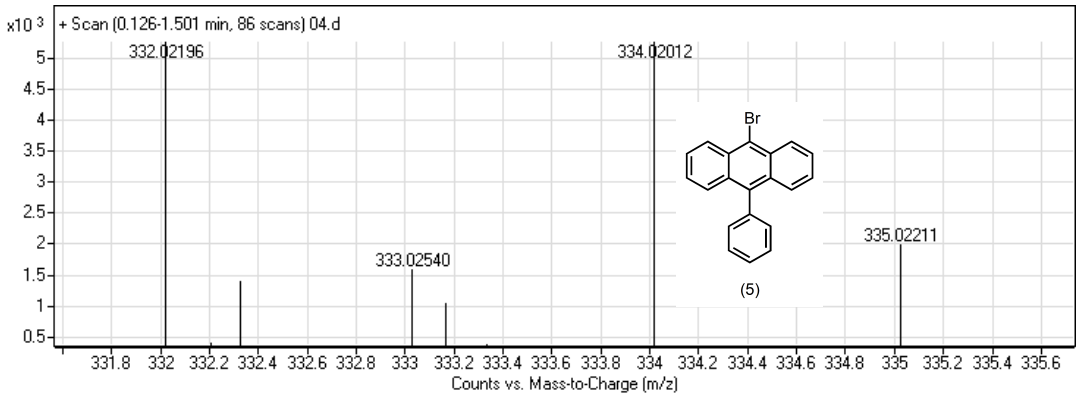

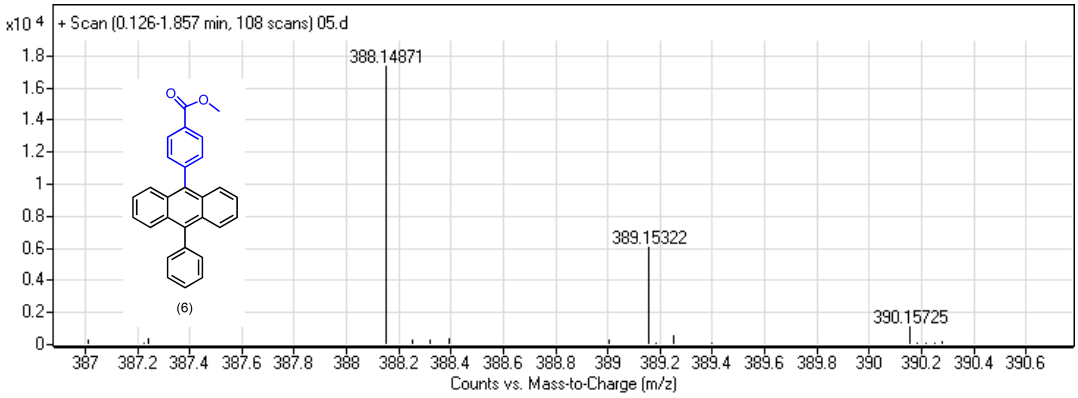
x10 4
+ Scan (0.126-1.857 min, 108 scans) 05.d
388.14871
389.15322
390.15725
(6)
Counts vs. Mass-to-Charge (m/z)

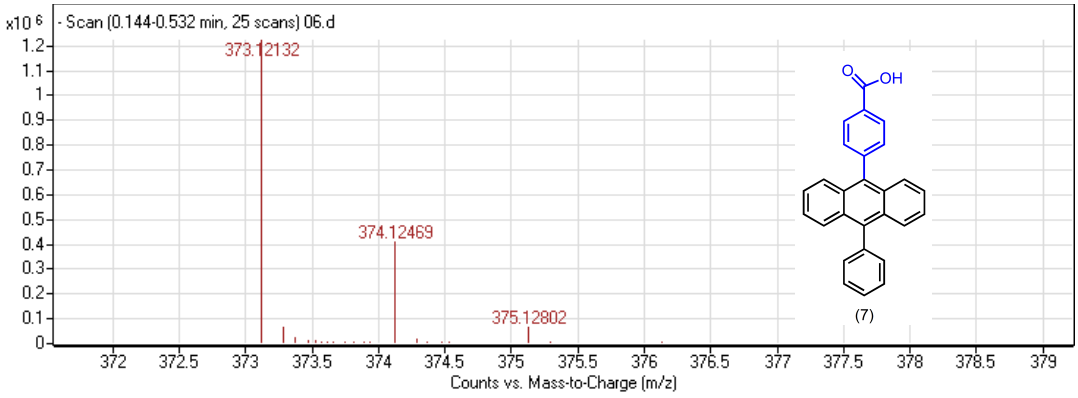
x10 6
- Scan (0.144-0.532 min, 25 scans) 06.d
373.12132
374.12469
375.12802
OH
(7)
Counts vs. Mass-to-Charge (m/z)

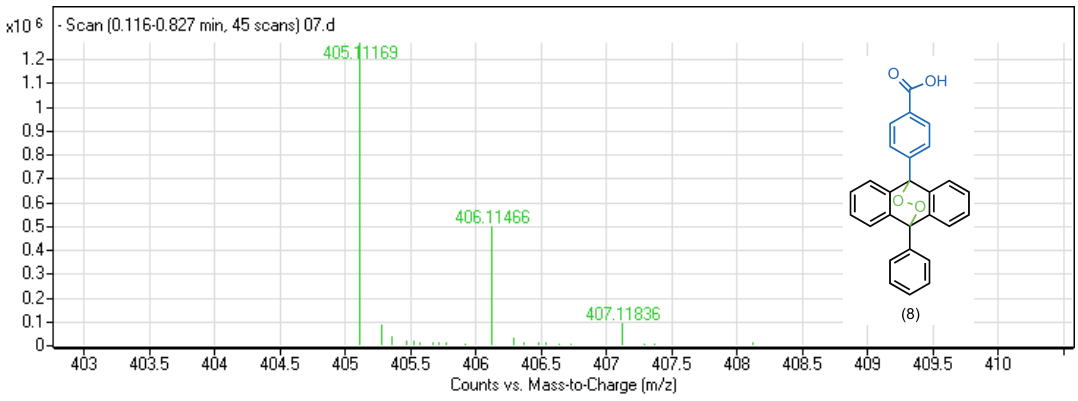
x10 6
- Scan (0.116-0.827 min, 45 scans) 07.d
405.11169
406.11466
407.11836
OH
(8)
Counts vs. Mass-to-Charge (m/z)